

# Numerical Relativity and Inhomogeneous Cosmologies

Simon David Hern  
Wolfson College

A dissertation submitted to the  
University of Cambridge  
for the degree of  
Doctor of Philosophy

August 1999

The work in sections 6.2 and 6.3 of this dissertation was done in collaboration with my supervisor, J. M. Stewart, and has been published as Hern and Stewart 1998. In addition, parts of this work have made use of a computer code (the adaptive mesh refinement algorithm described in chapter 3) which is an improved version of a code originally written by my supervisor. All other work described in this dissertation is my own.

This work was supported by a studentship from the Engineering and Physical Sciences Research Council.

I would like to thank

my supervisor, John Stewart, for initiating this project and nursing it through to completion with a wealth of helpful suggestions;

my parents and my sister, Trudy Lianne, for never being more than a phone call away;

and all the other people who have provided help or encouragement over the last few years, with individual name-calls being deserved by the following proof-readers and (coffee) drinking buddies: Roland Higginson, Madelaine Crush, Margarida Cunha, David Halls, Sean Rooney, Myriam Champenois, Tiarnán ÓCléirigh, Clara Ovenston and Ian Hawke.

# Contents

# Chapter 1.

## Introductory Comments

Some brief comments are made here as way of introduction to highlight themes that recur throughout this dissertation.

The field of numerical relativity is concerned with the development and application of methods for the generation of approximate numerical solutions for relativistic theories of gravity (possibly coupled to non-gravitational fields). While the subject is of relatively recent origin, the substantial increase in availability of computing power over recent years has led to it becoming very broad in scope. A history of the development of numerical relativity as a field of research can be reconstructed from the many review articles that have been written over the years, a sample of which are Piran 1981, Stewart 1984, Hobill and Smarr 1989, Bona and Massó 1993, Seidel 1996 and 1998, and Cook and Teukolsky 1999.

Much of the recent research in numerical relativity has concentrated on the modelling of collisions between black holes, the motivation for this being the possibility of observing such events through gravitational wave astronomy. As a contrast to this, the present work uses numerical methods to simulate inhomogeneous cosmological spacetimes, and while these spacetimes are not claimed to be realistic models of the observed universe (being ruled out by their lack of matter content and their high degrees of symmetry) they do provide a good arena in which new numerical and mathematical approaches can be tested.

This dissertation can be divided into three main parts. The first part comprises chapters 2 and 3 and discusses numerical techniques (specifically finite difference and high-resolution methods, and adaptive mesh refinement) that can be used to produce approximate solutions to Einstein's field equations. The mathematical representation of these equations is the subject of the second part, with chapter 4 examining hyperbolic formulations and chapter 5 examining the properties of different gauge conditions. The third part of this work (chapters 6 and 7) presents results from numerical simulations of inhomogeneous vacuum cosmologies with planar and  $U(1)$  symmetries. This dissertation concludes with a summary of the main results in chapter 8.

What follows is a summary of the contents of this dissertation, with emphasis being placed on ideas that connect the different chapters.

### *Development of Numerical Software*

In this dissertation results are presented from numerical simulations of a range of evolution systems which are introduced in chapters 4, 5, 6 and 7 (more details can be found in particular in sections 4.3, 6.2, 6.4 and 7.2). All of these simulations have been performed using a computer code developed for the purpose by the author. The code is capable of generating numerical solutions to first-order systems of hyperbolic partial differential equations in one or two spatial dimensions. It

implements two advanced numerical methods initially developed within the context of computational fluid dynamics.

The code numerically integrates systems of evolution equations using a multi-dimensional high-resolution algorithm which is described in section 2.3. This integration method operates by solving a sequence of Riemann problems for the equations under consideration, and provides significant improvements in performance over standard finite difference methods (discussed in section 2.1) when used to evolve solutions containing discontinuities. Riemann solvers for the systems of equations investigated here are developed in sections 2.2 and 4.3. While evolution schemes based on Riemann solvers have been used previously in numerical studies of relativistic hydrodynamics, this work represents the first use of such methods for the evolution of gravitational fields.

The high-resolution integration scheme is complemented by the inclusion in the code of adaptive mesh refinement capabilities, described in detail in chapter 3, which allow the local resolution of a simulation to vary dynamically in response to changing features of the evolved solution. Substantial improvements in performance have been achieved for the numerical simulations of chapters 5, 6 and 7 through the use of this method. (In addition, the code takes advantage of the availability of multiple processors, as discussed in section 3.4.) Although adaptive mesh refinement has previously been used in a number of one-dimensional simulations in numerical relativity (see the introduction to chapter 3), the present work represents one of only a few applications of the technique to relativistic simulations in more than one spatial dimension.

### *Formulations of the Einstein Field Equations*

One of the main topics investigated in this dissertation is the use of different formulations of the Einstein equations as bases for numerical simulations. In sections 6.1 and 7.1 reductions of the Einstein equations are introduced for two cosmological models having particular spatial symmetries, while in section 4.2 a family of formulations of the field equations suitable for evolving fully general spacetimes is discussed. Numerical results for these evolution systems are compared and contrasted in section 7.3, and some reasons are suggested for the differences in performance that are observed.

Formulations of the Einstein equations can be categorized according to various mathematical properties that they may possess, and for numerical simulations it may be judged desirable (section 4.1) for an evolution system to be strongly hyperbolic and to have only physically relevant characteristic speeds. Section 4.2 describes the derivation of a family of hyperbolic formulations of the Einstein equations which generalize an evolution system proposed by Frittelli and Reula such that the characteristic speeds can all be made to be physically relevant. Numerical simulations are described in this dissertation which are the first to employ the Frittelli-Reula hyperbolic formulation, and which are among only a relatively small number of numerical tests of hyperbolic formulations that have been carried out in more than one spatial dimension. Section 4.3 discusses some of the issues involved in implementing the Frittelli-Reula system for numerical work, and in particular explains how it can be used in conjunction with the advanced numerical methods described in chapter 2.

All of the evolution systems studied in this dissertation resolve ambiguities in the choice of spacetime coordinates by employing the harmonic time slicing condition. Section 5.2 discusses this and alternative gauge conditions that may be used in numerical simulations. Analytic results are derived which describe the reasonably general circumstances under which coordinate singularities form in harmonic slicings of some example spacetimes. These results are verified through computer simulations, and different slicings of the same spacetime are compared using an numerical algorithm presented in section 5.1.

### *Simulations of Cosmological Spacetimes*

The numerical methods of chapters 2 and 3 are used in this work to evolve solutions to cosmological models having varying degrees of inhomogeneity. In chapter 5 homogeneous Kasner spacetimes are evolved as part of an investigation into gauge effects in numerical simulations. Chapter 6 considers the Gowdy cosmological models which have two spacelike Killing vectors, while in chapter 7 more general spacetimes with  $U(1)$  isometry groups are studied using Moncrief's reduction of the field equations. These cosmological models are all vacuum and all have the spatial topology of a three-torus.

Although the cosmological spacetimes studied in this dissertation are not realistic models of the observed universe, they nevertheless provide a setting within which a range of physical phenomena can be investigated. In sections 6.2 and 7.2 results are presented from numerical simulations of inhomogeneous spacetimes as they collapse towards cosmological 'big bang' singularities; particular attention is paid to the spikes and other fine-scale features that are found to develop in the components of the evolved metrics. This behaviour appears to be a generic feature of gravitational collapse.

Extrapolation of the results for simulations of collapsing cosmologies allows a picture to be constructed of the spacetime behaviour at the 'big bang' singularity. In section 6.3 such numerical evidence is seen to suggest that the singularities in the Gowdy cosmological models are asymptotically velocity-term dominated, but that spatial derivatives in the Einstein equations do not become negligible as a singularity is approached.

Section 6.4 investigates the behaviour of gravitational waves in expanding cosmologies. Large amplitude waves close to the cosmological singularity are found to lead to the formation of fine-scale spatial structure (in the sense that modes of high frequency are excited); however numerical evidence suggests that at late times the waves behave much like linear perturbations of homogeneous spacetimes, regardless of their initial amplitudes. Differences between linear and nonlinear gravitational waves are investigated by comparing numerical simulations to results from linearized theory, and it is argued that some of the behaviour that has been attributed to nonlinear gravitational waves in the literature is better thought of as being a gauge effect.

### *Fine-Scale Features in Cosmological Simulations*

For numerical simulations of collapsing inhomogeneous cosmological models, it is found (sections 6.2 and 7.2) that features can develop in the evolved solutions on spatial scales which become increasingly small as the cosmological singularity is approached. These fine-scale features are very difficult to accurately capture using traditional numerical approaches, and the adaptive mesh refinement technique described in chapter 3 proves to be a very useful tool in this regard: applied to the simulations of planar cosmologies in chapter 6 it allows accurate results to be produced in very much shorter times than would otherwise be required, and for the simulations of  $U(1)$ -symmetric cosmologies in chapter 7 it allows much higher resolutions to be attained than the available computer resources would otherwise permit. (The question of whether fine-scale structure can also form in expanding cosmologies is addressed in section 6.4.)

Making use of some ideas on the identification of coordinate-independent behaviour discussed in section 5.1, it is argued that the fine-scale features found in the collapsing cosmological simulations of chapters 6 and 7 are physically relevant: they are observed in scalar quantities such as the invariants of the curvature tensor as well as in the metric components, and they are small with respect to proper measures of distance. The importance of this result is made clear by its contrast to the behaviour found in the numerical simulations of section 5.2. There, homogeneous Kasner spacetimes are evolved using harmonic time slicing, and for foliations in which coordinate singularities appear the metric components develop fine-scale features which are superficially similar to those found in the inhomogeneous models, but which are clearly without any physical significance.



# Chapter 2.

## High-Resolution Methods

The present work is concerned with the development and testing of methods for generating approximate numerical solutions to the vacuum field equations of general relativity. In later chapters (in particular chapter 4) the field equations are presented as a variety of first-order systems of hyperbolic partial differential equations, numerical solutions to which can be obtained by integrating in time sets of data specified on appropriate initial hypersurfaces. The present chapter describes the basic numerical methods used here to perform these integrations. There exists a vast literature discussing the theoretical and practical aspects of such numerical methods, and a formal introduction to the subject is beyond the scope of the present discussion; rather, this chapter is intended as a ‘user’s guide’ to the methods employed for reference in later chapters. Very much more extensive discussions can be found in the books by LeVeque (1992), Godlewski and Raviart (1996), Gustafsson, Kreiss and Olinger (1995), Hirsch (1988, 1990), Potter (1973), Press et al. (1992, chapter 19), Sod (1985), and Toro (1997), among many others.

The most commonly used methods for generating numerical solutions to systems of partial differential equations are based on finite differences, and these are discussed in section 2.1. The strengths and weaknesses of the standard finite difference methods are well understood, and they are used in the present work as a reference against which the performance of more sophisticated numerical methods may be judged. The methods discussed in this chapter are described in forms that are applicable to problems in one and two spatial dimensions.

A significant limitation of standard finite difference methods is that they usually only produce acceptable results when the evolved solution is sufficiently smooth. This is important because in many applications the models being studied are known to admit solutions in which discontinuities form even for smooth initial data. Much research has been done in the field of computational fluid dynamics into the development of advanced numerical methods which are capable of accurately evolving solutions irrespective of their smoothness. Finite volume methods achieve this by analysing a series of Riemann problems for the evolution system, and section 2.2 discusses how solutions to Riemann problems can be determined in some basic cases. The numerical simulations carried out in the present work use a particular finite volume method: the multi-dimensional high-resolution wave-propagation algorithm of LeVeque (1997). The appeal of this method is that it has been demonstrated to work on a range of different problems, and an implementation of it is freely available in the form of the CLAWPACK software (LeVeque 1998). A description of the method is given in section 2.3.

The main motivation for the use of high-resolution methods for work in numerical relativity is the need to correctly evolve the shock waves that occur in solutions to the Einstein equations when they are coupled to hydrodynamical sources. Even when the evolved spacetimes are vacuum (as is the case in the present work) it may be hoped that the use of a high-resolution method will

improve the accuracy of numerical results when steep gradients are present in the gravitational fields (a situation which appears to occur under a variety of circumstances). Furthermore, the ‘causal’ nature of such methods, which evolve solutions based on the propagation properties of different characteristic quantities, may simplify the imposition of physically realistic boundary conditions, for example at the horizon of a black hole.

## 2.1 Finite Difference Methods

This section summarizes some basic properties of standard one- and two-dimensional finite difference methods for the numerical evolution of solutions to first-order systems of hyperbolic partial differential equations. The evolution systems are assumed to be in flux-conservative form, and the finite difference methods considered here are numerically conservative. The use of operator splitting to extend the applicability of the methods to evolution systems with source terms is discussed.

### *Systems of Conservation Laws*

The systems of time-evolution equations considered in the present work are assumed to be expressible in the standard first-order form

$$\partial_t u(t, x, y) + \partial_x f(u) + \partial_y g(u) = s(u), \quad (2.1)$$

where  $u(t, x, y)$  is a vector of  $n$  unknown variables,  $f(u)$  and  $g(u)$  are *flux vectors* in the  $x$ - and  $y$ -directions respectively,  $s(u)$  is a vector of *source terms*, and  $\partial_t$ , etc. represent partial derivatives with respect to the independent variables. For the purposes of illustration, the system (2.1) is shown as depending on two spatial dimensions (coordinates  $x$  and  $y$ ) although the main points of the following discussion apply to systems in any number of dimensions.

The *Cauchy problem* for the system (2.1) comprises the determination of the value of  $u$  (at least within an interval of the coordinate  $t$ ) given that its value is known at an initial time  $t = t_0$ . It is assumed here that the evolution system is *hyperbolic* in the sense that the  $n \times n$  Jacobian matrices

$$A(u) = \frac{\partial f(u)}{\partial u} \quad \text{and} \quad B(u) = \frac{\partial g(u)}{\partial u} \quad (2.2)$$

have real eigenvalues and complete sets of eigenvectors, and consequently that the Cauchy problem is well posed. (A more complete discussion of hyperbolicity of systems of equations is given in section 4.1.)

In evolving solutions to systems of the form (2.1) numerically, it is usually possible to treat the influence of the source terms separately from the influence of the *transport part* (which is to say, the flux vectors  $f$  and  $g$ ). A splitting approach for doing this is described later in this section, and for much of this discussion it suffices to consider only evolution systems for which no source terms are present:

$$\partial_t u(t, x, y) + \partial_x f(u) + \partial_y g(u) = 0. \quad (2.3)$$

Systems of equations having the form of equation (2.3) are described as *flux conservative*, and they are frequently encountered as models for physical systems. The reason why systems of this form are so named is made clear if they are re-expressed in the integral form

$$\begin{aligned} \int_{y_A}^{y_B} \int_{x_A}^{x_B} u(t_1, x, y) dx dy &= \int_{y_A}^{y_B} \int_{x_A}^{x_B} u(t_0, x, y) dx dy \\ &- \left[ \int_{t_0}^{t_1} \int_{y_A}^{y_B} f(u(t, x_B, y)) dy dt - \int_{t_0}^{t_1} \int_{y_A}^{y_B} f(u(t, x_A, y)) dy dt \right] \\ &- \left[ \int_{t_0}^{t_1} \int_{x_A}^{x_B} g(u(t, x, y_B)) dx dt - \int_{t_0}^{t_1} \int_{x_A}^{x_B} g(u(t, x, y_A)) dx dt \right]. \end{aligned} \quad (2.4)$$

If the variables  $u$  are thought of as representing densities of unknown quantities, then equation (2.4) shows that the total amount of a quantity in a spatial region  $[x_A, x_B] \times [y_A, y_B]$  changes between times  $t = t_0$  and  $t = t_1$  only because of flow through the boundaries of the region, as represented by the fluxes  $f$  and  $g$ ; the variables  $u$  are conserved quantities.

As a first step towards generating numerical solutions to the evolution system (2.3), the temporal and spatial domain of the problem is discretized by defining a mesh of points

$$\{ (t^n, x_i, y_j) = (t^0 + n \Delta t, x_0 + i \Delta x, y_0 + j \Delta y) : n, i, j \in \mathbb{Z} \}. \quad (2.5)$$

The time step  $\Delta t$  and the mesh spacings  $\Delta x$  and  $\Delta y$  are assumed in the present chapter to be constant so that the discrete mesh is uniform in both time and space. For many of the numerical simulations described in later chapters, however, the size of the time step  $\Delta t$  is allowed to vary during the course of the simulation, with the appropriate modifications to the evolution procedures described here being straightforward.

There are two basic ways in which a numerical solution defined on the mesh (2.5) can be considered as approximating an exact solution  $u(t, x, y)$ . Most typically a numerical solution  $\hat{u}_{i,j}^n$  will approximate the values of the exact solution at the mesh points:

$$\hat{u}_{i,j}^n \simeq u(t^n, x_i, y_j). \quad (2.6)$$

Alternatively, in consideration of the integral form (2.4) of the evolution system, a numerical solution  $\bar{u}_{i,j}^n$  can approximate the average value of the exact solution taken over cells centred on the mesh points:

$$\bar{u}_{i,j}^n \simeq \frac{1}{\Delta x \Delta y} \int_{y_j - \frac{1}{2} \Delta y}^{y_j + \frac{1}{2} \Delta y} \int_{x_i - \frac{1}{2} \Delta x}^{x_i + \frac{1}{2} \Delta x} u(t^n, x, y) dx dy. \quad (2.7)$$

In the present work this cell-based interpretation of a numerical solution is the one usually employed, and the bar over the symbol for the conserved variables is often omitted from the notation.

The hyperbolicity of the system (2.3) means that information propagates within it at finite speeds, and a value for the numerical solution  $\bar{u}^{n+1}$  in a cell  $(x_i, y_j)$  can be determined as part of a numerical integration scheme based on the values  $\bar{u}^n$  within a region of cells, described as the *stencil* of the method, surrounding the cell  $(x_i, y_j)$ . (Such a ‘time-marching’ procedure for constructing a numerical solution may more generally make use of known values of the solution at earlier time

levels,  $\bar{u}^{n-1}$ , etc., but in the present discussion only *two-level* integration methods are considered.) Since meshes used in numerical simulations cannot be of infinite extent, for cells at the edges of a mesh the integration stencil will extend beyond the limits of the computational domain. To avoid having to use different integration procedures in different parts of the domain, the present work adopts an approach of enlarging the mesh to include *boundary cells* (typically a border region, one or two cells wide) in which the solution values are not evolved but instead are calculated at the start of each time step based on some specified boundary conditions.

Variables in numerical solutions may be conserved in the same way as in exact solutions if a discrete version of equation (2.4) is assumed. A cell-based numerical evolution method is *conservative* if it can be expressed in the form

$$\begin{aligned} \bar{u}_{i,j}^{n+1} = \bar{u}_{i,j}^n - \frac{\Delta t}{\Delta x} \left[ F(\bar{u}_{i,j}^n, \bar{u}_{i+1,j}^n) - F(\bar{u}_{i-1,j}^n, \bar{u}_{i,j}^n) \right] \\ - \frac{\Delta t}{\Delta y} \left[ G(\bar{u}_{i,j}^n, \bar{u}_{i,j+1}^n) - G(\bar{u}_{i,j-1}^n, \bar{u}_{i,j}^n) \right], \end{aligned} \quad (2.8)$$

where  $F$  and  $G$  are called the *numerical flux functions*. As an abbreviation of the notation, the numerical flux functions are shown in equation (2.8) as depending on the values of the numerical solution in two grid cells; in fact the functions may be based on the values of the numerical solution within a stencil of cells of arbitrary shape and size. In addition to their usefulness in conserving values of unknown variables which may have physical meanings as densities of some kind, conservative numerical methods are of particular importance when evolving solutions in which discontinuities may develop in some of the variables, as will be discussed in section 2.2.

### *The Lax-Friedrichs and Lax-Wendroff Methods*

In this subsection one- and two-dimensional versions of two standard numerical integration schemes are briefly described, together with some of their basic properties. These schemes are constructed by replacing the derivatives in the evolution equations (2.3) by finite difference approximations which are based on Taylor expansions of the functions. Both schemes are numerically conservative in the sense defined in the previous subsection.

The *Lax-Friedrichs* scheme is the simplest practical method for evolving numerical solutions to systems of the form (2.3). In one spatial dimension it is written as

$$u_i^{n+1} = \frac{1}{2}(u_{i-1}^n + u_{i+1}^n) - \frac{\Delta t}{2\Delta x} [f(u_{i+1}^n) - f(u_{i-1}^n)], \quad (2.9)$$

which generalizes in an obvious way to problems in two (or more) spatial dimensions:

$$\begin{aligned} u_{i,j}^{n+1} = \frac{1}{4}(u_{i-1,j}^n + u_{i+1,j}^n + u_{i,j-1}^n + u_{i,j+1}^n) \\ - \frac{\Delta t}{2\Delta x} [f(u_{i+1,j}^n) - f(u_{i-1,j}^n)] - \frac{\Delta t}{2\Delta y} [g(u_{i,j+1}^n) - g(u_{i,j-1}^n)]. \end{aligned} \quad (2.10)$$

The *two-step Lax-Wendroff* scheme produces more accurate results (in a sense made clear below) than the Lax-Friedrichs scheme by in effect using Lax-Friedrichs steps to construct solution

values at intermediate points. In one dimension it takes the form

$$u_i^{n+1} = u_i^n - \frac{\Delta t}{\Delta x} \left[ f(u_{i+1/2}^{n+1/2}) - f(u_{i-1/2}^{n+1/2}) \right], \quad (2.11)$$

where

$$u_{i+1/2}^{n+1/2} = \frac{1}{2}(u_i^n + u_{i+1}^n) - \frac{\Delta t}{2\Delta x} \left[ f(u_{i+1}^n) - f(u_i^n) \right].$$

There are various ways in which the two-step Lax-Wendroff method can be extended to higher spatial dimensions, and a version of the two-step Richtmyer scheme is used here:

$$\begin{aligned} u_i^{n+1} = u_i^n - \frac{\Delta t}{2\Delta x} & \left( \left[ f_{i+1/2, j-1/2}^{n+1/2} - f_{i-1/2, j-1/2}^{n+1/2} \right] + \left[ f_{i+1/2, j+1/2}^{n+1/2} - f_{i-1/2, j+1/2}^{n+1/2} \right] \right) \\ & - \frac{\Delta t}{2\Delta y} \left( \left[ g_{i-1/2, j+1/2}^{n+1/2} - g_{i-1/2, j-1/2}^{n+1/2} \right] + \left[ g_{i+1/2, j+1/2}^{n+1/2} - g_{i+1/2, j-1/2}^{n+1/2} \right] \right), \end{aligned} \quad (2.12)$$

where

$$\begin{aligned} u_{i+1/2, j+1/2}^{n+1/2} = \frac{1}{4} & (u_{i, j}^n + u_{i+1, j}^n + u_{i, j+1}^n + u_{i+1, j+1}^n) \\ & - \frac{\Delta t}{4\Delta x} \left( \left[ f_{i+1, j}^n - f_{i, j}^n \right] + \left[ f_{i+1, j+1}^n - f_{i, j+1}^n \right] \right) \\ & - \frac{\Delta t}{4\Delta y} \left( \left[ g_{i, j+1}^n - g_{i, j}^n \right] + \left[ g_{i+1, j+1}^n - g_{i+1, j}^n \right] \right), \end{aligned}$$

and, as a shorthand,  $f_{i, j}^n$  is used to mean  $f(u_{i, j}^n)$ , and so on.

Local stability of the above integration schemes requires conditions to be imposed on the size of the time step  $\Delta t$  relative to the mesh spacings  $\Delta x$  and  $\Delta y$ . The *Courant-Friedrichs-Lewy condition* is the requirement that the domain of dependence of the integration method include the domain of dependence of the system of evolution equations. For integration schemes like the ones described here which have stencils three cells wide, this condition translates as

$$\Delta t \leq \frac{\Delta x}{\max |\lambda_k|} \quad \text{or} \quad \Delta t \leq \min \left\{ \frac{\Delta x}{\max |\lambda_k|}, \frac{\Delta y}{\max |\mu_k|} \right\}, \quad (2.13)$$

depending on whether the scheme is in one or two spatial dimensions, where  $\lambda_1, \lambda_2, \dots$  and  $\mu_1, \mu_2, \dots$  are the eigenvalues of the Jacobian matrices defined in equation (2.2). For the one-dimensional Lax-Friedrichs and Lax-Wendroff methods, satisfaction of the Courant-Friedrichs-Lewy condition is sufficient for the scheme to be stable. Generally, for finite difference methods in two dimensions the stability restriction on the time step is more severe, with  $\Delta t$  required to be smaller by a factor of  $\sqrt{2}$  than the value given in equation (2.13); however, the two-dimensional Lax-Wendroff scheme of equation (2.12) is an exception to this, being restricted only by the standard Courant-Friedrichs-Lewy condition.

The main difference between the Lax-Friedrichs and Lax-Wendroff methods is that the former is accurate to first order whereas the latter is accurate to second order. Informally, the *order* of an integration scheme is the rate at which a numerical solution converges to an exact solution as the discrete mesh is refined; if the mesh spacings  $\Delta x$  and  $\Delta y$  are kept in fixed proportions to the time step  $\Delta t$ , and a numerical solution is evolved from a time  $t = t_0$  to a time  $t = T$  for different

time step sizes, then in general a measure of the error in the numerical solution at the final time will obey

$$\text{error} \sim O(\Delta t^p) \quad \text{as } \Delta t \rightarrow 0, \quad (2.14)$$

where  $p$  is the order of the integration scheme. (Mathematically rigorous definitions of the order of convergence can be found in the text books listed in the introduction to this chapter.) In practice, the relationship (2.14) is found to apply even to quantities only indirectly related to the numerical error, such as deviations in the Einstein constraint equations, and verification that numerical results converge at a rate appropriate to the integration method used is an important test of a numerical code. It should be noted, however, that equation (2.14) is only valid for exact solutions which are everywhere smooth; the accurate numerical evolution of non-smooth solutions is a topic returned to later in this chapter.

In the present work, finite difference methods (in particular the two-step Lax-Wendroff method) are used as a reference against which more sophisticated methods (section 2.3) can be compared. Since finite difference methods, unlike some more advanced methods, do not make explicit use of the eigenstructure of the Jacobian matrices of the evolved system, equation (2.2), they can in fact be applied to systems in which the hyperbolicity condition is weakened—the Jacobian matrices need not have complete sets of eigenvectors—and in chapter 7 the Lax-Wendroff method is used to evolve solutions to such systems.

Figure 2.1 shows example results produced using the Lax-Friedrichs and Lax-Wendroff schemes. As a test problem, the one-dimensional wave equation for the variable  $\Psi(t, x)$  is used,

$$\frac{\partial^2 \Psi}{\partial t^2} = c^2 \frac{\partial^2 \Psi}{\partial x^2}, \quad (2.15)$$

since this shares some basic properties with the full Einstein field equations. (In fact equation (2.15) can be seen to be very similar in form to the evolution equations for the Gowdy cosmological models considered in chapter 6.) The wave speed  $c$  is taken here to be a constant. The wave equation can be put into the first-order form of equation (2.1) by defining as new variables  $\phi = \partial_t \Psi$  and  $\chi = \partial_x \Psi$  so that

$$\partial_t \begin{bmatrix} \Psi \\ \phi \\ \chi \end{bmatrix} - \partial_x \begin{bmatrix} 0 \\ c^2 \chi \\ \phi \end{bmatrix} = \begin{bmatrix} \phi \\ 0 \\ 0 \end{bmatrix}. \quad (2.16)$$

(The source terms that appear in this evolution system are dealt with using the approach described in the next subsection.) The wave variable  $\Psi(t, x)$  is taken to be spatially periodic with period  $2\pi$ , and the following choice of initial data is made for time  $t = 0$ :

$$\begin{aligned} \Psi(0, x) &= \begin{cases} -\sin 2x & \text{if } \frac{1}{2}\pi < x < \frac{3}{2}\pi \\ 0 & \text{otherwise} \end{cases} \\ \partial_t \Psi(0, x) &= 0. \end{aligned} \quad (2.17)$$

This set of initial data is smooth except at two points, and there the variable  $\chi = \partial_x \Psi$  is discontinuous. The exact solution to the wave equation (2.15) is straightforward to derive, and it can be shown that for the initial data (2.17) the solution is periodic in time with period  $2\pi/c$ .

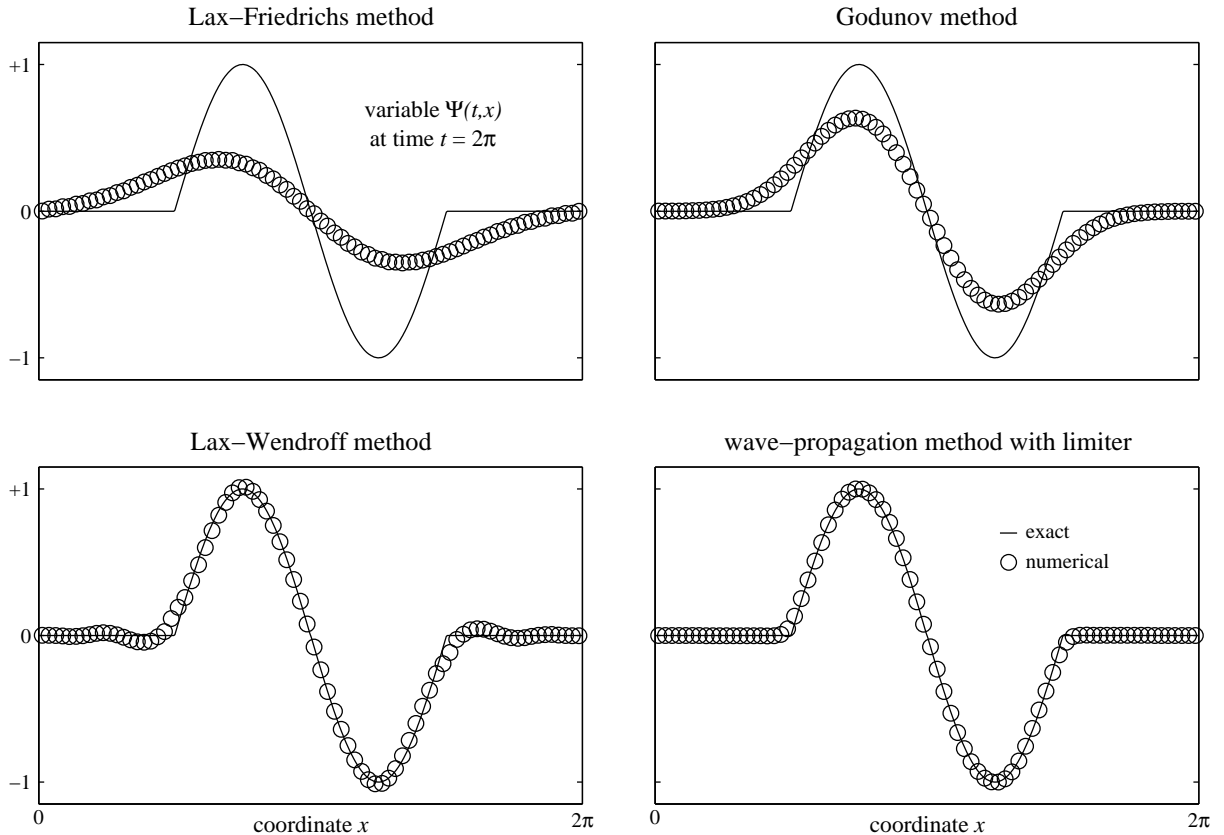


**Figure 2.1:** Comparison of results for four numerical integration schemes. The one-dimensional wave equation (2.15) with speed  $c = 1$  is evolved numerically based on the initial data (2.17), and exact and numerical solutions for the variable  $\Psi$  are shown. A mesh of 80 cells is evolved from time  $t = 0$  to time  $t = 2\pi$  in 160 steps. The finite difference methods used are discussed in section 2.1 while the finite volume methods are discussed in section 2.3. The results for the wave-propagation method are produced using the ‘superbee’ limiter.

The numerical results presented in figure 2.1 illustrate some basic traits of the finite difference methods used. The second-order convergence of the Lax-Wendroff method is responsible for the overall accuracy of its results in comparison with the first-order Lax-Friedrichs method. At the points where the solution is not smooth, however, the Lax-Wendroff method has introduced oscillations, and this behaviour is typical: the evolution method is *dispersive*. In contrast, the Lax-Friedrichs method has a tendency to smear out solutions in regions where they are discontinuous or non-smooth: it is a *diffusive* method. The oscillations introduced by the Lax-Wendroff method during the evolution of discontinuous solutions are a major drawback to its use in many applications, and, in response to this, much research has been done into the development of numerical schemes which are second-order accurate on smooth solutions, but at the same time give good resolution of discontinuities. Section 2.3 discusses one such scheme.

### Operator Splitting and Source Terms

Supposing that a numerical method is known by which a solution can be evolved to the system of equations (2.3), this subsection discusses a splitting approach that can be used to generate solutions to similar systems in which source terms are included, equation (2.1).

Denote by  $\mathcal{T}_{(\Delta t)}$  the operator for evolving a numerical solution  $u$  to the source-less system (2.3) through a time step  $\Delta t$  according to any appropriate integration scheme. A similar operator  $\mathcal{S}_{(\Delta t)}$  can be used to represent the advance by one time step of a numerical solution to the system of ordinary differential equations created by the removal of transport terms from the system (2.1),

$$\partial_t u = s(u), \quad (2.18)$$

and appropriate numerical methods for evolving such a solution are discussed below. A numerical solution to the full system (2.1) can then be advanced one step in time by using a combination of update operations for the component parts of the system:

$$u^{n+1} = \mathcal{S}_{(\Delta t/2)} \mathcal{T}_{(\Delta t)} \mathcal{S}_{(\Delta t/2)} u^n. \quad (2.19)$$

This approach is called *Strang splitting* (Strang 1968, Chapter 19 of Press et al. 1992, LeVeque 1998), and is in general second-order accurate provided that the two numerical methods represented by the  $\mathcal{S}$  and  $\mathcal{T}$  operators are individually second-order accurate.

Numerical methods for solving systems of the form (2.18) are well established, and a particularly good discussion of their practical application can be found in chapter 16 of Press et al. 1992. In the present work the source terms in the system (2.1) are evolved by using steps of the *second-order Runge-Kutta* method: the operator  $\mathcal{S}_{(\Delta t)}$  advances a numerical solution  $u$  through

$$u_{i,j}^{n+1} = u_{i,j}^n + \Delta t s(u_{i,j}^{n+1/2}), \quad (2.20)$$

where an intermediate state is defined by

$$u_{i,j}^{n+1/2} = u_{i,j}^n + \frac{\Delta t}{2} s(u_{i,j}^n),$$

and this procedure is applied to each computational cell individually.

Although the second-order Runge-Kutta method is unsophisticated in comparison to many other approaches that have been developed for the solution of systems of ordinary differential equations, it has been found to perform well for the problems it has been applied to in the present work. In particular, only very slight gains in overall accuracy have been observed when solutions to the system (2.1) have been evolved using  $N$  second-order Runge-Kutta steps of size  $\Delta t/N$  to advance the source terms at each stage rather than a single step of size  $\Delta t$ .



## 2.2 The Riemann Problem

In many problems, particularly when hydrodynamical effects are being modelled, discontinuities are a generic feature of solutions to the governing equations. As discussed in the previous section, standard finite difference methods are typically not well suited to the task of numerically evolving discontinuous solutions, and in section 2.3 a multi-dimensional high-resolution scheme is described which accurately resolves discontinuities while at the same time giving second-order accuracy in smooth regions of a solution. This evolution method operates based on information from the solution to the Riemann problem for the equations being evolved, and the nature of this problem and its solution in some simple cases are the topics of the present section. The scope of this discussion is limited to concepts that are referred to later in this work, and more complete accounts can be found in, for example, LeVeque 1992, and Godlewski and Raviart 1996.

### *Weak Solutions and Discontinuities*

It is a well-known property of nonlinear hyperbolic evolution systems that an initially smooth solution may become discontinuous after a finite amount of time, and such behaviour may often be physically reasonable, with shock waves in fluids being an obvious example. While solutions to systems of partial differential equations (specifically equation (2.3)) are only defined classically when they are smooth, it is possible to follow the behaviour of discontinuities using the conservative properties of a system: a *weak solution* to the evolution system (2.3) is a function  $u(t, x, y)$  which satisfies the integral form (2.4) of the system in all regions  $[t_0, t_1] \times [x_A, x_B] \times [y_A, y_B]$ . A consistent numerical method will always produce results which converge (if they converge at all) to weak solutions if the method is in the conservative form (2.8) introduced in the previous section.

The *Riemann problem* for a system of the form (2.3) demonstrates the behaviour of discontinuous solutions by evolving a set of initial data comprising two constant states  $u_L$  and  $u_R$  separated by a discontinuity:

$$u(0, x) = \begin{cases} u_L & \text{if } x < 0, \\ u_R & \text{if } x \geq 0, \end{cases} \quad \text{at time } t = 0, \quad (2.21)$$

where only one spatial dimension is relevant here. It can be shown that the solution to the Riemann problem is always of the form

$$u(t, x) = w(x/t) \quad \text{for } t > 0, \quad (2.22)$$

where the function  $w(\xi)$  comprises a number of regions of constant state separated by *waves* spreading out from the initial discontinuity:

$$w(\xi) = \begin{cases} u_L & \text{if } \xi < s_1 - \epsilon_1, \\ u_\alpha & \text{if } s_1 + \epsilon_1 \leq \xi < s_2 - \epsilon_2, \\ u_\beta & \text{if } s_2 + \epsilon_2 \leq \xi < s_3 - \epsilon_3, \\ \dots & \\ u_R & \text{if } s_m + \epsilon_m \leq \xi. \end{cases}$$

These waves are of two basic types: *shock waves* are simple discontinuities between neighbouring constant states such that  $\epsilon_k = 0$ , whereas *rarefaction waves* are extended regions (having  $\epsilon_k > 0$ )

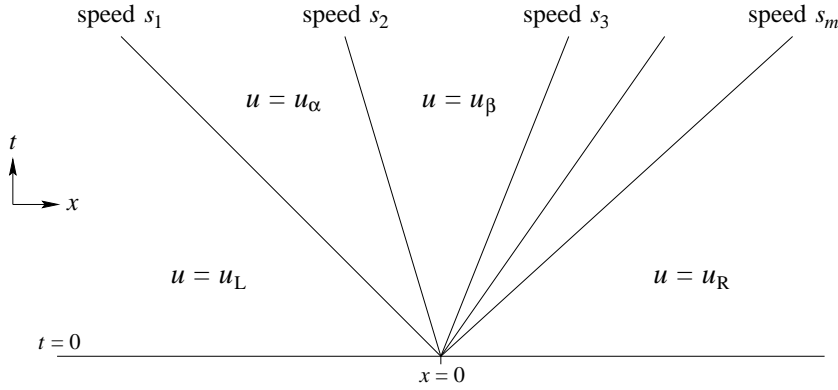


**Figure 2.2:** Solution to the Riemann problem containing only shock waves. A number of discontinuities propagating with constant speeds  $s_1, s_2, \dots, s_m$  separate regions where  $u$  is of constant value.

across which  $w(\xi)$  is continuous and inside of which it is smooth. For the evolution systems considered in the present work only shock waves (more accurately, *contact discontinuities*) are present in solutions to the Riemann problem, and this situation is illustrated in figure 2.2. Rarefaction waves are not considered further in this work.

A solution to the Riemann problem can thus be described by a list of  $m$  shock waves, each of which has a speed  $s_k$  (as in figure 2.2) and a jump value  $\mathcal{W}_k$ , where the jumps are the differences between neighbouring constant values of the state vector  $u$ :

$$\mathcal{W}_1 = u_\alpha - u_L, \quad \mathcal{W}_2 = u_\beta - u_\alpha, \quad \text{and so on,}$$

so that

$$u_R - u_L = \sum_{k=1}^m \mathcal{W}_k.$$

The waves are ordered such that  $s_1 < s_2 < \dots < s_m$ , and the number  $m$  of waves is not greater than the number  $n$  of unknown variables in the system. It can be shown from the integral form (2.4) of the evolution system that a shock wave with speed  $s$  separating two constant states  $u_A$  and  $u_B$  must satisfy

$$f(u_B) - f(u_A) = s(u_B - u_A), \quad (2.23)$$

and this is called the *Rankine-Hugoniot jump condition*. Provided  $u_L$  is sufficiently close to  $u_R$ , a unique set of shock waves  $(s_1, \mathcal{W}_1), \dots, (s_m, \mathcal{W}_m)$  for the solution to the Riemann problem (2.21) can always be determined by requiring that the condition (2.23) be satisfied across each wave:

$$f\left(u_L + \sum_{l=1}^k \mathcal{W}_l\right) - f\left(u_R - \sum_{l=k}^m \mathcal{W}_l\right) = s_k \mathcal{W}_k,$$

for  $k = 1, \dots, m$ .

### *Linear Systems and Approximate Riemann Solvers*

For a general nonlinear system (2.3), the Riemann problem (2.21) is typically very difficult to solve. However for linear systems the solution is straightforward to derive, and for many applications an approximate solution to the Riemann problem produced by consideration of a related linear system is an acceptable substitute for the exact nonlinear solution.

The system (2.3) is *linear (with constant coefficients)* if the components of the flux vectors are linear combinations of the variables  $u$ , and in this case the system can be rewritten as

$$\partial_t u + A \partial_x u = 0, \quad (2.24)$$

where only one spatial dimension is relevant here, and the Jacobian matrix  $A$  has constant coefficients. (If the matrix  $A$  has an explicit dependence on the independent variables  $t$  and  $x$ , then the system is described as *linear with variable coefficients*; such systems are considered further below.) It follows from the assumption that the constant-coefficient system is hyperbolic that the eigenvalues  $\lambda_1, \dots, \lambda_m$  of  $A$  are all real, and that the matrix has a complete set of eigenvectors such that any vector  $v$  can be decomposed as

$$v = \sum_{k=1}^m r_k \quad \text{where} \quad A r_k = \lambda_k r_k. \quad (2.25)$$

(The number  $m$  of distinct eigenvalues of  $A$  is not necessarily the same as the number  $n$  of variables in the evolution system.) For a linear system the Rankine-Hugoniot jump condition (2.23) reduces to a simple eigenvalue equation

$$A(u_B - u_A) = s(u_B - u_A),$$

and the solution to the Riemann problem (2.21) follows directly from this. Assuming the eigenvalues of  $A$  to be ordered in magnitude  $\lambda_1 < \lambda_2 < \dots < \lambda_m$ , then the solution comprises  $m$  shock waves with speeds

$$s_k = \lambda_k \quad \text{for} \quad k = 1, \dots, m, \quad (2.26)$$

and jumps  $\mathcal{W}_1, \dots, \mathcal{W}_m$  between constant states which are found by an eigenvector decomposition analogous to equation (2.25):

$$\Delta u = \sum_{k=1}^m \mathcal{W}_k \quad \text{where} \quad A \mathcal{W}_k = \lambda_k \mathcal{W}_k, \quad (2.27)$$

for  $\Delta u = u_R - u_L$ .

As a specific example, the solution to the Riemann problem for the transport part of the first-order form (2.16) of the wave equation is presented here. The system is linear, and has the Jacobian matrix

$$A = \begin{bmatrix} 0 & 0 & 0 \\ 0 & 0 & -c^2 \\ 0 & -1 & 0 \end{bmatrix},$$

where  $c$  is a constant. Writing the difference in initial states as  $\Delta u = [\Delta\Psi, \Delta\phi, \Delta\chi]^T = u_R - u_L$ , the solution to the Riemann problem comprises one stationary shock wave,

$$s_0 = 0, \quad \mathcal{W}_0 = \begin{bmatrix} \Delta\Psi \\ 0 \\ 0 \end{bmatrix},$$

and two shock waves propagating in opposite directions at the wave speed  $c$ ,

$$s_{\pm} = \pm c, \quad \mathcal{W}_{\pm} = \frac{1}{2} \begin{bmatrix} 0 \\ \Delta\phi \mp c \Delta\chi \\ \Delta\chi \mp c^{-1} \Delta\phi \end{bmatrix}.$$

(This situation is quite similar to the one illustrated in figure 4.2 for the transport part of the full Einstein equations.)

Analysis of the Riemann problem can be difficult even for linear systems if the flux vectors in equation (2.3) have an explicit dependence on the space or time coordinates. The simplest approach to dealing with this problem is to consider only the local behaviour of the system by solving the Riemann problem for a fixed value of the coordinates, and in section 6.2 this approach is applied to a linear system with variable coefficients which is effectively the wave equation (2.15) with a time-dependent speed  $c$ . In that case, the solution to the Riemann problem posed at a time  $t = t_0$  is needed at a time  $t = t_0 + \Delta t$ , and the pattern of shock waves produced by solving the problem for a fixed-speed system with  $c$  evaluated at the time  $t = t_0 + \Delta t/2$  is found to give second-order accuracy (as the time step  $\Delta t$  is refined) when used in place of the exact variable-speed solution. Section 4.3 discusses a more complicated example in which second-order accuracy is attained only through a more elaborate treatment of the coordinate-dependent flux terms.

Approximate solutions to the Riemann problem are typically just as effective as exact solutions when they are used as part of numerical integration schemes, and in many cases the former may actually be preferable, either because an approximate solution can be calculated very efficiently or because no simple form for the exact solution is known. Roe (1981) describes an approach for approximating the solution of the Riemann problem for a nonlinear system,

$$\partial_t u + \partial_x f(u) = 0,$$

by the exact solution for a related linear system,

$$\partial_t u + \tilde{A} \partial_x u = 0,$$

where the matrix  $\tilde{A}$  has constant coefficients which depend on the initial states  $u_L$  and  $u_R$  of the Riemann problem, and the linear system is hyperbolic in the sense defined in section 2.1. Roe suggests two conditions that should be satisfied by such a matrix  $\tilde{A}$ . Firstly, as  $u_L$  and  $u_R$  tend to a fixed value  $u_0$ , the matrix  $\tilde{A}(u_L, u_R)$  should tend smoothly to the value  $A(u_0)$ , where  $A(u)$  is the Jacobian matrix defined in equation (2.2). A simple way to satisfy this condition is to choose the matrix  $\tilde{A}$  as equalling  $A(u_*)$  for some state  $u_*$  representing an average of  $u_L$  and  $u_R$ . Roe's second condition is that the conservation property

$$\tilde{A}(u_R - u_L) = f(u_R) - f(u_L) \tag{2.28}$$

should hold. A choice of  $\tilde{A}$  which satisfies this condition may be difficult to find in general; however it can be shown (Roe 1981) that simply taking  $\tilde{A} = A(u_*)$  where  $u_* = \frac{1}{2}(u_L + u_R)$  will work for evolution systems in which the components of the flux vector  $f(u)$  are no more than quadratic in the components of  $u$ .

Roe's approach to the construction of approximate Riemann solutions is used in section 4.3. There the Riemann problem for the full Einstein equations (written in a hyperbolic form) is considered, and exact and approximate solutions are derived for use with the numerical integration schemes described in the next section.

## 2.3 Finite Volume Methods

This section describes a multi-dimensional high-resolution method for the numerical integration of hyperbolic systems of partial differential equations which have the flux-conservative form described in section 2.1. An integration method is described as being *high resolution* if it gives second-order (or better) accuracy when evolving solutions which are smooth, and in addition resolves discontinuities in solutions without producing oscillations.

The high-resolution method described here is the wave-propagation algorithm developed by LeVeque (1997). This method can be used for problems in one and two spatial dimensions (for its extension to three dimensions see Langseth and LeVeque 1999), and operates by considering sequences of Riemann problems (section 2.2) for the evolution equations under consideration. An implementation of the wave-propagation algorithm in Fortran 77, called CLAWPACK (Conservation LAWs PACKage), is freely available (LeVeque 1998). For the present work, in order to gain familiarity with the method, the CLAWPACK routines have been re-implemented in the C++ language, with the resulting software being named Claw++. (The adaptive mesh refinement code described in chapter 3 is written in C++, and while it would be possible in principle to link integration routines written in a different language to that code, there are many advantages in practice to both pieces of software being implemented in the same programming language.) A number of example problems related to fluid dynamics are included in the CLAWPACK software, and these have also been converted to C++ and have been used to verify that the Claw++ software performs correctly.

The wave-propagation algorithm is a second-order extension of Godunov's well-known integration method, and this is described here as a prelude to discussing the high-resolution scheme. The account given here is concerned only with aspects of the wave-propagation algorithm which are directly relevant to its use in numerical simulations; full details about the method and its theoretical background can be found in the references listed above together with LeVeque 1992, 1996.

The Claw++ software (which incorporates routines for evolving solutions according to the Lax-Friedrichs and Lax-Wendroff methods of section 2.1) is used as the basis for almost all of the numerical simulations described in this work. In particular, section 4.3 discusses how the wave-propagation algorithm can be used to evolve solutions to the vacuum Einstein equations when the latter are written in a flux-conservative hyperbolic form.

### Godunov's Method

The starting point for the construction of the high-resolution wave-propagation algorithm is Godunov's method, and this is briefly described in the present subsection. Godunov's method is applicable to evolution systems having the flux-conservative form of equation (2.3), and it can also be used to evolve solutions to more general systems having the form of equation (2.1) by employing the operator splitting approach described at the end of section 2.1 to treat the source terms. Where Godunov's method differs from the finite difference methods described in section 2.1 is in its use of Riemann problems (see section 2.2) to advance numerical solutions in time. As might be expected, Godunov's method gives better results for discontinuous solutions than standard finite difference methods.

Godunov's method in the one-dimensional case is considered first. Given a numerical solution  $u_i^n$  at a time  $t = t^n$ , Godunov's method for advancing the solution to a later time  $t = t^{n+1}$  considers a piecewise constant function  $U^n(x)$  defined according to

$$U^n(x) = u_i^n \quad \text{for } x \in [x_i - \frac{1}{2}\Delta x, x_i + \frac{1}{2}\Delta x]. \quad (2.29)$$

If the numerical solution  $u^n$  is a cell-based approximation to the exact solution in the sense of equation (2.7), then the function  $U^n(x)$  extends that discrete data to the real line in a way which preserves the original cell averages. If the function  $U^n(x)$  is taken as initial data for the evolution system (2.3), then the exact solution  $U(t, x)$  can be determined at least within a short time interval by piecing together the solutions to a sequence of Riemann problems centred at the cell interfaces. Values  $u_i^{n+1}$  for the numerical solution at the next time level are then determined by taking cell averages of the solution  $U(t^{n+1}, x)$ :

$$u_i^{n+1} = \frac{1}{\Delta x} \int_{x_i - \frac{1}{2}\Delta x}^{x_i + \frac{1}{2}\Delta x} U(t^{n+1}, x) dx. \quad (2.30)$$

In fact, it follows from the integral form (2.4) of the evolution system that the function  $U(t, x)$  need not be calculated in full in order to find  $u^{n+1}$ . Equation (2.30) can be rewritten as

$$u_i^{n+1} = u_i^n - \frac{\Delta t}{\Delta x} \left[ f(U_{i+1/2}^*) - f(U_{i-1/2}^*) \right], \quad (2.31)$$

where  $U_{i+1/2}^*$  is the value of  $U(t, x)$  evaluated at the cell interface  $x = x_{i+1/2}$ , and this value is known (from the general form (2.22) of the solution to the Riemann problem) to be independent of the time  $t$ .

Equation (2.31) is Godunov's method in one spatial dimension. It is explicitly conservative (as can be seen by comparison with equation (2.8)) and it is stable provided that the Courant-Friedrichs-Lewy condition (2.13) is satisfied. Godunov's method is first-order accurate, and it can be seen from figure 2.1 that numerical results produced using the method are not typically as good as results produced using a higher-order method such as the Lax-Wendroff scheme. However, no oscillations are produced by Godunov's method at points where the evolved solution is not smooth, and there is less smearing of the data than in results produced using the first-order Lax-Friedrichs finite difference scheme.

A slightly different form of equation (2.31) is useful when considering the extension of Godunov's method to a second-order scheme. The value of  $U_{i+1/2}^*$  is determined by solving a Riemann problem with initial states  $u_i^n$  and  $u_{i+1}^n$ , and from the discussion of section 2.2 it can be seen that

$$U_{i+1/2}^* = u_i + \sum_{k=1}^p \mathcal{W}_k = u_{i+1} - \sum_{k=p+1}^m \mathcal{W}_k,$$

where  $\mathcal{W}_1, \dots, \mathcal{W}_m$  are the shock jumps into which the vector  $\Delta u = u_{i+1}^n - u_i^n$  is decomposed, and the value  $p$  is such that the wave speeds satisfy

$$s_1 < \dots < s_p \leq 0 < s_{p+1} < \dots < s_m.$$

It is then convenient to define from the solution to this Riemann problem a *left-going fluctuation*, denoted  $\mathcal{A}^- \Delta u$ , and a *right-going fluctuation*, denoted  $\mathcal{A}^+ \Delta u$ , according to

$$\begin{aligned} \mathcal{A}^- \Delta u &= \sum_{k=1}^m \min(s_k, 0) \mathcal{W}_k, \\ \mathcal{A}^+ \Delta u &= \sum_{k=1}^m \max(s_k, 0) \mathcal{W}_k. \end{aligned} \tag{2.32}$$

From the Rankine-Hugoniot jump condition (2.23) these fluctuations can be seen to satisfy

$$\mathcal{A}^- \Delta u + \mathcal{A}^+ \Delta u = f(u_{i+1}) - f(u_i), \tag{2.33}$$

and with respect to them Godunov's method (2.31) can be written in the wave-propagation form

$$u_i^{n+1} = u_i^n - \frac{\Delta t}{\Delta x} [\mathcal{A}^+ \Delta u_{i-1/2} + \mathcal{A}^- \Delta u_{i+1/2}]. \tag{2.34}$$

The evaluation of the fluctuations  $\mathcal{A}^- \Delta u$  and  $\mathcal{A}^+ \Delta u$  can be done in a particularly neat way if the evolution system is linear or if a Roe solver is used. The constant-coefficient matrix  $A$  which represents the flux of the system can then be diagonalized as

$$A = R \operatorname{diag}[\lambda_1, \dots, \lambda_n] R^{-1},$$

where the non-singular matrix  $R$  has columns which are eigenvectors of  $A$ , and  $\lambda_1, \dots, \lambda_n$  are the corresponding eigenvalues (which are not necessarily distinct). If two new matrices are defined as

$$\begin{aligned} A^- &= R \operatorname{diag}[\min(\lambda_1, 0), \dots, \min(\lambda_n, 0)] R^{-1}, \\ A^+ &= R \operatorname{diag}[\max(\lambda_1, 0), \dots, \max(\lambda_n, 0)] R^{-1}, \end{aligned} \tag{2.35}$$

then  $A = A^+ + A^-$ , and the fluctuations for the Riemann problem can be calculated by performing matrix multiplications on the difference vector  $\Delta u$ :

$$\mathcal{A}^- \Delta u = A^- \Delta u \quad \text{and} \quad \mathcal{A}^+ \Delta u = A^+ \Delta u. \tag{2.36}$$

(Fluctuations and the wave-propagation form of Godunov's method are discussed in much greater detail in the references listed in the introduction to this section.)

In two dimensions, Godunov's method (in wave-propagation form) is a straightforward generalization of equation (2.34):

$$u_{i,j}^{n+1} = u_{i,j}^n - \frac{\Delta t}{\Delta x} [\mathcal{A}^+ \Delta u_{i-1/2,j} + \mathcal{A}^- \Delta u_{i+1/2,j}] - \frac{\Delta t}{\Delta y} [\mathcal{B}^+ \Delta u_{i,j-1/2} + \mathcal{B}^- \Delta u_{i,j+1/2}], \quad (2.37)$$

where the fluctuations  $\mathcal{B}^+ \Delta u$  and  $\mathcal{B}^- \Delta u$  are analogous to  $\mathcal{A}^+ \Delta u$  and  $\mathcal{A}^- \Delta u$ , and are defined by solving Riemann problems in the  $y$ -direction rather than the  $x$ -direction. The method (2.37) is first-order accurate, and is stable only for time steps  $\Delta t$  which are smaller by a factor 1/2 at least than the maximum value permitted by the Courant-Friedrichs-Lewy condition (2.13). (A better stability bound than this is one of the features of the two-dimensional wave-propagation method described below.)

### *Wave Propagation in One Dimension*

A high-resolution numerical algorithm is typically produced by combining two different integration schemes: a first-order scheme which produces good results for discontinuous solutions, and a higher-order scheme which is accurate for smooth solutions. The hybrid scheme then varies its order with position depending on whether the evolved solution is judged as being discontinuous there or not. (There exists an extensive literature on the theoretical aspects of high-resolution methods; for an overview relevant to the present discussion see chapter 16 of LeVeque 1992.)

The high-resolution wave-propagation method of LeVeque 1997 is based on Godunov's first-order scheme with correction terms being added to increase the accuracy of the method to second order when the solution is smooth. In one dimension the method can be written as

$$u_i^{n+1} = u_i^n - \frac{\Delta t}{\Delta x} [\mathcal{A}^+ \Delta u_{i-1/2} + \mathcal{A}^- \Delta u_{i+1/2}] - \frac{\Delta t}{\Delta x} [\tilde{F}_{i+1/2} - \tilde{F}_{i-1/2}], \quad (2.38)$$

where  $\tilde{F}_{i-1/2}$  and  $\tilde{F}_{i+1/2}$  are 'high-resolution' correction terms to equation (2.34). Whereas Godunov's method only makes use of the fluctuations  $\mathcal{A}^\pm \Delta u$  calculated at each cell interface, the correction terms in the wave-propagation algorithm incorporate information about each of the waves in the solution to the Riemann problem:

$$\tilde{F}_{i+1/2} = \frac{1}{2} \sum_{k=1}^m |s_k| \left( 1 - \frac{\Delta t}{\Delta x} |s_k| \right) \tilde{\mathcal{W}}_k, \quad (2.39)$$

where the wave speeds  $s_1, \dots, s_m$  and the (limited) wave jumps  $\tilde{\mathcal{W}}_1, \dots, \tilde{\mathcal{W}}_m$  are computed for the Riemann problem between the states  $u_i^n$  and  $u_{i+1}^n$ .

If the unmodified wave jumps  $\mathcal{W}_1, \dots, \mathcal{W}_m$  are used in equation (2.39) by setting  $\tilde{\mathcal{W}}_k = \mathcal{W}_k$ , then the method (2.38) is second-order accurate. It is not, however, high resolution since it still produces spurious oscillations at discontinuities in evolved solutions.

To enable the wave-propagation method to accurately evolve discontinuous solutions, a *limiter function*,  $\phi(\theta)$ , is used to define modified wave jumps  $\tilde{\mathcal{W}}_1, \dots, \tilde{\mathcal{W}}_m$  which are equal to the original



jumps only when the solution is sufficiently smooth. The limiter function is applied independently to each family of waves that appears in the solution to the Riemann problem. The limited version  $\tilde{\mathcal{W}}_k$  of the wave jump  $\mathcal{W}_k$  at the cell interface  $x = x_{i+1/2}$  depends on the speed  $s_k$  of that wave together with the jumps labelled by the same index  $k$  for the cell interfaces to the left and right, denoted here as  $\mathcal{W}_k^L$  and  $\mathcal{W}_k^R$ . A value  $\theta_k$  is defined as a measure of the smoothness of the solution (with respect to the  $k$ -th family of waves) according to

$$\theta_k = \begin{cases} (\mathcal{W}_k^L \cdot \mathcal{W}_k) / (\mathcal{W}_k \cdot \mathcal{W}_k) & \text{if } s_k > 0, \\ (\mathcal{W}_k^R \cdot \mathcal{W}_k) / (\mathcal{W}_k \cdot \mathcal{W}_k) & \text{if } s_k \leq 0, \end{cases}$$

where the dot represents inner product. A value of  $\theta_k$  close to unity is taken as an indication that the solution is smooth. Modified wave jumps are then defined by rescaling the original jumps by a factor determined through a limiter function  $\phi(\theta)$ :

$$\tilde{\mathcal{W}}_k = \phi(\theta_k) \mathcal{W}_k. \quad (2.40)$$

A range of different limiter functions have been proposed in the literature, and several of these (the *minmod* limiter, the *superbee* limiter, the *van Leer* limiter and the *monotonized centred* limiter; see LeVeque 1996 for details) have been incorporated in the implementation of the wave-propagation algorithm used in the present work.

Figure 2.1 presents some sample numerical results produced using the wave-propagation method with a limiter function. Where the exact solution is smooth it can be seen that the method produces accurate results which are comparable to those produced using the second-order Lax-Wendroff scheme; however, unlike the Lax-Wendroff scheme, the wave-propagation method accurately resolves the exact solution in regions where it is not smooth, and no spurious oscillations are introduced. The wave-propagation method (2.38) is stable for any time step  $\Delta t$  satisfying the Courant-Friedrichs-Lewy condition (2.13). Because of the way wave jumps are compared when applying the limiter function, the wave-propagation method differs from the other integration schemes that have been described so far in this chapter in that it has a stencil that is, strictly speaking, five (rather than three) cells wide.

### Wave Propagation in Two Dimensions

The extension of the wave-propagation method (2.38) to problems in two spatial dimensions is not straightforward. In particular, transverse propagation terms need to be included in the method, and these add complexity not only to the cell-update formula but also to the implementation of Riemann solver routines for the evolution systems to which the method is applied.

The basic form of the method generalizes the two-dimensional version of Godunov's scheme, equation (2.37), to

$$\begin{aligned} u_{i,j}^{n+1} = u_{i,j}^n & - \frac{\Delta t}{\Delta x} [\mathcal{A}^+ \Delta u_{i-1/2,j} + \mathcal{A}^- \Delta u_{i+1/2,j}] - \frac{\Delta t}{\Delta x} [\tilde{F}_{i+1/2,j} - \tilde{F}_{i-1/2,j}] \\ & - \frac{\Delta t}{\Delta y} [\mathcal{B}^+ \Delta u_{i,j-1/2} + \mathcal{B}^- \Delta u_{i,j+1/2}] - \frac{\Delta t}{\Delta y} [\tilde{G}_{i,j+1/2} - \tilde{G}_{i,j-1/2}], \end{aligned} \quad (2.41)$$

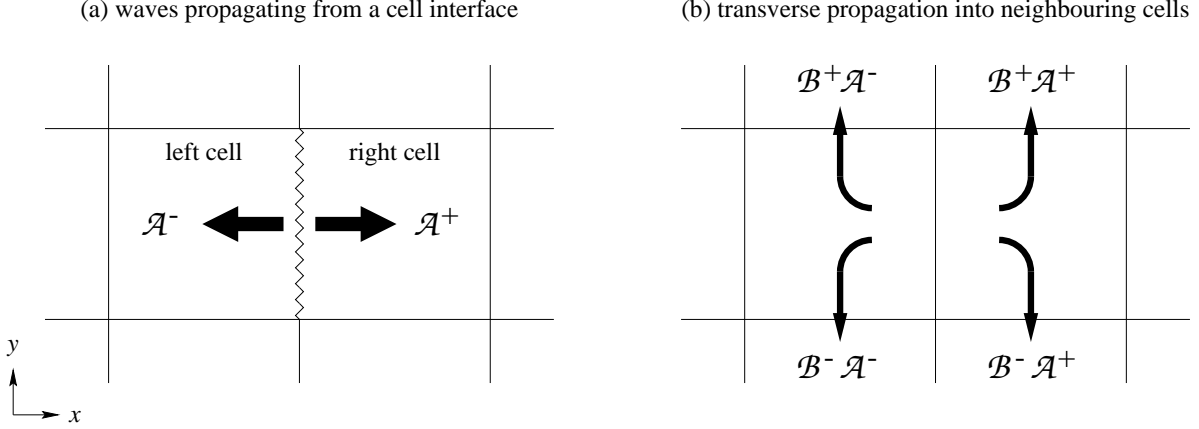


**Figure 2.3:** Transverse wave propagation. The left-going and right-going fluctuations  $\mathcal{A}^-\Delta u$  and  $\mathcal{A}^+\Delta u$  that emerge from the cell interface (first plot) are split into four transverse fluctuations  $\mathcal{B}^\pm\mathcal{A}^\pm\Delta u$  which affect the solution in the cells above and below the interface (second plot).

where  $\tilde{G}_{i,j-1/2}$  and  $\tilde{G}_{i,j+1/2}$  are second-order correction fluxes in the  $y$ -direction, analogous to the correction terms  $\tilde{F}$  for the  $x$ -direction in equation (2.38). While the flux corrections  $\tilde{F}$  and  $\tilde{G}$  could simply be defined according to equation (2.39) (with Riemann problems being solved independently in the  $x$ - and  $y$ -directions), such an approach is not by itself capable of making the scheme (2.41) second-order accurate.

One way to make the two-dimensional form of the wave-propagation algorithm second-order accurate follows from the realization that the left-going waves produced by the Riemann problem at the interface between the cells  $u_{i,j}^n$  and  $u_{i+1,j}^n$  should affect not only the solution value  $u_{i,j}^{n+1}$  but also the solution in the cells above and below:  $u_{i,j+1}^{n+1}$  and  $u_{i,j-1}^{n+1}$ . The wave-propagation algorithm accounts for transverse wave motion of this kind by splitting the left-going fluctuation  $\mathcal{A}^-\Delta u$  into two *transverse fluctuations*, one up-going,  $\mathcal{B}^+\mathcal{A}^-\Delta u$ , and one down-going,  $\mathcal{B}^-\mathcal{A}^-\Delta u$ . The right-going waves are treated in a similar manner, and for each Riemann problem that is solved, four transverse fluctuations  $\mathcal{B}^\pm\mathcal{A}^\pm\Delta u$  are calculated in total. (Analogous quantities  $\mathcal{A}^\pm\mathcal{B}^\pm\Delta u$  account for transverse wave propagation for Riemann problems in the  $y$ -direction.) This situation is illustrated in figure 2.3.

Transverse fluctuation terms are incorporated in the update step (2.41) through modifications made to the flux corrections  $\tilde{F}$  and  $\tilde{G}$ . The exact details of this can be found in LeVeque 1997, 1998. Limiters are applied to the waves produced at each cell interface according to equation (2.40), and the effect of the limiters can also be propagated transversely together with the second-order corrections of equation (2.39). A geometrical argument motivating the use of transverse fluctuations in the case of advection of a scalar quantity can be found in LeVeque 1996.

The exact definition of the transverse fluctuations  $\mathcal{B}^\pm\mathcal{A}^\pm\Delta u$  and  $\mathcal{A}^\pm\mathcal{B}^\pm\Delta u$  depends on the nature of the evolution system being studied. For a linear system, the Jacobian matrices  $A$  and  $B$  of equation (2.2) have constant coefficients, and the transverse fluctuations can be defined through

a generalization of equation (2.36):

$$\mathcal{B}^\pm \mathcal{A}^\pm \Delta u = B^\pm A^\pm \Delta u \quad \text{and} \quad \mathcal{A}^\pm \mathcal{B}^\pm \Delta u = A^\pm B^\pm \Delta u, \quad (2.42)$$

where the four matrices  $A^\pm$  and  $B^\pm$  are constructed as in equation (2.35). A similar approach can be employed for nonlinear systems if Roe's approach (section 2.2) is used to produce approximate solutions to the Riemann problem. Considering the waves produced between two cells  $u_{i,j}^n$  and  $u_{i,j+1}^n$ , a constant matrix  $\tilde{A}$  is used in Roe's approach to define left-going and right-going fluctuations  $\mathcal{A}^\pm \Delta u$ . This matrix  $\tilde{A}$  is typically determined by evaluating the Jacobian matrix  $A(u)$  at a fixed state  $u = u_*$ . A constant matrix  $\tilde{B}$  can be defined by evaluating the other Jacobian matrix  $B(u)$  at the same state  $u_*$ , and the transverse fluctuations  $\mathcal{B}^\pm \mathcal{A}^\pm \Delta u$  can then be evaluated using matrix multiplication as in equation (2.42). (An analogous argument determines values for the transverse fluctuations  $\mathcal{A}^\pm \mathcal{B}^\pm \Delta u$  in the  $y$ -direction.)

With transverse fluctuations appropriately determined, the two-dimensional wave-propagation method (2.41) is a second-order integration scheme for smooth solutions. Through the use of wave limiters, it can evolve solutions with discontinuities without introducing spurious oscillations. The method is stable for any time step  $\Delta t$  satisfying the Courant-Friedrichs-Lewy condition (2.13). As in the one-dimensional case, the way in which the limiters are applied means that the wave-propagation method uses an integration stencil of width five.

Example numerical results produced using the two-dimensional wave-propagation algorithm can be found in LeVeque 1997, 1998. In the present work, a range of numerical simulations of vacuum cosmological spacetimes have been carried out using the method. In particular, section 4.3 describes how exact and approximate Riemann solvers can be used in conjunction with the wave-propagation method to evolve solutions to a hyperbolic formulation of the Einstein equations. When spacetimes described by metrics with smooth components are evolved, it has been demonstrated that the wave-propagation method (without limiters) produces results which converge at second order and which are comparable in accuracy to results produced using the second-order Lax-Wendroff finite difference scheme; given the complexity of the evolution systems involved and the experimental nature of the wave-propagation method, this is a non-trivial result. None of the spacetimes that have been evolved in this work have developed discontinuities or steep gradients of the kind that benefit from the application of wave limiters (although in some simulations this does not at first sight appear to be the case; see section 6.2). The use of a high-resolution integration method in the present work may be thought of as preliminary research towards the use of the method to evolve Einstein's equations coupled to hydrodynamical matter fields, a situation in which the sophisticated behaviour of a high-resolution numerical scheme is sure to be needed.

# Chapter 3.

## Adaptive Mesh Refinement

The local accuracy of a numerical solution to a system of hyperbolic partial differential equations is typically a function of the mesh spacing of the discrete grid used, as explained in the previous chapter (section 2.1). Evolving a numerical solution on a single uniform grid can be very inefficient if a fine mesh spacing is needed in part of the spatial and temporal domain while a coarse mesh spacing would suffice elsewhere. Adaptive mesh refinement (henceforth AMR) is a method which allows the resolution of a numerical simulation to vary in space and time so that the accuracy of the evolved solution is maintained above a specified level across the entire solution.

The key reference to the AMR method is the 1984 paper by Berger and Olinger, and a number of other significant references are cited at relevant points in this chapter. An overview of some of the computational work performed using AMR is given by Plewa (1999). Worthy of note is the AMRCLAW software package (Berger and LeVeque 1997), a freely available two-dimensional implementation of the AMR algorithm combined with the CLAWPACK wave-propagation methods discussed in chapter 2. (Though the standard of the AMRCLAW software is very high, its implementation in Fortran 77 makes it complicated and too inflexible to be used in the present work; section 3.3 argues that a modern computer language such as Fortran 90 or C++ is much better suited to the development of an AMR code.)

Most applications of the AMR method have been to problems in fluid dynamics. The complexity of the algorithm, combined with the complexity of Einstein's equations, has meant that AMR has not to date been extensively used in numerical relativity. Its first use was by Choptuik (1989, 1992, 1993) to study the gravitational collapse of a massless scalar field in spherical symmetry, work which would have been impractical without the use of AMR since very fine mesh spacings are needed to resolve the small-scale structure that develops in the model. A different implementation of the AMR algorithm was used by Hamadé and Stewart (1996) to look at the same problem expressed in double-null coordinates. Several other spherically symmetric collapse scenarios have been examined using these two AMR codes: collapse of an  $SU(2)$  gauge field by Choptuik, Chmaj and Bizoń (1996), collapse of an axion/dilaton system by Hamadé, Horne and Stewart (1996), and collapse of a perfect fluid by Hamadé (1997). The development of fully three-dimensional AMR codes for use in relativity has been motivated by the massive computational requirements needed to simulate black hole collisions (as outlined in Seidel 1998; the first work in this direction, Massó, Seidel and Walker 1995, used a one-dimensional AMR code to evolve a Schwarzschild black hole). Brüggmann (1996, 1999) reports preliminary results of the BAM (bifunctional adaptive mesh) code in evolving single and double black hole spacetimes. Papadopoulos, Seidel and Wild (1998) use the HLL (hierarchical linked list) AMR code of Wild (1996) to simulate gravitational radiation produced by a perturbed black hole. Mitra, Parashar and Browne (1998) developed the DAGH (distributed adapted grid hierarchies) code for use by the Binary Black Hole NSF Grand Challenge

project. Diener et al. (1999) have constructed initial data sets for the Einstein equations by using an FTT (fully threaded tree) AMR code to solve elliptic equations. The Cactus code (Bona et al. 1998, Massó and Walker 1999), which is being developed by a number of researchers, is expected to incorporate AMR capabilities in the future.

This chapter discusses the AMR code developed for the present work. Section 3.1 summarizes the AMR algorithm and section 3.2 describes some of its details (in particular ideas which are new to this work, or which have received little attention in the standard literature). Section 3.3 describes the modular structure of the code and comments on some of the C++ object-oriented language features used to implement it. Section 3.4 explains how the code has been implemented to make use of multiple processors, and finally section 3.5 assesses how well the code performs in practice. The prototype of the code was written by J. M. Stewart. A brief description of it is given in Hern and Stewart 1998.

### 3.1 Outline of the AMR Algorithm

The AMR code developed for the present work functions on the same basic principles as do the majority of AMR codes described in the literature, of which Berger and Olinger 1984, Berger and Colella 1989, and Bell et al. 1994 form a good sample. This section summarizes the main features of the basic algorithm, which is essentially the same for all AMR codes, and about which more can be found in the above references. In section 3.2 some esoteric aspects of the algorithm—in particular some ideas new to this work—are discussed in greater depth.

In this work, AMR is used for numerical simulations in one and two spatial dimensions. As is the general case with AMR codes, the algorithm in one dimension is significantly simpler than the two-dimensional version, both in terms of the concepts involved and the programming required to implement them. By contrast, the algorithm in three or more dimensions is conceptually no different from the two-dimensional case, although the amount of work required to implement it is significantly greater. With this in mind, the discussion in this chapter concentrates on the two-dimensional version of the algorithm, with its application to higher dimensions, and its reduction to a single dimension, being straightforward.

The main features of the AMR algorithm are illustrated in figure 3.1.

#### *The Grid Hierarchy*

Chapter 2 introduced the uniform grid as a representation of data on a spatial domain in a discrete form. Uniform grids are used as building blocks by the AMR algorithm, with fine-meshed grids set in place to cover regions of coarse-meshed grids which would otherwise poorly represent the data in the underlying spatial domain. For the purposes of this discussion, a grid is taken to be a mesh of cells rather than points (see equations (2.7) and (2.6) of chapter 2), although the ideas in this section apply just as readily to grids of the latter type. The extent to which the AMR algorithm is affected by the type of grid used is a topic returned to later in this chapter.

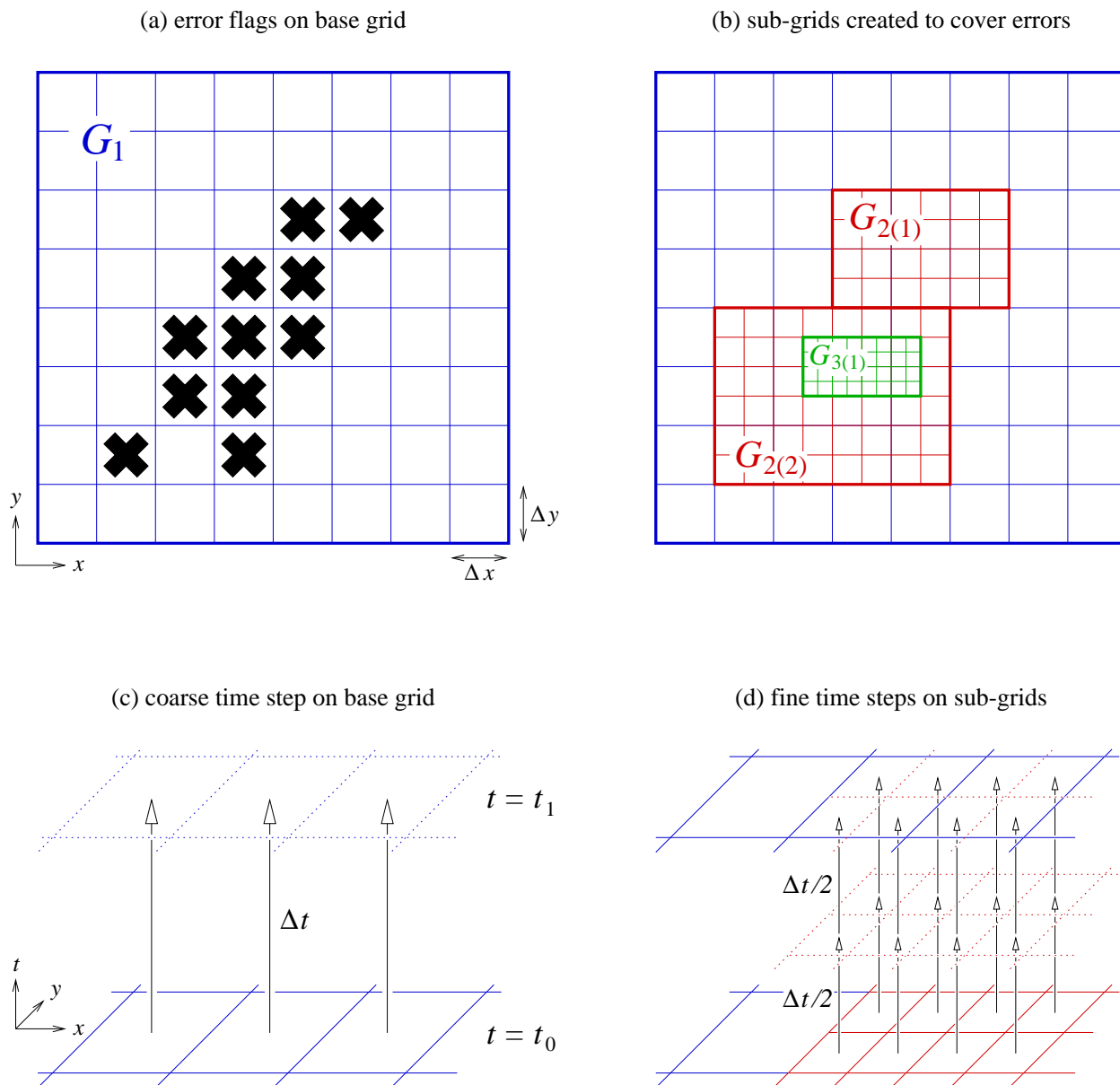


**Figure 3.1:** Basic features of an adaptive mesh refinement algorithm.

A hierarchical structure of grids is built up by the AMR algorithm in the following manner. Take as a starting point a grid  $G_1$  which has a mesh size  $(\Delta x, \Delta y)$  which is too coarse to accurately describe certain regions of the data it represents. The accuracy of the grid could be improved by decreasing its mesh size, but to do this everywhere on the grid would be a waste of computational resources, and to give the grid a non-uniform spacing would be, in all but simple cases, prohibitively complex. The AMR approach is to create a number of finely meshed sub-grids  $G_{2(1)}, \dots, G_{2(n)}$  that substitute for the original grid in the regions where it is lacking. The mesh size of a child grid  $G_{2(i)}$  will be related to that of its parent  $G_1$  by

$$\Delta x_{\text{child}} = \Delta x / \text{Refine}, \quad \Delta y_{\text{child}} = \Delta y / \text{Refine},$$

where **Refine** is an integer parameter in the code, a typical value for which is four.

If the newly formed sub-grids are still not sufficiently fine to resolve the data in all regions then the process of creating child grids continues recursively. The result is a family tree of grids in which each generation has a mesh spacing smaller than the last by a factor **Refine**. The original grid is said to form level one of the AMR grid hierarchy, with level two comprising the child grids, level three the grandchildren, and so on for an arbitrary number of levels. The construction of a grid hierarchy is illustrated in figure 3.1(a,b) for a value of **Refine** equal to two.

In principle a lot of freedom is allowed as to how grids can be arranged to form a grid hierarchy, with the early work of Berger (1982) testing out much of this freedom. However the AMR algorithm used for the present work applies some straightforward restrictions that lead to a significantly simpler code which is nonetheless (it is hoped) just as effective. First of all, children are required to be aligned with their parents, which is to say that the edges of cells in a child grid must be parallel to edges of the parent's cells, and the silhouette of the child must completely cover a rectangular block of cells in the parent. (This situation is shown in figure 3.1(b). More generally a child grid could use a completely different coordinate system to that of its parent.) Furthermore no grids at the same level may overlap, and every child grid must be completely contained within its parent. (The latter condition is not usually part of AMR algorithms, and complications caused by multiple parents result. Section 3.2 returns to this point.)

According to the description above, a grid hierarchy has only one grid in its first level. In fact this restriction is not enforced by the AMR algorithm, and section 3.4 suggests one reason for using multiple base grids. However, in practice a single base grid is more convenient to work with, and none of the simulations performed for this work have used multiple base grids.

### *Time-Stepping the Grid Hierarchy*

The discussion so far has concentrated on the structure of a grid hierarchy at one instant,  $t_0$ , in time. Taking the hierarchy itself to be fixed, this subsection outlines the way in which the AMR algorithm advances the family of grids to a later time,  $t_1 = t_0 + \Delta t_0$ .

The time-stepping operates by the following recursive procedure: all of the grids at level  $N$  are advanced one time step to time  $t + \Delta t$ , then all of the grids at level  $N + 1$  are advanced to the same

time. This is not as simple as it sounds since to be consistent with the Courant-Friedrichs-Lewy condition (equation (2.13)) the grids at level  $N + 1$  must be advanced by taking **Refine** steps of size  $\Delta t / \text{Refine}$ , rather than one step of size  $\Delta t$  (refinement takes place in time as well as in space); and since the time-stepping is recursive, each of the **Refine** steps at level  $N + 1$  is immediately followed by **Refine** correspondingly smaller steps at level  $N + 2$ , and so on up the grid tree. Advancing level one to time  $t_1 = t_0 + \Delta t_0$  in this way leads to the entire grid hierarchy being advanced to that time. This is illustrated in figure 3.1(c,d).

A grid can only be advanced in time if it has up-to-date boundary data (as discussed in section 2.1), and the AMR algorithm renews these data each time a step is taken by the grid. External and internal grid boundaries must be dealt with. External boundaries are the kind familiar from numerical simulations based on single grids, where the grid edges coincide with the edges of the spatial domain, and the boundary data are determined by the problem being solved. Grids at any level of the grid hierarchy can have external boundaries. The remaining boundaries are internal, and interpolation is used to supply the required boundary data; the construction of the grid hierarchy is such that a grid can always generate internal boundary data by interpolation of data in its parent grid. Since the time steps taken by a child grid are smaller than those taken by its parent, the times of child and parent often differ at the point when internal boundary data are needed by the child, and interpolation in time as well as in space becomes necessary; to allow for this each grid retains a copy of the data it held prior to its most recent time step. The use of interpolation is discussed further in section 3.2.

A child grid contains more accurate data than the region of its parent grid that it covers. In order for this difference in accuracy not to lead to a divergence in the approximations on the two grids as they are advanced in time, the data in the child grid must be used to update the data in the parent grid. This is done as part of the time-stepping procedure: whenever a child grid is advanced to the same time as its parent, the child's data are used to replace the parent's data in the region covered by the child.

### *Adaption of the Grid Hierarchy*

So far in this account the grid hierarchy has remained fixed while the grids in it have been advanced in time. The real power of the AMR algorithm comes from its ability to automatically adapt the hierarchy so as to maintain good resolution of data at all times during the evolution. A regridding phase in the algorithm creates, moves and destroys sub-grids in the hierarchy so that refined regions occur wherever and whenever they are needed.

A parameter **Regrid** (typically given the value four) determines the number of time steps taken by each level before it undergoes regridding, the result of which is rearrangement of grids on the levels above. This is worked into the recursive time-stepping procedure such that regridding at level  $N + 1$  takes place **Refine** times more often than at level  $N$ . The regridding phase includes two notable sub-problems: how to decide where refinement is needed, and how to arrange sub-grids to achieve this refinement.



Regions are marked for further refinement at the start of the regridding phase. Each grid cell has an error flag which is set if the data there fail to meet some kind of accuracy criterion. The nature of the problem itself may suggest appropriate criteria (such as close proximity to a shock front in a hydrodynamics simulation), but while such approaches are useful if they are available a more general method is to flag points at which an estimate of the local truncation error is higher than a pre-set tolerance. Berger and Olinger (1984) explain in detail how the local truncation error can be estimated using Richardson extrapolation; for the present discussion a quick sketch of the method will suffice. As a grid is advanced in time, the data on it are stored for the current time,  $t_n$ , and also for the previous two time steps,  $t_{n-1} = t_n - \Delta t$  and  $t_{n-2} = t_n - 2\Delta t$ . If the data at time  $t_{n-2}$  are coarsened such that their resolution is changed from  $(\Delta x, \Delta y)$  to  $(2\Delta x, 2\Delta y)$ , and then advanced by a time step  $2\Delta t$ , then the result is a second approximation to the exact solution at time  $t_n$ . The difference between the two approximations is an estimate of the local truncation error.

Given a set of error flags the next task is to find an arrangement of sub-grids which covers all of the flags but which has as small an area as possible. This process is described as clustering. While the original work by Berger (1982, 1986) used quite elaborate clustering heuristics, more straightforward approaches based on computer vision algorithms have since been developed (Bell et al. 1994), and these are adopted for the clustering algorithm used in the present work.

Regridding at level  $N$  means that all of the grids at level  $N + 1$  are replaced by a new arrangement of grids based on the results of the clustering of level  $N$ 's error flags; if level  $N + 1$  does not exist it is created at this stage. Typically some of the new level  $N$  grids will overlap the old ones, and where this happens the old data are copied across to the new grids. The remaining data needed to complete the new grids are provided by interpolation of the data in the level  $N$  grids. Interpolation methods and the regridding algorithm are topics considered in greater depth in the next section.

### 3.2 Details of the AMR Algorithm

The previous section summarized the AMR algorithm used in the present work. Most of the features discussed there are common to all AMR algorithms based on Berger and Olinger's original design (1984). In this section several extensions to the standard algorithm are considered. Flux conservation is achieved by implementing the ideas of Berger and Colella (1989), and some conservative interpolation methods are developed. The standard regridding algorithm (Berger and Olinger 1984) is replaced by a new approach which avoids some of the complexities usually associated with AMR in two (or more) dimensions. Provisions are made for variable time steps, and the importance of communication between neighbouring grids is acknowledged.

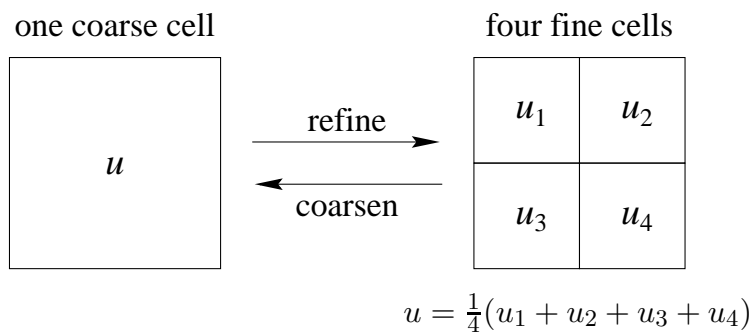


**Figure 3.2:** Conservation of data ‘mass’ when converting between coarse and fine grid cells. (Refinement here is by a factor of two.)

### *Flux Conservation*

The AMR algorithm described in section 3.1 uses grids which are made up of cells rather than points. Such grids can be time-stepped using the flux-conservative methods of chapter 2. However, for the AMR algorithm itself to be conservative, operations involving the transfer of data between grids must be appropriately designed. Berger and Colella (1989) and Berger and LeVeque (1998) describe the modifications needed to make the standard AMR algorithm fully conservative, and this subsection considers these modifications in the context of the present work. (For an alternative approach see Berger 1987.)

The main idea used to make the AMR algorithm conservative is straightforward: recalling that the unknown variables represent ‘densities’ of some kind (section 2.1), whenever grid cells are coarsened or refined it should be done in such a way as to conserve the total ‘mass’ of data contained within each of the coarse cells. This is illustrated in figure 3.2. Grid cells are coarsened whenever a parent grid is updated using data on a child grid, and as part of the local truncation error estimation procedure, and the conservative method for coarsening data is unambiguous: a coarse grid cell is produced by averaging the data in the fine grid cells. Sub-grids require data to be refined when they are created, and also to provide them with boundary data, and in both cases interpolation is used. Conservative interpolation methods are the subject of the next two subsections.

By using a flux-conservative integration method, conservation is guaranteed for individual grids as they are advanced in time. However problems still arise at the interfaces between grids. The fluxes at the edges of a child grid affect both the outermost cells of the child and the cells in the parent which surround that child, but their values depend on whether they are calculated as part of the parent’s time step or the child’s time step. For the AMR algorithm to be fully conservative, corrections must be made to all of the cells in a parent grid which border onto child grids to account for this discrepancy, as explained by Berger and LeVeque (1998). These corrections have not however been implemented in the AMR code used for the present work. Though the reasons for this are mainly practical, the omission can be partially justified. None of the numerical simulations performed for this work actually required global conservation since (because of the presence of source

terms) none of the systems of equations were themselves strictly conservative. Also, while numerical conservation is important for evolving solutions with discontinuities, it is only required locally; as long as the grids covering a discontinuity are at the same level of refinement there should be no need for boundary corrections. One final (mainly aesthetic) argument against the implementation of boundary corrections is that, because they introduce a lot of additional communication between grids on different levels, they make the scheme for separating grids from their data—described in section 3.3—significantly more convoluted.

This subsection ends on a brief technical aside. The flux-conservative wave-propagation methods described in chapter 2 have symmetrical integration stencils of width five, and consequently the grids used in the AMR algorithm have boundary regions two cells wide (see section 2.1). In many ways this is a disadvantage; in particular it increases the amount of work needed to advance each grid. However it turns out to be advantageous when it comes to interpolating boundary data for child grids: because a child’s boundary cells never extend to the limits of its parent, there is always sufficient data on the parent grid to allow interpolation. (This is not the case for some other AMR algorithms which occasionally need to interpolate boundary data from grandparent grids.)

### *Interpolation I: Piecewise Polynomial Methods*

An AMR algorithm frequently needs to refine regions of coarse data, and to do this some form of interpolation is used. The choice of interpolation method depends on whether the data to be interpolated are stored at grid points or (as in the present work) are averaged over grid cells. (The distinction is made clear in section 2.1.) This subsection and the one that follows describe conservative interpolation methods for grids of cells in two dimensions (though the arguments are straightforward to apply to any number of dimensions).

Consider first a coarse grid made up of a two-dimensional mesh of points,

$$(x_i, y_j) = (x_0 + i \Delta x, y_0 + j \Delta y), \quad i, j \in \mathbb{Z},$$

together with data  $f_{i,j}$  defined at these points. In order to generate fine data from this coarse grid an interpolating function  $F(x, y)$  which satisfies  $F(x_i, y_j) = f_{i,j}$  is needed. Given such a function, fine data can be defined at points which lie in between the points of the coarse mesh; for example,  $\hat{f}_{i+1/2, j+1/2} := F(x_i + \Delta x/2, y_j + \Delta y/2)$ . Chapter 3 of Press et al. 1992 describes a range of interpolation methods suitable for generating a function  $F(x, y)$ . First- or second-order polynomial interpolation is typically used in AMR algorithms.

For a flux-conservative AMR algorithm based on grid cells rather than points the situation is a little different. The data  $u_{i,j}$  in a coarse grid cell are defined by an average over the area of the cell, and an interpolating function  $U(x, y)$  for this coarse data is required to satisfy

$$\frac{1}{\Delta x \Delta y} \int_{x_i - \Delta x/2}^{x_i + \Delta x/2} \int_{y_j - \Delta y/2}^{y_j + \Delta y/2} U(x, y) dy dx = u_{i,j}.$$

Fine grid data are constructed by integrating an interpolating function over sub-intervals of the coarse grid cells. This is illustrated in one dimension in figure 3.3.

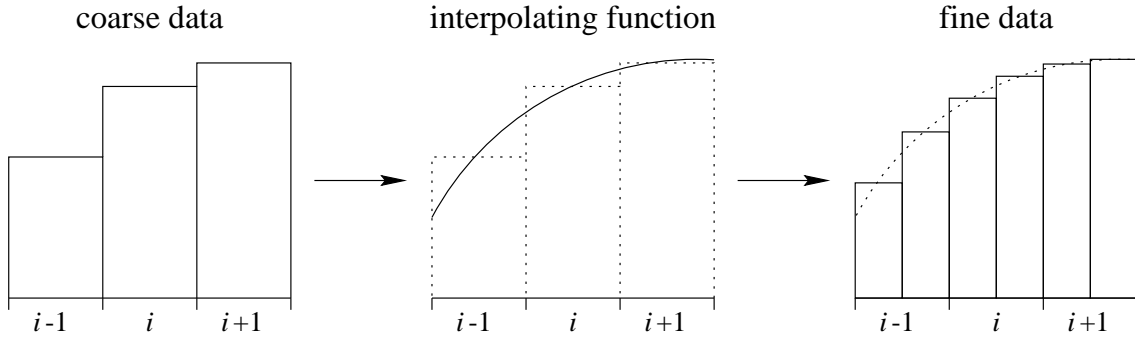


**Figure 3.3:** Conservative interpolation in one dimension. A set of fine data (third plot) is generated to replace the available coarse data (first plot) using an interpolating function as an intermediate step (second plot). The ‘mass’ of data in each coarse cell (represented by the area under the graph) is conserved. (Refinement here is by a factor of two.)

The AMR code used for the present work allows the user to choose from three different types of conservative interpolation: piecewise linear, piecewise quadratic and spline. Sample results are shown in figures 3.4 and 3.5. Other flux-conservative AMR codes described in the literature invariably use some form of linear interpolation, and the reasons for this are discussed below.

The idea underlying piecewise polynomial interpolation methods is to construct an interpolating function  $U(x, y)$  for the entire grid by piecing together polynomial functions  $U_{i,j}(x, y)$  which are defined only on individual grid cells. For linear interpolation a grid cell centred on  $(x_i, y_j)$  will have a local interpolating function of the form

$$U_{i,j}(x, y) = a + b_x(x - x_i) + b_y(y - y_j),$$

where  $a$ ,  $b_x$  and  $b_y$  are constants to be determined in some way from the cell averages  $u_{i,j}$ ,  $u_{i+1,j}$ ,  $u_{i-1,j}$ ,  $u_{i,j+1}$  and  $u_{i,j-1}$ ; in fact, the requirement that the integral of  $U_{i,j}$  over the grid cell be equal to the cell average automatically fixes  $a = u_{i,j}$ . Berger and LeVeque (1997) choose  $b_x$  and  $b_y$  to be

$$b_x = \text{minmod}(u_{i+1,j} - u_{i,j}, u_{i,j} - u_{i-1,j})/\Delta x,$$

$$b_y = \text{minmod}(u_{i,j+1} - u_{i,j}, u_{i,j} - u_{i,j-1})/\Delta y,$$

and this choice is adopted by the present work. Slopes in both the  $x$  and  $y$  directions are selected according to the min-mod function,

$$\text{minmod}(\alpha, \beta) = \begin{cases} \alpha & \text{if } |\alpha| < |\beta| \text{ and } \alpha\beta > 0, \\ \beta & \text{if } |\beta| < |\alpha| \text{ and } \alpha\beta > 0, \\ 0 & \text{if } \alpha\beta \leq 0, \end{cases}$$

which has its origins as a slope-limiter for high-resolution numerical methods (see LeVeque 1992, page 186), and which prevents the linear sections from overshooting their neighbours if the data to

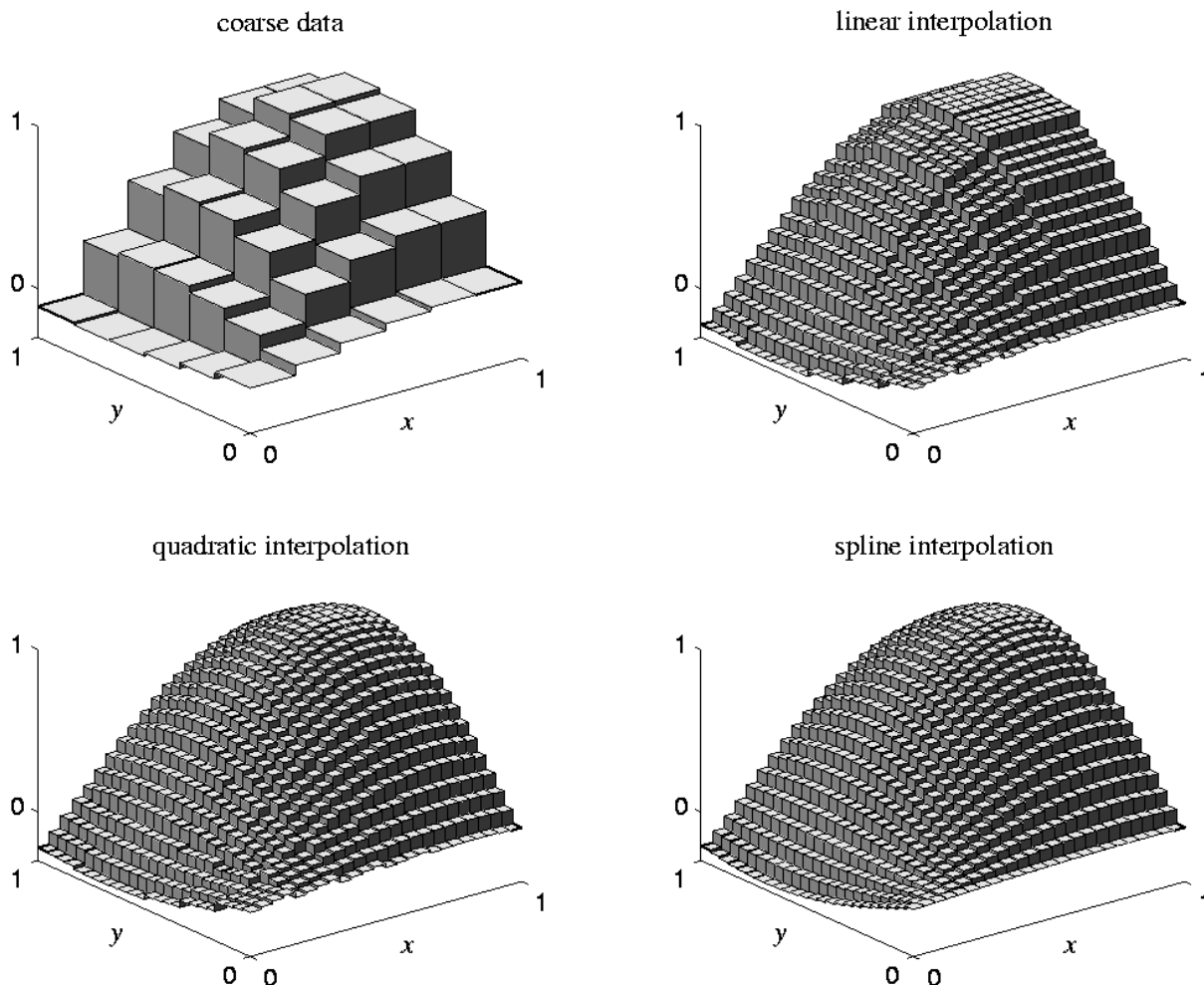


**Figure 3.4:** Sample interpolation results for smooth initial data. Three different conservative interpolation methods are used to refine a coarse grid of data by a factor of four. The coarse grid consists of  $8 \times 8$  cells (the outermost cells provide boundary data for the interpolation and only the  $6 \times 6$  innermost cells are shown) and this is refined to a grid of size  $24 \times 24$ . The coarse data are produced by taking cell averages of the function  $\sin(2.25x - 0.0125) \sin(2.25y - 0.3125)$ .

be interpolated are not particularly smooth: the interpolating function is monotonic if the coarse data are monotonic. There are of course other reasonable ways of choosing  $b_x$  and  $b_y$ .

For piecewise quadratic interpolation the local interpolating function takes the form

$$U_{i,j}(x,y) = a + b_x(x - x_i) + c_x(x - x_i)^2 + b_y(y - y_j) + c_y(y - y_j)^2.$$

The five constants  $a$ ,  $b_x$ ,  $b_y$ ,  $c_x$  and  $c_y$  can be fixed in a straightforward way by requiring that the integral of  $U_{i,j}(x,y)$  over the five centremost cells be equal to the respective coarse cell averages  $u_{i,j}$ ,  $u_{i+1,j}$ ,  $u_{i-1,j}$ ,  $u_{i,j+1}$  and  $u_{i,j-1}$ .

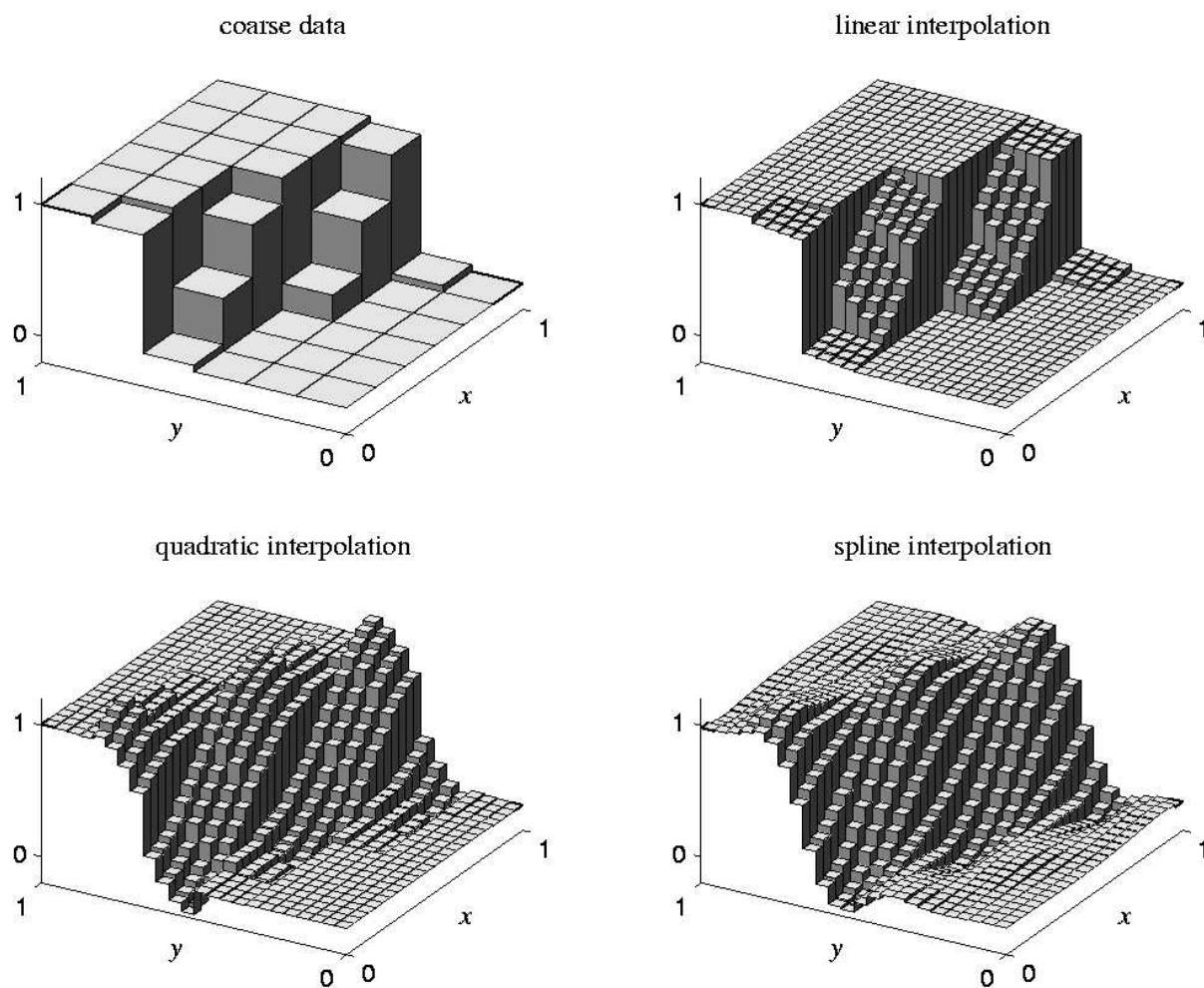


**Figure 3.5:** Sample interpolation results for discontinuous initial data. The setup is the same as in figure 3.4 except that here the coarse data are cell averages of a piecewise constant function which takes the value one for  $x + 2.5y \geq 1.75$  and is zero elsewhere.

The advantages and disadvantages of linear compared to quadratic interpolation are clear from figures 3.4 and 3.5. When the data to be interpolated are reasonably smooth then, as figure 3.4 shows, quadratic interpolation is preferable to linear interpolation, with the results of the latter being quite uneven and jagged. On the other hand, if the data on the coarse grid are discontinuous (figure 3.5), then the results of linear interpolation, though by no means perfect, are better than the results of quadratic interpolation in which the tops and bottoms of discontinuities may be overshoot quite badly. Linear interpolation is thus the method of choice for numerical simulations in which the data have, or are expected to develop, discontinuities, and this is the reason for its use as part of flux-conservative AMR codes.

However for many of the numerical simulations performed for the present work no discontinuities develop in the data and the shortcomings of linear interpolation become apparent. The jaggedness produced by linear interpolation introduces noise (with wavelengths on the order of the width of a coarse grid cell) into the solution every time a new sub-grid is created or internal boundary data for a sub-grid are produced. Over time this noise accumulates on the sub-grids and can eventually build up to such a level that the simulation is forced to terminate. Experimentation suggests that the noise is not significantly amplified by the evolution in comparison to the background solution, and its initial amplitude is the main concern. Increasing the accuracy of the interpolation would reduce the amplitude of the noise, and this can be done in two ways. Firstly, if the mesh spacing of a coarse grid is decreased such that the data on it are very well resolved then the inaccuracies in the interpolated data will be small. The effect of this is apparent in the differences between one- and two-dimensional simulations. In one dimension the meshes used are typically fine enough that linear interpolation produces good results, and noise is not found to be a problem. However the meshes used in two-dimensional simulations are much coarser and the resulting poor resolution of data means that errors in interpolation are significant. It is usually impractical to substantially decrease the mesh spacings used in numerical simulations (after all, this is the reason why AMR is used in the first place), and the alternative approach to improving interpolation accuracy is to use higher-order methods. This is the motivation for implementing quadratic interpolation in the AMR code used in this work, and the result is a reduction in noise amplitude with a corresponding increase in simulation long-term stability.

As can be seen from figure 3.4, quadratic interpolation still introduces some unevenness into the refined data (most obvious close to the  $x$ - $y$  origin in the figure), and the resulting level of noise is still unacceptable for some simulations. The piecewise nature of the interpolating function  $U(x, y)$  is the main cause of this problem, and by using conservative spline interpolation methods to produce globally smooth data it may be hoped that the effect of noise on sub-grids could be minimized.

### *Interpolation II: Spline Methods*

Press et al. (1992, section 3.3) describe how cubic splines can be used to interpolate data which are defined on a mesh of points. In this subsection a quadratic spline method is developed for the conservative interpolation of data defined on meshes of cells. In the same way as in cubic spline interpolation, one-dimensional quadratic splines are constructed as part of the interpolation procedure in two and higher dimensions, and these will be described first.

A one-dimensional cubic spline is an interpolating function  $F(x)$  which takes the values  $f_1, \dots, f_n$  at the points  $x_1, \dots, x_n$ , and is constructed by requiring that it be a cubic function on each interval  $[x_i, x_{i+1}]$  (for  $1 \leq i < n$ ) and that it be continuous and smooth with continuous second derivative at each point  $x_i$  (for  $1 < i < n$ ). The specification of a conservative quadratic spline proceeds along similar lines. For a uniform mesh,  $x_i = x_0 + i \Delta x$ , with cell averages  $u_1, \dots, u_n$ , an interpolating function  $U(x)$  is constructed which is quadratic on each interval  $[x_i - \Delta x/2, x_i + \Delta x/2]$

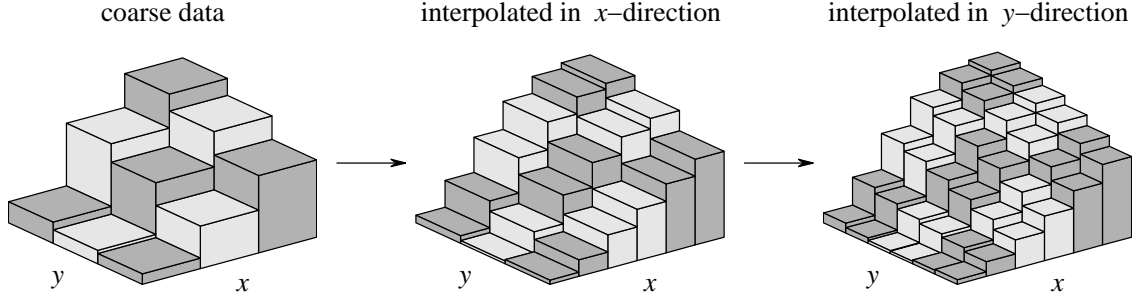


**Figure 3.6:** Conservative interpolation of two-dimensional data using a one-dimensional method. Interpolation sweeps in the  $x$ -direction are followed by sweeps in the  $y$ -direction. (Refinement here is by a factor of two.)

(for  $1 \leq i \leq n$ ), with

$$\frac{1}{\Delta x} \int_{x_i - \Delta x/2}^{x_i + \Delta x/2} U(x) dx = u_i$$

(for  $1 \leq i \leq n$ ), and which is continuous and smooth at each point  $x_i + \Delta x/2$  (for  $1 \leq i < n$ ). From these requirements the relationship

$$U_{i-1/2} + 4U_{i+1/2} + U_{i+3/2} = 3(u_i + u_{i+1})$$

is found for the values  $U_{i+1/2} := U(x_i + \Delta x/2)$  of the interpolating function at the cell edges, for  $2 \leq i \leq n - 2$ . Two boundary conditions are needed to uniquely specify the spline and these are provided by taking the spline to be linear in the first and last cells,  $[x_1 - \Delta x/2, x_1 + \Delta x/2]$  and  $[x_n - \Delta x/2, x_n + \Delta x/2]$ . The result is a system which completely determines the values of the interpolating function at the cell edges:

$$\begin{pmatrix} 3 & 1 & & & & & \\ 1 & 4 & 1 & & & & \\ & 1 & 4 & & & & \\ & & & \ddots & & & \\ & & & & 4 & 1 & \\ & & & & 1 & 4 & 1 \\ & & & & & 1 & 3 \end{pmatrix} \begin{pmatrix} U_{1+1/2} \\ U_{2+1/2} \\ U_{3+1/2} \\ \vdots \\ U_{n-2-1/2} \\ U_{n-1-1/2} \\ U_{n-1/2} \end{pmatrix} = \begin{pmatrix} 3u_2 + u_1 \\ 3(u_3 + u_2) \\ 3(u_4 + u_3) \\ \vdots \\ 3(u_{n-2} + u_{n-3}) \\ 3(u_{n-1} + u_{n-2}) \\ u_n + 3u_{n-1} \end{pmatrix}.$$

This tridiagonal system can be solved for the values  $U_{i+1/2}$  by a method of forward- and back-substitution (see Press et al. 1992, section 2.4). Knowledge of  $U_{1+1/2}, \dots, U_{n-1/2}$  and  $u_1, \dots, u_n$  is sufficient to evaluate the quadratic spline  $U(x)$  in its entirety, and from this cell averages on a more refined grid can be defined as before.

A conservative interpolation method in one dimension can be used to interpolate data conservatively in any number of dimensions, and this is the way quadratic spline interpolation is applied to two-dimensional grids. Figure 3.6 illustrates the procedure. The coarse grid cells are first interpolated along lines parallel to the  $x$ -axis. The partly-refined cells that result are then refined in the  $y$ -direction.



Figures 3.4 and 3.5 show examples of results produced by quadratic spline interpolation. For smooth initial data (figure 3.4) the results are smooth, without the jaggedness at the edges of coarse cells that occurs with the piecewise polynomial methods. However for discontinuous initial data (figure 3.5) quadratic spline interpolation suffers from the same problem that plagues piecewise quadratic interpolation: it produces oscillations around discontinuities, and in contrast to the piecewise method the oscillations affect (albeit very slightly) the entire grid not just the cells along the discontinuities. This aside, when spline interpolation has been used in simulations in which the data do not become discontinuous, it has been found to work well and the problem of build-up of noise on sub-grids is much less severe.

For data defined at points, spline interpolation might be expected to be less of an improvement over piecewise methods than it is in the case of data defined over cells since there is never any difficulty in constructing a pointwise interpolating function which is continuous. However in practice the lack of smoothness in piecewise interpolated data is still found to lead to higher levels of noise in some simulations than is acceptable.

The conservative interpolation methods described in this and the previous subsections have been developed by adapting in a natural way the ideas in chapter 3 of Press et al. 1992. In fact the methods in that reference can be used to derive conservative interpolation methods directly. For a one-dimensional uniform grid  $x_1, \dots, x_n$  with cell averages  $u_1, \dots, u_n$ , a discrete function  $f_{1/2}, \dots, f_{n+1/2}$  can be defined which takes values at the cell edges  $x_{1/2}, \dots, x_{n+1/2}$ :

$$f_{1/2} = 0, \quad f_{i+1/2} = \sum_{k=1}^i u_k \Delta x \quad \text{for } 1 \leq i \leq n.$$

Standard methods of interpolation can then be applied to find an interpolating function  $F(x)$  that passes through the points  $(x_{i+1/2}, f_{i+1/2})$ , and it can be seen that  $U(x) := F'(x)$  is a conservative interpolating function for the original grid cells. Bypassing the evaluation of  $U(x)$ , cell averages for a refined grid can be calculated directly from  $F(x)$ : for a cell  $[x_A, x_B]$ , the interpolated average  $\hat{u}_{AB}$  is

$$\begin{aligned} \hat{u}_{AB} &= \frac{1}{x_B - x_A} \int_{x_A}^{x_B} U(x) dx \\ &= \frac{F(x_B) - F(x_A)}{x_B - x_A}. \end{aligned}$$

If an order  $n$  interpolation method is used to determine  $F(x)$ , then  $U(x)$  is constructed by the equivalent of order  $(n - 1)$  interpolation, and this is why quadratic splines are natural for interpolating grid cells while cubic splines are used for grid points. This approach for constructing conservative interpolation methods extends in an obvious way to higher dimensions by taking

$$f_{i+1/2, j+1/2} = \sum_{k=1}^i \sum_{l=1}^j u_{k,l} \Delta x \Delta y, \quad \text{etc.}$$

Essentially the same results are produced by both approaches. However for some methods (in particular the min-mod interpolation method described in the previous subsection) the construction

is more intuitive when viewed as a cell interpolation method rather than the reduction of a point interpolation method.

### *The Regridding Procedure*

A surprising feature of Berger and Olinger’s AMR algorithm (1984) is that a child grid is not limited to having only one parent: a level  $N + 1$  grid is allowed to overlap any number of level  $N$  grids as long as it is completely contained within their union. This makes many of the grid operations performed in an AMR code based on Berger and Olinger’s design significantly more complicated than they would otherwise be since multiple parent grids must be accounted for during any communication of data between grids at different levels. The reason why multiple parents are usually allowed is that the standard AMR regridding procedure cannot maintain proper child-parent nesting when it makes alterations to the grid hierarchy. (This is actually only the case in two or more dimensions, and is part of the reason why one-dimensional AMR codes are much more common than multi-dimensional ones.) For the AMR algorithm used in the present work the author has designed a new regridding procedure which ensures proper child-parent nesting and which consequently simplifies the implementation of the code as a whole: each grid need only maintain a pointer to its parent, not a list of pointers to a number of parents. Figure 3.7 shows the new regridding algorithm.

Regridding at level  $N_{\text{regrid}}$  results in changes being made to the grid layouts on all of the more refined levels,  $N_{\text{regrid}} + 1$  to  $N_{\text{finest}}$ , as well as the possibility of a new level,  $N_{\text{finest}} + 1$ , being created. The standard method of regridding, as described by Berger and Colella (1989), operates as follows. Starting at level  $N = N_{\text{finest}}$  and working down to level  $N_{\text{regrid}}$ , error flags at level  $N$  are clustered and, based on the results, new sub-grids are created to replace the grids at level  $N + 1$  (that level being created if it does not already exist). To ensure that sub-grids are always contained within the union of grids at the level below, if level  $N + 2$  exists when level  $N$  is due to be clustered, error flags are set in level  $N$  in any region covered by a grid in level  $N + 2$ . At the time of its creation a child grid is always completely contained within a single parent grid; nesting problems arise because the parent’s level may be rearranged immediately after.

The regridding procedure used in the present work avoids nesting problems and the need for multiple parents by reversing the order in which the levels are regridded (coarse to fine instead of fine to coarse) and making a preliminary pass through the grid hierarchy to prepare the error flags. To ensure that no useful information is lost at the finest levels, before any alterations are made to the grid hierarchy the error flags on the coarser levels are made up-to-date. Starting at level  $N = N_{\text{finest}} - 1$  and working down to level  $N_{\text{regrid}}$ , for each grid at level  $N$  error flags are set at all points at which errors are flagged in its child grids. (The function `flag_errors_in_tree` performs this by recursion in figure 3.7.) The actual regridding then proceeds from level  $N = N_{\text{regrid}}$  up to level  $N_{\text{finest}}$ . For each grid at level  $N$  error flags are clustered and new child grids are created. These new grids are replacements for the existing grids at level  $N + 1$ , but before any grids are destroyed data and, importantly, error flags are copied from old grids to new wherever there is

```

void example() {
    Level base_level;
    base_level.regrid_tree();
}

void Level::regrid_tree() {
    flag_errors_in_tree();
    regrid_level();
}

void Level::flag_errors_in_tree() {
    flag errors in grids at this level
    if ( next_level.contains_grids() ) {
        next_level.flag_errors_in_tree();
        set flags in this level where there are errors in next_level's grids
    }
}

void Level::regrid_level() {
    Level new_level = (new sub-grids created to cover error flags at this level);
    copy data and flags from grids in next_level to overlapping grids in new_level
    destroy all grids in next_level
    move grids from new_level into next_level
    if ( next_level.contains_grids() ) {
        next_level.regrid_level();
    }
}

```

**Figure 3.7:** Skeleton code for the new regridding algorithm, written in C++. A `Level` object contains the grids at one level of refinement. The function `regrid_tree` regrids the hierarchy starting at the current level: grids at all finer levels are replaced. Child grids are always properly nested within their parents and hence multiple parents are avoided.

overlap between them. (The function `regrid_level` performs this by recursion in figure 3.7.) Since the grid hierarchy is always rebuilt starting from the coarsest levels, and since a child grid is always properly nested within a single parent when it is created, multiple parents are not a problem when this new regridding procedure is used.

### *Variable Time Steps*

The Courant-Friedrichs-Lewy condition (equation (2.13)) puts an upper limit on the sizes of time steps that can be taken when evolving numerical solutions to hyperbolic systems. Since the upper limit usually varies during the course of the evolution it is common practice for numerical codes to allow the time steps to adapt, with each new time step being chosen based on an estimate

of the current Courant-Friedrichs-Lewy upper limit. However, because of the complexity of the hierarchical time-stepping and the use of double time steps in the error estimation procedure, variable time steps are not as straightforward to implement in an AMR code as they are in a traditional single-grid code. (Examples of AMR codes using variable time steps are Hamadé 1997 and Berger and LeVeque 1997.)

The AMR code used for the present work allows variable time steps, but with limitations. The time steps can be changed only at the same time that level one of the grid hierarchy is regridded. (Recall that all grids on the same level are advanced with the same time step and that the time step for level  $N$  grids is  $\Delta t/\text{Refine}^{(N-1)}$  where  $\Delta t$  is the base level time step; obviously when the time step is changed it is changed consistently throughout the grid hierarchy.) This means that the time step size can only be altered after the grids on the coarsest level have taken **Regrid** time steps.

A side effect of the implementation of variable time steps concerns the production of internal boundary data for sub-grids. The interpolation of fine boundary data from coarse parent grids is performed temporally as well as spatially. Since data are stored on each grid for three stages in time (the current time and the two previous time steps; this is required by the error estimation routine), time interpolation could be performed at second order. However, while this was done in an early version of the AMR code, the implementation of variable time steps restricts interpolation in time to being first order.

The value of variable time steps is exemplified by the Gowdy cosmological collapse simulations of chapter 6. The Courant-Friedrichs-Lewy limit on the time steps in that problem increases exponentially with time, although in practice a limit lower than this must be accepted if the source terms in the system are to be dealt with accurately at late times. By allowing time steps to increase during the simulations (but only up to some preselected maximum), a dramatic decrease in running time is achieved compared to simulations which use fixed time steps.

### *Neighbouring Grids*

The AMR algorithm developed for the present work gives special attention to grids on the same level which abut, that is share a common edge. Each grid maintains a list of the grids that abut it, and data from these neighbouring grids can be used during some operations performed by the AMR algorithm. Most significantly, abutting grids provide boundary data for each other along their common edges, and these are used in preference to data interpolated from a parent grid (see Berger and Colella 1989). Similarly, boundary data from neighbouring grids can be used for the ‘coarsened steps’ taken by grids during the error estimation procedure. In addition, as part of the error clustering process the error flags on each grid are extended by a buffer region to pre-empt the movement of features in the evolved solution, and these buffer regions are allowed to cross into neighbouring grids.

By keeping track of neighbouring grids the AMR algorithm ensures that the results produced at grid interfaces are of no lesser accuracy than the results produced elsewhere. However, it could

be argued that the number of grids which abut is unlikely to be large enough to justify the increase in algorithm complexity required to take them into account. Furthermore, in one dimension there should be no neighbouring grids at all: two abutting grids can always be combined to form one single grid. The motivation for implementing communication between neighbouring grids in the present work is a consequence of the way in which the AMR code has been parallelized. As section 3.4 explains, large grids can be split into smaller abutting grids by the clustering process to improve code performance, and this can lead to a significant increase in the number of abutting grids even in the one-dimensional case.

Many of the numerical simulations performed for the present work use periodic boundary conditions and in such cases the situation can arise in which two grids abut along external (periodic) boundaries rather than along internal ones. In fact when periodic boundaries are used it is possible to have a grid which abuts itself on all sides. Periodic boundary conditions are sufficiently important in the present work that the AMR code takes them into account when constructing lists of neighbouring grids.

### 3.3 Structure of the AMR Code

The complexity of the AMR algorithm calls for more sophisticated programming techniques than are usually necessary for traditional numerical codes. In particular, an AMR code is likely to make extensive use of dynamic memory allocation, data structures and recursive functions, and its lack of support for these programming constructs makes implementing an AMR algorithm in Fortran 77 difficult (though certainly not impossible, as Berger and LeVeque 1997 demonstrates). The AMR code used in the present work is written in the C++ language (Stroustrup 1997, Lippman and Lajoie 1998) and the object-oriented features of that language are used to develop data structures within the code that reflect the conceptual structure of the algorithm. In particular the implementation respects the distinction between the AMR algorithm itself and the algorithm used to evolve data on grids, and makes it easy to link different evolution procedures to the same AMR code.

In this section the AMR algorithm is decomposed into four modules: clustering, grid management, grid evolution and grid interaction. (The term module is used here to refer to a collection of functions or classes which share a common purpose, and usually the same source files.) The interfaces between the modules are simple and well defined, and in principle each could be implemented by a different programmer in a different programming language. Some of the object-oriented capabilities of C++ which facilitate the implementation of these modules are discussed. The modules are entirely independent of the problem they are used to solve. (For the sake of clarity the names given to classes and functions in the following explanation often differ from the names used in the program source code.)

### *Clustering and Grid Management*

The first point to note is that the clustering phase of the AMR algorithm (see section 3.1) is completely self-contained, and should be implemented in a way that respects this. The clustering module takes an array of error flags and returns a list of regions where new sub-grids should be created. Its complex operation can be treated as a ‘black box’ by other parts of the AMR code. (Illustrating the independence of modules, during extensive writing and rewriting of the AMR code the clustering module, written by J. M. Stewart, has not needed altering at all.)

At the highest level of abstraction, the AMR algorithm is concerned solely with the manipulation of grids in the grid hierarchy: it creates and destroys grids, advances them in time, orchestrates the exchange of boundary data between neighbouring grids, and so on (recall figure 3.1). These aspects of the AMR algorithm form the grid management module. Although the module is, in terms of source code, relatively small, it contains the most complicated parts of the AMR algorithm. To a large extent the module is independent of the dimension of the grids it manages.

It is natural to create a data structure to represent grid objects that are manipulated by the grid management module, and figure 3.8 shows the outline of a suitable C++ class, `AmrGrid`. The contents of the class can be divided into three basic groups. The first group comprises information used directly by the grid management module to fit grids into the grid hierarchy, for example the size and coordinate origin of a grid and the details of its sub-grids. The second group comprises functions through which the grid management module manipulates the solution data stored on grids, for example a function `advance_grid` which integrates the data in time. The final group comprises additional data structures and functions used by the grids themselves; in particular it would be useful for each grid to maintain an array of error flags.

One thing conspicuously absent from the `AmrGrid` class is the actual solution data that a grid stores. The reason for this is that to specify a format for the solution data is to limit the AMR code to that format; among other things the code would be tied to either the grid point or the grid cell framework. Since the grid management module is not actually affected by the data format, there is no reason for the `AmrGrid` class to be, and instead it is declared an abstract class: by itself it is incomplete and objects of its type cannot be used in the AMR code. The member functions designed to manipulate the solution data are declared to be pure virtual functions by the syntax

```
virtual function = 0;
```

in the class declaration (figure 3.8), and this means that they have no definition within the `AmrGrid` class but must instead be defined in a class derived from it (as demonstrated in the next subsection).

The clustering and grid management modules by themselves form a basic AMR software package. The next subsection explains how extensions to the package allow it to work with different data formats and integration methods.

```

class AmrGrid {
public:

    // information used for grid management
    location of grid within spatial domain of the problem
    relative position of grid in hierarchy: pointer to parent, list of children, etc.

    // functions for manipulating solution data
    virtual void advance_grid(double dt) = 0;
    virtual void flag_errors(double tolerance) = 0;
    virtual AmrGrid* make_subgrid(sub-grid details) = 0;
    etc.

    // data and functions mainly for internal use
    array of error flags
    functions for manipulating error flags (buffering, etc.)

};

```

**Figure 3.8:** Sketch of the `AmrGrid` class. It is an abstract C++ class which represents the parts of a grid used by the grid management module. It contains no actual solution data.

### *Grid Evolution and Grid Interaction*

A grid evolution module comprises two elements: solution data, and an algorithm for time-stepping the data. By itself such a module is the central part of a standard single-grid numerical code, and rather than describing how a grid evolution module can be especially written for use in the AMR code, this subsection explains how a pre-existing grid evolution module can be connected to the grid management module of the previous subsection. Figure 3.9 gives an example grid evolution module, a C++ class called `DataGrid`. In practice this class could be a ‘wrapper’ for a time-stepping procedure written in a different programming language with each instance of the class being allocated its own set of solution data in the format required by the time-stepper.

The `AmrGrid` class and the `DataGrid` class represent different aspects of the grids used in the AMR algorithm. The two classes are unified within the grid interaction module: in figure 3.10 multiple inheritance is used to create a class `HyGrid` that contains all of the functions and data of both the `AmrGrid` class and the `DataGrid` class. Together with a battery of functions for copying, coarsening and interpolating data, the `HyGrid` class makes up the grid interaction module. This bridges the gap between the grid management module and the grid evolution module, and completes the AMR package.

Inheritance in C++ makes it simple to create new classes that are modified versions of existing classes or that, like the `HyGrid` class, combine the features of two or more classes. More than this though, an instance of a derived class such as the `HyGrid` class can be used just as if it were an

```

class DataGrid {
public:

    array of solution data
    void timestep(double dt);

};

```

**Figure 3.9:** Outline of a basic grid evolution module, the `DataGrid` class. Each `DataGrid` object contains solution data which it is capable of evolving in time using an appropriate approximation scheme.

```

class HyGrid : public AmrGrid, public DataGrid {
public:

    // implementation of AmrGrid's pure virtual functions
    virtual void advance_grid(double dt) { DataGrid::timestep(dt); ... }
    virtual void flag_errors(double tolerance);
    virtual AmrGrid* make_subgrid(sub-grid details);
    etc.

    // functions and data for internal use
    solution data from previous two time steps—used for error estimation
    functions for data interpolation
    etc.

};

```

**Figure 3.10:** The `HyGrid` class is crossbred from the `AmrGrid` and `DataGrid` classes of figures 3.8 and 3.9. Multiple inheritance allows the data and functions of the two base classes to be combined in a single class. The `HyGrid` class completes the definitions of the pure virtual functions declared in the `AmrGrid` class. It is the centre-piece of the grid interaction module.

instance of one of the base classes: the grid management module will manipulate a hierarchy of `HyGrid` objects without being aware that they are not the `AmrGrid` objects it has been programmed to use. Virtual functions complete the illusion: whenever the grid management module calls (for example) the `advance_grid` function of the `AmrGrid` class, it is actually the definition of the corresponding function in the `HyGrid` class that is used. (This is fortunate since `advance_grid` is a pure virtual function in the `AmrGrid` class and has no definition there.)

One of the member functions inherited by the `HyGrid` class from the `AmrGrid` class deserves more detailed consideration. The function `make_subgrid` causes a `HyGrid` object to create a new



HyGrid object, a sub-grid of the original grid. The grid management module always uses this function to create grids rather than creating them itself, and the reason for this is quite subtle. In the grid management module only one type of grid, the `AmrGrid` class, is recognized, and if that module were to create new grids directly they would be instances of that class. However the grids in the grid hierarchy are actually `HyGrid` objects; because the `HyGrid` class is derived from the `AmrGrid` class, instances of the former can be used as if they were instances of the latter. The problem is that the grid management module does not know enough about the grids it is using to create one directly, and so it uses `make_subgrid`, a member function of the `AmrGrid` class, to do the job for it. Since `make_subgrid` is a virtual function it can be implemented so that it always creates a sub-grid which has the same class as the parent grid, and this ensures that all the grids in the grid hierarchy have the same type. (A similar problem occurs when the grid management module destroys a grid, but the solution is slightly more technical and beyond the scope of this discussion.)

The AMR code developed for the present work actually includes two different grid evolution modules, each with an associated grid interaction module. During the early stages of its development the AMR code stored data at grids points and time-stepped them using a two-step Lax-Wendroff method. Independently, a single grid code, `Claw++`, was written that uses an advanced high-resolution method to evolve data stored on a mesh of cells (chapter 2 discusses this code). By adopting the modular construction described in this section in the AMR code, the `Claw++` code (transformed into a grid evolution module and outfitted with a grid interaction module) has become interchangeable with the original Lax-Wendroff integration routine and its associated data format. This approach has reduced the amount of source code needed to compile several different numerical codes and has been found to be very flexible; the same source code is compiled to produce both the standalone `Claw++` code and the related grid evolution module used in the AMR code. In addition, comparing the results produced by the two pairings of grid evolution and interaction modules has proved to be a useful way of identifying programming errors.

### *Problem-Specific Code*

The modules described in the previous two subsections make up the complete AMR package. However some additional code must be supplied before the package can be used to solve specific problems: the grid evolution module must be provided with the details of the equations it is to solve, typically in the form of procedures to evaluate flux and source terms; boundary conditions must be specified at the edges of the spatial domain; and initial data for the evolution must be set up. In addition, since data output is outside the scope of the AMR package, suitable routines for saving the results of the simulation must be written.

For some problems it may be useful for each grid in the hierarchy to carry with it auxiliary data fields that are not declared as part of the `HyGrid` class. For example, in a code for evolving solutions to the Frittelli-Reula equations (described in chapter 4) there might be some advantage to storing data describing the background gauge fields on each grid in addition to the data stored

for the unknown variables. Instead of rewriting the `HyGrid` class to include the extra data a neater solution is to create a new class, `FRGrid`, which derives from the `HyGrid` class and which makes additions and alterations to the latter to account for the additional data. (In particular, the `make_subgrid` function must be updated in the `FRGrid` class for the reasons given in the previous subsection.)

A driver program is used to initiate the AMR algorithm. It creates a grid of the appropriate type (either a `HyGrid` object or an `FRGrid` object) to form the first level of the grid hierarchy, and presents it to the AMR package. It then sets the AMR algorithm in motion.

### 3.4 Parallelization of the AMR Code

On a multiprocessor system, program performance can be improved by sharing the program's workload among a number of processors. To allow this, the program must have been written with parallel execution in mind: its workload must be decomposable into separate tasks that can be performed independently. Ideally the time taken to execute a program should be inversely proportional to the number of processors employed, but this is rarely the case since a program cannot usually be parallelized in its entirety (and, in addition, hardware limitations are a factor).

The AMR code developed for the present work has been parallelized to run on a Silicon Graphics Origin2000 multiprocessor (see Fier 1996 and Cortesi 1998 for technical details). The machine uses a shared memory architecture which allows all of the processors direct access to the full memory of the computer. To avoid bottlenecks, memory is physically distributed and as a consequence memory access times vary depending on which processor is accessing which memory address. To compensate for this the Origin2000 makes extensive use of data and instruction caching.

#### *Approaches to Parallelization*

This subsection weighs up the advantages and disadvantages of some of the possible approaches to parallelizing an AMR code.

Nearly all of an AMR code's time is spent performing data manipulation operations such as time-stepping the solution data on a grid or interpolating data for use in a sub-grid. One approach to parallelizing the code would be to individually parallelize each of these operations; for instance, when the AMR algorithm calls for the data on a grid to be time-stepped, all of the processors at the code's disposal could be employed for the operation. The advantage of this approach is that, if the individual operations are parallelized well, a very even distribution of work between processors should be achieved. However the approach suffers from two disadvantages. Firstly, since all of the processors operate in parallel on the same data (for example, all helping to time-step the same grid) performance is certain to be hampered by memory contention and poor access times due to memory locality. The other disadvantage is that a lot of work would be needed to implement parallelization in this form: each operation to be parallelized would need special treatment, and for some operations (such as time-stepping by a high-resolution method) the parallelization would be

particularly complicated. In addition, since parallelization by this approach affects only the grid evolution and the grid interaction modules (to use the terminology of section 3.3) it would need to be implemented anew for each time-stepping algorithm included in the AMR code.

Another approach to AMR parallelization would be to assign grids to different processors such that all the data manipulation operations on one grid are performed by the same processor. The majority of operations can be performed for the grids on one level independently (for example, all of the grids on level  $N$  can take one time step independently, provided they have appropriate boundary data), and so the code can be run in parallel as long as the processors are synchronized between stages. This is the approach adopted for the present work, and Quirk and Hanebutte (1993) also use it for an AMR code built on a message passing paradigm. Since grids are to a large extent independent entities there should be few memory conflict problems in a code parallelized in this way. The approach is also simple from the programming point of view, and all of the parallelization takes place in the grid management module. The main drawback with the method is that for good performance it relies on grids being assigned to processors in such a way that each processor has the same workload, and this may be difficult to achieve in practice; it may be necessary to break big grids into a lot of much smaller grids.

Wild (1996) has developed an AMR code that is based on a different design to the standard algorithm described in section 3.1, and it is interesting to consider this code in the context of AMR parallelization. Instead of overlaying grids of varying resolutions to adaptively refine data, Wild's 'hierarchical linked list' approach uses a single base grid into which additional points are inserted to increase the local resolution. This method avoids the need for clustering during the regridding phase of the algorithm, and does not wastefully refine regions that are not flagged as needing refinement. However its extensive use of linked lists does add a degree of complexity to many of the operations that are used to manipulate solution data, and the code's performance may suffer because of this. Wild's design can be thought of as a standard AMR code in which only very small, uniformly sized sub-grids are used, and as such it seems to lend itself to a parallelization approach midway between the operation-based and the grid-based approaches of the preceding paragraphs (see Wild 1996, appendix A); however it is possible that the disadvantages described above would affect a parallelization of Wild's code less severely than they would a standard AMR code.

The final parallelization approach discussed here offers very good performance, but is probably unusable in practice. If the spatial domain of the problem is split into separate regions then each could be evolved by an AMR code executing on a different processor, with synchronization between processors only being needed at the end of each coarse time step to allow boundary data to be exchanged. This approach would be simple to implement and would almost completely avoid memory contention problems. However it suffers from two serious problems: it only achieves a good workload balance for simulations in which refined regions are evenly distributed across the spatial domain, and it suffers from a loss of accuracy in the refined data at the 'physical boundaries' between the domains of the different processors. While both of these problems could in principle

```

// parallel code to replace:
// for ( each grid gr in this level ) gr.do_something();

#pragma parallel
{ // begin parallel region

    int this_cpu = mp_my_threadnum();
    for ( each grid gr in this level ) {
        if ( gr.cpu == this_cpu ) gr.do_something();
    }

} // end parallel region

```

**Figure 3.11:** Code fragment to illustrate parallelization. The member function `do_something` is called for each grid in the current level. The code is made to run in parallel by assigning grids to different processors.

be circumvented, it seems unlikely that the approach could be made to work wholly satisfactorily in the general case.

### *Grid-Based Parallelization and Scheduling*

The AMR code used in the present work has been parallelized using a grid-based approach, briefly described in the previous subsection. Operations such as integration of solution data and error flagging can be performed simultaneously for all of the grids at one level of the grid hierarchy, and the code exploits this by assigning grids to different processors. Figure 3.11 shows how simple modifications to the code (all within the grid management module) allow the grid operations to be performed in parallel.

Grids are assigned to processors at the time of their creation and for the code to give good performance it is important that the same processor be used for all operations on a grid, particularly those involving memory allocation. The assignment of grids to processors needs to be done such that the total amount of work required to deal with the grids on one level is distributed among the processors as evenly as possible, and how well this is done is the main factor affecting the reduction in execution time of the code when it runs in parallel. During the regridding of level  $N$  a list of suggested sub-grids for level  $N + 1$  is generated by the clustering module, and for a code running in parallel this list must be analysed before the sub-grids are created to decide on a mapping of grids to processors. This involves two stages: grid splitting and grid scheduling.

The number of cells making up a grid is taken to be a measure of the amount of work required to perform operations on that grid. (This is only a first approximation and it does not take into account factors such as cache usage and number of boundary cells.) Suppose that  $n$  grids are to be created at the current level by the regridding procedure, and that these grids are estimated as having work requirements  $w_1, \dots, w_n$ . The total amount of work needing to be performed on this

level is then

$$W_{\text{total}} = \sum_{i=1}^n w_i,$$

and if that work is distributed evenly between  $m$  processors the workload of each will be

$$W_{\text{ideal}} = \frac{W_{\text{total}}}{m}.$$

In assigning grids to processors the aim is to minimize the amount by which the workload of the most overworked processor exceeds  $W_{\text{ideal}}$ . This problem is known as task scheduling in the computer science literature, and good results can be obtained by using a simple heuristic method, described below.

When assigning grids to processors in an AMR code an additional element of freedom is available: large grids can be split into a number of smaller grids. For the measure of work used here, the value of  $W_{\text{total}}$  is not affected if grids are split into smaller grids, although in practice there will be an overhead for each additional grid created. (On the other hand, cache behaviour may mean that splitting grids up sometimes reduces the total workload. This effect was investigated, but it was found to be too complicated to make allowances for in the code.) For the present work, the creation of large numbers of small grids is avoided and splitting of grids is limited to one frequently encountered situation: if a single grid has a work requirement that exceeds  $W_{\text{ideal}}$  then that grid is split into smaller grids, all of them requiring less than  $W_{\text{ideal}}$  units of work. This avoids the inefficient case in which there are less grids on a level than there are processors available to deal with them. A side-effect of the grid splitting is that, since  $W_{\text{ideal}}$  depends on the number of processors being used, so does the final arrangement of grids, and consequently so do the code's results. While this may not be an ideal situation, the dependence of the results on the number of processors is in practice only slight, and splitting of grids allows substantial improvements in performance.

When all of the grids are of an appropriate size, the code assigns them to processors using the LPT (longest or largest processing time) scheduling rule. This simple but effective algorithm is discussed by Horowitz, Sahni and Rajasekaran (1998, sections 12.3.1 and 12.4.1) and Cosnard and Trystram (1995, chapter 10). It operates by iteration of the following step: of the remaining grids, assign the one with the highest work requirement to the processor with the smallest workload. While this algorithm is not guaranteed to produce an optimal grid schedule, its results are usually good, and the following bound can be proven (Horowitz, Sahni and Rajasekaran 1998, theorem 12.5):

$$W_{\text{LPT}} \leq W_{\text{optimal}} \left( \frac{4}{3} - \frac{1}{3m} \right),$$

where  $W_{\text{LPT}}$  and  $W_{\text{optimal}}$  are the workloads of the most overworked processors for an LPT schedule and an optimal schedule, and  $m$  is the number of processors. It is usually not practical to try to calculate an optimal schedule directly (the problem is NP-complete).

The performance of the parallelized AMR code is analysed in the next subsection. Although the scheduling system described here works well, there is room for improvement in all aspects of it: the workload estimation could be made more accurate, a more advanced task scheduling algorithm could be used and more sophisticated use could be made of grid splitting.

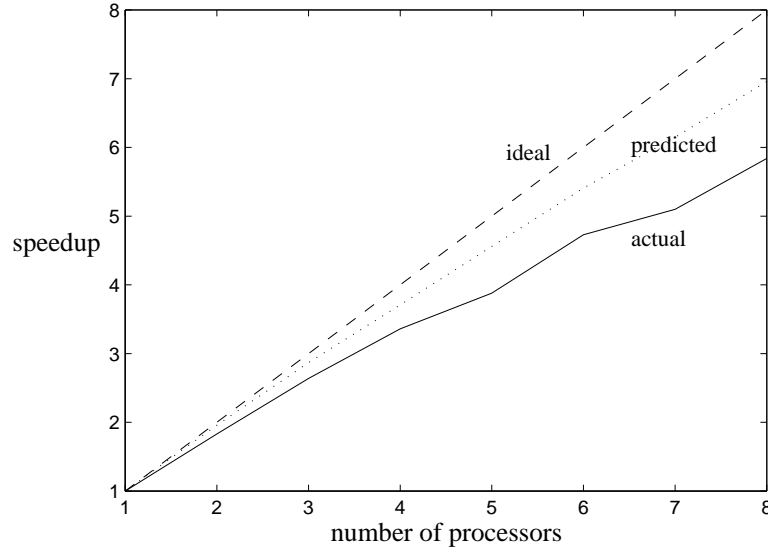


**Figure 3.12:** Typical speedup results for the parallelized AMR code. The dotted line is the speedup predicted from the processor workload schedule. The solid line is the actual speedup measured. The dashed line shows the ideal case of linear speedup.

### *Performance of the Parallel AMR Code*

The speedup of a program when it runs using multiple processors is calculated as

$$\text{speedup}(m) = \frac{\text{completion time on one processor}}{\text{completion time on } m \text{ processors}}.$$

Ideally the speedup will be equal to the number of processors the program employs, but in practice hardware limitations and incomplete program parallelization mean that the speedup is generally less than this.

Figure 3.12 shows speedup results for a typical simulation performed by the parallelized AMR code. The actual (elapsed time) speedup is compared with the speedup that would be expected based on the processor workload schedules generated during the regridding process. (In producing these results, grids were split to fit the number of available processors, and consequently each speedup value in figure 3.12 was calculated based on the times of two slightly different evolutions.)

The speedup predicted from the distribution of work between processors is the maximum speedup that could be expected from the code. It falls short of the ideal case of linear speedup because the workload scheduling procedure described in the previous subsection is not able to produce a perfectly even distribution of work between processors. For the simulation used to produce the results in figure 3.12, as with all of the simulations performed for this work, only one grid was used in the first level of the grid hierarchy, and so operations on that level were never run in parallel. Allowing the code to split the base grid would improve the code’s parallel performance, particularly for simulations which use only a small amount of refinement, although in general the

base grid accounts for only a very small amount of the overall work performed by the code. For the results plotted in figure 3.12, splitting the base grid would increase the predicted speedup of the code to about 7.2 (from 7.0) in the eight processor case.

There are several reasons why the actual speedup is less than the speedup predicted from the workload distribution results. First of all, the work scheduling procedure is quite unsophisticated, and the amount of ‘work’ it assigns to a processor is only a first approximation to the amount of time that the processor will be occupied for. Secondly, the predicted speedup does not account for grid management operations that the code cannot perform in parallel. However, excluding the output of solution data to disk, these operations take up an insignificant amount of the code’s time: execution profiles for the simulation used in figure 3.12 reveal that only a tiny fraction of a percent of the code’s time is spent performing functions which are not parallelized. Thirdly, hardware factors (memory contentions, lack of cache reuse and inefficient data placement) add an overhead to the code’s running time when multiple processors are used. Profiles of the simulation used in figure 3.12 show that the total time spent performing data manipulation operations increases as the number of processors increases. For eight processors the increase is approximately seven percent, and this accounts for about half of the discrepancy between the predicted speedup and the actual speedup. (An additional factor affecting the code’s speedup results is the environment in which it runs: in a multi-user system several tasks may be competing for the available processors, and if one of the processors used by the code is delayed by another task the remaining processors must wait for it to catch up. This skews the timing measurements.)

The parallel performance of a code is usually described using Amdahl’s law, a formula which relates speedup to the fraction  $p$  of the code that can be run in parallel:

$$\text{speedup}(m) = \frac{1}{(p/m) + (1 - p)},$$

where  $m$  is the number of processors used (see Fier 1996). Although this simplistic breakdown into serial parts and parallel parts is not altogether appropriate for the AMR code, for comparison purposes approximate values of  $p$  can be calculated for the data plotted in figure 3.12. The predicted speedup corresponds to a parallel fraction of  $p \simeq 0.97$  while the actual speedup has  $p \simeq 0.93$ .

The discussion here has been illustrated with performance statistics from a ‘typical’ AMR simulation. In fact the parallel performance can vary significantly from one simulation to another, and from one set of input parameters to another, with the best results usually being produced when a large amount of refinement is used. The results shown in figure 3.12 are from a two-dimensional gas dynamics test simulation (an example problem from LeVeque 1998) and represent good-to-average performance of the AMR code; much better code performance has been observed, together with much which was significantly worse.

### 3.5 AMR in Practice

This section concludes the discussion of AMR by looking at how the algorithm operates on some example problems and by examining the general advantages and disadvantages of the method.

Figure 3.13 shows the time evolution of a one-dimensional grid hierarchy produced during the integration of a collapsing Gowdy  $T^3$  cosmological model, a system described in detail in chapter 6. The base grid comprising two thousand grid cells is refined by a factor of two at each new level, with no sub-grids being created above level four. (A refinement factor of four is usually used in full-scale simulations.) During the evolution the Gowdy variables show very complicated behaviour and sharp spikes form in them at various points. The grid hierarchy adapts to track this behaviour and positions highly refined grids over the emerging spikes. (Figures 6.5 and 6.6 illustrate the complexity of the behaviour in the Gowdy models; their similarity with figure 3.13 is clear.)

The grid arrangement for a two-dimensional simulation (a collapsing  $U(1)$ -symmetric cosmology, discussed in chapter 7) is shown at one instant in time in figure 3.14. As structure begins to form at small scales in the solution, refined sub-grids are created to keep it well resolved. The difference in resolution of data between grids on different levels can be seen in the shaded contour plot of the figure. Grid splitting (for three processors running in parallel) was used by the code as part of the regridding procedure in this example.

An approximate breakdown of the time spent by the AMR code in performing different operations is given in figure 3.15. The grid evolution module accounts for the majority of the code's running time, whereas the amount of time spent performing grid management and clustering operations is negligible. (The values in the table were produced by profiling a two-dimensional evolution based on the Frittelli-Reula system of equations described in chapter 4. The code evolved grid data using the wave-propagation method of chapter 2 with an exact Riemann solver, and interpolation was by quadratic splines.)

It is worth emphasising that the AMR code does not produce numerical solutions which are more accurate than those produced by single grid methods; rather it produces solutions attaining a pre-specified accuracy in less time than would be taken using a single high-resolution grid. Figure 3.16 illustrates this point. Also, the use of sub-grids has an advantage in addition to reducing the local error in the data on the base grid: it allows fine-scale features of the solution to be resolved even though they may be less than a coarse grid cell width in size.

The adaptive nature of the AMR algorithm means that a simulation can run very fast at times at which a low resolution of data is sufficient (typically during its initial stages). However this adaptivity makes it very difficult to predict the overall running time of a simulation: if a low error tolerance is used such that a lot of grid cells are flagged for refinement then the time required to run the simulation increases massively (though, of course, it does produce more accurate results). Successful use of the AMR code requires experimentation for each new problem being investigated. In particular, there is no single ideal criterion for deciding which grid cells should be flagged for refinement: although the error estimation process (section 3.1) is unambiguous, how best to



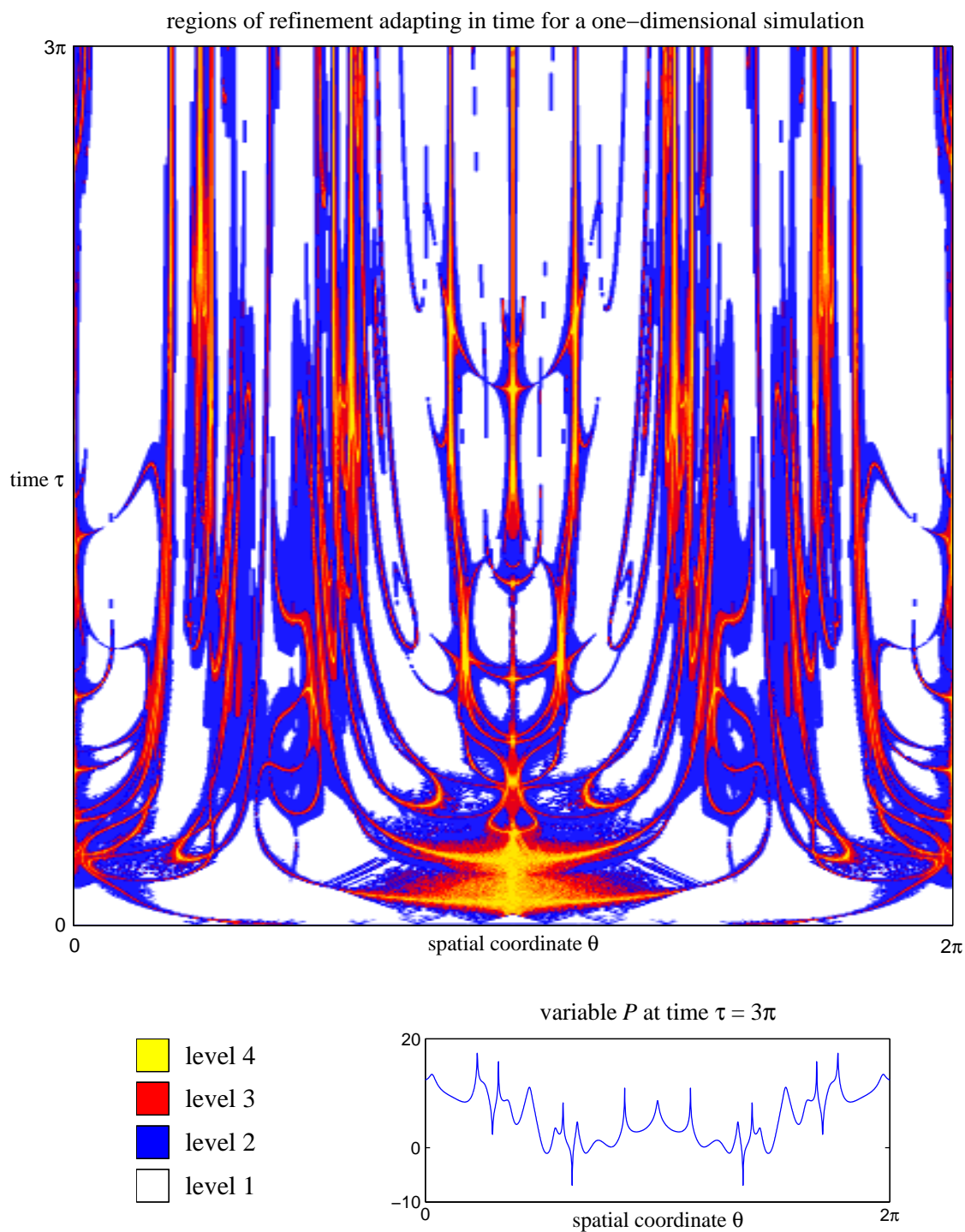


**Figure 3.13:** The AMR grid hierarchy adapts over time to follow features of the evolving solution data. The top frame shows the level of refinement used by the AMR code varying in space and time for a simulation of a one-dimensional cosmological model (see chapter 6 for details). The bottom frame shows one of the variables at the end of the simulation.

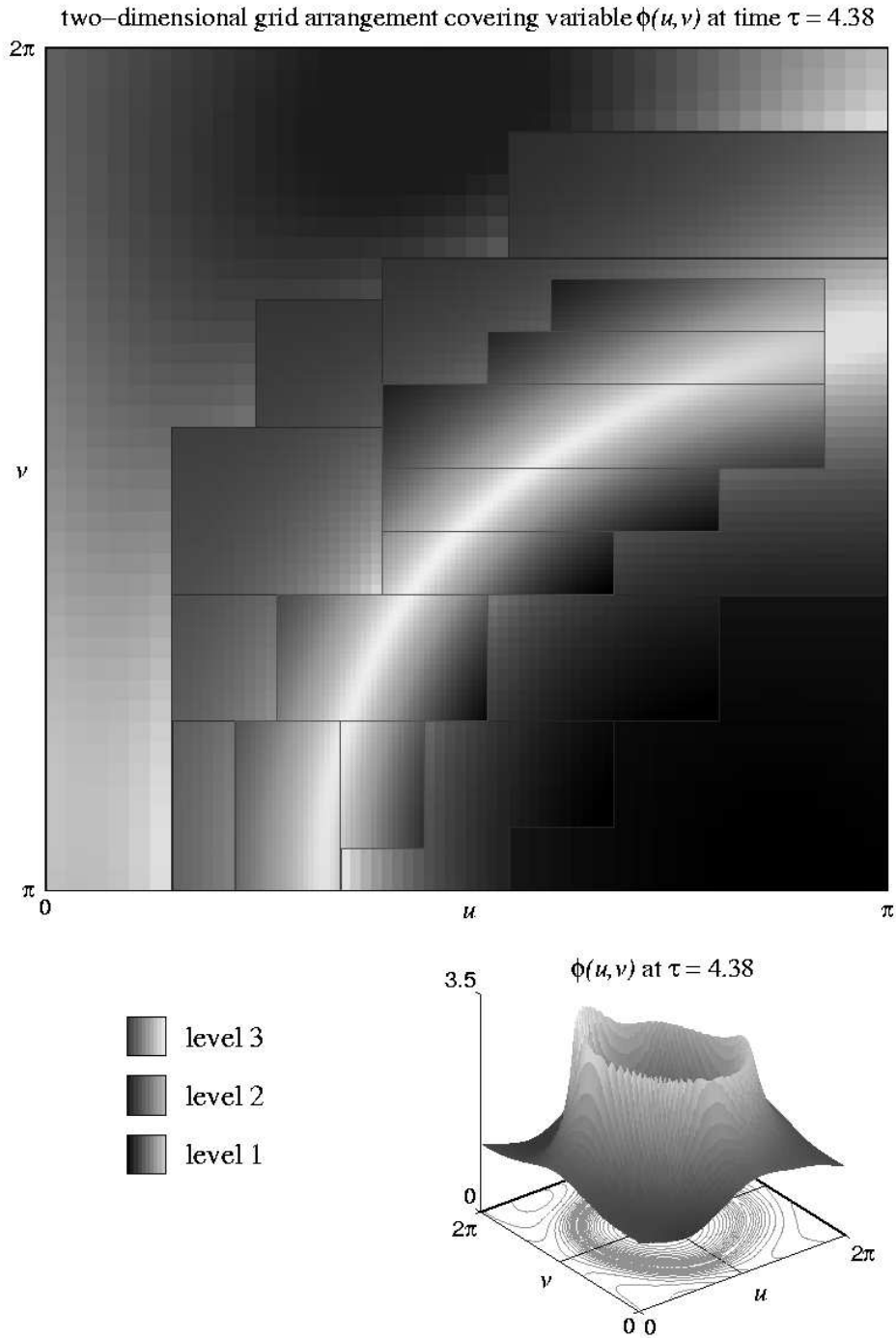


**Figure 3.14:** Grids at different resolutions for a two-dimensional simulation. The top frame shows part of a shaded contour plot of one of the evolved variables at a fixed time. Data from all grids are plotted, with different colour schemes used for grids at different levels. The  $80 \times 80$  base grid is refined by a factor of two at each new level. The bottom frame shows a surface plot of the same variable for the whole spatial domain. Chapter 7 discusses the cosmological model used.

| Module            | Time% | Breakdown   |
|-------------------|-------|---|
| Grid evolution:   | 95%   | { Riemann solver: 50%<br>Wave propagation: 24%<br>Source terms: 21% |
| Grid interaction: | 5%    | { Interpolation: 2%<br>Parent update: 2%<br>Other: 1%               |
| Grid management:  | 0%    |   |
| Clustering:       | 0%    |   |

**Figure 3.15:** Timing measurements for the AMR code, broken down by module and operation. Times marked as 0% are non-zero but negligible. (The error estimation procedure contributes to the times measured for the grid evolution module.)

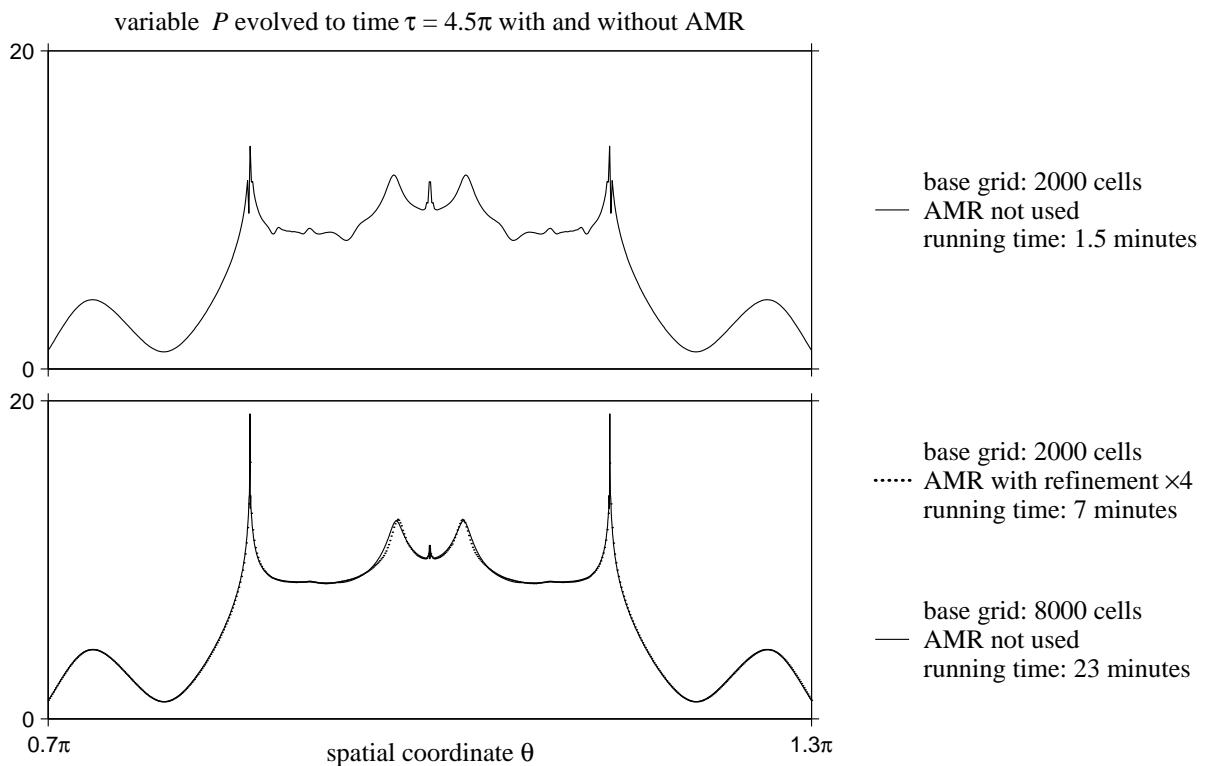


**Figure 3.16:** Comparison of running times with and without AMR. The same simulation is performed for three different set-ups. In two cases AMR is not used: for one the base grid has low resolution, for the other high resolution. In the third case AMR is used on a low-resolution base grid such that it has sub-grids which are as finely meshed as the high-resolution base grid. The results with AMR are comparable with the results on the high-resolution base grid; however the former are produced in significantly less time. (The one-dimensional cosmological model used for the simulations is described in chapter 6.)

weight the errors in the different unknown variables, and whether to use absolute or relative error magnitudes, depends on the nature of the simulation.

The production of internal boundary data for sub-grids has long been recognized as a potential source of problems in the AMR approach. Berger (1982, 1985) has proved some basic stability results for interfaces between coarse and fine grids when dissipative numerical evolution methods are used. However, analysis by Wild (1996, chapter 5) shows that phase and amplitude errors inevitably occur when waves cross between regions of high and low resolution, and that there is a tendency for high frequency waves to become trapped in high-resolution regions. Wild's results are based on the use of non-dissipative integration methods, and it may be hoped that the effects of the grid interfaces will be less severe if dissipative integration methods are used. In the present work using high-resolution and Lax-Wendroff integration methods, small amounts of noise are found at the edges of child grids where boundary data are produced by interpolation from parent grid data. The effect is similar to, but less severe than, the production of noise by insufficiently accurate interpolation, as discussed in section 3.2, and a similar remedy might be applicable: boundary data could be required to match smoothly onto the existing data on the sub-grid. (Indeed, smoothing data at grid interfaces was found by Wild to be a potential cure for the problem of noise build-up.) Taking into consideration the points made about interpolation of continuous and discontinuous data in section 3.2, an advanced interpolation method could be developed which varies its order automatically according to the smoothness of the data being interpolated, and which interpolates coarse data to give a smooth match onto existing regions of fine data.

The AMR code described in this chapter has played a very important role in the work presented here. Without it the numerical simulations performed for chapters 6 and 7 would have taken up significantly more computer time and would have been greatly restricted by memory limitations, and the formation of fine-scale structure that occurs in the cosmological models studied could not have been tracked with such high accuracy.

# Chapter 4.

## Hyperbolic Formulations

The preceding chapters 2 and 3 describe a range of sophisticated numerical methods which can be used to produce approximate solutions to systems of hyperbolic partial differential equations. The present chapter considers the application of such methods to general relativity. Because of their covariant nature the Einstein equations do not in their standard form constitute a time evolution system, and the ADM formulation of the equations as a Cauchy problem is usually used as a basis for numerical simulations. However, written in the ADM form, the Einstein equations become an evolution system which is hyperbolic only in a weak sense, and there are many drawbacks to this lack of hyperbolicity, not least of which is a restriction on the range of numerical methods that can be used to evolve the equations. The needs of numerical relativity have led to a number of new hyperbolic formulations of the Einstein equations being proposed in recent years. For a review of some of the theoretical aspects of these formulations see Reula 1998.

This chapter concentrates on a particular hyperbolic formulation proposed by Frittelli and Reula (1996). The formulation is extended to a family of evolution systems, a subset of which have properties which make them well-suited for numerical work; they are the most compact of the hyperbolic formulations of the Einstein equations that have been constructed to date. Section 4.2 discusses the generalized Frittelli-Reula formulation, with section 4.1 reviewing relevant background material (including the ADM formulation, some basic definitions of hyperbolicity, and the factors that have motivated the development of hyperbolic formulations).

In section 4.3 a numerical code that implements the Frittelli-Reula hyperbolic formulation is discussed. This is, to the author's knowledge, the first time the Frittelli-Reula formulation has been used for numerical work. The code is spatially two-dimensional in the sense that it assumes the spacetime being investigated to have a single spacelike Killing vector. By solving the Riemann problem for the Frittelli-Reula evolution system, the code is able to use the high-resolution wave-propagation method of chapter 2 to evolve spacetimes at second-order accuracy. The code has been used to evolve  $U(1)$ -symmetric vacuum cosmological models, and results from these simulations are presented much later in this work in section 7.3.

### 4.1 Hyperbolicity and the Einstein Equations

This section reviews background material relevant to the discussion of the Frittelli-Reula hyperbolic formulation of the Einstein equations which follows in section 4.2. The standard ADM formulation upon which the Frittelli-Reula system is based is discussed and some basic definitions of hyperbolicity for first-order systems of partial differential equations are given. The reasoning behind the development of hyperbolic formulations for the Einstein equations is explained and the distinguishing features of a number of hyperbolic formulations are summarized.

## The ADM Formulation of the Einstein Equations

The most commonly used approach for producing numerical solutions to the Einstein equations is to reformulate the equations as a Cauchy problem: given suitable data describing the geometry of an initial spacelike hypersurface  $\Sigma_{t_0}$ , the Einstein equations are used to describe the evolution, with respect to some time coordinate  $t$ , of the data into a foliation of spacelike hypersurfaces  $\{\Sigma_t : t_0 \leq t < T\}$  making up a region of spacetime. This decomposition of four-dimensional spacetime into space and time parts is described as a ‘three-plus-one’ splitting, and the standard approach to splitting the Einstein equations is the Arnowitt-Deser-Misner (typically abbreviated as ADM) formulation, which is described in standard references such as Misner, Thorne and Wheeler 1973 (chapter 21) and Wald 1984 (chapter 10). The classic 1979 article by York discusses the ADM formulation from the point of view of numerical relativity, and in the present subsection the main features of York’s interpretation of the ADM formulation are reviewed.

While the ADM description of a spacetime is fully covariant, for simplicity the following account assumes that a coordinate system  $\{t, x^1, x^2, x^3\}$  adapted to the formulation has already been chosen: the hypersurfaces of constant time coordinate  $t$  are the spacelike slices of a *foliation* of the spacetime, with the spatial coordinates  $x^1, x^2$  and  $x^3$  describing the individual slices. The geometry of the spacetime is interpreted in terms of time-dependent three-dimensional scalars, vectors and tensors defined on the spatial slices. The *intrinsic metric*,  $h_{ij}$ , is, for each value of  $t$ , a three-dimensional Riemannian metric defined by the projection of the four-dimensional spacetime metric,  $g_{\mu\nu}$ , onto the spatial slices. The convention adopted in the present work is that the indices  $i, j, \dots$  range over the set  $\{1, 2, 3\}$  while the indices  $\mu, \nu, \dots$  range over the set  $\{0, 1, 2, 3\}$ . Viewed as  $3 \times 3$  matrices, the inverse of the intrinsic metric  $h_{ij}$  is denoted by  $h^{ij}$ , and the indices of spatial tensors are raised and lowered using this metric. The *extrinsic curvature*,  $K_{ij}$ , of the foliation is another symmetric spatial tensor which is, in effect, the time derivative of the intrinsic metric; it is defined via equation (4.4a).

The coordinate freedom present in the Einstein equations appears in the ADM formulation through the lapse,  $N$ , and the shift vector,  $N^i$ . The *lapse*,  $N$ , is a positive scalar quantity which determines how the hypersurfaces of constant  $t$  foliate the spacetime. The magnitude of the lapse determines (in a sense made explicit below) the separation in proper time of two adjacent spatial slices with coordinate times  $t$  and  $t + dt$ . The *shift vector*,  $N^i$ , accounts for the freedom to redefine spatial coordinates on the slices of the foliation. When the shift vector is identically zero the world lines described by fixed values of the spatial coordinates,  $x^i = \text{constant}$ , run normal to the spatial slices. In the general case, for a point  $(t, x^i)$ , the normal to the spatial slice leads to a point  $(t + dt, x^i - N^i dt)$  on a second spatial slice infinitesimally removed. The two points are separated by a proper time of

$$d\tau = N dt,$$

demonstrating how the structure of the foliation is related to the lapse.

Given values for the intrinsic metric, lapse, and shift on a slice of the foliation, the four-metric of the spacetime can be reconstructed. In the coordinate system  $\{t, x^1, x^2, x^3\}$  it takes the form

$$g_{\mu\nu} = \begin{pmatrix} g_{00} & g_{0j} \\ g_{i0} & g_{ij} \end{pmatrix} = \begin{pmatrix} N^k N_k - N^2 & N_j \\ N_i & h_{ij} \end{pmatrix}, \quad (4.1)$$

where, as stated earlier, the indices of the shift vector,  $N^i$ , are lowered using the three-metric,  $h_{ij}$ .

The Einstein equations,

$$G_{\mu\nu} = \kappa T_{\mu\nu},$$

where  $\kappa$  is the matter coupling constant, can now be decomposed into equations for the spatial quantities. On the left-hand side of the equations are expressions based on the four-dimensional Riemann curvature tensor  $R^\mu{}_{\nu\eta\sigma}$  associated with the metric  $g_{\mu\nu}$ ; the Gauss-Codazzi equations can be used to rewrite these in terms of the three-dimensional curvature tensor  $\bar{R}^i{}_{jkn}$  associated with the intrinsic metric  $h_{ij}$ . The energy-momentum tensor,  $T^{\mu\nu}$ , on the right-hand side of the equations is decomposed into three spatial quantities according to

$$\begin{aligned} \rho &= N^2 T^{00}, \\ J^i &= N(T^{0i} + N^i T^{00}), \\ S^{ij} &= T^{ij} + 2N^{(i} T^{j)0} + N^i N^j T^{00}, \end{aligned} \quad (4.2)$$

which are, respectively, the *energy density*, the *momentum density* and the *stress* relative to the foliation. The standard index symmetrization notation is used throughout this work:  $A^{(i}B^j) = \frac{1}{2}(A^iB^j + A^jB^i)$ , and so on.

The time-time and time-space components of the Einstein equations give rise to equations which only involve quantities that can be entirely determined on a single spatial slice, that is, they involve no explicit derivatives with respect to the time coordinate. These are the *constraint equations*,

$$\bar{R} + K^2 - K_{ij}K^{ij} = 2\kappa\rho, \quad (4.3a)$$

$$\bar{\nabla}_k(K^{ik} - Kh^{ik}) = \kappa J^i, \quad (4.3b)$$

where  $K = K^i{}_i$ , and  $\bar{R}$  and  $\bar{\nabla}_i$  are the Ricci scalar and the covariant derivative associated with the spatial metric  $h_{ij}$ . Equation (4.3a) is the *Hamiltonian* or *energy constraint*, and equation (4.3b) is the *vector* or *momentum constraint*. These equations are independent of the lapse and the shift vector.

The space-space components of the Einstein equations relate the time derivative of the extrinsic curvature,  $K_{ij}$ , to quantities which are fully determined within each spatial slice. Recalling that the extrinsic curvature is closely related to the time derivative of the intrinsic metric, it is possible now to write a set of *evolution equations* for the two quantities:

$$\partial_t h_{ij} = -2NK_{ij} + 2\bar{\nabla}_{(i}N_{j)}, \quad (4.4a)$$

$$\begin{aligned} \partial_t K_{ij} &= N(KK_{ij} - 2K_{ik}K^k{}_j - \kappa S_{ij} + \frac{1}{2}\kappa h_{ij}(S - \rho) + \bar{R}_{ij}) \\ &\quad - \bar{\nabla}_i\bar{\nabla}_j N + N^k\bar{\nabla}_k K_{ij} + 2K_{k(i}\bar{\nabla}_{j)}N^k, \end{aligned} \quad (4.4b)$$

where  $S = S^i_i$ , and  $\bar{R}_{ij}$  is the spatial Ricci tensor, and  $\partial_t$  denotes differentiation with respect to the time coordinate  $t$ . The conservation laws for the energy-momentum tensor,

$$\nabla_\mu T^{\mu\nu} = 0,$$

allow additional evolution equations to be derived for the energy and momentum densities of the matter fields:

$$\partial_t \rho = N(S^{ij} K_{ij} + K\rho - \bar{\nabla}_i J^i) - 2J^i \bar{\nabla}_i N + N^i \bar{\nabla}_i \rho, \quad (4.5a)$$

$$\partial_t J^i = N(2K^{ik} J_k + KJ^i - \bar{\nabla}_k S^{ik}) - S^{ik} \bar{\nabla}_k N - \rho \bar{\nabla}^i N + N^k \bar{\nabla}_k J^i - J^k \bar{\nabla}_k N^i. \quad (4.5b)$$

These equations are generalizations of, respectively, the continuity and Euler equations.

For the evolution system (4.4) and (4.5) to be complete, some method must be prescribed for determining the behaviour of the lapse,  $N$ , the shift,  $N^i$ , and the stress,  $S^{ij}$ , on each spatial slice; no information about the evolution of these quantities is supplied by the Einstein equations. The behaviour of the stress tensor,  $S^{ij}$ , will be determined by the properties of the matter present in the spacetime, and in simple cases (for example, when the matter is a perfect fluid) an equation of state will specify the stress in terms of the energy and momentum of the matter. However typically it may be more appropriate to replace the evolution equations (4.5) with an evolution system which is specialized to the type of matter being treated, with the quantities  $\rho$ ,  $J^i$  and  $S^{ij}$  in equations (4.3) and (4.4) being rewritten in terms of an alternative set of matter variables.

The specification of a method for determining the lapse,  $N$ , and the shift,  $N^i$ , constitutes a choice of coordinate system for the spacetime being studied. The question of how best to determine these quantities is a difficult one: poor choices can result in foliations which develop coordinate singularities, which only cover a small region of the spacetime, or which intersect curvature singularities. York (1979) discusses a variety of methods for choosing the lapse and the shift which are believed to avoid some of these problems. The role of the lapse in numerical relativity is a topic which is considered further in chapter 5.

Assuming that a suitable specification of the lapse,  $N$ , the shift vector,  $N^i$ , and the stress tensor,  $S^{ij}$ , on each spatial slice is given, then if the intrinsic metric,  $h_{ij}$ , the extrinsic curvature,  $K_{ij}$ , the energy density,  $\rho$ , and the momentum density,  $J^i$ , are all known at an initial time  $t = t_0$ , the evolution equations (4.4) and (4.5) can be used to determine their values at later times  $t_0 \leq t < T$  (where  $T$  is not usually known beforehand and may be infinite). Such a solution will satisfy the Einstein equations if the constraints (4.3) hold for every value of  $t$ , and it follows from the Bianchi identity,

$$\nabla_\mu G^{\mu\nu} = 0,$$

that this will be the case if they hold at the initial time  $t = t_0$ . One way in which the ADM formulation can be used to generate numerical solutions to the Einstein equations is now clear: an initial data set  $\{h_{ij}, K_{ij}, \rho, J^i\}$  is chosen which satisfies a discretized version of the constraint equations (4.3) and, with appropriate conditions determining the auxiliary variables  $\{N, N^i, S^{ij}\}$



at each step, the data are advanced in time based on a discretized version of the evolution equations (4.4) and (4.5). (The failure of numerical solutions of the evolution equations to exactly satisfy the constraint equations away from the initial time slice has led to the use of ‘constrained’ evolution methods by some researchers in which some of the unknown variables are determined at each time step by solving the constraint equations instead of the evolution equations; while such methods typically show improved stability, their use is not without drawbacks, and in the present work only unconstrained evolution is used.)

Direct numerical implementations of the ADM formulation have been used to successfully evolve solutions to the Einstein equations in a large number of cases. However some properties of the formulation make it less well suited for numerical work than might be hoped, and this has led to the development of various alternative ‘hyperbolic’ formulations, the subject of the present chapter.

### *Hyperbolic Partial Differential Equations*

In this subsection some basic properties of first-order systems of partial differential equations relevant to the present work are briefly reviewed, with attention being given to systems for which the Cauchy problem is well posed. Much more detailed discussions of this subject can be found in the books by Gustafsson, Kreiss and Oliger (1995), Courant and Hilbert (1962), Kreiss and Lorenz (1989), and John (1982), among many others.

Consider a  $k$ -dimensional first-order system,

$$\partial_t u + B^i(u, t, x^j) \partial_i u = S(u, t, x^j), \quad (4.6)$$

where  $u(t, x^j)$  is a vector of  $n$  unknowns, the  $B^i$  are  $n \times n$  matrices with the index  $i$  taking values  $1, \dots, k$ , and  $S$  is a column vector. (For simplicity here the components of  $u$ ,  $B^i$  and  $S$  are assumed to be real.) It is worth noting that the flux-conservative system of equation (2.1) can easily be rewritten so that it takes the above form. The Cauchy problem for the system (4.6) involves finding a solution  $u(t, x^i)$  which satisfies the equations on a time interval  $t_0 \leq t < T$  (for  $T$  as large as possible) and which coincides with a specified set of initial data:  $u(t_0, x^i) = f(x^i)$ . If the system (4.6) represents a physical process then it may be expected that a unique solution  $u(t, x^i)$  to the Cauchy problem will always exist given a reasonable set of initial data  $f(x^i)$ , and furthermore that the solution will depend continuously (in some sense) on the initial data. A first-order system for which these properties, defined in a rigorous way, are known to hold is described as having a *well-posed* Cauchy problem. (Formal definitions of well-posedness, as given in Kreiss and Lorenz 1989, usually consider the rate of growth of an ‘energy norm’ defined on the solution, with well-posedness typically requiring that the norm grow no faster than exponentially.)

The well-posedness of the system (4.6) can be determined from its *principal part*, by which is meant the spatial derivative terms  $B^i \partial_i$ . With this in mind the *symbol* of the system is defined to be

$$P(\omega) = \omega_i B^i, \quad \text{where } \omega = (\omega_1, \dots, \omega_k) \in \mathbb{R}^k, \quad (4.7)$$

a linear combination of the matrices  $B^1, \dots, B^k$ . The symbol  $P$  can be classified according to its *hyperbolicity*, with well-posedness of the Cauchy problem holding for systems in which  $P$  satisfies sufficiently strong hyperbolicity conditions. (The kinds of hyperbolicity discussed here are the same as in Gustafsson, Kreiss and Olinger 1995.)

The system (4.6) is (*strongly*) *hyperbolic* if the matrix  $P(\omega)$  has real eigenvalues and a complete set of eigenvectors for all non-trivial  $\omega$ , and in this case it has a well-posed Cauchy problem. If the eigenvalues of  $P(\omega)$  are real but its eigenvectors do not form a complete set then the system is only *weakly hyperbolic* and it is not well posed. (These definitions of hyperbolicity are extensions of the definitions used for constant-coefficient linear systems in which  $P$  does not depend on the unknowns  $u$  or the coordinates  $\{t, x^i\}$ . For nonlinear systems the hyperbolicity conditions on  $P$  are required to hold for all physically reasonable values of the unknowns and the coordinates.)

Two more restrictive classes of hyperbolicity are also defined, both of them implying (by standard results of linear algebra) strong hyperbolicity and hence well-posedness of the system. If for all non-trivial  $\omega$  the eigenvalues of  $P(\omega)$  are real and distinct, then the system is *strictly hyperbolic*. (This type of hyperbolicity, though powerful, occurs rarely in physical systems.) If for all  $\omega$  the matrix  $P(\omega)$  is symmetric, then the system is *symmetric hyperbolic*. This latter form of hyperbolicity is important for physical systems, and its definition is often extended: the system (4.6) may be described as symmetric hyperbolic (strictly speaking it is *symmetrizable*) if there exists a positive-definite symmetric  $n \times n$  matrix  $M$  such that  $MP(\omega)$  is a symmetric matrix for all  $\omega$ . Symmetric (or symmetrizable) hyperbolicity of a system can also be demonstrated by explicit construction of a suitable ‘energy norm’ for the principal part.

In hyperbolic systems, information always propagates at finite speeds: if two solutions to a system are identical outside of a region of  $x^i$ -space given by  $|x^i| < \epsilon$  at some time  $t$ , then at a later time  $t + \delta t$  the solutions will still be identical outside of a region  $|x^i| < \alpha$  for some value  $\alpha < \infty$ . The *characteristic surfaces* of a hyperbolic system provide important details about how information propagates within the system: different combinations of the unknown variables can be pictured as advecting along the different characteristic surfaces, with the outermost surfaces defining the maximum propagation speed within the system. Different characteristic surfaces may be identified with different physical processes occurring within the system.

A local picture of the characteristic surfaces that pass through a point  $O$  can be built up using the symbol  $P(\omega)$  evaluated at that point. A spatial direction vector  $v = (v_1, \dots, v_k)$  is chosen at  $O$ , normalized so that  $|v| = 1$  (where the standard  $L_2$ -norm is used here, and the speeds referred to below are with respect to the spatial coordinates; the presence of a metric in general relativity provides an alternative way by which the vector could be normalized). The eigenvalues of the matrix  $P(v)$  are then the *characteristic speeds* of the system in the direction  $v$ : if  $\lambda$  is an eigenvalue of  $P(v)$  then the vector  $(1, \lambda v_i)$  in  $(t, x^i)$ -space is tangential to a characteristic surface at the point  $O$ ; furthermore the eigenvector of  $P(v)$  associated with  $\lambda$  indicates which combinations of the unknowns  $u$  propagate along that characteristic surface.

It is worth noting that the hyperbolic properties and the characteristic structure of a system are essentially unaffected by changes in its dependent variables. It is straightforward to show that for a change of variables  $u \rightarrow \hat{u}$  for which the Jacobian matrix  $J = \partial u / \partial \hat{u}$  is non-singular, the eigenvalues and the number of associated independent eigenvectors of the new symbol  $\hat{P}(\omega) = J^{-1}P(\omega)J$  do not change. Consequently the characteristic speeds and the satisfaction of conditions for weak, strong and strict hyperbolicity are the same for the new system as for the original one. While the explicit symmetry of the symbol is in general affected by a change of variables, a system which is symmetrizable remains so: if  $M$  is a symmetrizer for the original system then  $J^T M J$  is a symmetrizer for the new system.

### *Motivation for the Development of Hyperbolic Formulations*

It is well known that Einstein's equations form a hyperbolic system in suitable coordinates (see, for example, chapter 10 of Wald 1984). What is surprising, however, is that the ADM formulation of the equations is not hyperbolic in any strong sense, and does not constitute a well-posed Cauchy problem for general relativity. (In section 4.2 it is demonstrated that a first-order form of the ADM formulation which uses harmonic time slicing is only weakly hyperbolic in the sense defined in the previous subsection.) In recent years there has been much interest in the development of formulations of Einstein's equations which are explicitly hyperbolic, and for which the characteristic speeds correspond to the physical speeds of the system, with the main motivation for this being the possible use of such systems in numerical relativity. Hyperbolicity of first-order evolution systems is important for the construction of proofs of existence and uniqueness of solutions, and it is perhaps incongruous that numerical solutions to a system should be generated without these fundamental properties of analytic solutions having been established. Hyperbolicity should also facilitate the demonstration of well-posedness in other aspects of numerical relativity: given that violations of the Einstein constraint equations in numerical solutions are unavoidable, a hyperbolic system describing their propagation may be important when considering the stability of numerical simulations (see, for example, Frittelli 1997); also, little is known about the stability of Einstein's equations when boundary data are specified at the edges of numerical grids, and hyperbolicity may allow the well-posedness of this 'initial boundary value problem' to be investigated (see, for example, Stewart 1998).

Hyperbolic formulations are expected to be particularly important for long-term numerical evolutions of black hole spacetimes. Since these formulations respect the causality of the Einstein equations, black hole horizons can be considered as natural internal boundaries for numerical simulations, and the problematic regions inside the black holes can be excised from the domain of evolution. Bona, Massó and Stela (1995) demonstrate the potential of this approach using a hyperbolic formulation with a causal numerical evolution method.

Another advantage of hyperbolic formulations is that they can be used in conjunction with sophisticated numerical evolution methods. As discussed in chapter 2, many advanced numerical methods developed for use in computational fluid dynamics require the evolution equations to be

expressed in first-order flux-conservative form (see equations (2.1)), and furthermore some make use of the characteristic structure of the equations, requiring the evolution systems to be strongly hyperbolic. Most hyperbolic formulations of the Einstein equations are compatible with these requirements, and in cases where the Einstein equations are coupled to hydrodynamical fields, a hyperbolic formulation for the former would allow the complete system to be treated in a unified manner using standard methods from computational fluid dynamics.

An idea that is often quoted in the literature concerning hyperbolic formulations suggests that if a system of equations has mathematical properties which closely resemble the properties of the physical system being modelled (in particular, if a formulation of general relativity is hyperbolic and has only physically relevant characteristic speeds) then it may be expected to perform better in numerical simulations than alternative systems. While this idea is appealing, it does not appear to be supported by empirical evidence: in section 7.3 results from a direct numerical comparison of a number of formulations of Einstein's equations are presented, and it can be seen that hyperbolic formulations (without their hyperbolicity being exploited) do not in general produce significantly more accurate results than the standard ADM formulation.

The next subsection briefly reviews some of the hyperbolic formulations that have been developed for the Einstein equations. Prior to that a comment is made here concerning gauge conditions for hyperbolic formulations. As described earlier in this section, the ADM formulation puts no restrictions on the possible values taken by the lapse  $N$  (except that it be positive) or the shift vector  $N^i$ . However several hyperbolic formulations of the Einstein equations require the lapse to satisfy a relation with the intrinsic metric,

$$N = Q(t, x^k) \sqrt{\det h_{ij}}, \quad (4.8)$$

where  $Q(t, x^i)$ , called the slicing density, is an arbitrary (positive) function of the spacetime coordinates which cannot depend on any of the unknown variables. Typically the shift vector is also required to be independent of the unknowns, although it is otherwise arbitrary:  $N^i \equiv N^i(t, x^j)$ . The condition (4.8) on the lapse is described as generalized harmonic time slicing, and an alternative way of expressing it is as an evolution equation,

$$(\partial_t - N^i \partial_i) N = N f(t, x^i) - N^2 K, \quad (4.9)$$

where  $K$  is the trace of the extrinsic curvature, and  $f(t, x^i)$  is another arbitrary gauge function related to  $Q(t, x^j)$  and  $N^i(t, x^j)$  by

$$f = (\partial_t - N^i \partial_i) \ln Q + \partial_i N^i.$$

If the gauge function  $f$  is identically zero then the time slicing is described as simple harmonic; in the case that the shift  $N^i$  is zero this corresponds to the slicing density  $Q$  being independent of the time coordinate. Equation (4.8) may be used to remove the lapse completely from the evolution equations of the formulation; alternatively, the lapse (possibly in addition to its spatial derivatives) may be included in the set of dynamical variables of the formulation using equation (4.9). Although,

as equation (4.8) makes clear, any spacetime foliation can be reproduced using generalized harmonic time slicing, in practice it is not clear how the gauge functions should be chosen so as to produce well-behaved foliations; for this reason generalized harmonic time slicing may be considered less useful than gauges such as maximal slicing for which singularity avoidance properties have been established. Time slicing conditions are considered further in section 5.2.

### *A Review of Hyperbolic Formulations*

In the present work a family of hyperbolic formulations based on a system constructed by Frittelli and Reula (1996) is developed for use in numerical simulations, and the remainder of this chapter concentrates on this generalized formulation. In the next section the literature relating to the Frittelli-Reula system is reviewed. The present section ends by briefly reviewing work that has been done on other hyperbolic formulations, concentrating on those which have been used or have been proposed to be used in numerical simulations.

The hyperbolic formulation of Bona, Massó and co-workers has been the one most widely used in numerical simulations to date. It has developed through several incarnations: Bona and Massó 1989, 1992; Bona et al. 1995, 1997. The formulation is based on the ADM equations and comprises a one-parameter family of physically equivalent evolution systems (with the parameter controlling the inclusion of terms based on the Hamiltonian constraint) which are strongly hyperbolic and can be written in first-order flux-conservative form. For vacuum spacetimes the formulation uses thirty-seven unknowns of which thirty are the intrinsic metric and its derivatives (including the extrinsic curvature), four are the lapse and its spatial derivatives (treated in this case as dynamical variables), and three are additional variables related to the momentum constraints. The formulation is hyperbolic for a variety of algebraic time slicing conditions (including maximal slicing as a limit) but of these only simple harmonic slicing leads to the system having physically relevant characteristic speeds. The shift vector in the formulation is an arbitrary gauge function allowed to depend on the spacetime coordinates but not the unknown variables.

The range of spacetimes studied using numerical implementations of the Bona-Massó hyperbolic formulation is extensive. It has been used to evolve spherically symmetric (Bona, Massó and Stela 1995) and three-dimensional (Bona et al. 1998) black hole spacetimes as well as to study the propagation of gravitational waves in three dimensions (Anninos et al. 1997). Boson stars have been evolved in spherical symmetry (Arbona and Bona 1999), and a three-dimensional code has been constructed which couples the hyperbolic formulation to a perfect fluid source (Font et al. 1998). The formulation has also been used to investigate the behaviour produced by algebraic slicing conditions (Alcubierre 1997).

Choquet-Bruhat, York and co-workers have constructed several hyperbolic formulations of the Einstein equations which are reviewed in Choquet-Bruhat, York and Anderson 1998. Their ‘Einstein-Ricci’ formulation (Choquet-Bruhat and York 1995, Abrahams et al. 1995, 1997) resembles the ADM formulation but uses evolution equations derived from a wave equation for the spatial components of the Ricci tensor. It incorporates time derivatives of the metric up to third order.

The formulation is spatially covariant and uses the generalized harmonic slicing condition. Written as a flux-conservative first-order system it is symmetric hyperbolic and has only physically relevant characteristic speeds. With the lapse included as a dependent variable, the formulation uses a total of sixty-seven unknowns to describe vacuum spacetimes.

The Einstein-Ricci hyperbolic formulation has been used in a one-dimensional numerical code for the evolution of spherically symmetric vacuum spacetimes by Scheel et al. (1997, 1998) (see also Cook and Scheel 1997). It has also been used in a form linearized about the Schwarzschild metric to extract gravitational radiation and to provide outer boundary conditions for three-dimensional numerical evolutions (Rupright, Abrahams and Rezzolla 1998). A ‘fourth-order’ form of the Einstein-Ricci system has also been derived (Abrahams et al. 1996) in which the lapse and the shift can be specified arbitrarily. Although this system is probably not suitable for numerical work it has been used as the basis of a gauge-invariant perturbation theory by Anderson, Abrahams and Lea 1998.

The ‘Einstein-Bianchi’ system (Anderson, Choquet-Bruhat and York 1997) is a variation of the Einstein-Ricci system in which the dynamical variables all have clear interpretations: they are the intrinsic metric, the extrinsic curvature, the lapse, the spatial Christoffel symbols, and the Riemann curvature tensor decomposed into separate ‘electric’ and ‘magnetic’ parts. This formulation has the same hyperbolic structure and the same number of variables as the Einstein-Ricci system.

Van Putten and Eardley (1996) use the orthonormal frame formalism to derive a fully covariant hyperbolic formulation of the Einstein equations based on the Bianchi identity for the Riemann tensor. Using the tetrad elements and their connections as dynamical variables a wave equation is derived from which a first-order evolution system may be obtained if the components of the Riemann tensor are introduced as variables. As with most other hyperbolic formulations, four arbitrary gauge functions are available through which the slicing of the spacetime can be controlled. In van Putten 1997 a one-dimensional numerical implementation of the formulation is tested against the Gowdy  $T^3$  cosmological model.

Friedrich (1996) discusses various approaches for constructing symmetric hyperbolic formulations of the Einstein equations. The Bianchi equation for the Riemann tensor is used to construct hyperbolic systems based on both the ADM formulation and the orthonormal frame formalism. (A side effect of using the Bianchi identity in this form is that unphysical, albeit slower than light, characteristic speeds appear in all of the systems constructed.) The hyperbolic ADM systems use variables formed by decomposing the Weyl tensor into electric and magnetic parts, and they slice spacetimes according to the generalized harmonic gauge condition. These systems can be written in flux-conservative form, and for the evolution of vacuum spacetimes they use either forty or fifty unknowns, depending on how various gauge quantities are specified. The hyperbolic formulations based on the orthonormal frame formalism (which are similar to the formulation of van Putten and Eardley described above) use around forty unknowns and are based on a variety of gauge conditions which provide alternatives to the standard time slicing conditions used in numerical relativity. It is not clear that these systems can be written in flux-conservative form. (In related work, symmetric

hyperbolic evolution systems are used to investigate the initial boundary value problem for general relativity; Friedrich and Nagy 1999.)

Although no numerical work directly implementing any of Friedrich's (1996) hyperbolic formulations has been published to date, Hübner (1998) and Frauendiener (1998) have both developed conformally rescaled versions of the equations for numerical use. The conformal approach allows asymptotically flat spacetimes sliced by hyperboloidal hypersurfaces to be compactified and treated using finite numerical grids. Both evolution systems are symmetric hyperbolic and in the vacuum case employ around fifty unknown variables.

Other symmetric hyperbolic formulations based on the use of orthonormal frames have been constructed by Estabrook, Robinson and Wahlquist (1997), Friedrich (1998), and van Elst and Ellis (1999); the latter two both consider spacetimes in which perfect fluid sources are present, and attach the orthonormal frames to the matter flow vectors. There has also been some interest in the construction of symmetric hyperbolic formulations based on the Ashtekar variables (Iriando, Leguizamón and Reula 1997, 1998; Yoneda and Shinkai 1999a,b; Shinkai and Yoneda 1999).

Recently, Anderson and York (1999) have proposed a new symmetric hyperbolic formulation, called the 'Einstein-Christoffel' system, which is closely related to the generalized Frittelli-Reula formulation described in section 4.2: both formulations use sets of thirty unknown variables which are essentially the components of the intrinsic metric and the first derivatives of these components with respect to space and time. Apart from the (essentially cosmetic) differences in the sets of variables used, the Einstein-Christoffel system is distinguished from the generalized Frittelli-Reula formulation in that it adds slightly different multiples of the constraint quantities to the ADM evolution equations. (If the generalized Frittelli-Reula formulation were to be generalized further by the addition of a term  $-2N\chi h^{ij}C_k$  to the right-hand side of equation (4.13b), then the Einstein-Christoffel system could be considered as a special case of the formulation corresponding to the parameter choice  $\chi = \eta = 1$ ,  $\gamma = \Theta = 0$ .)

In other recent work Alcubierre et al. (1999) have constructed a family of first-order strongly hyperbolic evolution systems with physically relevant characteristic speeds which separate out the non-conformal degrees of freedom from the conformal ones. (The determinant of the intrinsic metric and the trace of the extrinsic curvature are assumed to be known functions of the spacetime coordinates.) Although these evolution systems are different from the generalized Frittelli-Reula systems described in the next section, the method by which they are derived is similar. Frittelli and Reula (1999) have also investigated similar conformally-decomposed evolution systems.

## 4.2 The Generalized Frittelli-Reula Hyperbolic Formulation

In their 1996 paper Frittelli and Reula (expanding on a result from their 1994 paper on the Newtonian limit of general relativity) present a one-parameter family of symmetric hyperbolic formulations of the Einstein equations, one of which (described here as the *original* FR system) has only physically relevant characteristic speeds. Frittelli and Reula derive their result by writing the ADM formulation of the Einstein equations as a first-order system into which five parameters have been

introduced (two through the definition of new variables, one through a condition on the lapse, and two controlling the addition of constraint terms to the evolution equations). By positing an energy norm for the system they find a one-dimensional parameter subspace for which the equations are symmetric hyperbolic, and by requiring the characteristic surfaces to coincide with the light cones they fix the parameter values uniquely.

Unfortunately a mistake in Frittelli and Reula’s proof of symmetric hyperbolicity results in the original FR system being, in actual fact, only weakly hyperbolic (although its characteristic speeds are as claimed). It is reasonably straightforward to ‘correct’ the evolution system so that the energy norm argument given by Frittelli and Reula is valid, and the resulting system (which is similar to the one originally considered in Frittelli and Reula 1994) is referred to here as the *modified* FR system. It admits a number of unphysical characteristic speeds. The complete set of evolution equations for the modified FR system was derived by the author in collaboration with J. M. Stewart. In Stewart 1998 the equations are used as the basis of an analysis of the numerical tractability of Einstein’s equations formulated as an unconstrained initial boundary value problem. In Brodbeck et al. 1999 the modified FR equations are embedded in a much larger evolution system of seventy unknowns for which (it is suggested) constraint violations will be dissipated away during the course of numerical simulations.

In the present work a ‘generalized’ version of the Frittelli-Reula formulation is derived in which additional parameters are introduced. By examining the principal part of the generalized formulation a one-parameter family of strongly hyperbolic evolution systems each having only physically relevant characteristic speeds is identified. These are described as the *causal* FR systems. The generalized formulation is described in detail in the present section, and in section 4.3 its implementation in a numerical code is described. Using  $U(1)$ -symmetric vacuum cosmological models as a test bed, in section 7.3 the relative numerical performances of a number of special cases of the generalized formulation are assessed.

### *Derivation of the Generalized Frittelli-Reula Formulation*

In this subsection the derivation of a generalized form of the Frittelli-Reula (henceforth FR) hyperbolic formulation of Einstein’s equations is outlined. In the next subsection the characteristic structure of the formulation is examined and a one-parameter family of strongly hyperbolic systems with physical characteristic speeds is identified.

The FR formulation is based on the ADM evolution equations (4.4a) and (4.4b) for the intrinsic metric  $h_{ij}$  and the extrinsic curvature  $K_{ij}$ . These equations constitute an evolution system which is first order in time but second order in space, and new variables representing the spatial derivatives of the intrinsic metric must be introduced to reduce the equations to first order. The FR formulation uses the variables

$$\begin{aligned} h^{ij} &= (h_{mn})^{-1}, \\ M^{ij}{}_k &= \frac{1}{2}(\partial_k h^{ij} - h^{ij} h_{mn} \partial_k h^{mn}), \\ P^{ij} &= K^{ij} - h^{ij} K, \end{aligned} \tag{4.10}$$



where  $h^{ij}$  is the contravariant form of the intrinsic metric, and as a notational convenience all indices  $i, j, \dots$  are raised and lowered using the metric  $h^{ij}$ , even for quantities like  $M^{ij}_k$  which are not tensors. Taking into account the symmetry of the quantities in their  $i$ - $j$  indices, equation (4.10) represents a set of thirty unknown variables.

(In Frittelli and Reula 1996 the definitions of the variables  $M^{ij}_k$  and  $P^{ij}$  include two parameters,  $\alpha$  and  $\beta$ , through which the form of the resulting evolution system can be controlled. However, as was noted in section 4.1, the hyperbolicity of a first-order system is essentially unaffected by non-singular transformations of its dependent variables, and so there is no loss of generality in fixing the definitions of the variables from the start. The definitions of equation (4.10) correspond to the parameter choice  $\alpha = \beta = -1$  which is used in the original FR system.)

The gauge quantities  $N$  and  $N^i$  in the ADM formulation are fixed in the FR system by imposing the generalized harmonic time slicing condition described in section 4.1: the lapse  $N$  is determined from the determinant of the three-metric according to equation (4.8) with a slicing density  $Q$  which is a known (that is, not dynamically determined) function of the spacetime coordinates, and the shift vector  $N^i$  is also a known function of the coordinates. To summarize,

$$\begin{aligned} N &= Q(t, x^k) \sqrt{\det h_{ij}}, \\ N^i &= N^i(t, x^k). \end{aligned} \quad (4.11)$$

(In Frittelli and Reula 1996 a parameter  $\epsilon$  is included in the relationship between the lapse and the intrinsic metric. Since none of the slicing conditions that result from this appear to be any more useful than harmonic slicing, in the present work the parameter is fixed at  $\epsilon = 1/2$ , the same value that is used for the original FR system.)

The constraint equations (4.3a) and (4.3b) of the ADM formulation can be rewritten in terms of the FR variables: the Hamiltonian constraint is  $\mathcal{C}^0 = 0$  and the momentum constraint is  $\mathcal{C}^i = 0$  where

$$\begin{aligned} \mathcal{C}^0 &= -\partial_k M^{kn}_n + M^{km}_n M_k{}^n{}_m - M_k M^{kn}_n + \frac{1}{4} M_k M^k \\ &\quad - \frac{1}{2} M^k{}_n{}^m M_k{}^n{}_m - \frac{1}{2} P_k{}^n P_n{}^k + \frac{1}{4} P^2 - \kappa \rho, \end{aligned} \quad (4.12a)$$

$$\mathcal{C}^i = \partial_k P^{ik} - 2M^{in}_k P_n{}^k - \frac{1}{2} M^i P + M^n{}_k{}^i P_n{}^k + \frac{3}{2} P^{ik} M_k - \kappa J^i. \quad (4.12b)$$

The notation  $P = P_k{}^k$  and  $M_i = M_k{}^k{}_i$  is used throughout this work. Recalling that the constraint equations are satisfied for any (analytic) solution of the Einstein equations, it is clear that evolution systems can differ in terms that are proportional to the constraint quantities  $\mathcal{C}^\mu$  while still admitting the same physical solutions. The FR formulation makes use of this by introducing constraint terms, controlled by parameters  $\eta$  and  $\gamma$ , into a first-order form of the ADM evolution system, with factors chosen such that cancellations can occur in the principal part. Schematically the FR evolution equations are

$$\partial_t h^{ij} = (\dots), \quad (4.13a)$$

$$\partial_t M^{ij}_k = (\dots) - 2\eta N \delta_k^{(i} \mathcal{C}^{j)}, \quad (4.13b)$$

$$\partial_t P^{ij} = (\dots) + 2\gamma N h^{ij} \mathcal{C}^0, \quad (4.13c)$$

where the equations for  $h^{ij}$  and  $P^{ij}$  follow from the ADM equations (4.4a,b), and the equation for  $M^{ij}_k$  is found by differentiating its definition (4.10) with respect to time and commuting spatial and temporal derivatives of the intrinsic metric. (The parameter  $\eta$  does not explicitly appear in Frittelli and Reula 1996; its value there is fixed at  $\eta = 1$  throughout.)

Since spatial derivatives of the intrinsic metric commute, it follows from the definition (4.10) of  $M^{ij}_k$  that the FR variables must satisfy

$$\partial_n M^{ij}_k + M_n M^{ij}_k = \partial_k M^{ij}_n + M_k M^{ij}_n. \quad (4.14)$$

This can be viewed as another constraint equation for the FR system. Spatial derivatives of  $M^{ij}_k$  occur in the principal part of the evolution equation for  $P^{ij}$ , and multiples of equation (4.14) can be added to the evolution system to alter its hyperbolicity just as multiples of the Hamiltonian and momentum constraints are added. A parameter  $\Theta$  is introduced here to control the extent to which equation (4.14) is used to modify the system. (In Frittelli and Reula 1996 the parameter value  $\Theta = 1$  is implicitly assumed, while the modified FR system of Stewart 1998 uses  $\Theta = 0$ .)

The energy-momentum quantities  $\rho$ ,  $J^i$  and  $S^{ij}$  from equation (4.2) are assumed to be determined from the behaviour of the matter that is present in the spacetime. (For a vacuum spacetime the quantities are of course zero.) Typically the matter model considered will provide a hyperbolic evolution system (coupled to gravity) through which values for the quantities can be determined. Alternatively the conservation laws (4.5a,b) can be written as evolution equations for  $\rho$  and  $J^i$  which are closed by an equation of state specifying  $S^{ij}$ :

$$\partial_t \rho + \partial_k (N J^k - N^k \rho) = N (S_k^n P_n^k - \frac{1}{2} P (S + \rho) - J^k M_k - Q_{,k} Q^{-1} J^k) - \rho N^k_{,k}, \quad (4.15a)$$

$$\begin{aligned} \partial_t J^i + \partial_k (N S^{ik} - N^k J^i) = & N (2 S_k^n M_n^{ik} - S_k^n M_n^{ki} + \frac{1}{2} S M^i - \frac{3}{2} S^{ik} M_k + 2 P^{ik} J_k \\ & - \frac{3}{2} P J^i - \frac{1}{2} \rho M^i - Q^i Q^{-1} \rho) - J^k N^i_{,k} - J^i N^k_{,k}, \end{aligned} \quad (4.15b)$$

$$S^{ij} = S^{ij}(\rho, J^k, h^{nm}), \quad (4.15c)$$

where derivatives of the gauge functions  $Q$  and  $N^i$  are denoted by, for example,  $Q^{,ij} = h^{ik} h^{jn} \partial_n \partial_k Q$ , and these terms appear in the source part of the system rather than in its principal part.

The complete evolution system for the generalized FR formulation which incorporates the parameters  $\eta$ ,  $\gamma$  and  $\Theta$  is given in figure 4.1. The system is written in the flux-conservative form of equation (2.1). The REDUCE computer algebra package (Hearn 1995, MacCallum and Wright 1991) played an important part in deriving and checking these equations. In the next subsection the hyperbolicity of the generalized system is considered and several interesting ranges of the parameters are identified.

### *Characteristic Structure of the Generalized Frittelli-Reula Formulation*

In this subsection the principal part of the FR evolution system of figure 4.1 is investigated for general values of the parameters  $\eta$ ,  $\gamma$  and  $\Theta$ . A one-parameter family of strongly hyperbolic evolution systems is identified for which the characteristic speeds coincide with the physical speeds of the system.

$$\begin{aligned}
& \partial_t h^{ij} - \partial_n (N^n h^{ij}) = N(2P^{ij} - Ph^{ij}) - 2N^{(i,j)} - h^{ij} N^n_{,n}, \\
& \partial_t M^{ij}_k + \partial_n (2N\eta \delta_k^{(i} P^{j)n} - N\delta_k^n P^{ij} - N^n M^{ij}_k) \\
& \quad = N \left( P^{ij} M_k - PM^{ij}_k - 2\eta \delta_k^{(i} [P^{j)n} M_n - \frac{1}{2} PM^j] - Q_{,n} Q^{-1} P^{j)n} \right. \\
& \quad \quad \quad \left. + M_{nm}^{j)} P^{nm} - 2M^{j)m}_n P_m^n - \kappa J^j \right) \\
& \quad - 2N^{(i,n} M^{j)n}_k + N^m_{,k} M^{ij}_m - N^n_{,n} M^{ij}_k + h^{ij} N^n_{,nk} - N^{(i,j)}_k, \\
& \partial_t P^{ij} + \partial_n \left( 2N(1 - \Theta) h^{n(i} M^{j)k}_k + 2N\Theta M^{n(ij)} - NM^{ijn} + 2(\gamma - 1)Nh^{ij} M^{nk}_k - N^n P^{ij} \right) \\
& \quad = N \left( 4M^n_{,k} ({}^i M^j)_n{}^k - M^k_n {}^i M^n{}_k{}^j - 2M^i{}_k {}^n M^{jk}_n + \frac{3}{2} M^{ij}_k M^k - 3(1 - \Theta) M^{(i} M^{j)n}_n \right. \\
& \quad \quad + \frac{1}{2} M^i M^j + 4(1 - \Theta) M^{in}_n M^{jk}_k + 2(2\Theta - 1) M^{ik}_n M^{jn}_k - 3\Theta M_k M^{k(ij)} \\
& \quad \quad + 4(\gamma - 1) M^{ij}_k M^{kn}_n - Q_{,k} Q^{-1} - 2(1 - \Theta) [Q_{,k} Q^{-1} M^{k(ij)} - Q_{,i} Q^{-1} M^{j)n}_n] \\
& \quad \quad + h^{ij} [Q_{,k}{}^k Q^{-1} + \gamma(2Q_{,k} Q^{-1} M^{kn}_n + \frac{1}{2} P^2 - P_n{}^k P_k{}^n) + (1 - 2\gamma)\kappa\rho \\
& \quad \quad \quad + 2(\gamma - 1)(M^{km}_n M_k{}^n{}_m - \frac{3}{2} M_k M^{kn}_n + \frac{1}{4} M_k M^k - \frac{1}{2} M^k_n{}^m M_k{}^n{}_m)] \\
& \quad \quad \left. + 2P_k{}^i P^{kj} - \frac{3}{2} PP^{ij} - \kappa S^{ij} \right) \\
& \quad - 2P^{k(i} N^{j)}_{,k} - P^{ij} N^k_{,k}
\end{aligned}$$

**Figure 4.1:** The generalized Frittelli-Reula evolution equations incorporating parameters  $\eta$ ,  $\gamma$  and  $\Theta$ . The unknown variables  $h^{ij}$ ,  $M^{ij}_k$  and  $P^{ij}$  are defined by equation (4.10), and the gauge quantities  $N$  and  $N^i$  are defined by equation (4.11). The system satisfies the constraint equations (4.12a,b) and (4.14). The matter variables  $\rho$ ,  $J^i$  and  $S^{ij}$  are assumed to satisfy a hyperbolic evolution system of their own, possibly derived from the conservation equations (4.15), and  $\kappa$  is the constant coupling the Einstein tensor to the energy-momentum tensor.

Recalling the discussion of hyperbolic first-order systems in section 4.1, the evolution equations of figure 4.1 should be rewritten in the form of equation (4.6) to allow their characteristic structure to be investigated. Neglecting undifferentiated terms this gives

$$\begin{aligned}
& (\partial_t - N^n \partial_n) h^{ij} = \dots, \\
& (\partial_t - N^n \partial_n) M^{ij}_k + NC^{nij}_{kpq} \partial_n P^{pq} = \dots, \\
& (\partial_t - N^n \partial_n) P^{ij} + ND^{nij}_{pq}{}^r \partial_n M^{pq}_r = \dots,
\end{aligned} \tag{4.16}$$

where

$$\begin{aligned}
C^{nij}_{kpq} &= 2\eta \delta_k^{(i} \delta_p{}^j) \delta_q{}^n - \delta_k{}^n \delta_p{}^i \delta_q{}^j, \\
D^{nij}_{pq}{}^r &= 2(1 - \Theta) h^{n(i} \delta_p{}^j) \delta_q{}^r + 2\Theta h^r(i} \delta_p{}^j) \delta_q{}^n - h^{nr} \delta_p{}^i \delta_q{}^j + 2(\gamma - 1) h^{ij} \delta_p{}^n \delta_q{}^r.
\end{aligned}$$

The symbol of the FR system, in the form (4.16), is a  $30 \times 30$  matrix  $P(\omega_n)$  defined by equation (4.7) where  $\omega_n$  is a three-tuple of real values. While the symbol  $P(\omega_n)$  could be written out in full, it

is more convenient here to allow it to be defined by the effect that it has on an arbitrary column vector  $u = [\bar{h}^{ij}, \bar{M}^{ij}_k, \bar{P}^{ij}]^T$ :

$$P(\omega_n) \begin{bmatrix} \bar{h}^{ij} \\ \bar{M}^{ij}_k \\ \bar{P}^{ij} \end{bmatrix} = N \begin{bmatrix} 0 \\ \omega_n C^{n ij}_{k pq} \bar{P}^{pq} \\ \omega_n D^{n ij}_{pq r} \bar{M}^{pq}_r \end{bmatrix} - \omega_n N^n \begin{bmatrix} \bar{h}^{ij} \\ \bar{M}^{ij}_k \\ \bar{P}^{ij} \end{bmatrix}, \quad (4.17)$$

where the ordering of the thirty components of the vector  $u$  corresponds to the ordering of the evolution equations in the system (4.16).

To determine the hyperbolicity and the characteristic speeds of the FR formulation the eigenvalues and eigenvectors of the symbol  $P(\omega_n)$  must be evaluated. While this may seem to be a task requiring the use of a computer algebra package (and, indeed, the following results were verified using the REDUCE package), the calculation can in fact be performed by hand following the approach of Friedrich 1996. Using equation (4.17), solutions  $(\lambda, u)$  are sought to the eigenvalue equation

$$P(\omega_n)u = \lambda u \quad \Leftrightarrow \quad N \begin{bmatrix} 0 \\ \omega_n C^{n ij}_{k pq} \bar{P}^{pq} \\ \omega_n D^{n ij}_{pq r} \bar{M}^{pq}_r \end{bmatrix} = (\lambda + \omega_n N^n) \begin{bmatrix} \bar{h}^{ij} \\ \bar{M}^{ij}_k \\ \bar{P}^{ij} \end{bmatrix}, \quad (4.18)$$

where it is important to note that the values  $\bar{h}^{ij}$  used to denote six of the components of the eigenvector  $u$  are different from the values  $h^{ij}$  of the components of the intrinsic metric which appear in the quantities  $C^{n ij}_{k pq}$  and  $D^{n ij}_{pq r}$ . For simplicity the value of the direction vector  $\omega_n$  is fixed at  $\omega_n = (1, 0, 0)$  corresponding to the  $x^1$ -direction of the system. Although the FR equations are not spatially covariant, their principal part maintains its form under rotations of the spatial axes, and results for the  $x^1$ -direction generalize to other spatial directions.

To solve the eigenvalue equation (4.18) a number of different cases must be considered. The simplest case is for the eigenvalue  $\lambda = -\omega_n N^n = -N^1$ , and it can be seen that  $\bar{h}^{ij}$  may then take any value while  $\bar{P}^{ij}$  must be zero, and six equations must be satisfied by the eighteen components of  $\bar{M}^{ij}_k$ . There are thus eighteen linearly independent eigenvectors  $u$  associated with this eigenvalue. For  $\lambda \neq -N^1$  it can be seen that the  $\bar{h}^{ij}$  components of the eigenvector  $u$  must be zero, and that equation (4.18) can be written as a set of six equations for the components  $\bar{P}^{ij}$ , with the values of  $\bar{M}^{ij}_k$  being determined from these. Analysis of this set of equations for  $\bar{P}^{ij}$  is straightforward but made tedious by the number of special cases that must be considered. The seven possible eigenvalues  $\lambda$  of the symbol  $P(\omega_n)$  are found to be

$$\begin{aligned} \lambda_0 &= -N^1, \\ \lambda_{\pm A} &= -N^1 \pm N\sqrt{h^{11}}, \\ \lambda_{\pm B} &= -N^1 \pm N\sqrt{3\eta(1-\Theta)h^{11}}, \\ \lambda_{\pm C} &= -N^1 \pm N\sqrt{(1+2\gamma[4\eta-1]-2\eta[1+2\Theta])h^{11}}, \end{aligned} \quad (4.19)$$

for  $\omega_n$  the unit vector in the  $x^1$ -direction, with analogous expressions holding for other spatial directions. (The lapse  $N$  is assumed to be positive, and the spatial metric  $h^{ij}$  is assumed to be Riemannian so that  $h^{11}$  is also positive.) If it is the case that the eigenvalues of equation (4.19) are

all real and distinct then in addition to the eighteen linearly independent eigenvectors associated with  $\lambda_0$ , the eigenvalues  $\lambda_{\pm A}$  are each found to be associated with a set of three independent eigenvectors (for which the components  $\bar{P}^{22}$ ,  $\bar{P}^{23}$  and  $\bar{P}^{33}$  can be chosen arbitrarily and determine the values of  $\bar{M}^{ij}_k$ ; the components  $\bar{P}^{i1}$  and  $\bar{h}^{ij}$  are zero), the eigenvalues  $\lambda_{\pm B}$  are each associated with a set of two eigenvectors (for which the components  $\bar{P}^{12}$  and  $\bar{P}^{13}$  can be chosen arbitrarily and determine the values of  $\bar{P}^{22}$ ,  $\bar{P}^{23}$ ,  $\bar{P}^{33}$  and  $\bar{M}^{ij}_k$ ; the components  $\bar{P}^{11}$  and  $\bar{h}^{ij}$  are zero), and the eigenvalues  $\lambda_{\pm C}$  are each associated with one eigenvector (for which the component  $\bar{P}^{11}$  can be chosen arbitrarily and determines the values of  $\bar{M}^{ij}_k$  and the remaining  $\bar{P}^{ij}$ ; the components  $\bar{h}^{ij}$  are zero), and in this case the eigenvectors form a complete set. However, if the parameter values  $\eta$ ,  $\gamma$  and  $\Theta$  are such that some of the eigenvalues in equation (4.19) coincide, then it is possible that the set of eigenvectors may degenerate such that it no longer has thirty linearly independent members; this is found to occur if any of the values  $\lambda_{\pm B}$  or  $\lambda_{\pm C}$  coincides with  $\lambda_0$ , or if  $\lambda_{\pm A} = \lambda_{\pm C} \neq \lambda_{\pm B}$ . One particularly interesting case in which the set of eigenvectors is complete occurs when  $\lambda_{\pm A} = \lambda_{\pm B} = \lambda_{\pm C}$ : the set then comprises eighteen eigenvectors associated with  $\lambda_0$  (for which the components  $\bar{P}^{ij}$  are zero), and two sets of six eigenvectors associated with each of the  $\lambda_{\pm A}$  (for which the components  $\bar{P}^{ij}$  can be chosen arbitrarily).

As the parameters  $\eta$ ,  $\gamma$  and  $\Theta$  are varied, it can be seen from the above analysis of the eigenvalues and eigenvectors of the symbol  $P(\omega_n)$  that the properties of the evolution system of figure 4.1 change substantially. If the eigenvalues in equation (4.19) are all real then, recalling section 4.1, the evolution system is at least weakly hyperbolic, with it being strongly hyperbolic if in addition the set of eigenvectors is complete. The values in equation (4.19) are the characteristic speeds of the system in the  $x^1$ -direction, and three of these speeds can be considered as being physically significant: the characteristic speed  $\lambda_0$  describes motion that is normal to the spacelike hypersurfaces of the ADM foliation, while  $\lambda_{+A}$  and  $\lambda_{-A}$  are the speeds (relative to the spacetime coordinates) of photons travelling in the  $x^1$ -direction. For an evolution system to have only physically relevant characteristic speeds, the values of  $\lambda_{\pm B}$  and  $\lambda_{\pm C}$  must coincide with the values of  $\lambda_{\pm A}$  or  $\lambda_0$ .

Within the generalized FR formulation certain evolution systems can be singled out as being of particular interest. The *original* FR system described by Frittelli and Reula (1996) is reproduced by the parameter choice  $\eta = \gamma = \Theta = 1$ . From equation (4.19) it can be seen that the characteristic speeds of this system are all physically relevant:  $\lambda_{\pm B} = \lambda_0$  and  $\lambda_{\pm C} = \lambda_{\pm A}$ . However as a consequence of this the eigenvectors of the principal part degenerate and, in contrast to what Frittelli and Reula claim in their paper, the system is only weakly hyperbolic. If the original FR system is altered so that Frittelli and Reula's proof of symmetric hyperbolicity can be correctly applied, then what results is the *modified* FR system (as used in Stewart 1998) for which the parameters are  $\eta = \gamma = 1$  and  $\Theta = 0$ . This system has seven distinct characteristic speeds, four of which are faster than the local light speed: from equation (4.19),  $\lambda_{\pm B} = -N^1 \pm N\sqrt{3h^{11}}$  and  $\lambda_{\pm C} = -N^1 \pm N\sqrt{5h^{11}}$ . From the earlier discussion of eigenvectors it is clear that this system is at least strongly hyperbolic.

If the parameters are chosen to be  $\eta = \gamma = 0$  with  $\Theta$  arbitrary, then the FR formulation reduces to a first-order form of the standard ADM formulation: no additional constraint quantities are introduced when the ADM evolution equations (4.4) are written in terms of the FR variables (4.10). The characteristic structure of these first-order ADM systems is essentially the same as for the original FR system: the characteristic speeds are physically relevant but the evolution equations are only weakly hyperbolic.

An obvious question that can be asked about the generalized FR formulation is whether there exist parameter choices which lead to evolution systems that both are strongly hyperbolic and have physically relevant characteristic speeds. It turns out that there is a one-parameter family of such evolution systems, described here as the *causal* FR systems. The parameters  $\eta$ ,  $\gamma$  and  $\Theta$  must be chosen such that the eigenvalues of equation (4.19) satisfy  $\lambda_{\pm A} = \lambda_{\pm B} = \lambda_{\pm C}$ , and the solution to this condition can be expressed as

$$\Theta = 1 - \frac{1}{3\eta}, \quad \gamma = \frac{9\eta - 2}{12\eta - 3}, \quad \text{for } \eta \in \mathbb{R} \setminus \{0, \frac{1}{4}\}. \quad (4.20)$$

The causal FR systems described by the equations of figure 4.1 with the parameter settings (4.20) are well suited to numerical applications. Their strong hyperbolicity allows them to be used in conjunction with sophisticated numerical methods (for instance those described in section 2.3), and the causal nature of their characteristic speeds should facilitate the imposition of well-behaved boundary conditions. A key feature of the FR systems which makes them particularly appealing from the point of view of numerical work is that they use only thirty unknown variables; by way of comparison the Bona-Massó hyperbolic formulation (reviewed at the end of the previous section) which in many respects is similar to the causal FR system and which has been used in many numerical simulations, requires three additional dependent variables (seven if the lapse and its derivatives are treated as unknowns).

(Another way by which the individual evolution systems of the generalized FR formulation could be classified is by the hyperbolicity of their constraint propagation equations. The constraint quantities  $C^\mu$  of equations (4.12), together with similar quantities based on equation (4.14), can be considered as dependent variables in a first-order evolution system which is linear with coefficients based on the values of  $h^{ij}$ ,  $M^{ij}_k$  and  $P^{ij}$ , which are assumed to be known. Although for exact solutions of the Einstein equations the constraint quantities will be identically zero, in numerical work constraint violations are inevitable, and the question then arises as to whether the system describing the propagation of the constraint violations is well posed or not. In Stewart 1998, as part of a discussion of the mathematical properties of the Einstein equations, it is shown that for the modified FR system the constraints evolve according to a strongly hyperbolic system of equations. It may be speculated that the hyperbolicity of the constraint evolution system could have some bearing on the stability of numerical simulations, but to date there is no empirical evidence to support this, and evolution systems for the constraints are not examined in the present work.)

In the next section a numerical code is described which implements the generalized FR formulation. Results produced using this code are presented in section 7.3, and in particular a comparison

is made between the numerical performances of the original, modified and causal FR systems and the first-order ADM system.

### 4.3 Numerical Implementation of the Frittelli-Reula Formulation

This section discusses the implementation of a computer code for the numerical evolution of the generalized Frittelli-Reula formulation of Einstein's equations, described in section 4.2. The code is two-dimensional in the sense that it assumes the spacetime metric to depend on only two of the three spatial coordinates, and is restricted to the investigation of spacetimes in which no matter fields are present. It has been used to evolve the planar and  $U(1)$ -symmetric cosmological models described in chapters 6 and 7, and section 7.3 discusses its performance on these problems in comparison to codes which use specialized sets of evolution equations. Section 7.3 also examines how the numerical performance of the generalized Frittelli-Reula evolution system is affected when its parameters  $\eta$ ,  $\gamma$  and  $\Theta$  are varied.

In addition to a general discussion of the implementation of the Frittelli-Reula code, this section considers in detail two technical aspects of it. Firstly, while the evolution equations of the Frittelli-Reula formulation can be simplified based on the symmetry assumed for the spacetimes, care must be taken to ensure that this is not done in a way that affects the hyperbolicity of the system; although it is not immediately apparent that it should be the case, some seemingly trivial simplifications of the evolution equations can lead to significant changes in their characteristic speeds. Secondly, to enable the code to use the high-resolution numerical integration scheme of chapter 2, a method for solving the Riemann problem for the principal part of the evolution system must be devised, and in the present work both exact and approximate Riemann solvers for the Frittelli-Reula equations are implemented. While numerical methods based on Riemann solvers have been used extensively in work on relativistic hydrodynamics (with the spacetime metric either being given by an exact solution or evolved separately using a standard finite difference method; see Font et al. 1998 for a recent review), this is, to the author's knowledge, the first time such methods have been used to evolve gravitational fields.

#### *Overview of the Frittelli-Reula Code*

The code presented here for the numerical evolution of the Frittelli-Reula (FR) equations is built upon the numerical methods described in chapters 2 and 3, and can be used to simulate any spatially two-dimensional vacuum spacetime. The restriction of the code to two spatial dimensions (discussed at length in the next subsection) significantly reduces the complexity of the numerical integration routines and the demands they make on computational resources, but does not simplify the evolution equations in any fundamental way: the generalization of the code to three spatial dimensions is conceptually straightforward. Since the motivation for the construction of the code is to investigate the behaviour of the FR formulation and its usefulness in numerical relativity, the additional complexity of including matter fields in the code is forgone in the present work; however

it should be noted that the numerical approach used here would be particularly appropriate for simulations in which the FR equations are coupled to hydrodynamical sources.

The set of equations presented in figure 4.1 represents an evolution system for thirty unknown variables (although, as pointed out in the next subsection, a set of twenty-seven variables is sufficient given the symmetry of the spacetimes considered) which has the flux-conservative form of equation (2.1). Since only vacuum spacetimes are considered here, the quantities  $\rho$ ,  $J^i$  and  $S^{ij}$  are taken to be identically zero. The values of the lapse  $N$  and the shift vector  $N^i$  are defined by equation (4.11), and thus the code uses generalized harmonic time slicing with a given shift vector. Arbitrary values for  $Q(t, x, y)$  and  $N^i(t, x, y)$  and their first and second spatial derivatives can be specified in the code through user-defined functions.

The Strang splitting approach, described in section 2.1, is used to separate the transport and the source parts of the FR evolution system. The transport part of the system is evolved using either a high-resolution wave-propagation method (discussed in section 2.3 and later in this section) or the standard two-step Lax-Wendroff method of section 2.1. The Lax-Wendroff method is simple to apply since it only requires the values of the flux vectors to be programmed into the code, and is useful in the present work because, unlike high-resolution methods, it can be used to evolve systems of equations which are only weakly hyperbolic. Time steps of variable size can be used by the code, with the Courant-Friedrichs-Lewy condition (equation (2.13)) limiting the size of the time steps to

$$\Delta t \leq \min \left\{ \frac{\Delta x}{|N^1| + N\sqrt{h^{11}}}, \frac{\Delta y}{|N^2| + N\sqrt{h^{22}}} \right\}, \quad (4.21)$$

for an evolution system which has only physically relevant characteristic speeds, or to a value smaller than this for evolution systems (such as the modified FR system) in which gauge information can propagate faster than the local light speed.

The source part of the FR evolution system can be evolved using standard numerical methods for solving ordinary differential equations, and in the present work a second-order Runge-Kutta method, as discussed in section 2.1, is employed. As can be seen from the right-hand sides of the equations in figure 4.1, the FR system includes a large number of source terms, and programming the code to evaluate these efficiently is not a trivial matter. A convenient approach is to use the natural factorization present in the tensor notation: from a knowledge of the values of the variables  $h^{ij}$ ,  $M^{ij}_k$  and  $P^{ij}$ , a range of intermediate quantities such as  $h_{ij}$ ,  $M^i_j{}^k$  and  $P_i{}^j$  are constructed by the code, and these quantities are then added together in the combinations required to construct the source terms. As an illustration of this approach, if a quantity  $A^{ij} = M^n{}_k{}^i M^k{}_n{}^j$  is to be evaluated from the values  $M^{ij}_k$ , then it is much more efficient (in terms of the total number of multiplication operations performed) to construct the quantity in several stages, for example

$$M_i{}^j{}_k := \sum_n h_{in} M^{nj}_k \quad \longrightarrow \quad M_i{}^{jk} := \sum_n h^{kn} M_i{}^j{}_n \quad \longrightarrow \quad A^{ij} := \sum_{n,m} M_n{}^{mi} M_m{}^{nj},$$

than it is to evaluate the quantity in one step,

$$A^{ij} := \sum_{k,l,m,n,p,q} h^{ik} h^{jl} h_{mp} h_{nq} M^{mn}{}_k M^{pq}{}_l.$$



Since the source terms in the evolution equations are evaluated by the code independently at each spatial point, the temporary construction of a range of intermediate quantities involves no significant memory overhead.

As a precaution against errors being introduced when programming in the source and flux terms of the FR equations, prototypes of the routines for evaluating these terms were first implemented in the REDUCE computer algebra system before being straightforwardly converted into the C++ language. This allowed the evolution equations implemented in the FR code to be verified against equations which were derived in a manner much less prone to programming errors.

The FR code has been thoroughly tested to ensure that it can reproduce a range of exact solutions to the vacuum Einstein equations. In addition to the standard Minkowski, Schwarzschild, Kasner, stationary cylindrical, and polarized Gowdy metrics, the code has also been tested on versions of these metrics transformed to unusual coordinate systems. In particular, a useful test of the code has been provided by the Minkowski metric written in coordinates for which its ADM representation has a shift vector  $N^i$  which depends in a non-trivial way on the spacetime coordinates. The test of the FR code is then whether, given exact initial data and exact values for the gauge functions  $Q(t, x^k)$  and  $N^i(t, x^k)$ , it is able to evolve an approximate solution in which the errors decrease in magnitude at second order as the numerical grid is refined. (In practice the order of convergence may be less than the ideal value near to the edges of the grid where the exact solution is used to provide boundary data.) In all cases the FR code has demonstrated second-order convergence, both of the error values and of the violations of the constraint equations.

In chapters 6 and 7, inhomogeneous cosmological models are examined for which exact solutions are not known in general. The FR code has been used to evolve numerical solutions to these models, and second-order convergence of the constraint violations in these solutions provides evidence that the code is performing correctly. Furthermore, alternative sets of evolution equations have been used to evolve the same spacetimes and the results have been found to converge at second order to the results of the FR code. Section 7.3 discusses the performance of the FR code in more detail.

### *Two-Dimensional Reduction of the Frittelli-Reula System*

The Frittelli-Reula (FR) code described in the previous subsection is implemented based on the assumption that any spacetime under investigation has a single spacelike Killing vector and is described using a coordinate system in which the spacetime metric  $g_{\mu\nu}$  has no dependence on the spatial  $x^3$ -coordinate:  $\partial_3 g_{\mu\nu} = 0$ . The code thus deals with the time evolution of fields defined on a two-dimensional spatial domain. This subsection discusses some technical points that arise in the reduction of the FR formulation to two spatial dimensions, and in particular shows that care must be taken to perform the reduction in such a way that the hyperbolicity of the evolution system is not compromised.

Some of the simplifications that can be applied to the FR equations of figure 4.1 in two dimensions are obvious. Since all of the quantities that describe the spacetime are independent of the  $x^3$ -coordinate, the flux vector corresponding to that direction can be removed and the derivatives

with respect to that coordinate of the gauge functions  $Q$  and  $N^i$  in the source terms can be set to zero; by considering how a fully three-dimensional code would evolve two-dimensional solutions, it is clear that these simplifications will have no effect on the behaviour of the evolution equations. However, this turns out not to be the case for simplifications of the formulation based on the removal of some seemingly redundant variables. From their definition (4.10) it is clear that the six variables  $M^{ij}_3$  must be identically zero for exact two-dimensional solutions, and naively it would seem that the evolution system could be simplified by removing these quantities from the set of dependent variables; but doing this in fact changes the hyperbolicity and the characteristic speeds of the system. Examining the evolution equations for the variables  $M^{ij}_3$  in figure 4.1 it can be seen that the constraint quantities which have been added to the equations contribute terms to the principal part of the system which do not vanish when the  $x^3$ -coordinate symmetry is imposed; the transport part of the system (through which hyperbolicity is determined) drives the variables  $M^{ij}_3$  away from zero but the source part counteracts the effect, and while for exact solutions there is precise cancellation, in numerical simulations the variables will not in general remain zero.

The failure of the FR formulation to maintain its hyperbolic character under imposition of symmetry conditions is quite surprising, and to investigate this behaviour further a simple one-dimensional reduction of the evolution system is considered. The analysis of section 4.2 of the eigenvalues and eigenvectors of the symbol  $P(\omega_n)$  of the equations of figure 4.1 is repeated under the assumption that the spacetime metric  $g_{\mu\nu}$  is independent of both the  $x^2$ - and the  $x^3$ -coordinates: the twelve variables  $M^{ij}_2$  and  $M^{ij}_3$  are taken to be identically zero, and only the flux in the  $x^1$ -direction is considered. In this case, in contrast to the equations (4.19), the eigenvalues of the symbol are found to be

$$\begin{aligned}\lambda_0 &= -N^1, \\ \lambda_{\pm A} &= -N^1 \pm N\sqrt{h^{11}}, \\ \lambda_{\pm D} &= -N^1 \pm N\sqrt{(2\gamma - 1)(2\eta - 1)h^{11}}.\end{aligned}$$

There is thus one less pair of eigenvalues in the one-dimensional case as compared to the three-dimensional case, and the parameter  $\Theta$  no longer has any influence on the system. Strong hyperbolicity here requires (in addition to the eigenvalues being real) the parameter choice  $\eta = 1$ , and in contrast to the three-dimensional case two fields related to the extrinsic curvature ( $\bar{P}^{12}$  and  $\bar{P}^{13}$ ) propagate in the system normal to the ADM foliation. An analogue of the causal FR systems described in section 4.2 (for which strong hyperbolicity is combined with physically relevant characteristic speeds) is only possible in the one-dimensional case for the parameter choice  $\eta = \gamma = 1$ . It is clear from this analysis that the removal of the  $M^{ij}_2$  and  $M^{ij}_3$  variables leads to a one-dimensional reduction of the FR system which has substantially different properties to the original.

Returning to the two-dimensional reduction, it can be seen that changes in hyperbolicity are not a phenomenon restricted only to the one-dimensional case: with the  $M^{ij}_3$  variables removed,

the eigenvalues of the symbol in the  $x^1$ -direction are (cf. equation (4.19))

$$\begin{aligned}\lambda_0 &= -N^1, \\ \lambda_{\pm A} &= -N^1 \pm N\sqrt{h^{11}}, \\ \lambda_{\pm E} &= -N^1 \pm N\sqrt{\eta(1-\Theta)h^{11}}, \\ \lambda_{\pm F} &= -N^1 \pm N\sqrt{2\eta(1-\Theta)h^{11}}, \\ \lambda_{\pm G} &= -N^1 \pm N\sqrt{(1+2\gamma[3\eta-1]-2\eta[1+\Theta])h^{11}}.\end{aligned}$$

From the point of view of constructing a two-dimensional FR code there are thus two possibilities: either the variables  $M^{ij}_3$  are retained in the evolution system, or they are removed and the hyperbolicity of the resulting set of equations is re-analysed to determine which parameter choices lead to well-posed systems. In the present work, since the main aim is to study the suitability of the full FR formulation for performing numerical simulations, the former approach is taken.

While without fundamentally changing the nature of the FR formulation it is not possible to remove the variables  $M^{ij}_3$  completely from the evolution system, some simplifications based on the two-dimensional symmetry of the spacetimes can still be made. First of all, note that  $M^{ij}_3 = 0$  can be thought of as an additional constraint equation for the system: it is imposed on the initial data and conserved in exact solutions, and like the other constraints multiples of it may be added to the evolution equations without changing their physical solutions. Since this new constraint contains no (explicit) derivatives of the dependent variables it can be used to modify the evolution system without affecting its principal part, and in particular it can be used to cancel out all of the  $M^{ij}_3$  terms that appear on the right-hand sides of the evolution equations. This means that when the source terms of the FR formulation are evaluated by the two-dimensional code, the values of the variables  $M^{ij}_3$  can be assumed to be zero without altering the hyperbolicity or the physical solutions of the system.

A second simplification that can be applied to the two-dimensional FR formulation follows from the observation that the evolution equations for the particular three variables  $M^{11}_3$ ,  $M^{12}_3 (= M^{21}_3)$  and  $M^{22}_3$  do not in fact involve any constraint quantities; these variables can be omitted altogether from the evolution system without affecting its hyperbolicity. Relabelling the remaining variables  $\{M^{13}_3, M^{23}_3, M^{33}_3\}$  as  $\{m_1, m_2, m_3\}$ , the reduced evolution equations for these quantities can be seen to take the form

$$\partial_t m_i - \partial_n(N^n m_i) = (\text{combinations of } \mathcal{C}^k \text{ quantities with all } M^{ij}_3 \text{ terms removed}),$$

with the only other appearance of the variables  $m_i$  in the reduced formulation being in the flux terms of the evolution equations for the variables  $P^{ij}$ . Analytically the variables  $m_i$  will remain zero if they are zero initially, but in numerical simulations truncation errors and constraint violations will prevent this from being the case, and the overall accuracy of the numerical solution may suffer because of errors in the variables  $m_i$ . One possible way in which the growth of errors in these variables could be limited would be to add damping terms to their evolution equations:

$$\partial_t m_i - \partial_n(N^n m_i) = (\dots) - \varepsilon m_i,$$

where  $\varepsilon$  is a suitably chosen constant. However, it turns out that a simpler approach can be used in practice: empirical evidence shows that the values of the variables  $m_i$  can be set to zero intermittently by the code (possibly at the end of each time step) without affecting its convergence, and this has been observed to lead to an improvement in simulation accuracy.

To summarize, the two-dimensional FR code uses a slightly simplified version of the FR evolution system which nonetheless has the same characteristic structure as the original. (This turns out to be a much less trivial point than at first it may seem.) The six variables  $M^{ij}_3$  (which encode the derivatives of the intrinsic metric with respect to the  $x^3$ -coordinate) are removed from the formulation and replaced by three variables  $m_i$  which are identically zero in exact solutions but may deviate from this in numerical solutions.

### *The Frittelli-Reula Riemann Problem I: The Case of Zero Shift*

In chapter 2 a multi-dimensional high-resolution wave-propagation method for the numerical integration of strongly hyperbolic flux-conservative evolution systems is described. The method, which was developed for use in computational fluid dynamics, exploits information about the characteristic structure of the evolution equations to give second-order accurate integration of smooth solutions while also accurately resolving any discontinuities that may develop. In the present work a standard implementation of the wave-propagation method (the CLAWPACK package; LeVeque 1998) is incorporated into the numerical code described above for evolving the Frittelli-Reula (FR) formulation of Einstein's equations.

As described earlier in this section, a splitting approach is used in the FR code to separate the evolution of the source terms of the equations from the evolution of the transport part, and the wave-propagation algorithm applies to the latter stage only; for the remainder of this section the right-hand sides of the FR equations of figure 4.1 will in general be assumed to be zero. As discussed in section 2.3, the wave-propagation method operates by considering a series of Riemann problems for the system, and the FR code is required to provide solutions to these. In the present work both exact and approximate solutions to the general Riemann problem for the FR equations are derived; this subsection discusses the Riemann problem for the special case when the shift vector  $N^i$  is identically zero while the next subsection extends the discussion to the fully general case. The implementation of the Riemann solvers described here has enabled the FR code to use the wave-propagation method to evolve a range of known solutions to the Einstein equations with second-order accuracy. Further evidence for the correctness of the Riemann solvers is seen from the agreement between numerical results produced using the wave-propagation methods and results produced using the standard Lax-Wendroff method.

For the purposes of the discussion here only FR evolution systems which have physically relevant characteristic speeds are considered. (Given that an evolution system must be strongly hyperbolic for high-resolution numerical methods to be applied, this narrows the choice down to the family of causal FR systems defined by equation (4.20).) This restriction to systems with only three characteristic speeds significantly simplifies the construction of a Riemann solver since each distinct

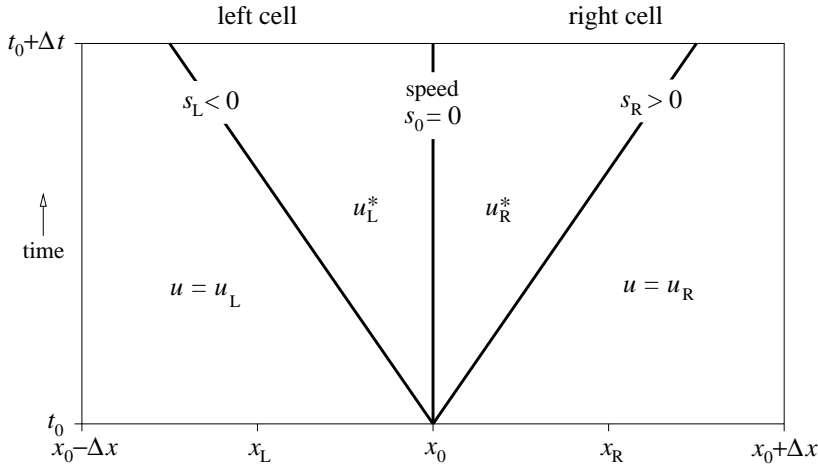


**Figure 4.2:** Solution of the Riemann problem for the Frittelli-Reula system with zero shift. Two computational cells are shown with constant states  $u_L$  and  $u_R$  at initial time  $t = t_0$ . The discontinuity at the interface between the cells splits into three waves (assuming the evolution system to have only physically relevant characteristic speeds): one left-going, one right-going, and one stationary. Two constant states  $u_L^*$  and  $u_R^*$  separate the three waves.

speed corresponds to a wave in the solution to the Riemann problem. For historical reasons, the Riemann solver that has actually been implemented in the present work only applies to the modified FR system and thus has to deal with the complicated situation in which seven waves are produced in each Riemann problem.

Figure 4.2 illustrates the solution to the Riemann problem for the FR system under the assumptions that the shift vector is zero, only physically relevant characteristic speeds are present, and the evolution equations include no source terms. (An additional assumption, that the slicing density  $Q$  is a constant, is discussed below.) The plane  $x = x_0$  separates two constant states  $u = u_L$  and  $u = u_R$  at an initial time  $t = t_0$ . At subsequent times the initial discontinuity breaks up into three waves, each travelling at a constant speed. Two of the waves propagate (at what is effectively the speed of light) in opposite directions into the initially constant regions, leaving in their wakes constant states  $u_L^*$  and  $u_R^*$ , while the third wave is a stationary discontinuity separating these two new states. (Strictly speaking the three waves are ‘contact discontinuities’, and this fact makes it feasible to try to derive an exact solution to the Riemann problem.) A Riemann solver for the FR system must determine from a knowledge of the initial states  $u_L$  and  $u_R$  the values of the speeds of the three waves,  $s_L < 0$ ,  $s_0 = 0$  and  $s_R > 0$ , and the jumps they produce between the constant states,

$$\mathcal{W}_L = u_L^* - u_L, \quad \mathcal{W}_0 = u_R^* - u_L^* \quad \text{and} \quad \mathcal{W}_R = u_R - u_R^*. \quad (4.22)$$

In the discussion here only the Riemann problem in the  $x$ -direction is considered; the solutions for the other spatial directions can be derived following analogous arguments.

The following notation is used here. The state vector  $u$  for the FR system consists of thirty dependent variables  $h^{ij}$ ,  $M^{ij}_k$  and  $P^{ij}$  which are written with their indices suppressed:  $u = [h, M, P]^T$ ,

such that  $h$  and  $P$  are column vectors with six components, and  $M$  is a column vector with eighteen components. (The full FR system is considered here although the discussion applies equally to the two-dimensional reduction of the system described in the previous subsection for which the state vector has three less components.) It will also be convenient to define here a reduced state vector  $v = [M, P]^T$  from which the six variables  $h^{ij}$  are omitted. The FR evolution equations of figure 4.1 (in the absence of source terms and shift) can be written as

$$\partial_t u + \partial_x f(u) = \partial_t \begin{bmatrix} h \\ M \\ P \end{bmatrix} + \partial_x \begin{bmatrix} 0 \\ f_M(h, P) \\ f_P(h, M) \end{bmatrix} = 0, \quad (4.23)$$

where  $f(u)$  is the flux vector in the  $x$ -direction, and the other spatial directions play no part in the one-dimensional Riemann problem. A reduced Jacobian matrix for the system is also defined as

$$A = \begin{bmatrix} 0 & C \\ D & 0 \end{bmatrix} = \begin{bmatrix} 0 & \partial f_M / \partial P \\ \partial f_P / \partial M & 0 \end{bmatrix}, \quad (4.24)$$

where the  $18 \times 6$  matrix  $C$  and the  $6 \times 18$  matrix  $D$  both depend only on the variables  $h^{ij}$  (and the slicing density  $Q$ ). The analysis of section 4.2 shows that the matrix  $A$  has three eigenvalues: the two eigenvalues  $\lambda^\pm = \pm N\sqrt{h^{11}}$  each corresponds to six independent eigenvectors, and the eigenvalue  $\lambda^0 = 0$  corresponds to twelve independent eigenvectors.

The exact solution to the Riemann problem illustrated in figure 4.2 can now be derived. (An approximate solution, which has proved to be useful in the present work, is also derived later in this subsection.) It is convenient in the following argument to treat the slicing density  $Q(t, x^i)$  as a constant; variations in the value of  $Q$  are taken into account in the implementation of the Riemann solver in the FR code, and are considered below. The key point to note in deriving the exact Riemann solution is that, from equation (4.23), the variables  $h^{ij}$  remain constant in time, and so, using the subscript and superscript notation of figure 4.2,

$$h_L^* = h_L \quad \text{and} \quad h_R^* = h_R.$$

Since the flux vector  $f$  is linear in the variables  $M^{ij}_k$  and  $P^{ij}$  (with coefficients depending on  $h^{ij}$ ) it follows that the left-going and right-going waves of the Riemann solution both propagate as if they were produced by two different linear evolution systems, and the theory of shock waves in such systems (see LeVeque 1992, and the discussion in section 2.2) is straightforward to apply. The left- and right-going waves have speeds

$$s_L = \lambda_L^- = -N_L\sqrt{h_L^{11}} < 0 \quad \text{and} \quad s_R = \lambda_R^+ = +N_R\sqrt{h_R^{11}} > 0, \quad (4.25)$$

and (omitting the variables  $h^{ij}$  from the state vectors) the intermediate states  $v_L^*$  and  $v_R^*$  are related to the initial states  $v_L$  and  $v_R$  by

$$v_L^* = v_L + \sum_{i=1}^6 \alpha_i r_L^i \quad \text{and} \quad v_R^* = v_R - \sum_{i=1}^6 \beta_i r_R^i,$$

where  $r_L^1, \dots, r_L^6$  are the six eigenvectors of  $A_L$  associated with the eigenvalue  $\lambda_L^- < 0$ , and  $r_R^1, \dots, r_R^6$  are the six eigenvectors of  $A_R$  associated with the eigenvalue  $\lambda_R^+ > 0$ , and these eigenvectors are assumed to be known. The twelve real values  $\alpha_1, \dots, \alpha_6$  and  $\beta_1, \dots, \beta_6$  must be determined in order to solve the Riemann problem. (The subscripts ‘L’ and ‘R’ are used here to distinguish between quantities which are evaluated based on the values  $h_L^{ij}$  and those which are based on the values  $h_R^{ij}$ .)

From consideration of the Rankine-Hugoniot jump conditions across the individual waves (equation (2.23)) it can be seen that the intermediate states must satisfy

$$f(u_R) - f(u_L) = s_R(u_R - u_R^*) - s_L(u_L - u_L^*), \quad (4.26)$$

and from equations (4.23) and (4.24) this condition can be written as

$$A_R v_R - A_L v_L = s_L \sum_{i=1}^6 \alpha_i r_L^i + s_R \sum_{i=1}^6 \beta_i r_R^i. \quad (4.27)$$

All of the quantities in this equation are known (given the initial states  $u_L$  and  $u_R$ ) except for the twelve values  $\alpha_i$  and  $\beta_i$ , and it turns out that the equation, viewed as a linear system of twenty-four equations, can be inverted in a relatively straightforward manner to determine the exact solution of the Riemann problem. If the components of the eigenvectors  $r_{L/R}^i$  are separated as  $r = [\mu, \pi]^T$  in an analogous manner to the variables in the state vector  $v$ , then equation (4.27) can be re-expressed in block matrix form as

$$\begin{bmatrix} s_L \boldsymbol{\mu}_L & s_R \boldsymbol{\mu}_R \\ s_L \boldsymbol{\pi}_L & s_R \boldsymbol{\pi}_R \end{bmatrix} \begin{bmatrix} \boldsymbol{\alpha} \\ \boldsymbol{\beta} \end{bmatrix} = \begin{bmatrix} C_R P_R - C_L P_L \\ D_R M_R - D_L M_L \end{bmatrix}, \quad (4.28)$$

(24 × 12)      (12 × 1)                      (24 × 1)

where  $\boldsymbol{\mu}$  and  $\boldsymbol{\pi}$  are (respectively)  $18 \times 6$  and  $6 \times 6$  matrices with columns equal to the vectors  $\mu^1, \dots, \mu^6$  and  $\pi^1, \dots, \pi^6$ , and the unknowns  $\alpha_i$  and  $\beta_i$  are written here combined as a column vector. The form of the FR evolution equations is such that a  $6 \times 18$  matrix  $\xi$  with constant coefficients can be found which multiplies the matrix  $C$  to give  $\bar{C} = \xi C$ , a non-singular  $6 \times 6$  matrix; in fact  $\xi$  can be chosen such that the new matrix  $\bar{C}$  is proportional to the identity matrix. Multiplying through the upper part of equation (4.28) by  $\xi$  and defining  $\bar{\boldsymbol{\mu}} = \xi \boldsymbol{\mu}$  then gives

$$\begin{bmatrix} s_L \bar{\boldsymbol{\mu}}_L & s_R \bar{\boldsymbol{\mu}}_R \\ s_L \boldsymbol{\pi}_L & s_R \boldsymbol{\pi}_R \end{bmatrix} \begin{bmatrix} \boldsymbol{\alpha} \\ \boldsymbol{\beta} \end{bmatrix} = \begin{bmatrix} \bar{C}_R P_R - \bar{C}_L P_L \\ D_R M_R - D_L M_L \end{bmatrix}. \quad (4.29)$$

(12 × 12)      (12 × 1)                      (12 × 1)

Recalling that  $r = [\mu, \pi]^T$  is defined to be an eigenvector of the matrix  $A$  of equation (4.24), it is easy to show that each of the vectors  $\bar{\mu}^i$  must be proportional to its corresponding vector  $\pi^i$ . Further noting that the eigenvectors of the matrix  $A$  can always be chosen such that the matrix  $\boldsymbol{\pi}$  is the identity matrix, it becomes clear that the  $12 \times 12$  matrix on the left-hand side of equation (4.29) is non-singular and can be straightforwardly inverted to give the values of  $\alpha_i$  and  $\beta_i$  in terms of the initial states  $u_L$  and  $u_R$ .

The exact solution to the Riemann problem is thus found, with the speeds  $s_L$ ,  $s_0$  and  $s_R$  known (see equation (4.25)) and the wave jumps  $\mathcal{W}_L$ ,  $\mathcal{W}_0$  and  $\mathcal{W}_R$  of equation (4.22) being simple to construct once the intermediate states  $u_L^*$  and  $u_R^*$  are determined from the values  $\alpha_i$  and  $\beta_i$ . (For FR systems in which characteristic speeds other than the three physically relevant ones are present, the solution to the Riemann problem can be found by following essentially the same argument as above, but the algebra involved will be considerably more complicated. In particular the matrix inversion required to solve the analogue of equation (4.29) is no longer straightforward.)

An approximate solution to the Riemann problem can also be derived by following an approach similar to the one described in the classic 1981 paper by Roe (see also section 2.2) with the nonlinear problem (4.23) being in effect replaced by a linear problem

$$\partial_t u + \tilde{A}_0 \partial_x u = 0, \quad (4.30)$$

for a suitable  $30 \times 30$  matrix  $\tilde{A}_0$  with constant coefficients. The matrix  $\tilde{A}_0$  is chosen to be the Jacobian matrix  $\tilde{A}(u) = \partial f / \partial u$  evaluated at a state  $u = u_0$ , where in calculating  $\tilde{A}(u)$  the lapse  $N$  (which of course depends on the variables  $h^{ij}$  and the slicing density  $Q$ ) is treated as having a constant value  $N = N_0$ . The state  $u_0$  is chosen here to be the average of the two initial states in the Riemann problem:  $u_0 = \frac{1}{2}(u_L + u_R)$ . If the lapse  $N$  is truly a constant then the components of the flux vector  $f$  in the FR system (4.23) are at most quadratic in the unknowns  $u$ , and it can be shown (Roe 1981) that the following property holds:

$$\tilde{A}_0(u_R - u_L) = f(u_R) - f(u_L),$$

which is required in order for the approximate solution to the Riemann problem to be conservative. In the general case however this equation will not be satisfied, although in the next subsection a reformulation of the FR equations is described which admits a conservative approximate Riemann solver of this form.

The three waves in the approximate Riemann solution have speeds equal to the eigenvalues of the matrix  $\tilde{A}_0$ , that is  $s_L = -N_0 \sqrt{\tilde{h}_0^{\text{II}}}$ ,  $s_0 = 0$  and  $s_R = +N_0 \sqrt{\tilde{h}_0^{\text{II}}}$ , and jumps  $\mathcal{W}_L$ ,  $\mathcal{W}_0$  and  $\mathcal{W}_R$  which are eigenvectors of  $\tilde{A}_0$  corresponding to these eigenvalues and which satisfy

$$\Delta u = \mathcal{W}_L + \mathcal{W}_0 + \mathcal{W}_R, \quad (4.31)$$

where  $\Delta u = u_R - u_L$ . That three such wave jumps can be found is a consequence of the strong hyperbolicity of the FR system, and their values may be determined by noting that, by definition,

$$\tilde{A}_0 \Delta u = s_L \mathcal{W}_L + s_R \mathcal{W}_R,$$

and that this can be solved in basically the same way as equation (4.26), or that

$$\mathcal{W}_L = \frac{\tilde{A}_0(\tilde{A}_0 - s_R I) \Delta u}{s_L(s_L - s_R)} \quad \text{and} \quad \mathcal{W}_R = \frac{\tilde{A}_0(\tilde{A}_0 - s_L I) \Delta u}{s_R(s_R - s_L)},$$

where  $I$  is the identity matrix, and the final wave jump  $\mathcal{W}_0$  can be calculated from equation (4.31).



Either of the two Riemann solvers described above can be implemented to allow solutions of the FR equations to be evolved using the wave-propagation algorithm. The Riemann problem at the interface between two computational cells (figure 4.2) which are centred at coordinate positions  $x = x_L$  and  $x = x_R$  (with fixed values for the other spatial coordinates  $y$  and  $z$ ) forms the basic component of the evolution procedure that advances a numerical solution from a time  $t = t_0$  to a time  $t = t_0 + \Delta t$ . The wave speeds and jumps that comprise the solution to the Riemann problem are calculated using the cell-averaged data  $u_L$  and  $u_R$  together with values  $N_L$ ,  $N_0$  and  $N_R$  for the lapse which are evaluated according to

$$N_\gamma = Q(t_0 + \frac{1}{2}\Delta t, x_\gamma, y, z) \sqrt{\det(h_{ij})_\gamma} \quad \text{for } \gamma = L, 0, R,$$

where  $x_0 = \frac{1}{2}(x_L + x_R)$ . The wave-propagation algorithm also requires the ‘fluctuations’ between the cells to be specified, and these are calculated following equation (2.32) as

$$\mathcal{A}^+ = \sum_{\gamma=L,0,R} \max(s_\gamma, 0) \mathcal{W}_\gamma \quad \text{and} \quad \mathcal{A}^- = \sum_{\gamma=L,0,R} \min(s_\gamma, 0) \mathcal{W}_\gamma. \quad (4.32)$$

For simulations that depend on only one spatial dimension, this information is sufficient for a numerical solution to the FR equations to be evolved using the wave-propagation method—the update step is shown in equation (2.38)—and when the exact Riemann solver is used the solution is found to converge at second order as the numerical grid is refined. In contrast, the approximate Riemann solver, because of the ad hoc way in which it treats the lapse, does not in general produce solutions that are second-order convergent.

The usefulness of the approximate Riemann solver is realized when simulations in more than one spatial dimension are performed. As described in section 2.3, for two-dimensional evolutions the wave-propagation algorithm applies correction terms to the solution of each one-dimensional Riemann problem to account for effects of wave propagation transverse to the original direction: as figure 2.3 illustrates, the waves produced by a Riemann problem at the interface between two adjacent computational cells are propagated in a multi-dimensional way so that they affect the data in all of the cells surrounding the interface. The transverse correction terms are calculated by splitting the original fluctuations  $\mathcal{A}^+$  and  $\mathcal{A}^-$  of equation (4.32) for the  $x$ -direction according to an approximate Riemann solution for the  $y$ -direction (with similar transverse corrections being also calculated with the spatial directions switched around). A matrix  $\tilde{B}_0$  is evaluated at the interface between the cells in the same way as the matrix  $\tilde{A}_0$  is evaluated in the approximate Riemann solver described above (and using the same values of  $u_0$  and  $N_0$ ) but in this case it is based on the Jacobian matrix  $\tilde{B}(u)$  for the flux vector in the transverse direction. Instead of calculating waves based on the vector  $\Delta u$ , the transverse approximate Riemann solver is applied in turn to the two fluctuations  $\mathcal{A}^\pm$  to construct, in analogy with equation (4.32), four transverse fluctuations  $\mathcal{B}^\pm \mathcal{A}^\pm$ . These then contribute to the second-order correction terms which are used to update the data in the surrounding cells according to the two-dimensional wave-propagation step of equation (2.41).

This use of an approximate Riemann solver to produce transverse corrections to exact Riemann solutions has been found to lead to the production of second-order accurate numerical solutions to

the FR evolution equations when using the wave-propagation algorithm. Unfortunately the method does not generalize to the case when the shift vector  $N^i$  is not identically zero, and some alternative approaches for dealing with that case are considered in the next subsection.

*The Frittelli-Reula Riemann Problem II: The Case of General Shift*

The incorporation of a non-trivial shift vector into the Riemann solvers described in the previous subsection has proven to be problematic. The status of the shift vector  $N^i$ , together with the slicing density  $Q$ , as given functions of the spacetime coordinates rather than either constants or dependent variables causes complexities when attempting to use the wave-propagation algorithm to produce second-order accurate solutions to the FR equations. In this subsection two approaches for constructing Riemann solvers which give second-order convergence in the presence of a non-zero shift vector are discussed. (As an aside, it may be noted that alternative methods for dealing with the shift vector are available. For example, in Scheel et al. 1997 a ‘causal differencing’ method is developed in which the influence of the shift vector is removed from the time advancement step of the integration algorithm and accounted for by shifting the numerical solution using spatial interpolation. Such a method has the practical advantage that, as equation (4.21) shows, the Courant-Friedrichs-Lewy condition allows large time steps to be taken if the shift vector is zero during the time evolution phase.)

As can be seen from the equations of figure 4.1, the shift vector in effect introduces an advection term to the transport part of the FR system. If  $N^i$  has a constant value then it is straightforward to take its presence into account in the Riemann solvers described in the previous subsection: for the Riemann problem in the  $x$ -direction the wave speeds are simply modified as

$$s_\gamma^{\text{new}} = s_\gamma - N^1 \quad \text{for } \gamma = L, 0, R,$$

with these new speeds being used to calculate the fluctuations of equation (4.32). An extension to this approach which accounts for spatial and temporal variations in the value of the shift vector is to include ‘second-order’ corrections in the modifications made to the wave speeds:

$$\left. \begin{aligned} \hat{s}_\gamma &= s_\gamma - N^1(t_0, x_0, y, z) \\ \hat{x} &= x_0 + \frac{1}{2}\Delta t \hat{s}_\gamma \\ s_\gamma^{\text{new}} &= s_\gamma - N^1(t_0 + \frac{1}{2}\Delta t, \hat{x}, y, z) \end{aligned} \right\} \text{for } \gamma = L, 0, R. \quad (4.33)$$

However, in modelling the influence of the shift vector on the transport part of the FR equations in this way the evolution system is in effect rewritten so that derivatives of the shift vector no longer appear on the left-hand side; schematically,

$$\partial_t u + \partial_i [f^i(u) - N^i u] = s(u) \quad \longrightarrow \quad \partial_t u + \partial_i f^i(u) - N^i \partial_i u = s(u) + N^i_{,i} u, \quad (4.34)$$

and the numerical implementation of the equations must be adjusted to take into account the appearance of additional terms in the source part of the system.

Inclusion of the above modifications in the Riemann solvers described in the previous subsection is not sufficient to allow the wave-propagation algorithm to evolve second-order accurate numerical solutions to the FR equations when the shift vector is non-trivial. However two methods which do give second-order accuracy have been found: in both cases the FR evolution system is reformulated so that the slicing density  $Q$  does not appear in the transport part of the equations. In the first approach the lapse  $N$ , which in the evolution equations of figure 4.1 is used as a shorthand for the expression  $Q\sqrt{\det h_{ij}}$ , is raised to the status of an unknown variable which evolves according to

$$\partial_t N - \partial_n(N^n N) = N\left(\frac{1}{2}NP + Q_{,t}Q^{-1} - Q_{,k}Q^{-1}N^k\right), \quad (4.35)$$

(cf. equation (4.9)) and an extended FR system of thirty-one variables is produced. With the lapse treated as an unknown in this way the explicit dependence of the FR flux vectors on the slicing density  $Q$  is removed, although it is still present in the source terms. The exact expression for the lapse in terms of the slicing density and the spatial metric may be used to intermittently update the value of the variable  $N$  during the course of numerical simulations; however doing this is not found to lead to any substantial improvement in the performance of the code.

The second method considered here to simplify the transport part of the FR equations redefines the dependent variables so that the lapse is removed from the system altogether. If a new set of FR variables is defined in terms of the standard variables and powers of the lapse according to

$$\begin{aligned} \tilde{h}^{ij} &= N^2 h^{ij}, \\ \tilde{M}^{ij}_k &= N^\alpha M^{ij}_k, \\ \tilde{P}^{ij} &= N^{\alpha+1} P^{ij}, \end{aligned} \quad (4.36)$$

then the transformed evolution system is found to have exactly the same transport part as in figure 4.1 (with the new variables replacing the standard variables) but with the lapse in effect set to  $N = 1$ . Furthermore, if the constant in equation (4.36) is chosen to be  $\alpha = 2$ , then the source terms of the new evolution system are also independent of  $N$ , although they do still depend on the slicing density  $Q$ . (If non-vacuum spacetimes are considered then a similar redefinition of the variables  $\rho$ ,  $J^i$  and  $S^{ij}$  can be used to remove the lapse from the matter terms in the equations.) Although this ‘hidden lapse’ version of the FR formulation is slightly more awkward to interpret than the standard version, the simplicity of its transport part makes it well suited for use with the wave-propagation method: there are no problems in evaluating the slicing density  $Q$  to give second-order accuracy, and since the flux vectors are no more than quadratic in the dependent variables an approximate Riemann solver constructed as described in the previous subsection will be flux-conservative.

These two alternative versions of the FR system, one in which the lapse is evolved as an unknown variable and one in which the lapse is hidden by a redefinition of the variables, have both been successfully used to give second-order convergence with the wave-propagation algorithm in two-dimensional simulations of vacuum spacetimes for which the shift vector has a non-trivial dependence on the spacetime coordinates. The exact and approximate Riemann solvers of the

previous subsection are used (these generalize straightforwardly to the new systems) with the latter providing transverse corrections to the former, and the shift vector is treated using the modifications shown in equations (4.33) and (4.34). (In fact, for the two alternative FR systems second-order convergence is still obtained if the approximate Riemann solver is used exclusively in the wave-propagation method.)

In all cases for which the evolution is second-order accurate, the wave-propagation method has been found to produce results which are comparable in accuracy to those produced using the standard Lax-Wendroff method. No significant differences in accuracy have been observed between simulations based on the three different versions of the FR equations, and, when both are second-order convergent, the exact and the approximate Riemann solvers have been found to give nearly indistinguishable results. Unsurprisingly given its complexity, the wave-propagation method is found to be much slower than the Lax-Wendroff method: for the implementation of the FR equations used here, evolving the transport part of the system based on exact Riemann solutions takes about twelve times longer than if the Lax-Wendroff method is used, and for approximate Riemann solutions it takes about ten times longer. For comparison, more than twice as much time is spent by the code evolving the source part of the system than is spent evolving the transport part by the Lax-Wendroff method. (It should be noted however that these performance results concern the *modified* FR system—using the terminology of section 4.2—for which seven rather than three waves are present in the solution to each Riemann problem. This makes the operation of a Riemann solver significantly more complex, and undoubtedly makes a sizeable contribution to the running times for the wave-propagation method.)

In this and the previous subsection a number of approaches have been described that allow the equations of the FR formulation to be numerically evolved using the high-resolution wave-propagation method of chapter 2. As might be expected, for spacetimes in which the metric fields are suitably smooth the results produced using the wave-propagation method are no more accurate than those produced using a standard finite difference method. In chapters 6 and 7, cosmological models in which steep gradients develop in the components of the metric are investigated, and while it may be hoped that the use of high-resolution numerical methods would lead to improvements in performance for these spacetimes, in practice this is not found to be the case. Besides their possible usefulness in implementing well-posed boundary conditions, the main motivation for exploring the use of high-resolution methods to evolve Einstein’s equations comes from the gains in performance that may be expected when simulating spacetimes in which the gravitational fields are coupled to hydrodynamical sources: both metric and matter variables can be evolved then in a unified manner with shock waves in the fluid (and any knock-on effects in the gravitational fields) receiving a sophisticated numerical treatment. The extension of the FR code to non-vacuum spacetimes is, however, beyond the scope of the present work.

# Chapter 5.

## Homogeneous Cosmologies

The preceding three chapters discuss the development and implementation of a computer code capable of generating approximate solutions to the field equations of general relativity. The code has been used to study inhomogeneous cosmologies, and the two chapters that follow present results from numerical simulations of planar and  $U(1)$ -symmetric cosmological models. In the present chapter consideration is given to some problems that are often encountered in work on numerical relativity resulting from freedom in the choice of spacetime coordinates, and the discussion is illustrated using numerical simulations of simple homogeneous cosmological models.

Homogeneous and inhomogeneous cosmologies are discussed at length in the books by Ryan and Shepley (1975) and Krasinski (1997); the latter includes a discussion of the relevance of inhomogeneous models given the widespread acceptance of the homogeneous standard cosmological model. Analytic work on inhomogeneous cosmologies is typically limited to spacetimes which have a high degree of symmetry or which are within the ‘linear regime’ of a known solution. In the general case progress in understanding the behaviour of inhomogeneous cosmologies seems only to be possible through the use of numerical simulations (see Anninos 1998b for a review). In the present work (chapters 6 and 7) inhomogeneous cosmological models are studied numerically with the aim being to develop and test numerical approaches to solving the Einstein equations. The symmetry, topology, and lack of matter content of the spacetimes considered here rules them out as realistic models of the physical universe; however a number of aspects of the behaviour of inhomogeneous cosmologies are investigated in the following chapters including the propagation of linear and nonlinear gravitational waves, the formation of fine-scale structure during gravitational collapse, and the nature of cosmological singularities.

Even for cases in which exact solutions are known, homogeneous models can still be of interest in numerical relativity. When written in a coordinate system for which its homogeneity is not explicit, a homogeneous cosmology is indistinguishable from an inhomogeneous one for the purposes of performing numerical simulations, and in this way provides a non-trivial test case for numerical codes; furthermore, homogeneous cosmologies can be used to assess the performance of different gauge conditions that could be employed in simulations of inhomogeneous models. The first of these points motivates the discussion in section 5.1. There the question is considered as to how a numerical solution for a homogeneous cosmology which is constructed using an inhomogeneous time slicing condition can be compared to a standard solution for the model, and, conversely, how a genuinely inhomogeneous spacetime can be distinguished from a homogeneous one evaluated in a non-standard gauge. In addition, an algorithm is presented for comparing different time slicings of the same spacetime: the coordinate system of a numerically evolved solution is reconstructed relative to a known metric using the values taken by the foliation’s lapse function.

Section 5.2 considers time slicing conditions for numerical simulations, with particular attention being given to the harmonic slicing condition introduced in chapter 4. Analytic and numerical

approaches are used to investigate the behaviour of foliations of a homogeneous cosmological model which are generated using a harmonic time coordinate, and it is demonstrated that such foliations may, under quite general circumstances, fail to cover the whole of the spacetime due to the formation of coordinate singularities. The behaviour of the metric components during the formation of coordinate singularities is examined and compared to the behaviour seen in numerical simulations of inhomogeneous cosmologies in chapters 6 and 7, and the implications that these results have for numerical work in general are discussed.

## 5.1 Comparing Numerical Spacetimes with Different Gauge Conditions

Chapter 4 describes the standard ‘three-plus-one’ approach to producing numerical solutions to the Einstein equations, and two quantities—the lapse function  $N$  and the shift vector  $N^i$ —are introduced there which encode the freedom in the choice of spacetime coordinates for a numerical simulation. Although a number of standard ways of specifying the lapse and the shift exist (properties of some of these are considered in section 5.2), in general two independent numerical simulations of the same spacetime will produce results which are with respect to completely different coordinate systems. In the present section consideration is given to the question of how such results can be compared in practice, and two points in particular are discussed: how coordinate independent quantities can be used to describe spacetimes, and how different coordinate systems for a spacetime can be compared. In the next section these ideas are applied to simulations of a homogeneous cosmological model.

### *Scalar Quantities and Curvature Invariants*

In presenting results from numerical simulations in chapters 6 and 7 an attempt has been made to use (where possible) scalar quantities to describe the evolved spacetimes. This subsection considers some of the types of scalar quantities that can be used in this way, and examines the possible advantages their use has in practice.

Typically the unknown variables that are used in numerical simulations have a non-trivial dependence on the gauge conditions employed: they are not in general four-dimensional scalars, and often they obey complicated transformation laws under changes of spacetime coordinates. For the purposes of describing the evolved spacetimes it is more practical to use the variables to construct scalar quantities which are independent of the spacetime coordinate system than it is to use the variables themselves, and there are several approaches to doing this. For spacetimes which have symmetries, the properties of Killing vectors can be used to define scalar quantities which have simple physical interpretations. This is done for the inhomogeneous cosmologies investigated in chapters 6 and 7, with, for example, the proper area of the symmetry plane providing scalar information about the planar models. (The ‘areal radius’ defines an analogous quantity for spherically symmetric spacetimes.) Furthermore, for non-vacuum spacetimes the matter fields may naturally

define scalar quantities, with examples being, depending on the type of matter present, wave functions and fluid rest densities.

The types of scalar quantities described above are clearly not appropriate for presenting results for vacuum spacetimes which have no simplifying symmetries, and in such cases the invariants of the Riemann curvature tensor may provide useful alternatives. It is well known (see for example Witten 1959, York 1989) that fourteen independent (pseudo-)scalars can be constructed from the Riemann tensor  $R_{\mu\nu\rho\sigma}$ , and that for a vacuum spacetime all but four of these curvature invariants vanish identically. In the present work, the four curvature invariants which are non-trivial for vacuum spacetimes are expressed as

$$\begin{aligned} w_{\text{I}} &= \frac{1}{8} C_{\mu\nu\rho\sigma} C^{\mu\nu\rho\sigma}, & w_{\text{II}} &= \frac{1}{8} C_{\mu\nu\rho\sigma}^* C^{\mu\nu\rho\sigma}, \\ w_{\text{III}} &= -\frac{1}{16} C_{\mu\nu}{}^{\rho\sigma} C_{\rho\sigma}{}^{\eta\omega} C_{\eta\omega}{}^{\mu\nu}, & w_{\text{IV}} &= -\frac{1}{16} C_{\mu\nu}{}^{\rho\sigma} C_{\rho\sigma}{}^{\eta\omega} C_{\eta\omega}{}^{\mu\nu}, \end{aligned} \quad (5.1)$$

where  $C_{\mu\nu\rho\sigma}$  is the Weyl tensor (which for vacuum spacetimes is equal to the Riemann tensor), and  $C_{\mu\nu\rho\sigma}^* = \frac{1}{2} \varepsilon_{\mu\nu\eta\omega} C^{\eta\omega}{}_{\rho\sigma}$  where  $\varepsilon_{\mu\nu\rho\sigma}$  is the Levi-Civita tensor. (These definitions of the curvature invariants are the same as those used in the GRTensorII package for MapleV; see Musgrave, Pollney and Lake 1996.) Curvature invariants are used in the presentation of numerical results for the inhomogeneous cosmological models studied in chapters 6 and 7. These quantities can be particularly useful in interpreting the behaviour of evolved spacetimes since their divergence to infinity indicates the presence of a curvature singularity; however it should be noted that non-trivial ('pp wave') spacetimes exist for which the curvature invariants never vary from zero. As an example of the behaviour of the curvature invariants, for the axisymmetric Kasner metric

$$ds^2 = t^{-1/2}(-dt^2 + dx^2) + t(dy^2 + dz^2), \quad (5.2)$$

which is considered further in the next section, the invariants take the values

$$w_{\text{I}} = \frac{3}{32t^3}, \quad w_{\text{II}} = 0, \quad w_{\text{III}} = -\frac{3}{256t^{9/2}}, \quad w_{\text{IV}} = 0. \quad (5.3)$$

The use of scalar quantities to describe numerically generated spacetimes goes some way to allowing genuine physical behaviour to be distinguished from effects caused by unfortunate choices of spacetime coordinates or metric variables. For the inhomogeneous cosmologies studied in chapters 6 and 7, consideration of the values taken by the symmetry scalars and the curvature invariants makes it immediately clear that the spacetimes being evolved are genuinely inhomogeneous and are not simply homogeneous models constructed using inhomogeneous gauge conditions. (Further comparisons are made between features of numerically evolved homogeneous and inhomogeneous spacetimes in section 5.2.)

Presenting results in terms of scalar quantities simplifies the comparison of numerical simulations of the same spacetime for which different gauge conditions are used. This idea can be extended to the construction of test problems for verifying the correctness of a numerical code. While exact solutions are often used as test bed calculations for codes, it may not always be practical to write a

solution in a form appropriate to the gauge conditions used by a code. (For examples of how complex such transformations of exact solutions can be see Petrich, Shapiro and Teukolsky 1985, 1986.) However, if the values of two or more scalar quantities are known for an exact solution, then the correlation between them can be used as a measure of the accuracy of a numerical simulation of that spacetime, even if the gauge conditions used are different from those of the exact solution; for example, for the axisymmetric Kasner model (5.2) mentioned above, it follows from the equations (5.3) for the curvature invariants that the relationship  $(w_I)^3 = 6(w_{III})^2$  should hold at every spacetime point regardless of how a coordinate system for the spacetime is constructed.

Besides judging the accuracy of a computer code, comparisons between two numerical solutions or between an exact and a numerical solution can be useful for investigating properties of different gauge conditions that may be used in numerical simulations, such as how much of a spacetime they cover or whether they develop coordinate singularities. The direct approach to computing the effects of different gauge conditions by explicit construction of a transformation between two sets of spacetime coordinates is, as was mentioned above, not practical in general; however an example of such a transformation is given for a simple case in section 5.2 where properties of different gauge conditions are considered in more detail. The evaluation of scalar quantities provides an alternative way of comparing coordinate systems. As an example, the curvature invariant  $w_I$ , evaluated at a point in a numerical solution for the axisymmetric Kasner spacetime, determines via equation (5.3) the label  $t$  of the time slice of the metric (5.2) which includes that point; if more independent scalar quantities are known for a spacetime, then more information can be determined about the locations of points in the numerical solution. A third way of comparing different coordinate systems for a spacetime is discussed in the next subsection where an algorithm is presented for numerically evolving a coordinate chart with respect to a known background chart.

### *Numerical Integration of Observer World Lines*

In the previous subsection some approaches are discussed for comparing the results and the coordinate systems of different numerical simulations of the same spacetime. The present subsection expands on the idea of comparing coordinate systems and describes an algorithm for numerically integrating the world lines of one coordinate system with respect to another. Some of the ideas discussed in both this and the previous subsection are put into practice in section 5.2.

The problem can be specified as follows. Consider a spacetime for which the metric  $g_{\mu\nu}$  is known (either as an exact solution or as a numerical solution of sufficient accuracy) with respect to a coordinate system  $(t, x^i) = (t, x, y, z)$ . Suppose that there is also, as described in chapter 4, an ADM foliation  $\{\Sigma_T : T \in \mathbb{R}\}$  of the spacetime, the spatial hypersurfaces of which are unrelated to the  $t = \text{constant}$  surfaces of the first coordinate system. If one of the spatial slices,  $\Sigma_{T_0}$  say, of the foliation is known to have the description  $t = f_0(x^i)$  with respect to the original coordinates, then the question is: given a knowledge of the ADM quantities defined on the foliation, what are the coordinate locations of the other hypersurfaces in the foliation?



In practice the foliation  $\Sigma_T$  will have been generated as part of a numerical simulation. Two simplifying assumptions are made for the purposes of the discussion here: that the shift vector  $N^i$  of the foliation is identically zero, and that the spatial hypersurfaces of the foliation do not have boundaries. Both of these assumptions are valid for the example problems considered in this chapter; the latter point holds because the spacetime models investigated here are all spatially periodic.

Suppose that each hypersurface  $\Sigma_T$  of the spacetime foliation is described by a spatial coordinate system  $X^i = (X, Y, Z)$ , and that the timelike world line of an observer who remains stationary with respect to these spatial coordinates is given by  $p^\mu(T; X^i)$  where the parametrization is such that the spacetime point  $p^\mu(T_*)$  falls within the spatial slice  $\Sigma_{T_*}$ . Since the shift vector  $N^i$  of the foliation is assumed to be zero, the world line of this observer must run normal to the slices of the foliation: if  $n^\mu$  is the vector field normal to the foliation, normalized such that  $n^\mu n_\mu = -1$ , then the velocity four-vector of the observer  $p^\mu(T)$  is

$$v^\mu = \frac{dp^\mu}{dT} \propto n^\mu .$$

With respect to the spacetime coordinate system  $(T, X^i)$  defined by the foliation, it is clear that  $v^\mu = (1, 0, 0, 0)$ , and it is also known (see section 4.1) that  $n^\mu = (1/N, 0, 0, 0)$  where  $N \equiv N(T, X^i)$  is the lapse function of the foliation. Thus,

$$\frac{dp^\mu}{dT} = N n^\mu \tag{5.4}$$

describes the motion of the observer in terms of the properties of the foliation.

Now consider a single slice  $\Sigma_{T_0}$  of the foliation with observers  $p^\mu(T_0; X^i)$  at each point. With respect to the original coordinate system  $(t, x^i)$ , assuming that the spacetime metric  $g_{\mu\nu}$  is known, it is possible to determine the vector field  $n^\mu$  normal to  $\Sigma_{T_0}$  from a knowledge of the positions of the observers. If in addition the lapse function  $N(T_0, X^i)$  is known on the slice, then equation (5.4) is sufficient to determine the location of a second spatial slice  $\Sigma_{T_0+\delta T}$  infinitesimally removed from the first one. In this way a description with respect to the coordinates  $(t, x^i)$  of the foliation  $\Sigma_T$  can be built up from a knowledge of the lapse function and the location of an initial slice  $\Sigma_{T_0}$ .

If the foliation  $\Sigma_T$  is generated as the result of a numerical simulation, then equation (5.4) can be implemented as part of a computer code to locate slices of the foliation with respect to a reference coordinate system. The numerical simulation produces results at discrete time intervals corresponding to a set of slices

$$\{\Sigma_T : T = T^0, T^1, \dots, T^m, \dots\},$$

where the sizes of the time steps are not necessarily uniform, and in addition each spatial slice is discretized by a mesh of points

$$\{(X_j, Y_k, Z_l) = (X_0 + j \Delta X, Y_0 + k \Delta Y, Z_0 + l \Delta Z) : j, k, l \in \mathbb{Z}\}.$$

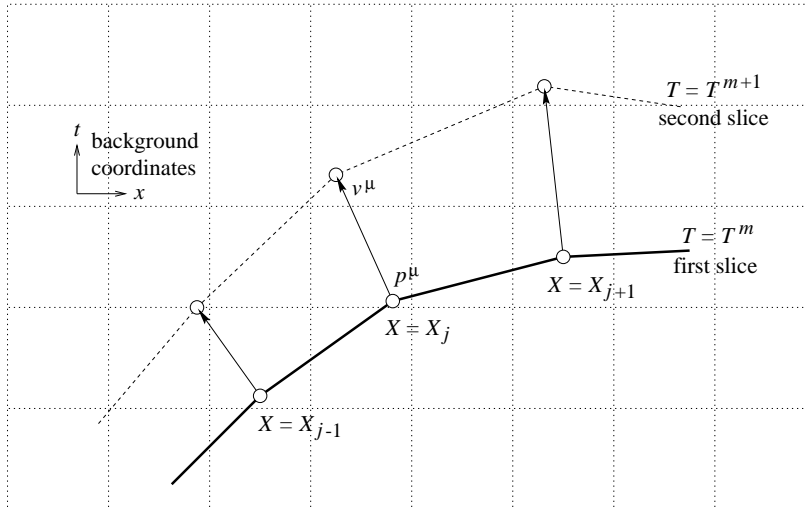


**Figure 5.1:** Numerical evolution of spatial slices with respect to a background coordinate system. A mesh of points  $\{X_j, Y_k, Z_l\}$  describing a spacelike hypersurface is evolved as part of a numerical simulation into a spacetime foliation with slices labelled by time values  $\{T^m\}$ . The positions  $p^\mu$  of the mesh points with respect to a background coordinate system  $(t, x, y, z)$  can be tracked using a time-stepping approach based on the velocity vector  $v^\mu$  which points in the direction normal to the slices. Only one spatial coordinate is shown here.

The value of a quantity  $f$  which is known at a point  $(T^m, X_j, Y_k, Z_l)$  of the foliation is denoted here by  $f|_{jkl}^m$ . The lapse function  $N$  of the foliation is assumed to be known at each point: in practice it is output as part of the results of the numerical simulation.

Figure 5.1 illustrates the evolution of the discretized foliation with respect to a background coordinate system  $(t, x, y, z)$ . The metric  $g_{\mu\nu}$  is assumed to be known in terms of these background coordinates, either as an exact solution or an accurate numerical solution. The position of a mesh point  $(T^m, X_j, Y_k, Z_l)$  of the foliation with respect to the background coordinates is denoted by  $p^\mu|_{jkl}^m = (t, x, y, z)|_{jkl}^m$ , and it is assumed that the positions  $p^\mu|_{jkl}^0$  of all of the mesh points in the initial slice  $\Sigma_{T^0}$  are known. A numerical algorithm for finding the approximate positions (with respect to the background coordinate system) of the other mesh points in the foliation then proceeds by iteration of the following procedure.

Given that the positions  $p^\mu|_{jkl}^m$  of observers in a spatial slice  $\Sigma_{T^m}$  are known, approximations to the positions  $p^\mu|_{jkl}^{m+1}$  of the same observers in a later slice can be made using a discretized version of equation (5.4). The first step is to construct a value for the velocity (with respect to the foliation time  $T$ ) of each observer:  $v^\mu = Nn^\mu$ . As mentioned above, the value of the lapse function  $N$  is assumed to be known at each point of the mesh, and so the task here is to determine a value for the vector  $n^\mu$  normal to the slice. In the continuous case the location of the slice  $\Sigma_{T^m}$  is given by the expression  $t = f(x, y, z)$  where  $f = p^0(T^m; X, Y, Z)$ , and so the normal vector has the covariant form

$$n_\mu = \kappa \nabla_\mu (f - t) = \kappa (-1, \partial f / \partial x^i), \quad (5.5)$$

where  $\kappa$  is a constant (different for each point on the slice), the value of which is determined below. The partial derivatives in equation (5.5) can be expressed in terms of the functions  $\partial p^\mu / \partial X^i$  using the chain rule for differentiation. For example, in the one-dimensional case for which only the spatial coordinates  $X$  and  $x$  are significant, the normal vector is given by

$$n_\mu = \kappa(-1, \frac{\partial p^0 / \partial X}{\partial p^1 / \partial X}, 0, 0).$$

Returning to the case in which only the positions of discrete points in the spatial slice are known, finite differences can be used to give approximate values for the derivatives in equation (5.5) in the obvious way; for example, to second order,

$$(\partial p^\mu / \partial X)|_{jkl}^m = \frac{p^\mu|_{j+1kl}^m - p^\mu|_{j-1kl}^m}{2 \Delta X}.$$

The normal vector  $n^\mu$  can now be determined by using the metric  $g_{\mu\nu}$  evaluated at the spacetime point  $p^\mu$  to raise the index in equation (5.5), and the value of the constant  $\kappa$  can be fixed by requiring that  $n^\mu n_\mu = -1$ .

At this stage an approximate velocity vector  $v^\mu|_{jkl}^m = N|_{jkl}^m n^\mu|_{jkl}^m$  is known at each mesh point  $p^\mu|_{jkl}^m$  of the spatial slice  $\Sigma_{T^m}$ . The next step is to use a discretized version of equation (5.4) to advance the mesh points to the next slice  $\Sigma_{T^{m+1}}$ . A simple first-order approximation to the time derivative in the equation yields a discrete evolution equation for the observers:

$$p^\mu|_{jkl}^{m+1} = p^\mu|_{jkl}^m + \Delta T v^\mu|_{jkl}^m, \quad (5.6)$$

where  $\Delta T = T^{m+1} - T^m$ . Alternatively, if the values of the velocity vectors on the previous spatial slice  $\Sigma_{T^{m-1}}$  are known, then second-order corrections based on quadratic extrapolation can be added to the evolution equation:

$$p^\mu|_{jkl}^{m+1} = p^\mu|_{jkl}^m + \Delta T v^\mu|_{jkl}^m + \frac{(\Delta T)^2}{2 \Delta T_-} (v^\mu|_{jkl}^m - v^\mu|_{jkl}^{m-1}), \quad (5.7)$$

where  $\Delta T_- = T^m - T^{m-1}$ . However, this latter equation may overshoot in its extrapolation of the world line of the observer; in particular, if the value of  $p^0$  decreases during the evolution step then the new position for that observer should be recalculated using equation (5.6).

Using a sequence of evolution steps based on a discretized form of equation (5.4) with the normal vector  $n^\mu$  determined through equation (5.5), approximate values for the positions  $p^\mu$  of observers can be found on a range of spatial slices  $\Sigma_{T^0}$  through to  $\Sigma_{T^M}$  for some  $M$ . Truncation errors in the difference equations, together with errors in the values for the lapse  $N$  produced by the original numerical simulation, build up during the course of the evolution and may cause it to terminate before the observers reach the final slice of the simulation; in particular the normal vector  $n^\mu$  must be timelike for the evolution to proceed. Aside from this gradual build-up of errors, the algorithm has been found to perform well in practice and has not shown signs of instability.

The algorithm has been implemented in a one-dimensional form suitable for studying different slicings of planar cosmological models. In tests using simple spacetimes for which exact solutions

can be written with respect to two different coordinate systems (so that the values used for the lapse  $N$  are exact rather than the product of a numerical simulation) the code has been found to converge at the appropriate order (first or second, depending on which of the equations (5.6) or (5.7) is used). Results produced with the algorithm for non-standard slicings of a homogeneous cosmological model are presented in the next section; see in particular figure 5.3 there.

## 5.2 Harmonic Time Slicing and Coordinate Singularities

This section examines properties of the harmonic time slicing condition introduced in chapter 4 and considers its usefulness from the point of view of numerical relativity. A simple homogeneous cosmological model provides a focal point for this investigation, and analysis of the behaviour of harmonic slices of that spacetime makes use of some of the ideas presented in the previous section together with an analytic approach similar to that of Geyer and Herold (1995, 1997). (The latter makes extensive use of Bessel functions, and these are briefly reviewed as part of the discussion.) The results of this investigation suggest that coordinate singularities, much like those originally found by Alcubierre (1997), can develop under reasonably general conditions in numerical simulations which use harmonic time slicing, and some of the implications of this for numerical work are discussed.

### *On the Choice of Time Slicing Condition*

As discussed in chapter 4, most of the hyperbolic formulations of Einstein's equations which have been developed in recent years require a spacetime to be foliated according to a harmonic time slicing condition if the characteristic speeds of the equations are to coincide with physical speeds of the system. In this subsection some basic features of harmonic time slicing are considered.

Traditionally, work in numerical relativity has been based on maximal or constant mean curvature slicing conditions, initially developed for this purpose by Smarr and York (1978), York (1979), and Eardley and Smarr (1979), among others. A spatial slice has constant mean curvature if  $K$ , the trace of the extrinsic curvature tensor, takes a constant value on that slice, and if values for  $K$  are specified across a range of slices as a function of the time coordinate  $t$ , then the ADM evolution equation (4.4b) for the extrinsic curvature yields (when combined with the Hamiltonian constraint (4.3a)) an elliptic equation determining the value of the lapse function  $N$  on each slice:

$$\Delta N - N[K_{ij}K^{ij} + \frac{1}{2}\kappa(\rho + S)] = -K'(t), \quad (5.8)$$

where  $\Delta = h^{ij}\nabla_i\nabla_j$ . If the value of  $K$  is zero on a slice then that slice is described as maximal, and if the function  $K(t)$  is identically zero then the spacetime is maximally sliced. Maximal slicing has been found to work well in numerical simulations of asymptotically flat spacetimes, while for closed cosmologies (in which at most one maximal slice can exist) the more general constant mean curvature slicing condition is appropriate. Based on their behaviour in simple examples and their success in numerical simulations, it is believed that the maximal and constant mean curvature slicing conditions will in general produce foliations which cover most, if not all, of a spacetime

being investigated, and which at the same time avoid getting too close to any singularities that may form in that spacetime.

The generalized harmonic time slicing condition contrasts in several ways with the maximal and constant mean curvature conditions. The lapse function  $N$  in a harmonically sliced spacetime is determined either through an algebraic condition or a simple evolution equation, and not through an elliptic condition as in equation (5.8). This is advantageous from the point of view of implementing a numerical code to evolve solutions to Einstein's equations since elliptic partial differential equations are computationally very expensive to solve. The harmonic time slicing condition also differs from the maximal and constant mean curvature time slicing conditions in that it specifies a relationship between two adjacent slices in a foliation rather than determining properties of each individual slice: while an isolated spacetime slice can be characterized as maximal or of constant mean curvature, there is no such thing as an individual harmonic slice. One consequence of this is that the choice of lapse function on the initial slice of a foliation is arbitrary if the harmonic time slicing condition is used.

To simplify the discussion in this section, all spacetime foliations considered here are assumed to have shift vectors  $N^i$  which are identically zero; since the shift vector controls only the positioning of the spatial coordinates and not the slicing of a spacetime, this assumption does not limit the generality of the following discussion in any essential way. Recalling equations (4.8) and (4.9) of the previous chapter, the generalized harmonic time slicing condition can be expressed in either algebraic form,

$$N = Q(t, x^k) \sqrt{\det h_{ij}}, \quad (5.9)$$

or as an evolution equation,

$$\frac{\partial N}{\partial t} = N(\ln Q)_{,t} - N^2 K, \quad (5.10)$$

where the slicing density  $Q(t, x^i)$  is an arbitrary function of the spacetime coordinates. If the slicing density is independent of the time coordinate  $t$ , then the harmonic slicing is described as simple, and in this case a choice of the value of the lapse  $N$  on an initial slice completely determines the value of the slicing density  $Q$ . If the slicing density has only a simple dependence on the time coordinate,  $Q(t, x^i) = f(t)\bar{Q}(x^i)$ , then the foliation that develops has the same slices as the foliation produced by using  $\bar{Q}(x^i)$  as the slicing density, but with a different time coordinate labelling the slices. In general it is not obvious how a useful slicing density  $Q$  which has a non-trivial dependence on the time coordinate may be chosen, and so the simple form of harmonic slicing is most commonly used in practice; this point is returned to later in the section.

The main question addressed in this section is that of how suitable the harmonic time slicing condition is for numerical work. Several authors have already considered this question from various different viewpoints. Bona and Massó (1988) have shown that the (simple) harmonic time slicing condition can be used to foliate several standard spacetimes, and also that 'focusing singularities' are avoided by the slicing condition in much the same way as they are in maximally sliced spacetimes with the slices of the foliation not reaching the singularity in a finite coordinate time. (It should be noted that for a harmonically sliced spacetime a focusing singularity is essentially a point at which

the lapse  $N$  becomes zero—this is in contrast to the behaviour found at the ‘gauge pathologies’ described below.) Cook and Scheel (1997) have investigated the construction of well-behaved harmonic foliations for Kerr-Newmann black hole spacetimes, and present numerical evidence that (in the uncharged, spherically symmetric case) a particular time-independent harmonic foliation acts in some sense as an attractor to other harmonic foliations.

The work of Alcubierre (1997) and Alcubierre and Massó (1998) is of particular relevance to the present discussion. They have shown that ‘gauge pathologies’ (described as ‘coordinate shocks’ in the earlier paper) can occur in numerical simulations based on hyperbolic formulations of Einstein’s equations which use harmonic time slicing. (In fact, a range of gauge conditions are considered by the authors, with simple harmonic slicing—the only gauge choice of interest here—corresponding to the special case  $f = 1$  in their formulation. None of the alternative gauge choices they use corresponds to the generalized harmonic time slicing condition.) These gauge pathologies manifest as a loss of continuity at points in the evolved solution, with in particular large spikes appearing in the lapse. After the time at which the pathologies appear the numerical solution no longer converges at the expected order. Alcubierre and Massó explain the appearance of gauge pathologies in terms of nonlinear behaviour in the hyperbolic evolution equations; however this fails to adequately answer questions about how common the gauge pathologies are, what happens to the foliation at the points where pathologies appear, and what approaches can be used to prevent the pathologies from occurring.

Harmonic slicings for the Schwarzschild and Oppenheimer-Snyder spacetimes have been investigated by Geyer and Herold (1995, 1997). The approach they use is based on an alternative representation of equations (5.9) and (5.10) in the simple harmonic case: if  $T$  is a scalar function on a spacetime, the level surfaces of which represent the spatial slices of a foliation  $\{\Sigma_T\}$ , then the spacetime will be (simple) harmonically sliced if

$$\square T \equiv g^{\mu\nu} \nabla_\mu \nabla_\nu T = 0. \quad (5.11)$$

(This equation explains, of course, how the harmonic slicing condition acquires its name.) No simple analogue of equation (5.11) exists for the generalized harmonic time slicing condition. By numerically integrating equation (5.11) with respect to known background metrics, Geyer and Herold construct simple harmonic slicings which they compare to maximal slicings of the spacetimes. Some properties of a slicing can be determined straightforwardly from its time function  $T$ , and in particular the lapse  $N$  can be evaluated through the equation

$$g^{\mu\nu} (\nabla_\mu T)(\nabla_\nu T) = -1/N^2, \quad (5.12)$$

where it is clear that the vector field normal to the foliation must remain timelike if the lapse is to have a positive real value. In fact, Geyer and Herold (1997) find that for simple harmonic slicings of the Oppenheimer-Snyder spacetime, foliations which are initially timelike can at later times become null or spacelike, with the development of the foliation thus terminating at a coordinate singularity. The lapse becomes infinite as these singular points are reached, and this is consistent with the behaviour found at the gauge pathologies of Alcubierre and Massó.

In the present work equations (5.11) and (5.12) are used to investigate the formation of coordinate singularities in simple harmonic slicings of cosmological models. The following approach is employed. The metric  $g_{\mu\nu}$  of the spacetime being investigated is assumed to be known with respect to a coordinate system  $(t, x, y, z)$ . An alternative foliation of the spacetime is constructed by taking as an initial slice one of the constant time hypersurfaces of the background coordinate system: the foliation time coordinate  $T(t, x, y, z)$  is given an initial value

$$T(t_0, x, y, z) = t_0, \quad (5.13)$$

for some value  $t_0$  of the coordinate  $t$ . (It is assumed here that the hypersurface  $t = t_0$  is spacelike.) The lapse function of the foliation can be specified arbitrarily on the initial slice (subject to the requirement that it be positive), and this determines via equation (5.12) the value of the first derivative of  $T$  away from that slice:

$$T_{,t}(t_0, x, y, z) = \frac{1}{N_0(x, y, z)\sqrt{-g^{00}(t_0, x, y, z)}}. \quad (5.14)$$

Equations (5.13) and (5.14) provide initial data for the wave equation (5.11), and the solution  $T$  describes a new simple harmonic slicing of the spacetime.

This method for locating the slices of a foliation with respect to a background coordinate system is very similar to the algorithm presented in the previous section for integrating the world lines of coordinate observers, and both methods can be useful in investigating the formation of coordinate singularities in harmonic slicings. The advantage of using equation (5.11) is its simplicity: analytic solutions can be found in some cases, and when this is not possible numerical methods are straightforward to apply. However the method has the drawback that it provides no information about the spatial coordinates describing the slices of the foliation; these can only be found by the integration of world lines. Furthermore, equation (5.11) is only applicable in the case of simple harmonic time slicing whereas the approach of section 5.1 can be used for arbitrary slicing conditions. Results for both of the methods are compared later in this section.

As an example of how equation (5.11) can be used to find coordinate singularities, consider harmonic foliations of the Minkowski spacetime, written in standard coordinates as

$$g_{\mu\nu}dx^\mu dx^\nu = -dt^2 + dx^2 + dy^2 + dz^2.$$

Suppose that a ‘planar’ slicing of the spacetime is constructed such that the time function  $T$  depends only on the Minkowski coordinates  $t$  and  $x$ . Then equation (5.11) takes the form of the one-dimensional wave equation

$$T_{,tt} = T_{,xx},$$

and, as is well known, this has the general solution

$$T(t, x) = f(t + x) + h(t - x),$$

for arbitrary functions  $f(u)$  and  $h(u)$ . The lapse associated with this time function can be found from equation (5.12):

$$\begin{aligned} -1/N^2 &= -T_{,t}^2 + T_{,x}^2 \\ &= -4f'(t+x)h'(t-x), \end{aligned}$$

and the lapse will be well behaved as long as the function  $f'(t+x)h'(t-x)$  is positive. For most problems the next step in the analysis would be to use equations (5.13) and (5.14) to specify a value for the lapse on an initial slice of the foliation; however the present case is sufficiently simple that the appearance of coordinate singularities can be studied without needing to specify an initial slice. If the lapse becomes infinite at a point in the foliation then the function  $f'(t+x)h'(t-x)$  must be zero there, and it is clear that the function must then be zero at all points along a line  $t+x = \text{constant}$  or  $t-x = \text{constant}$ . Consequently, any spacelike slice of that foliation must include a point in it at which the lapse is infinite. It follows that for simple harmonic time slicings of the ‘planar’ Minkowski spacetime no coordinate singularities will be present provided that the initial slice of the foliation is everywhere spacelike. (This result is consistent with the numerical simulations of Minkowski spacetime reported on in Alcubierre 1997. No gauge pathologies are discovered there for ‘planar’ harmonic slicings of flat spacetime, although they are found in the spherically symmetric case.)

The remaining part of this section considers the appearance of coordinate singularities in harmonic slicings of the homogeneous Kasner cosmological model. Analysis of the foliation equation (5.11) in this case makes use of Bessel functions, and these are briefly reviewed in the next subsection.

### *Some Properties of Bessel Functions*

At various points in this and the following chapters Bessel functions are used to solve equations describing aspects of homogeneous and inhomogeneous cosmologies, and for convenience the present subsection summarizes some of their basic properties. A complete exposition of Bessel functions can be found in chapter 9 of Abramowitz and Stegun 1964.

The Bessel functions of the first kind,  $J_\nu(t)$ , and the second kind,  $Y_\nu(t)$ , are solutions to the differential equation

$$t^2 \frac{d^2 A}{dt^2} + t \frac{dA}{dt} + (t^2 - \nu^2)A = 0 \quad (5.15)$$

for  $A(t)$ . While the argument  $t$  and the order  $\nu$  may be complex in general, for the present work it suffices to consider only real values with  $t$  being positive and  $\nu$  being non-negative.

The derivatives of the Bessel functions are

$$J'_\nu(t) = -J_{\nu+1}(t) + (\nu/t)J_\nu(t), \quad (5.16a)$$

$$Y'_\nu(t) = -Y_{\nu+1}(t) + (\nu/t)Y_\nu(t), \quad (5.16b)$$

and the following identities prove to be useful,

$$J_{\nu-1}(t) + J_{\nu+1}(t) = (2\nu/t)J_\nu(t), \quad (5.17a)$$

$$Y_{\nu-1}(t) + Y_{\nu+1}(t) = (2\nu/t)Y_\nu(t), \quad (5.17b)$$



together with

$$J_{\nu+1}(t)Y_\nu(t) - J_\nu(t)Y_{\nu+1}(t) = \frac{2}{\pi t}. \quad (5.18)$$

The asymptotic expansions of the Bessel functions for large values of the argument  $t$  are

$$J_\nu(t) = \sqrt{\frac{2}{\pi t}} \left( P(t) \cos \Phi(t) - Q(t) \sin \Phi(t) \right), \quad (5.19a)$$

$$Y_\nu(t) = \sqrt{\frac{2}{\pi t}} \left( P(t) \sin \Phi(t) + Q(t) \cos \Phi(t) \right), \quad (5.19b)$$

where

$$\begin{aligned} \Phi(t) &= t - \left(\frac{1}{2}\nu + \frac{1}{4}\right)\pi, \\ P(t) &\sim 1 - \frac{(4\nu^2 - 1)(4\nu^2 - 9)}{128t^2} + O(t^{-4}), \\ Q(t) &\sim \frac{(4\nu^2 - 1)}{8t} + O(t^{-3}), \end{aligned}$$

and to leading order these yield very useful approximations:

$$J_\nu(t) \sim \sqrt{\frac{2}{\pi t}} \cos\left(t - \left[\frac{1}{2}\nu + \frac{1}{4}\right]\pi\right) + O(t^{-3/2}), \quad (5.20a)$$

$$Y_\nu(t) \sim \sqrt{\frac{2}{\pi t}} \sin\left(t - \left[\frac{1}{2}\nu + \frac{1}{4}\right]\pi\right) + O(t^{-3/2}). \quad (5.20b)$$

As the argument  $t$  approaches zero the Bessel functions of the first kind behave as

$$J_\nu(t) \sim \frac{(t/2)^\nu}{\Gamma(\nu+1)} + O(t^{\nu+2}), \quad (5.21a)$$

so that  $J_0(0) = 1$  and  $J_\mu(0) = 0$  for  $\mu > 0$ . In addition,  $|J_\nu(t)| \leq 1$  for all  $\nu$  and  $t$ . The Bessel functions of the second kind diverge as  $t$  tends to zero, and for orders zero and one the asymptotic forms are

$$Y_0(t) \sim (2/\pi)[\ln(t/2) + \gamma] + O(t^2 \ln t), \quad (5.21b)$$

$$Y_1(t) \sim -2/(\pi t) + O(t \ln t), \quad (5.21c)$$

for the constant  $\gamma \simeq 0.577$ .

Values of the Bessel functions can be calculated numerically using standard procedures in mathematical software packages and programming libraries; see also chapter 6 of Press et al. 1992.

### *Harmonic Slicings of the Kasner Spacetime I: An Analytic Approach*

In this subsection equation (5.11) is used to construct simple harmonic foliations of the Kasner spacetime, with the main point of interest being the question of whether or not coordinate singularities (gauge pathologies in the terminology of Alcubierre and Massó 1998) form in the slicings. The next subsection compares these results to numerical simulations of the spacetime.

The Kasner cosmological models are described in most standard references (see, for example, chapter 30 of Misner, Thorne and Wheeler 1973) and the present work uses the axisymmetric model described by the metric

$$ds^2 = t^{-1/2}(-dt^2 + dx^2) + t(dy^2 + dz^2). \quad (5.22)$$

This spacetime is vacuum and explicitly homogeneous, and features a cosmological singularity at time  $t = 0$ . The form of the metric used here is in fact the expanding version (6.5) of the Gowdy  $T^3$  metric studied in chapter 6 with variables  $P$ ,  $Q$  and  $\lambda$  all taken to be identically zero. The connection between the homogeneous model (5.22) and the inhomogeneous cosmologies of chapters 6 and 7 is further strengthened by imposing a three-torus spatial topology on the Kasner spacetime: periodicity is assumed in each of the coordinates  $x$ ,  $y$  and  $z$  over the range  $[0, 2\pi)$ .

As in the simple example for the Minkowski spacetime given earlier in this section, here ‘planar’ slicings of the Kasner spacetime are considered for which the time function  $T$  depends only on the coordinates  $t$  and  $x$ . A straightforward calculation of connection coefficients then shows that for the metric (5.22), equation (5.11) for the time function of a harmonically sliced foliation is equivalent to

$$T_{,tt} - T_{,xx} + t^{-1}T_{,t} = 0. \quad (5.23)$$

This equation can be solved by decomposing  $T$  spatially as a sum of Fourier modes (recalling that, since the model is spatially closed, the function  $T$  must be periodic in the coordinate  $x$ ) and the general solution is found to be

$$T = a_0 \ln t + b_0 + \sum_{n=1}^{\infty} \left( Z_{+n}(t) \cos(nx) + Z_{-n}(t) \sin(nx) \right), \quad (5.24)$$

with  $Z_{\pm n}(t) = a_{\pm n} J_0(|n|t) + b_{\pm n} Y_0(|n|t)$  for  $n \neq 0$ ,

where  $a_{\pm n}$  and  $b_{\pm n}$  are constants, and the Bessel functions  $J_0$  and  $Y_0$  are discussed in the previous subsection.

Equation (5.12) for the lapse function  $N$  of the foliation can be written in the present case as

$$\sqrt{t}(T_{,t}^2 - T_{,x}^2) = 1/N^2, \quad (5.25)$$

and the requirement that the foliation be well behaved can then be expressed as

$$T_{,t} > |T_{,x}|, \quad (5.26)$$

where it is assumed that the orientation of the time function  $T$  of the foliation is the same as that of the Kasner time  $t$ , and thus that  $T_{,t}$  is positive. If the time function  $T$  of equation (5.24) fails to satisfy the condition (5.26) at a point, then the harmonic slicing must have a coordinate singularity there.

The constants  $a_{\pm n}$  and  $b_{\pm n}$  in equation (5.24) can be determined by specifying a value  $N_0(x)$  for the lapse on an initial hypersurface  $t = t_0$  as in equations (5.13) and (5.14). In fact, rather than choosing the initial value for the lapse directly, it proves to be more convenient to choose instead an initial value  $I(x)$  for the time derivative of  $T$ , with this being specified as a Fourier sum,

$$T_{,t}(t_0, x) = I(x) \equiv k_0 + \sum_{n=1}^{\infty} \left( k_{+n} \cos(nx) + k_{-n} \sin(nx) \right), \quad (5.27)$$

where the constants  $k_{\pm n}$  must be such that  $I(x)$  is everywhere positive. The value of the lapse on the initial slice can then be determined through equation (5.14):

$$N_0(x) = \frac{1}{t_0^{1/4} I(x)}. \quad (5.28)$$

The particular time function  $T$  of equation (5.24) which fits the initial data of equations (5.13) and (5.27) is then found to be

$$T = t_0 + k_0 t_0 \ln(t/t_0) - \frac{\pi t_0}{2} \sum_{n=1}^{\infty} \left( J_0(nt) Y_0(nt_0) - Y_0(nt) J_0(nt_0) \right) \left( k_{+n} \cos(nx) + k_{-n} \sin(nx) \right). \quad (5.29)$$

The simplest harmonic foliations of the Kasner metric (5.22) are the homogeneous ones for which the time function  $T$  is independent of the coordinate  $x$ . Then, to within a linear rescaling, the function  $T$  equals the logarithm of  $t$ , and so the cosmological singularity in the spacetime occurs in the harmonic foliation only in the limit as  $T$  tends to negative infinity. Clearly the foliation covers the entire Kasner spacetime and (as can be seen from equation (5.26)) contains no coordinate singularities.

The behaviour of homogeneous harmonic slicings is, however, not representative of the general inhomogeneous case, as is demonstrated below. As an example, figure 5.2 shows the foliation which results from setting the lapse on the initial slice to be

$$N_0(x) = \frac{1}{1 + \frac{1}{2} \sin x} \quad \text{for } t_0 = 1, \quad (5.30)$$

which corresponds to the choice of coefficients  $k_0 = 1$  and  $k_{-1} = 1/2$  (the others being zero) in equation (5.27). When equation (5.25) is evaluated to determine the lapse on this foliation, it is found that in some spacetime regions to the future of the initial slice the quantity  $1/N^2$  is non-positive; the right-hand plot of figure 5.2 is filled in where this happens. Coordinate singularities must appear in any slices of the foliation which intersect these regions, and the development of the foliation cannot proceed beyond a time  $T = T_{\text{sing}} \simeq 2.45$  with the lapse  $N$  tending to infinity at points as the limiting slice is approached. In contrast, if the foliation is extended backwards in time from the initial slice towards the cosmological singularity, then the lapse appears to be well behaved on all of the slices.

It can in fact be shown that, in general, harmonic foliations of the Kasner spacetime always develop coordinate singularities at sufficiently late (future) times. From equation (5.29) it follows that

$$T_{,t} = \frac{\pi t_0}{2} \sum_{n=1}^{\infty} n \left( J_1(nt) Y_0(nt_0) - Y_1(nt) J_0(nt_0) \right) \left( k_{+n} \cos(nx) + k_{-n} \sin(nx) \right) + \frac{k_0 t_0}{t}, \quad (5.31a)$$

$$T_{,x} = \frac{\pi t_0}{2} \sum_{n=1}^{\infty} n \left( J_0(nt) Y_0(nt_0) - Y_0(nt) J_0(nt_0) \right) \left( k_{+n} \sin(nx) - k_{-n} \cos(nx) \right), \quad (5.31b)$$

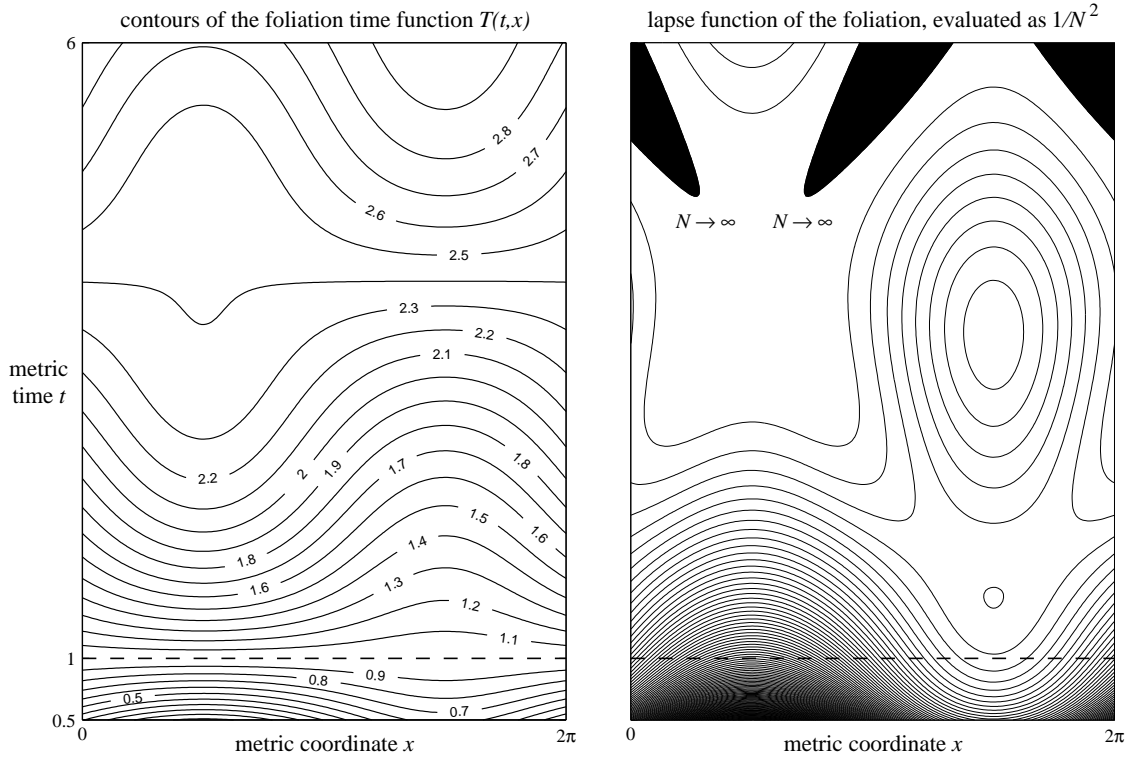


**Figure 5.2:** A simple harmonic foliation and its lapse function as seen in the background Kasner metric. The initial slice of the foliation coincides with the  $t = 1$  hypersurface of the metric (5.22) and is given an inhomogeneous initial lapse by equation (5.30). The time function  $T$  for the foliation, and its lapse  $N$ , are evaluated numerically from equations (5.29) and (5.25), and are presented as contour plots with respect to the coordinates  $(t, x)$  of the original metric. The left-hand plot shows level surfaces of the time function  $T$  which represent slices of the foliation. The dashed line marks the position of the initial slice. The right-hand plot shows evenly spaced contours of the function  $1/N^2$  for the foliation as determined through equation (5.25). The filled-in regions at the top of the plot show where  $1/N^2$  ceases to be a positive function, and thus where coordinate singularities must appear in the slices of the foliation.

and the first of these expressions can be written for a fixed spatial coordinate  $x = x_0$  as

$$T_{,t}(t, x_0) = \frac{\pi t_0}{2} \sum_{n=1}^{\infty} n c_n \left( J_1(nt) Y_0(nt_0) - Y_1(nt) J_0(nt_0) \right) + \frac{k_0 t_0}{t},$$

where it is assumed that the value  $x_0$  has been chosen such that at least one of the constants  $c_n$  is non-zero. For sufficiently large values of the coordinate  $t$ , the approximations (5.20) can be applied to the Bessel functions in this equation for  $T_{,t}$  with the result (which disregards the possibility of convergence problems occurring when the summation is over an infinite number of modes)

$$\begin{aligned} T_{,t}(t, x_0) &\simeq \frac{k_0 t_0}{t} + \sqrt{\frac{\pi}{2t}} t_0 \sum_{n=1}^{\infty} \sqrt{n} c_n \left( Y_0(nt_0) \cos\left(nt - \frac{3}{4}\pi\right) - J_0(nt_0) \sin\left(nt - \frac{3}{4}\pi\right) \right) \\ &= \frac{k_0 t_0}{t} + \frac{\Theta(t)}{\sqrt{t}}, \end{aligned}$$

where  $\Theta(t)$  is a periodic function which (by consideration of its Fourier decomposition) can be seen to take both positive and negative values. It then follows that, for some sufficiently large value of the coordinate  $t$ , the value of  $T_t$  must be negative at a point. Since this violates the condition (5.26), it must be the case that a coordinate singularity is present in the foliation.

The above argument shows that coordinate singularities must in general appear in harmonic slicings of an expanding Kasner cosmology but gives no indication of how much of the spacetime a slicing will cover before it becomes pathological. To investigate this, consider the simple case of a time function  $T$  from equation (5.29) which, like the foliation produced by the initial data (5.30), contains only one non-trivial mode:

$$T = t_0 + k_0 t_0 \ln(t/t_0) - k \frac{\pi t_0}{2} \left( J_0(nt) Y_0(nt_0) - Y_0(nt) J_0(nt_0) \right) \sin(nx), \quad (5.32)$$

where  $0 < k < k_0$ . For a fixed value of the Kasner time  $t$  the foliation will be well behaved (in that condition (5.26) is satisfied) if and only if

$$\frac{k_0 t_0}{t} > \frac{kn\pi t_0}{2} \max_x \left\{ |A(t) \cos(nx)| - B(t) \sin(nx) \right\},$$

where

$$A(t) = J_0(nt) Y_0(nt_0) - Y_0(nt) J_0(nt_0),$$

$$B(t) = J_1(nt) Y_0(nt_0) - Y_1(nt) J_0(nt_0),$$

and this condition is equivalent to

$$F(t) \equiv t^2 [A(t)^2 + B(t)^2] < \left( \frac{2k_0}{kn\pi} \right)^2. \quad (5.33)$$

It is straightforward to show (using the formulae from the previous subsection) that  $F'(t) \geq 0$ . Furthermore, if the time  $t$  is assumed to be sufficiently large that the approximations (5.20) can be applied to  $A(t)$  and  $B(t)$ , then  $F(t) \simeq t \Pi(t)$  where  $\Pi(t)$  is a positive, periodic function. An estimate of the time  $t = t_{\text{sing}}$  at which a coordinate singularity develops can then be seen to obey

$$t_{\text{sing}} \propto (k_0/k)^2, \quad (5.34)$$

and so, for a harmonic slicing which is perturbed from homogeneity by a single mode of amplitude  $k$ , the amount of the spacetime covered by the slicing becomes infinite as  $k$  tends to zero.

Considering now the behaviour of the slicing in the region of spacetime between the initial slice and the cosmological singularity, it follows from equation (5.33) that, for the single mode case, coordinate singularities never appear. To see this, note that the function  $F(t)$  must satisfy the inequality at time  $t = t_0$  since the lapse is required to be well behaved on the initial slice, and since it is an increasing function of time it must then also satisfy the inequality at all earlier times. Moreover, it can be seen from equation (5.32) together with the equations (5.21) that in the limit as  $t$  tends to zero while  $x$  remains constant, the time function  $T$  must have the form

$$T \sim t_0 [k_0 + k J_0(nt_0) \cos(nx)] \ln t + (\text{terms that tend to a constant}), \quad (5.35)$$

and since the factor multiplying the logarithm is always positive, the value of  $T$  must tend to negative infinity as the cosmological singularity is approached. Thus a single mode harmonic slicing will always cover the whole of the Kasner spacetime to the past of the initial slice.

Returning to the general case in which an arbitrary number of modes are present in the time function  $T$ , the above argument can be used to derive a simple condition on the initial data (5.27) which ensures that a slicing is well behaved in the region of spacetime between the initial slice and the cosmological singularity. Suppose that equation (5.29) is split up as

$$T = t_0 + \sum_{n=1}^{\infty} \left( T^{(+n)} + T^{(-n)} \right), \quad (5.36)$$

where

$$\begin{aligned} T^{(+n)} &= k_0^{(+n)} t_0 \ln(t/t_0) - k_{+n} \frac{\pi t_0}{2} \left( J_0(nt) Y_0(nt_0) - Y_0(nt) J_0(nt_0) \right) \cos(nx), \\ T^{(-n)} &= k_0^{(-n)} t_0 \ln(t/t_0) - k_{-n} \frac{\pi t_0}{2} \left( J_0(nt) Y_0(nt_0) - Y_0(nt) J_0(nt_0) \right) \sin(nx), \end{aligned}$$

and the values  $k_0^{(\pm n)}$  are arbitrary subject to the condition

$$\sum_{n=1}^{\infty} \left( k_0^{(+n)} + k_0^{(-n)} \right) = k_0.$$

The condition (5.26) will then certainly be satisfied if

$$T^{(+n)}_{,t} > |T^{(+n)}_{,x}| \quad \text{and} \quad T^{(-n)}_{,t} > |T^{(-n)}_{,x}| \quad \text{for all } n,$$

and as the analysis of the single mode case shows, this will be true for  $0 < t < t_0$  if it is true for  $t = t_0$ . The time derivative of each function  $T^{(\pm n)}$  must therefore be positive on the initial hypersurface  $t = t_0$ , and for this to be the case the values  $k_0^{(\pm n)}$  must be chosen such that

$$k_0^{(+n)} > |k_{+n}| \quad \text{and} \quad k_0^{(-n)} > |k_{-n}| \quad \text{for all } n.$$

This can always be done if

$$k_0 > \sum_{n=1}^{\infty} \left( |k_{+n}| + |k_{-n}| \right), \quad (5.37)$$

and so any initial value for the lapse which satisfies this condition must produce a foliation which is free of coordinate singularities to the past of the initial slice. In addition to this, if the behaviour of the time function  $T$  is considered as  $t$  tends to zero, then it is straightforward to show (in analogy with equation (5.35) for the single mode case) that condition (5.37) ensures that  $T$  tends to negative infinity for all values of  $x$  as the cosmological singularity is approached, and hence that the foliation covers all of the spacetime up to the singularity. The condition (5.37) on the initial lapse is sufficient but not necessary for the harmonic foliation to be well behaved to the past of the initial slice; in fact, experimentation with different choices of initial data (5.27) suggests that, even when condition (5.37) is not satisfied, harmonic foliations may never develop coordinate singularities as the cosmological singularity is approached, although no proof (or disproof) of this has yet been constructed.

To summarize the above results, foliations of the Kasner spacetime (5.22) based on the simple harmonic slicing condition (5.11) have been investigated under the assumptions that one slice of the foliation coincides with a  $t = \text{constant}$  hypersurface of the original metric, and that the foliation is independent of two of the standard spatial coordinates. It is found that when the Kasner cosmology is expanding, the slices of the foliation must eventually develop coordinate singularities, with this happening at late times for foliations which are initially close to homogeneous. In contrast, when the Kasner cosmology is collapsing, the results suggest that coordinate singularities never develop in the foliation and that the slices extend all the way to the cosmological singularity. (This is certainly true if the lapse on the initial slice is chosen such that the coefficients of equation (5.27) satisfy the condition (5.37), and it may in fact be the case for all reasonable choices of initial lapse.)

The behavioural differences found in harmonic foliations according to whether the Kasner spacetime is expanding or collapsing can be explained by considering the relationship between the lapse function  $N$  and the mean curvature  $K$  of the slicing. In any foliation, the mean curvature provides a measure of the local convergence of world lines running normal to the spatial slices:

$$K = -\nabla_\mu n^\mu = -\mathcal{L}_n(\ln \sqrt{\det h_{ij}}),$$

where  $n^\mu$  is the vector normal to the slices,  $\mathcal{L}_n$  is the Lie derivative along that vector, and  $\sqrt{\det h_{ij}}$  is the spatial volume element. The value of  $K$  is positive when the foliation world lines are locally converging, and negative when they are expanding. The harmonic time slicing condition can be written in terms of the mean curvature of the foliation using equation (5.10):

$$\frac{\partial(1/N)}{\partial t} = K,$$

where it is assumed here that the shift vector  $N^i$  of the foliation is zero, and that the harmonic slicing is of the simple type ( $Q_{,t} = 0$ ). It then follows that when the mean curvature  $K$  is positive (as it may be expected to be for slices of a collapsing cosmology) the value of  $1/N$  will increase, and so the lapse will approach (but usually not reach) zero. (The ability of the harmonic slicing condition to avoid ‘focusing’ singularities at which the lapse vanishes is discussed in Bona and Massó 1988.) Conversely, when the mean curvature is negative (as it typically will be in an expanding spacetime) the value of  $1/N$  will decrease, and if it reaches zero then a coordinate singularity of the type investigated in this subsection will develop in the foliation.

### *Harmonic slicings of the Kasner Spacetime II: Numerical Implications*

The results of the previous subsection show that coordinate singularities are a generic feature of harmonic foliations of the expanding axisymmetric Kasner cosmology. It follows then that numerical simulations of that spacetime which use the harmonic slicing condition will be forced to terminate after a finite number of time steps, regardless of their accuracy, and the practical details of this are examined in the present subsection. Some of the methods for comparing spacetime slicings described in section 5.1 are put into practice here, and the implications of these results for numerical simulations of other spacetimes are discussed.

In chapter 4 a computer code for numerically evolving solutions to the vacuum Einstein equations is described. Here the code is used to evolve initial data for the Kasner spacetime given by the metric (5.22) using the harmonic time slicing condition and the initial value (5.30) for the lapse. The foliation of the Kasner spacetime which results is the one pictured in figure 5.2, and the numerical simulation thus allows the prediction made in the previous subsection—that coordinate singularities prevent the foliation from developing beyond a time  $T = T_{\text{sing}} \simeq 2.45$ —to be verified. The metric variables (4.10) evolved by the code are given homogeneous initial values appropriate to a slice  $t = t_0$  of the metric (5.22):

$$\begin{aligned} h^{11} &= t_0^{1/2}, & h^{22} &= h^{33} = t_0^{-1}, \\ P^{11} &= t_0^{-1/4}, & P^{22} &= P^{33} = \frac{1}{4}t_0^{-7/4}, \end{aligned} \quad \text{for } t_0 = 1, \quad (5.38)$$

with the other variables all being initially zero. The initial value of the lapse is given the inhomogeneous form of equation (5.30) by setting the slicing density of the foliation to be

$$Q(T, X, Y, Z) = \frac{t_0^{-3/4}}{1 + \frac{1}{2} \sin X}, \quad (5.39)$$

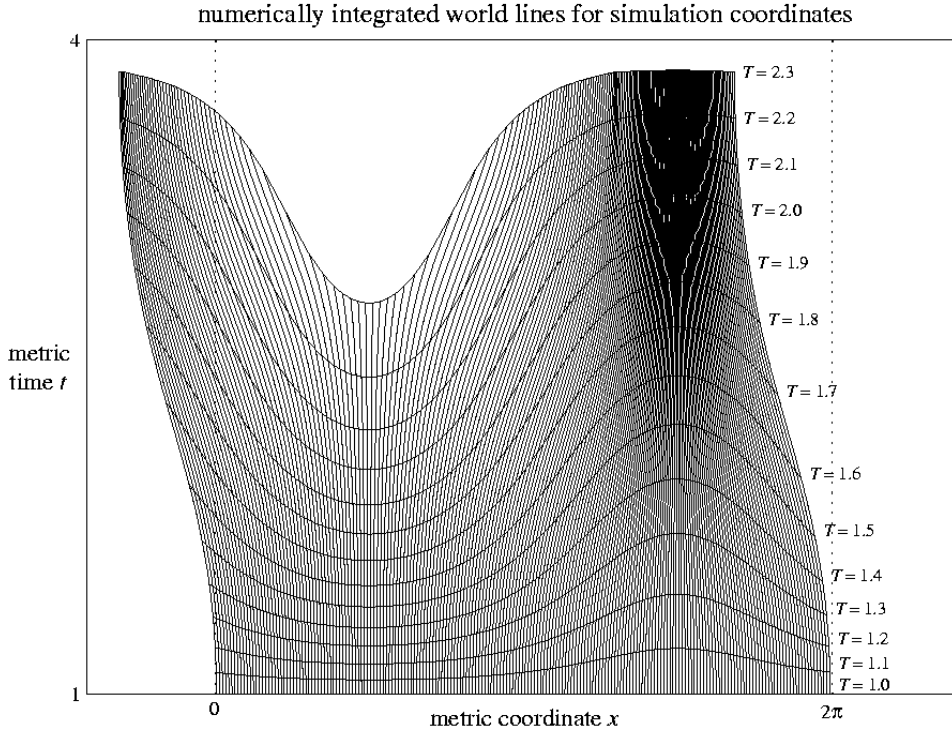
where  $(T, X, Y, Z)$  is the coordinate system of the numerical simulation, and is distinct from the coordinate system  $(t, x, y, z)$  of the original Kasner metric, except on the initial slice which is labelled  $T = t_0$  and on which  $(X, Y, Z) = (x, y, z)$ . The shift vector  $N^i$  is taken to be zero throughout the simulation, and the lack of dependence of the slicing density  $Q$  on the foliation time  $T$  then means that the harmonic slicing is of the simple type. Since all of the quantities involved in the numerical simulation are independent of the spatial coordinates  $Y$  and  $Z$ , the evolved spacetime in effect has a planar symmetry, and a one-dimensional grid with a cell size  $\Delta X = 2\pi/200$  is used to discretize the spatial domain. The adaptive mesh refinement capabilities of the code are described in chapter 3, and are used here to allow the local resolution of the simulation to increase as needed to a maximum of  $\Delta X = 2\pi/3200$ .

Figure 5.3 plots the  $(T, X)$  coordinate system of the numerical simulation as it appears in the  $(t, x)$  coordinates of the homogeneous background metric. This comparison between coordinate systems is made using the algorithm described in section 5.1 for tracking the positions  $p^\mu$  of the observers at rest in the slices of a foliation, and is based on the values  $N(T, X)$  taken by the lapse during the course of the simulation. The observers are positioned at the centres of the cells in the simulation grid, and their initial positions with respect to the  $(t, x)$  coordinates are

$$p^\mu|_j^0 = (t, x)|_j^0 = (t_0, X_0 + j \Delta X).$$

The observer world lines are plotted up until a simulation time  $T = 2.3$ ; although the inaccuracies in the numerical solution which are present at that time are not sufficient to stop the simulation, they do make it increasingly difficult to accurately track the positions of the observers. The  $T = \text{constant}$  surfaces reconstructed in figure 5.3 can be seen to be in good agreement with the exact results shown in the left-hand plot of figure 5.2.





**Figure 5.3:** Coordinate world lines for a numerical simulation as seen in the background Kasner metric. The homogeneous initial data set (5.38) is numerically evolved using harmonic slicing based on the inhomogeneous gauge function (5.39), and the world lines of the simulation’s grid points are tracked relative to the coordinate system  $(t, x)$  of the background metric (5.22) using the algorithm described in section 5.1. Two hundred grid points are evenly spaced on the  $t = 1$  hypersurface of the background metric at the initial simulation time  $T = 1$ , and the paths they subsequently follow are plotted up until the end of the simulation at time  $T = 2.3$ . Periodicity of the spatial domain means that observers who ‘go off’ at  $x = 0$  will ‘come on’ at  $x = 2\pi$ . This figure is to be compared with the left-hand plot of figure 5.2.

The analysis of the previous subsection (as presented in figure 5.2) shows that at a time  $T = T_{\text{sing}} \simeq 2.45$  the lapse  $N$  must become infinite at points of the evolved foliation. The left-hand plot of figure 5.4 shows the actual value taken by the lapse at the earlier time  $T = 2.3$  in the simulation, and it can be seen that two sharp spikes are already present in the solution. As the evolution progresses these spikes grow in size, and if the evolved solution were exact they would reach infinite heights within a short time. As they grow, the two spikes also narrow and become closer together. The reason for this can be seen from the paths of the coordinate observers plotted in figure 5.3: in the region  $0 < x < \pi$  where the coordinate singularities eventually form, the world lines normal to the foliation are diverging (with respect to the background coordinates), and so the region is resolved by a diminishing number of grid points. It should be noted that this divergence of observers is not itself the cause of the coordinate singularities; it could in principle be counteracted by an appropriate choice of shift vector for the foliation, but this would not prevent the lapse

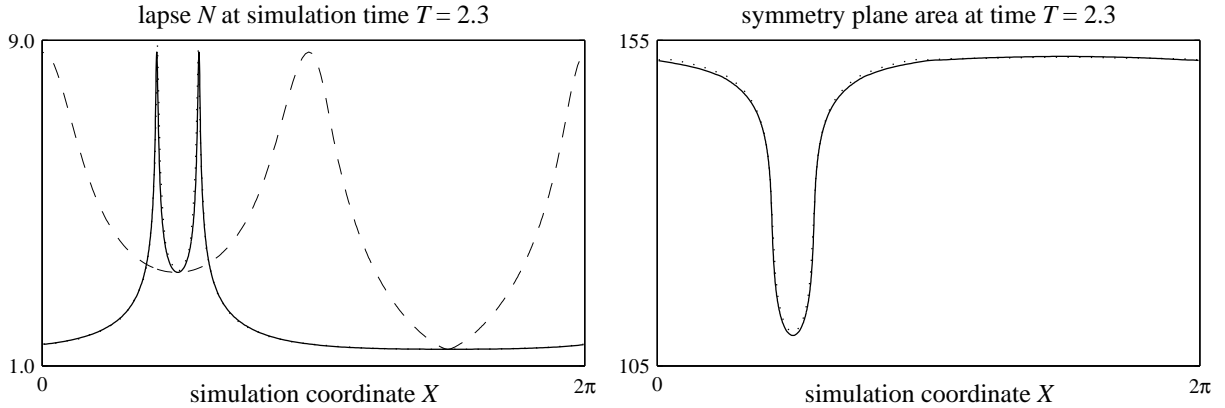


**Figure 5.4:** The lapse and the symmetry plane area for a numerical simulation of an inhomogeneously sliced Kasner spacetime. The quantities plotted here as solid lines are evaluated based on the evolved variables at the final time of the simulation shown in figure 5.3. Dotted lines in the plots show the same quantities evaluated indirectly using the final positions  $p^\mu(X) = (t, x)$  estimated for the simulation grid points with respect to the known metric (5.22). The simple relation (5.40) between the coordinate  $t$  and the symmetry plane area allows an alternative approximation for the latter to be calculated, while an alternative value for the lapse can be estimated from the positions  $p^\mu$  together with the data plotted in the second half of figure 5.2. The dashed line in the left-hand plot shows the lapse as a function of proper distance along the  $X$ -axis rather than coordinate distance. (The measure of proper distance is rescaled to be consistent with the horizontal axis of the plot.)

from becoming infinite. The narrowing and effective coalescence of the spikes is problematic for the simulation since features which are smaller than the grid spacing  $\Delta X$  cannot be accurately resolved, and while the adaptive mesh refinement capabilities of the numerical code prove to be very effective in extending the useful running time of the simulation, eventually the numerical solution fails to accurately model the behaviour of the exact solution. In fact, with the spikes being inadequately resolved, the evolved value of the lapse fails to become infinite (or even the computer representation of this) as the coordinate singularities are reached, and it is possible for the simulation to continue beyond the time at which the slices of the foliation cease to be spacelike in the exact solution. However, as pointed out by Alcubierre and Massó (1998), the numerical solution has no physical meaning past the points at which coordinate singularities form, and in particular it will no longer converge as the grid is refined.

A check on the accuracy of both the numerical solution produced by the simulation and the world line reconstruction shown in figure 5.3 can be made by utilizing some of the ideas presented in section 5.1. For a spatially closed spacetime with planar symmetry (which for the purposes of the present discussion the inhomogeneously sliced Kasner cosmology is taken to be), the proper area of the symmetry plane defines a scalar field on the spacetime. For the metric (5.22) this can be seen to take the value

$$\text{proper area of } y\text{-}z \text{ symmetry plane} = 4\pi^2 t. \quad (5.40)$$

A value for the area can also be readily calculated from the metric components at any point  $(T, X)$  of a numerically evolved solution, in which case equation (5.40) can be used to determine how much of the Kasner spacetime the simulation has covered. The right-hand plot of figure 5.4 shows two values calculated for the symmetry plane area at a fixed time in the simulation: one of the values is calculated directly from the metric variables evolved by the simulation, while the other is calculated by substituting the observer positions plotted in figure 5.3 into the equation (5.40). The two values can be seen to be in good agreement. (Figure 5.4 also shows an alternative value for the lapse calculated in a similar though more convoluted manner by using the observer positions of figure 5.3 to evaluate the exact expression (5.25). Again, good agreement with the evolved value is seen.)

The spikes that develop in the lapse function as the coordinate singularities are approached are at face value very similar to some features that are seen in numerical solutions for collapsing inhomogeneous cosmologies, as studied in chapters 6 and 7 (see for example figure 6.1). The question then arises as to whether the features seen in the inhomogeneous cosmologies have any physical relevance or whether they are, like the features in the Kasner simulation, entirely a coordinate effect. While a full investigation of this point is postponed until the following chapter, a comment is worth making here about the nature of the spikes seen in the lapse in figure 5.4. If the metric component  $h_{11}$ , which measures the proper distance in the  $X$ -direction of the simulation, is examined for the data plotted in figure 5.4, it is found that sharp spikes (towards positive infinity) are coincident there with the spikes in the lapse, and hence that the apparently narrow spikes are in fact spread over large physical distances. As the dashed line in figure 5.4 demonstrates, if instead of being plotted against the coordinate  $X$ , the lapse is shown as a function of the proper distance along the  $X$ -axis, then the spikes no longer appear as notable features of the solution.

One of the main conclusions of the present section is that coordinate singularities can appear in numerical simulations which use the simple harmonic time slicing condition under reasonably general circumstances (seemingly whenever the foliation locally undergoes a protracted period of expansion). As was shown in the previous subsection, the coordinate singularities are a feature of the exact solution, and cannot be avoided by employing alternative numerical methods. This is clearly a drawback to the use of harmonic slicing in numerical simulations, and by extension to the use of hyperbolic formulations of Einstein's equation which, as discussed in chapter 4, typically rely on this type of slicing. It should be realized though that no known slicing condition is guaranteed to completely cover an arbitrary spacetime, and potential problems with coordinate singularities do not necessarily outweigh the advantages in using hyperbolic formulations for numerical work. Of course, the formation of coordinate singularities has only been discussed here for simple harmonic slicing, and it is possible that the freedom in choosing the time dependence of the slicing density in generalized harmonic slicing could be put to use in controlling the development of the spacetime foliation such that coordinate singularities are avoided. Although when used in the context of a hyperbolic formulation the slicing density is formally required to be independent of the evolved variables, in practice there seems to be no problem in allowing occasional 'corrections' to be made

to its value in response to the behaviour of the foliation; in effect this amounts to intermittently halting the simulation and choosing a new value for the lapse on the current slice. (An important point here is that changes to the slicing density should be made only at fixed time intervals, rather than after a fixed number of time steps, since otherwise the exact solution being sought will depend on the resolution of the simulation.) This ‘piecewise harmonic’ form of time slicing has been used in some preliminary tests employing simple heuristics for making alterations to the value of the slicing density, with the resulting foliations being examined using the world line integration algorithm of section 5.1 (which was in fact originally developed for this purpose); however no definite conclusions regarding the effectiveness of the approach have yet been reached.

The present chapter has considered some of the difficulties that may be encountered because of gauge effects in numerical simulations of even very simple spacetimes. In the two chapters that follow numerical methods are used to study inhomogeneous cosmological models (many aspects of the behaviour of which are largely unknown), and the ideas developed in the present chapter help to distinguish coordinate effects in the numerical results from genuine physical behaviour. For the majority of the work done on the inhomogeneous models, specialized reductions of the Einstein equations are used rather than the hyperbolic formulation described in chapter 4; however, these reductions are all still based on harmonic time slicings, with fixed forms being assumed for the slicing densities. While little is known about the behaviour of harmonic slicings of the  $U(1)$ -symmetric cosmologies discussed in chapter 7, for the Gowdy cosmologies of chapter 6 it is known that the  $t = \text{constant}$  slices of the metric (6.5) cover the entire spacetime for  $0 < t < \infty$  (see section 6.1 for further details) and hence that coordinate singularities are not an issue for simulations based on this form of the metric. Following on from the work of the present section, it is natural to enquire as to the extent to which more general harmonic slicings of these inhomogeneous cosmologies are well behaved. A partial answer can be readily obtained in the case of the Gowdy  $T^3$  model. If the analysis of the previous subsection for harmonic slicings of the axisymmetric Kasner spacetime (5.22) is applied to the Gowdy metric (6.5) then it is found that the time function  $T$  must satisfy

$$T_{,tt} - T_{,\theta\theta} + t^{-1}T_{,t} = 0,$$

while the lapse  $N$  of the associated foliation is defined through

$$e^{-\lambda/2}\sqrt{t}(T_{,t}{}^2 - T_{,\theta}{}^2) = 1/N^2,$$

where  $\lambda(t, \theta)$  is one of the variables describing the Gowdy spacetime. Comparing these expressions to equations (5.23) and (5.25), it is clear that the Gowdy spacetimes admit the same harmonic foliations as the Kasner spacetime, and furthermore that the condition that foliations must satisfy to be free of coordinate singularities is the same. It thus turns out that all the results of the present section on the behaviour of harmonic slicings of a Kasner cosmology carry over directly to a fairly general class of planar cosmological models.

# Chapter 6.

## Planar Cosmologies

Even under assumptions of high degrees of symmetry, the general behaviour of inhomogeneous cosmological spacetimes cannot readily be described using analytic methods. The simplest inhomogeneous cosmological models assume the existence of two spacelike Killing vectors and have either planar, spherical or cylindrical symmetry. In the present chapter a class of spatially closed vacuum planar cosmologies are investigated using the numerical methods described earlier in this work.

Planar cosmologies have been an area of interest in numerical relativity since its early days. Since the late seventies Centrella, Matzner, Wilson, Anninos and co-workers have developed four generations of planar codes which have been used to investigate a variety of cosmological phenomena. The first code (Centrella 1979, 1980a, 1980b; Centrella and Matzner 1979, 1982) evolved gravitational shock waves in vacuum spacetimes. It used geodesic slicing and unconstrained evolution, and restricted the metric to diagonal form so that only one polarization of gravitational radiation was present in the simulations. Centrella and Wilson (1983, 1984) developed a second code capable of evolving planar cosmologies containing a single polarization of gravitational radiation together with matter in the form of a perfect fluid. This code used constant mean curvature slicing and fully constrained evolution. It was subsequently used to study nucleosynthesis (Centrella et al. 1986) and inflation (Kurki-Suonio et al. 1987) in inhomogeneous model universes. The third generation planar code (Anninos, Centrella and Matzner 1991a, 1991b) updated the algorithms used by Centrella and Wilson while discarding the hydrodynamical sources and was used to investigate nonlinear wave propagation in the vacuum Einstein equations. Recently, Anninos (1998a) has developed a new planar code which evolves a perfect fluid together with both polarizations of gravitational radiation. The code is capable of using a variety of slicing conditions and its evolution is unconstrained.

Other numerical work investigating planar cosmologies has been carried out by Shinkai and Maeda (1993, 1994) who considered inflationary scenarios involving a positive cosmological constant and an inhomogeneous inflaton field. They allowed for both polarizations of gravitational radiation, and used geodesic slicing and unconstrained evolution. Ove (1990a, 1990b) used a two-dimensional vacuum cosmology code restricted to planar symmetry to investigate nonlinear effects in gravitational wave propagation. His code implemented Moncrief's (1986) reduction of the Einstein equations, discussed in depth in chapter 7.

In contrast to the investigations cited above which are concerned with expanding spacetimes, Berger and Moncrief (1993) have performed simulations of collapsing planar cosmologies, their aim being to study the behaviour of spacetimes close to 'big bang' singularities. Berger and Moncrief's work is based on the Gowdy  $T^3$  family of vacuum spacetimes, and these models have been adopted for the work presented in this chapter; they are described in section 6.1.

In this chapter vacuum planar cosmological models are evolved numerically both forwards and backwards in cosmic time. The work of Berger and Moncrief (1993) provides a reference for the investigation of the collapsing case, and the fine-scale structure that develops in the evolved solutions proves to be an excellent test of the capabilities of the adaptive mesh refinement code described in chapter 3. Results from numerical simulations are presented in section 6.2, and in section 6.3 these are used to assess well-known conjectures regarding the nature of inhomogeneous cosmological singularities. (Much of the work in these sections was previously published in Hern and Stewart 1998.)

Expanding planar cosmologies are considered in section 6.4; there the results from numerical simulations of Gowdy spacetimes are compared to the studies of other planar cosmological models mentioned above. Three types of behaviour are investigated in particular: the formation of spatial structure in expanding spacetimes, the late-time fate of initially inhomogeneous cosmologies, and the differences between linear and nonlinear gravitational waves.

Some further work making use of the Gowdy cosmological models is presented in chapter 7. Section 7.2 addresses the question of how the fine-scale spatial structure found in collapsing Gowdy spacetimes generalizes to spacetimes with less symmetry. In section 7.3 Gowdy spacetimes are used as test cases for the Frittelli-Reula evolution system described in chapter 4.

## 6.1 The Gowdy Cosmological Models

In Gowdy 1974 a family of vacuum metrics having closed spacelike hypersurfaces and two-parameter isometry groups is constructed. These metrics are interpreted as describing closed inhomogeneous cosmologies containing two polarizations of gravitational waves. The Einstein equations for the Gowdy spacetimes reduce to a simple set of partial differential equations which can be studied by analytic methods, but for which exact solutions can in general only be constructed numerically. The simplicity of the equations, together with the body of existing analytic work describing their global properties, makes the Gowdy metrics well-suited to numerical investigations of the behaviour of inhomogeneous cosmologies.

This section presents an overview of the Gowdy models and considers in detail the subclass which are spatially of three-torus ( $T^3$ ) topology. The Gowdy  $T^3$  metrics describe closed vacuum planar cosmologies, and their behaviour is investigated numerically in the remainder of this chapter.

### *Topologies of the Gowdy Models*

Gowdy 1974 considers spacetimes which have two-parameter isometry groups with spacelike Killing vectors (which are assumed, without loss of generality, to commute) together with compact spacelike hypersurfaces of finite volume. The natural coordinates of the isometry group provide two spatial coordinates, angles  $\sigma$  and  $\delta$ , for the spacetime; the components of the metric are independent of these coordinates. Two other spacetime coordinates,  $\theta$  and  $t$ , label the orbits of the isometry group, and Gowdy assumes a ‘two-surface orthogonality’ condition to ensure that the

coordinate system is a global one. (Details of  $T^2$ -isometric spacetimes without such restrictions are given in Berger et al. 1997.) It follows from the original compactness assumption that the spacelike hypersurfaces of the spacetime must be homeomorphic to the three-torus ( $T^3$ ), the three-handle ( $S^1 \times S^2$ ), the three-sphere ( $S^3$ ), or to a manifold covered by one of these. (Alternative topologies are possible if assumptions about the global nature of the Killing vectors are weakened; see Tanimoto 1998.) By applying the vacuum Einstein equations, and making use of the available coordinate freedom, the Gowdy metrics are written in a form that depends only on three functions of  $\theta$  and  $t$  satisfying simple systems of evolution and constraint equations.

If the Killing vector fields which generate the isometry group are everywhere mutually orthogonal then the Gowdy model is said to be polarized and in such cases exact solutions can be obtained. Gowdy 1971 discusses polarized spacetimes having  $S^1 \times S^2$  and  $S^3$  spatial topologies. Polarized Gowdy  $T^3$  spacetimes are considered later in this section.

The Gowdy  $S^1 \times S^2$  and Gowdy  $S^3$  spacetimes have similar global structures. In both models the spacelike hypersurfaces connect two timelike regions where the trajectories of the isometry group degenerate; this manifests in the metric as two ‘cylindrical’ coordinate axes at the limits of the  $\theta$  coordinate range. In addition, these models have both initial and final spacelike singularities with each spacetime first expanding, then collapsing during the course of its evolution. In contrast, the Gowdy  $T^3$  spacetimes have no degenerate trajectories on their spacelike hypersurfaces, and their metric components are periodic in the angle  $\theta$ . These spacetimes begin at initial singularities and expand forever.

The Gowdy cosmological models have been studied in a variety of contexts. They have been used as background spacetimes in which to investigate quantum effects and approaches to quantization (Misner 1973, Berger 1974 and 1984, McGuigan 1991, Ashtekar and Husain 1998). They have provided example cases for tests of the strong cosmic censorship conjecture (Moncrief 1981, Chruściel, Isenberg and Moncrief 1990, Grubišić and Moncrief 1993) and investigations of the nature of cosmological singularities (Isenberg and Moncrief 1990, Berger and Moncrief 1993, Kichenassamy and Rendall 1998, Garfinkle 1999; also see section 6.3 of the present work). They have been used as backgrounds on which to visualize gravitational wave motion (Berger, Garfinkle and Swamy 1995) and, most recently, as known metrics against which to test the performance of numerical methods and formulations (van Putten 1997, New et al. 1998).

The Gowdy spacetimes with  $T^3$  spatial topology are the simplest kind, in terms of both equations and boundary conditions, and for this reason they have received most attention in the literature. For the remainder of this chapter the three-torus models are considered exclusively. The Gowdy  $T^3$  models provide a simple, practical framework within which the behaviour of planar cosmologies can be investigated, and the results presented here can be compared with the numerical studies of planar cosmologies cited in the introduction to this chapter. (Since those studies invariably use periodic boundary conditions the topologies of the different models are effectively the same.) The advantage of studying the Gowdy  $T^3$  models is that their Einstein equations reduce to a very simple form; the disadvantage is that extending the models to include fluid matter sources is

not straightforward. (Generalized Gowdy spacetimes containing scalar and electromagnetic fields are discussed in Carmeli, Charach and Malin 1981; for models including matter in the form of collisionless particles see Andréasson 1998.)

### *The Gowdy $T^3$ Cosmology*

The Gowdy  $T^3$  line element is written here following Berger and Moncrief 1993 as

$$ds^2 = e^{(\lambda+\tau)/2}(-e^{-2\tau}d\tau^2 + d\theta^2) + e^{-\tau}(e^P d\sigma^2 + 2e^P Q d\sigma d\delta + (e^P Q^2 + e^{-P}) d\delta^2). \quad (6.1)$$

The spatial coordinates  $\theta$ ,  $\sigma$  and  $\delta$  range from 0 to  $2\pi$  and describe a three-torus. The time coordinate  $\tau$  can take any real value;  $\tau = +\infty$  marks the cosmological singularity and  $\tau = -\infty$  corresponds to an infinitely expanded universe. The functions  $\lambda$ ,  $P$  and  $Q$  depend on the coordinates  $\theta$  and  $\tau$  only and are required to be periodic in  $\theta$ .

The vacuum Einstein equations for the metric reduce to two wave equations for  $P$  and  $Q$ ,

$$P_{,\tau\tau} = e^{-2\tau}P_{,\theta\theta} + e^{2P}(Q_{,\tau}^2 - e^{-2\tau}Q_{,\theta}^2), \quad (6.2a)$$

$$Q_{,\tau\tau} = e^{-2\tau}Q_{,\theta\theta} - 2(P_{,\tau}Q_{,\tau} - e^{-2\tau}P_{,\theta}Q_{,\theta}), \quad (6.2b)$$

and two equations for  $\lambda$  deriving from the Hamiltonian and momentum constraints,

$$-\lambda_{,\tau} = P_{,\tau}^2 + e^{-2\tau}P_{,\theta}^2 + e^{2P}(Q_{,\tau}^2 + e^{-2\tau}Q_{,\theta}^2), \quad (6.2c)$$

$$-\lambda_{,\theta} = 2(P_{,\tau}P_{,\theta} + e^{2P}Q_{,\tau}Q_{,\theta}). \quad (6.2d)$$

It is important to note that equations (6.2a) and (6.2b) do not involve  $\lambda$ ; they form an independent sub-system within which  $P$  and  $Q$  are completely determined from appropriate initial data. Subsequently, if  $P$  and  $Q$  are known, then equation (6.2c) can be integrated to find  $\lambda$ . Equation (6.2d) then remains as a constraint which determines (up to addition of a constant) the initial value of  $\lambda$  from the initial values of  $P$  and  $Q$  (and their first time derivatives). This constraint is conserved in the sense that, provided the evolution equations (6.2a,b,c) hold, equation (6.2d) is satisfied for all time if it is satisfied initially. Arbitrary (periodic) values of  $P$ ,  $Q$ ,  $P_{,\tau}$  and  $Q_{,\tau}$  thus provide sufficient initial data for the system, subject to one condition: periodicity in  $\lambda$  is required, and from equation (6.2d),

$$\lambda|_{\theta=0} = \lambda|_{\theta=2\pi} \iff \int_0^{2\pi} (P_{,\tau}P_{,\theta} + e^{2P}Q_{,\tau}Q_{,\theta}) d\theta = 0. \quad (6.3)$$

Gowdy (1974) notes that this is equivalent to demanding that the total  $\theta$ -momentum of the system be zero.

The choice of time coordinate in the metric (6.1) is well suited to numerical investigations of a Gowdy  $T^3$  spacetime as it collapses: the cosmological singularity is approached arbitrarily closely but not reached in finite coordinate time. However, for studying expanding cosmologies Gowdy's original time coordinate  $t$  is more appropriate. It is defined by

$$t = e^{-\tau}, \quad (6.4)$$



and transforms the metric (6.1) to

$$ds^2 = e^{\lambda/2} t^{-1/2} (-dt^2 + d\theta^2) + t(e^P d\sigma^2 + 2e^P Q d\sigma d\delta + (e^P Q^2 + e^{-P}) d\delta^2), \quad (6.5)$$

with evolution and constraint equations

$$P_{,tt} = P_{,\theta\theta} + e^{2P}(Q_{,t}^2 - Q_{,\theta}^2) - (1/t)P_{,t}, \quad (6.6a)$$

$$Q_{,tt} = Q_{,\theta\theta} - 2(P_{,t}Q_{,t} - P_{,\theta}Q_{,\theta}) - (1/t)Q_{,t}, \quad (6.6b)$$

$$\lambda_{,t} = t(P_{,t}^2 + P_{,\theta}^2) + te^{2P}(Q_{,t}^2 + Q_{,\theta}^2), \quad (6.6c)$$

$$\lambda_{,\theta} = 2t(P_{,t}P_{,\theta} + e^{2P}Q_{,t}Q_{,\theta}). \quad (6.6d)$$

The cosmological singularity occurs at time  $t = 0$  and the universe expands forever through positive values of  $t$ .

Some important results can be read straight off the metrics (6.1) and (6.5). The areas of the trajectories of the isometry group define a scalar field on the spacetime equal to

$$\text{area of } \sigma\text{-}\delta \text{ symmetry plane} = 4\pi^2 e^{-\tau} = 4\pi^2 t. \quad (6.7)$$

(This field is independent of the  $\theta$  coordinate by construction; see Gowdy 1974.) The constant time hypersurfaces for both metrics (6.1) and (6.5) slice the spacetime harmonically (see section 4.1; the slicing density depends on the time coordinate only) and the slices are not in general of constant mean curvature. The coordinate speeds of photons moving orthogonal to the trajectories of the isometry group are

$$\text{coordinate light speed in } \theta\text{-direction} = \begin{cases} \pm e^{-\tau} & \text{for metric (6.1),} \\ \pm 1 & \text{for metric (6.5),} \end{cases} \quad (6.8)$$

and these are the (non-trivial) characteristic speeds of the evolution equations of the two metrics. For the expanding form (6.5) of the metric, light rays complete an orbit of the universe in a time period  $\Delta t = 2\pi$ . In the collapsing case (6.1) the coordinate light speed tends to zero as the cosmological singularity is approached, and the total distance that can be travelled by a light ray released at time  $\tau = \tau_0$  before it hits the singularity at  $\tau = +\infty$  is  $\Delta\theta = \exp(-\tau_0)$ ; in the numerical work performed here with the collapsing model, a starting time of  $\tau_0 = 0$  is typical and light rays never travel more than a fraction of the distance around the universe.

Moncrief (1981) has shown that no singularities appear in the Gowdy  $T^3$  spacetimes for  $0 < t < +\infty$ , and that this coordinate range describes the maximal Cauchy development of the models. (In particular, no coordinate singularities of the type investigated in section 5.2 can be present in the standard Gowdy slicing.) The singularity at  $t = 0$  is ‘crushing’ (the trace of the extrinsic curvature of the  $t = \text{constant}$  slices blows up uniformly as  $t \rightarrow 0+$ ; see Eardley and Smarr 1979) and is conjectured to be a curvature singularity. Isenberg and Moncrief (1982) have further shown that time slices of constant mean curvature can be used to foliate the maximally extended Gowdy  $T^3$  spacetimes.

### Exact and Approximate Solutions

If the time slices of the Gowdy  $T^3$  spacetimes are assumed to be homogeneous then the reduced Einstein equations (6.2) can be solved exactly to give (from Berger and Moncrief 1993)

$$P = \begin{cases} \ln(\alpha e^{-\beta\tau}(1 + \xi^2 e^{2\beta\tau})), \\ \ln(\alpha t^\beta(1 + \xi^2 t^{-2\beta})), \end{cases} \quad Q = \begin{cases} \eta - \frac{\xi e^{2\beta\tau}}{\alpha(1 + \xi^2 e^{2\beta\tau})}, \\ \eta - \frac{\xi t^{-2\beta}}{\alpha(1 + \xi^2 t^{-2\beta})}, \end{cases} \quad \lambda = \begin{cases} \chi - \beta^2 \tau, \\ \chi + \beta^2 \ln t, \end{cases} \quad (6.9)$$

where  $\alpha$ ,  $\beta$ ,  $\eta$ ,  $\chi$  and  $\xi$  are constants, with  $\alpha$  strictly positive, and  $\beta$  assumed non-negative without loss of generality. The resulting Gowdy metric (6.1) or (6.5) then describes a Kasner spacetime (with imposed three-torus spatial topology) which can be written in the standard form

$$ds^2 = -dT^2 + T^{2p_1} dX^2 + T^{2p_2} dY^2 + T^{2p_3} dZ^2, \quad (6.10)$$

where  $T$  is positive and  $p_1$ ,  $p_2$  and  $p_3$  are constants (see, for example, section 7.2 of Wald 1984). If the  $X$ -axis of the metric (6.10) is assumed to correspond to the  $\theta$ -axis of the Gowdy metric, then the constant  $\beta$  determines the Kasner expansion parameters:

$$p_1 = \frac{(\beta^2 - 1)}{(\beta^2 + 3)}, \quad p_2 = \frac{2(1 + \beta)}{(\beta^2 + 3)}, \quad p_3 = \frac{2(1 - \beta)}{(\beta^2 + 3)}, \quad (6.11)$$

with the values for  $p_2$  and  $p_3$  being interchangeable. The other constants  $\alpha$ ,  $\eta$ ,  $\chi$  and  $\xi$  in the solution (6.9) choose the scaling of the Gowdy coordinates relative to the Kasner coordinates and the rotation of the  $\sigma$ - and  $\delta$ -axes relative to the  $Y$ - and  $Z$ -axes. In the case that the Gowdy variables  $P$ ,  $Q$  and  $\lambda$  are constants, the parameter  $\beta$  is zero and the spacetime is axisymmetric about the  $\theta$ -axis. For  $\beta = \pm 1$  the spacetime is flat (although this is not immediately obvious from the form of the metric) and the initial singularity at  $t = 0$  is a coordinate singularity.

The homogeneous solutions (6.9) provide a useful reference against which to compare the behaviour of more general Gowdy  $T^3$  spacetimes. In section 6.4 first-order perturbations of the homogeneous metrics are studied and the resulting approximate solutions are compared with numerically evolved spacetimes. As discussed by Berger and Moncrief (1993), linearized theory provides an interpretation of the Gowdy metric functions  $P$  and  $Q$  as amplitudes of orthogonal polarizations of gravitational waves propagating in a background spacetime described by the function  $\lambda$ . If  $P$  and  $Q$  are both close to zero then their evolution equations (6.2a) and (6.2b) can be approximated to first order as  $P_{,\tau\tau} = e^{-2\tau} P_{,\theta\theta}$  and  $Q_{,\tau\tau} = e^{-2\tau} Q_{,\theta\theta}$ , two decoupled wave equations. The metric (6.1) can then be expanded as

$$g_{\mu\nu} = g_{\mu\nu}^{\text{background}} + e^{-\tau} P \varepsilon_{\mu\nu}^+ + e^{-\tau} Q \varepsilon_{\mu\nu}^\times + (\text{second- and higher-order terms}),$$

where the background part of the metric depends only on the function  $\lambda$ , and  $\varepsilon^+$  and  $\varepsilon^\times$  are the two polarization tensors for gravitational waves propagating along the  $\theta$ -axis (see Misner, Thorne and Wheeler 1973, section 35.6).

The Gowdy  $T^3$  metrics are said to be polarized if the function  $Q$  is identically zero. (If  $Q$  is zero on an initial time slice then the evolution equation (6.2b) ensures that it remains zero throughout the spacetime; the corresponding statement does not hold in general for the polarization of radiation represented by  $P$ .) The polarized Gowdy  $T^3$  spacetimes have been extensively studied (see Berger 1974 and 1984, and Misner 1973) and are of particular interest because their evolution equations can be solved exactly. If  $Q$  is zero then equation (6.2a) is linear in  $P$  and has the general solution

$$P = a_0\tau + b_0 + \sum_{n=1}^{\infty} \left( Z_{+n}(\tau) \cos(n\theta) + Z_{-n}(\tau) \sin(n\theta) \right), \quad (6.12)$$

$$\text{with } Z_{\pm n}(\tau) = a_{\pm n} J_0(|n|e^{-\tau}) + b_{\pm n} Y_0(|n|e^{-\tau}) \quad \text{for } n \neq 0,$$

where  $J_i(x)$  and  $Y_i(x)$  are Bessel functions (reviewed in section 5.2) and the  $a_{\pm n}$  and  $b_{\pm n}$  are constants. The general solution for  $\lambda$  (obtained from equations (6.2c) and (6.2d)) is given in Berger 1974, along with the restrictions imposed on the constants  $a_{\pm n}$  and  $b_{\pm n}$  by the momentum constraint (6.3). For the current work a particular polarized solution has been chosen:

$$\begin{aligned} P &= J_0(e^{-\tau}) \cos(\theta) + Y_0(2e^{-\tau}) \sin(2\theta), \\ \lambda &= -e^{-\tau} \left( J_1(e^{-\tau}) J_0(e^{-\tau}) \cos^2(\theta) + J_1(e^{-\tau}) Y_0(2e^{-\tau}) \left[ \frac{2}{3} \sin(3\theta) + 2 \sin(\theta) \right] \right. \\ &\quad \left. + J_0(e^{-\tau}) Y_1(2e^{-\tau}) \left[ \frac{2}{3} \sin(3\theta) - 2 \sin(\theta) \right] - Y_0(2e^{-\tau}) Y_1(2e^{-\tau}) [\cos(4\theta) - 1] \right) \\ &\quad + e^{-2\tau} \left( \frac{1}{2} [J_0(e^{-\tau})^2 + J_1(e^{-\tau})^2] + 2 [Y_0(2e^{-\tau})^2 + Y_1(2e^{-\tau})^2] \right). \end{aligned} \quad (6.13)$$

Berger and Moncrief (1993) note that a class of coordinate transformations which leave the form of the metric (6.1) unchanged can be used to generate new exact solutions from known ones; in particular an exact polarized solution can be transformed into a ‘pseudo-unpolarized’ solution for which the function  $Q$  is not identically zero (although the metrics are physically equivalent). A simple example of such a transformation converts a polarized solution,  $P_{\text{pol}}$  and  $\lambda_{\text{pol}}$ , into a pseudo-unpolarized solution,

$$P_{\text{pseudo}} = \ln(\cosh P_{\text{pol}}), \quad Q_{\text{pseudo}} = \tanh P_{\text{pol}}, \quad \lambda_{\text{pseudo}} = \lambda_{\text{pol}}. \quad (6.14)$$

Polarized and pseudo-unpolarized solutions play an important part in the work described in this chapter: they provide non-trivial exact solutions against which numerical codes developed to evolve genuinely unpolarized Gowdy  $T^3$  metrics can be tested. (Recent work in Griffiths and Alekseev 1998 shows that polarized solutions can also be transformed to produce a class of genuinely unpolarized solutions, and in principle these too could be used as code tests.)

Another class of Gowdy solutions is discussed by Grubišić and Moncrief (1993) who use different variables to describe the metric (6.1). Their ‘circular loop’ solutions have simple spatial profiles which evolve according to ordinary differential equations.

## 6.2 Collapsing Planar Cosmologies

In this section the results of numerical simulations of collapsing unpolarized Gowdy  $T^3$  spacetimes are presented. The starting point for this work is the 1993 paper of Berger and Moncrief. They used a symplectic integration scheme (described in their paper) to evolve the Gowdy equations (6.2a,b), and found that the metric variables developed structure on very fine scales which their code could not reliably resolve. The present work uses the adaptive mesh refinement code described in chapter 3 to repeat and extend Berger and Moncrief's calculations.

Work following on from Berger and Moncrief 1993 has been published by Berger (1997) and, recently, Berger and Garfinkle (1998). Berger et al. 1998 summarizes the findings of a long-term investigation into the behaviour of collapsing cosmological models which includes results from the Gowdy  $T^3$  studies.

The metric variables in the collapsing Gowdy  $T^3$  simulations show complicated behaviour which, at a first glance, appears to be evidence of numerical instabilities in the code. However careful observation of the variables at high resolutions (made possible through the use of adaptive mesh refinement) reveals the behaviour to be a genuine nonlinear effect. Numerical results are presented in this section in sufficient detail to allow the unpolarized Gowdy  $T^3$  spacetimes to be used as a non-trivial test bed calculation in the development of other codes for numerical relativity. The following discussion concentrates on each metric variable in turn, and attempts to distinguish covariant behaviour from coordinate effects by examining the curvature invariants of the simulated spacetimes. In section 6.3 the results of these simulations are re-examined to see what evidence they provide as to the nature of the initial singularity. In section 7.2 a similar investigation of the behaviour of collapsing  $U(1)$ -symmetric cosmologies is undertaken.

### *Numerical Simulations of Collapsing Gowdy $T^3$ Spacetimes*

The variables  $P(\tau, \theta)$ ,  $Q(\tau, \theta)$  and  $\lambda(\tau, \theta)$  of the collapsing Gowdy metric (6.1) are evolved here using the numerical methods of chapters 2 and 3. New variables are defined as

$$A \equiv P_{,\tau}, \quad B \equiv Q_{,\tau}, \quad C \equiv P_{,\theta}, \quad D \equiv Q_{,\theta}, \quad (6.15)$$

and the evolution equations (6.2a,b,c) become a one-dimensional first-order system suitable for numerical integration (recall equation (2.1)):

$$A_{,\tau} - e^{-2\tau} C_{,\theta} = e^{2P} (B^2 - e^{-2\tau} D^2), \quad (6.16a)$$

$$B_{,\tau} - e^{-2\tau} D_{,\theta} = -2(AB - e^{-2\tau} CD), \quad (6.16b)$$

$$C_{,\tau} - A_{,\theta} = 0, \quad (6.16c)$$

$$D_{,\tau} - B_{,\theta} = 0, \quad (6.16d)$$

$$P_{,\tau} = A, \quad (6.16e)$$

$$Q_{,\tau} = B, \quad (6.16f)$$

$$\lambda_{,\tau} = -A^2 - e^{-2\tau} C^2 - e^{2P} (B^2 + e^{-2\tau} D^2). \quad (6.16g)$$

For the present work the variable  $\lambda$  is evolved according to equation (6.16g) and consequently

$$\lambda_{,\theta} = -2(AC + e^{2P}BD) \quad (6.17)$$

from equation (6.2d) acts as a constraint on the evolution. An alternative approach would be to reconstruct  $\lambda$  at each time level using equation (6.17) so that the numerical evolution is constrained. This idea is returned to later in the section.

The initial data set for the simulations is

$$\begin{aligned} P &= 0, & Q &= \cos \theta, & \lambda &= 0, \\ P_{,\tau} &= v_0 \cos \theta, & Q_{,\tau} &= 0, & \text{at time } \tau &= 0, \end{aligned} \quad (6.18)$$

which (with variables  $A$ ,  $B$ ,  $C$  and  $D$  defined according to equations (6.15)) clearly satisfies the constraint (6.17). This choice of initial data was used by Berger and Moncrief (1993) and can be interpreted as two (initially) standing gravitational waves in a homogeneous background. The magnitude of the parameter  $v_0$  affects the amount of fine-scale structure that develops in the spacetime. Here, as in Berger and Moncrief 1993, the choice of  $v_0 = 10$  is made, and the behaviour of the evolved spacetime is complicated. The results presented in Berger 1997 take  $v_0$  to be 5 and include significantly less fine-scale structure. The choice (6.18) of initial data has been found to be reasonably generic: other initial data sets produce qualitatively similar behaviour, but with varying amounts of fine-scale structure.

The numerical code used to evolve the system (6.16) has been thoroughly tested. Section 6.1 presents three types of exact Gowdy  $T^3$  solution—homogeneous, equation (6.9), polarized, equation (6.13), and pseudo-unpolarized, equation (6.14)—which the code successfully reproduces. As with all of the numerical results presented here, the evolved quantities have been checked to ensure that they converge at second order as the resolution increases (see section 2.1); in particular, the error in the constraint equation (6.17) converges to zero at the expected rate. During the course of this work, codes for evolving a variety of formulations of Einstein’s equations have been developed, and wherever possible the different codes have been used to evolve data for Gowdy spacetimes. The consistency between the results of these codes is further evidence that the system of equations (6.16) is being evolved correctly.

Two different numerical integration schemes have been used in this work: a high-resolution wave-propagation method and the standard two-step Lax-Wendroff finite difference method, both of which are discussed in chapter 2. (In fact, two different implementations of the Lax-Wendroff method were used; see sections 2.1 and 3.3.) The schemes have been found to perform comparably well in evolving numerical solutions to the Gowdy equations. The wave-propagation algorithm uses the solution to the Riemann problem for the transport part (left-hand side) of the system (6.16), which is simply a combination of linear wave equations, discussed in chapter 2 (equation (2.15)). Using operator splitting (section 2.1) the source part (right-hand side) of the system (6.16) can be treated using standard numerical techniques for solving ordinary differential equations, and in the present case second-order Runge-Kutta steps are used (see equation (2.20)). Periodic boundary conditions are used for the Gowdy simulations.

The Gowdy equations have been evolved using the adaptive mesh refinement code described in chapter 3. A base grid with a mesh spacing of  $\Delta\theta = 2\pi/2000$  is refined by the code up to a maximum resolution of  $\Delta\theta = 2\pi/512\,000$  (the result of four stages of refinement each by a factor of four). Such small mesh spacings are needed to resolve the fine-scale features that appear during the simulations, but lower resolution simulations can still adequately determine the overall profile of the solution: a test of the adaptive mesh refinement code using a base grid of mesh size  $\Delta\theta = 2\pi/8000$  produces similar results to those plotted in figures 6.1, 6.2, and 6.3 even when the mesh refinement is switched off. Figure 3.13 shows an example grid hierarchy used by the code during a Gowdy simulation.

The time steps taken by the code are allowed to vary in size according to the characteristic speeds of the equations (6.16) (see the discussion in section 3.2). From equation (6.8) it is clear that the time steps can increase in size exponentially without breaking the Courant-Friedrichs-Lewy condition, but in practice an upper limit (of about five times the mesh spacing) is imposed.

In section 3.2 several different interpolation methods used for mesh refinement are discussed. To obtain the results presented here, linear and quadratic piecewise interpolation methods were used. Because of the spiky features that develop during the simulations at scales too small to fully resolve, smooth spline interpolation methods cannot be used effectively here: they produce spurious effects in the vicinity of the spikes (recall figure 3.5).

The use of adaptive mesh refinement in the simulations serves two main purposes: it increases the overall accuracy of the results on the coarse base grid without substantially increasing the times taken to produce them, and it allows fine-scale features of the solution to be resolved without requiring a high density of grid points everywhere in the spatial domain. The code uses estimates of local truncation errors to decide where refined regions should be positioned. While this approach works well in increasing the overall accuracy, it is found to be inefficient in tracking regions of fine-scale structure. A simple heuristic algorithm for identifying spiky features in the solution has been used to improve the code's performance, but the most effective way to make the code refine a particular region of emerging fine-scale structure is to program it to do so explicitly.

By using (parallelized) adaptive mesh refinement, together with variable time steps, the Gowdy simulations take minutes rather than hours to run. It is interesting to note that a significant portion (around 25%) of the code's total running time is spent doing nothing other than calculating values of exponentials.

### *Behaviour of the First Gowdy Wave Variable*

In this and the following two subsections the behaviour of the variables  $P$ ,  $Q$  and  $\lambda$  during the evolution of equations (6.16) from initial data set (6.18) is discussed. Figures 6.1, 6.2 and 6.3 show the variables at various times, with data from three levels of refinement being plotted. (The first two of these figures can be compared with figures 4 and 5 of Berger and Moncrief 1993.)

The structure of the variable  $P$  becomes complicated soon after the start of the evolution and by time  $\tau = 4\pi$  (as figure 6.1 shows) it includes a number of fine spikes. At first sight these spikes

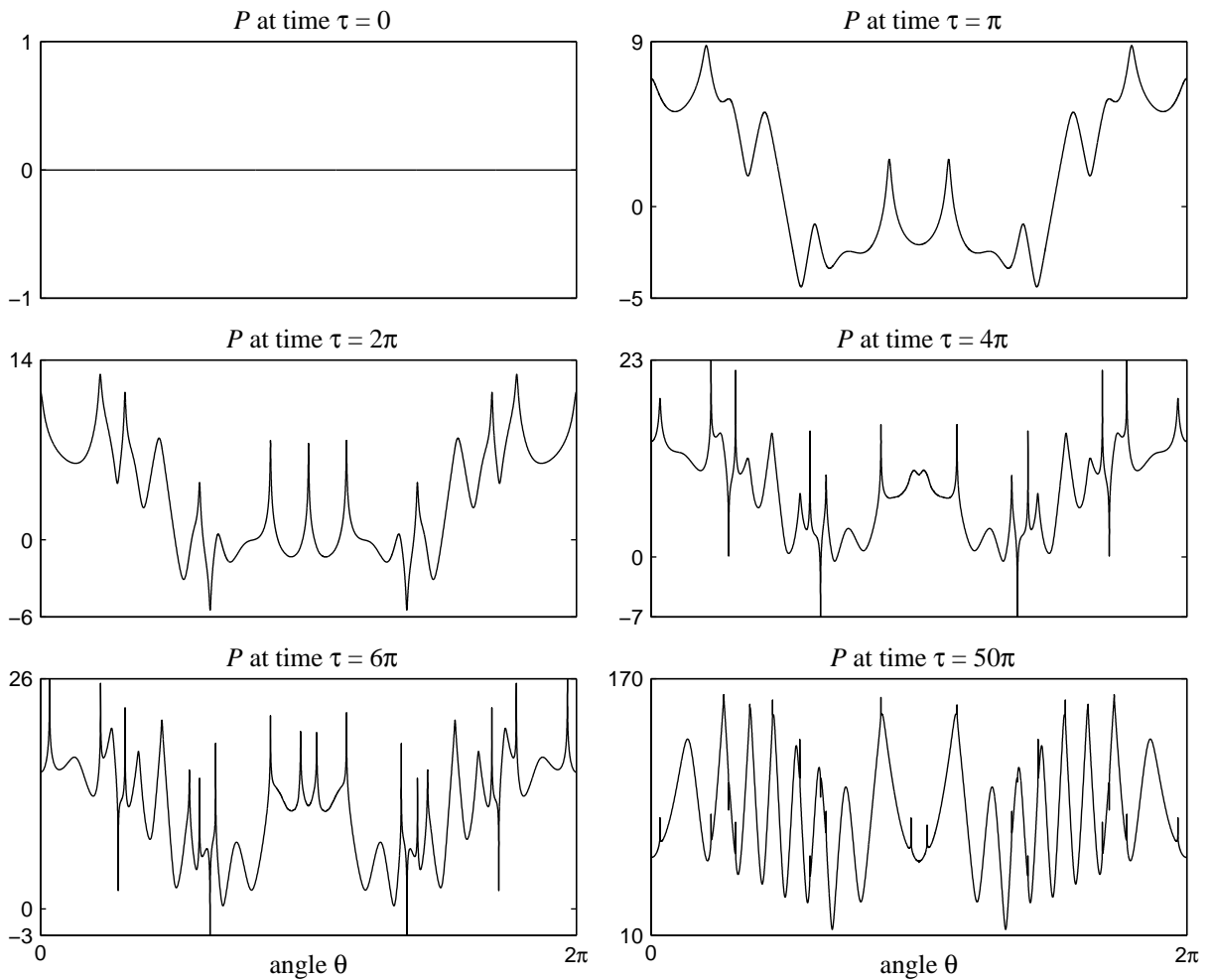


**Figure 6.1:** Wave variable  $P(\tau, \theta)$  of metric (6.1) at six different times. Initial data set (6.18) is evolved using equations (6.16). The vertical scales chosen for the plots truncate some of the larger spikes.

might seem to be errors in the evolution, and indeed when Berger and Moncrief first found spikes in their data they considered them unreliable and used spatial averaging to remove them from figures 4 and 5 of their paper (1993). However, the adaptive mesh refinement code of chapter 3 automatically refines the regions where spikes start to form, increasing the grid resolution so that the spikes appear smooth and the evolution can continue without loss of accuracy. This is demonstrated in figure 6.4 where an emerging spike in  $P$  is shown for the coarse base grid together with two levels of refined sub-grids.

Spikes form in  $P$  in both the positive and negative directions. Examining the development of the positive spikes (the negative spikes are discussed in the following subsection) it is found that their peaks grow linearly at rates  $P_{,\tau} = \text{constant} > 1$ , while at the same time they decrease in width. As a spike narrows (and there is no indication that the spikes ever stop growing or narrowing) the mesh refinement code is forced to use finer and finer grids to keep it well resolved.

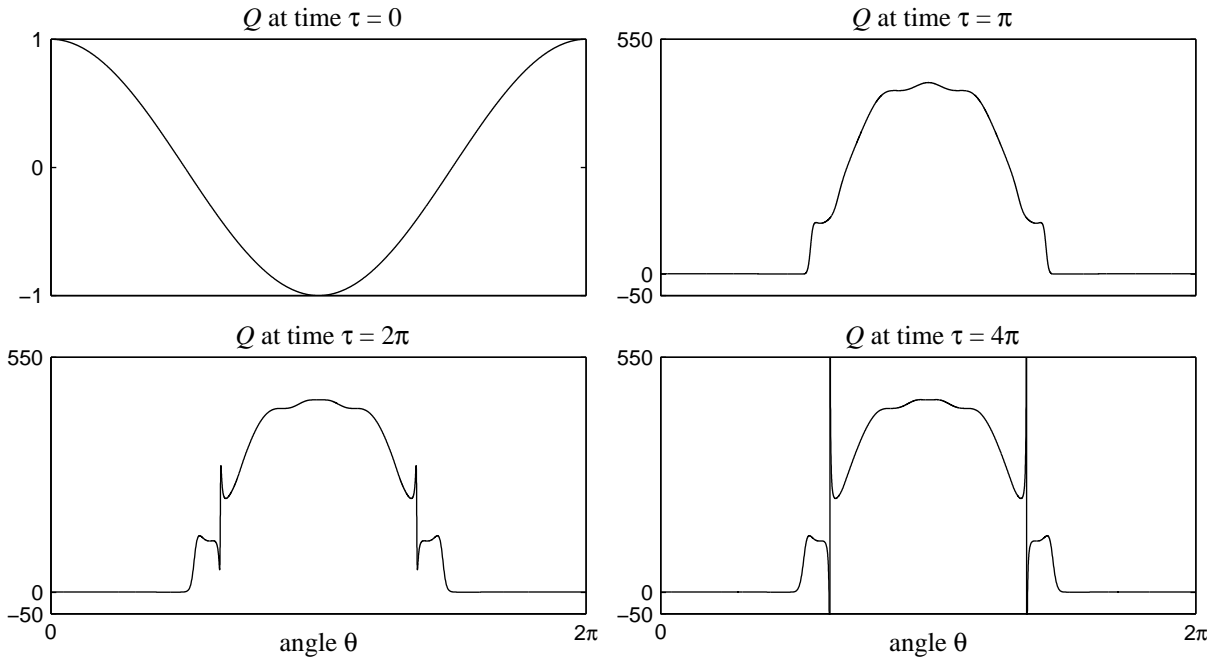


**Figure 6.2:** Wave variable  $Q(\tau, \theta)$  of metric (6.1) at four different times. Initial data set (6.18) is evolved using equations (6.16). The vertical scale of the final plot truncates the large spikes. The profile of the variable does not change noticeably after the time of the final plot (except for the heights of the spikes).

Eventually, it becomes narrower than the smallest grid spacing that the code has been instructed to use, and from that point on it cannot be assumed that the code is accurately evolving the spike. It is therefore inevitable that, as the evolution progresses, the calculated heights of the spikes in  $P$  must be significantly in error, but this does not imply that there must be large errors elsewhere in the data: since the characteristic speed of the model is  $\exp(-\tau)$  (from equation (6.8)), deviations from the exact solution that develop at some time not too soon after the start of the evolution can only propagate very small distances from their points of origin.

At late times  $P_{,\tau\tau} \equiv A_{,\tau}$  is seen to become very small, and so  $A$  freezes and  $P$  grows linearly in time with the spatial profile shown in the final plot of figure 6.1. Except at the points where spikes formed, the spatial profile of  $P$  at late times has quite a simple form, much less intricate than early on in its evolution. For the reasons discussed above, the numerical simulation is unable to accurately determine the late-time behaviour of the spikes. While small spikes and lumps appear in the plot of  $P$  at time  $\tau = 50\pi$  in figure 6.1, these are just the residue left by spikes that have narrowed beyond the resolution of the simulation. The spikes themselves, assuming they continued to grow at their initial rates, would all go off the scale of the graph.

In suggesting reasons for the observed behaviour it is useful to know which are the dominant terms in the governing equations. Here a term on the right-hand side of an equation is defined as being *dominant* if its absolute value exceeds ten times the absolute value of the sum of the



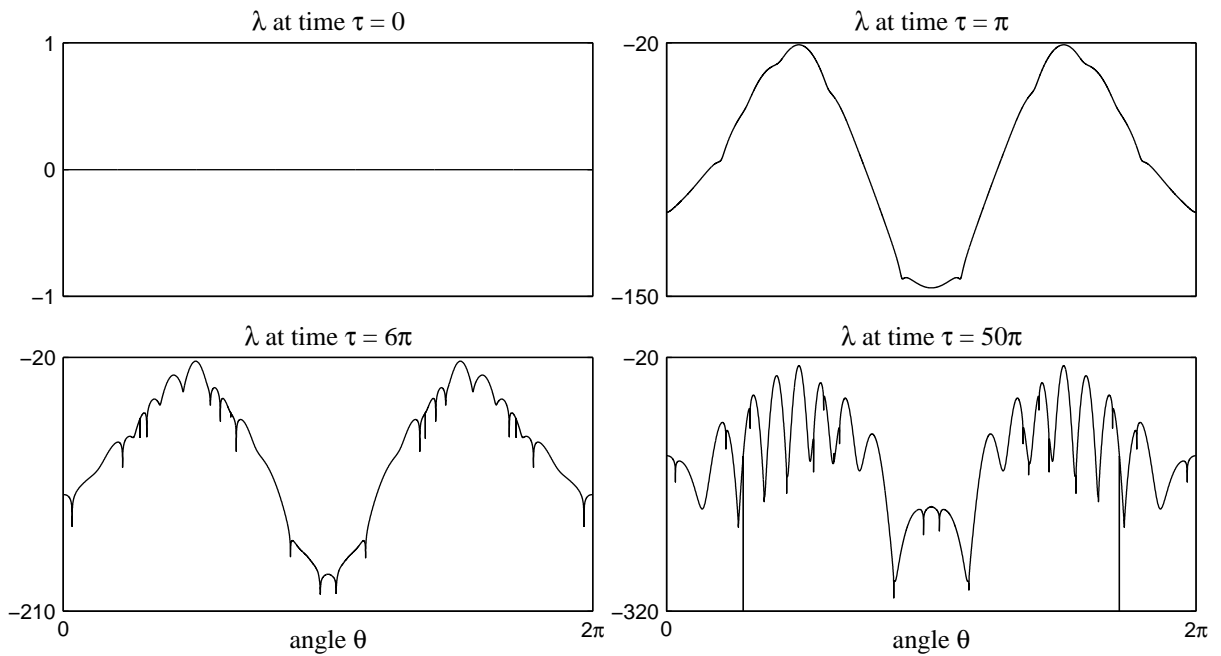


**Figure 6.3:** Background variable  $\lambda(\tau, \theta)$  of metric (6.1) at four different times. Initial data set (6.18) is evolved using equations (6.16). The vertical scale of the final plot truncates some of the larger spikes.

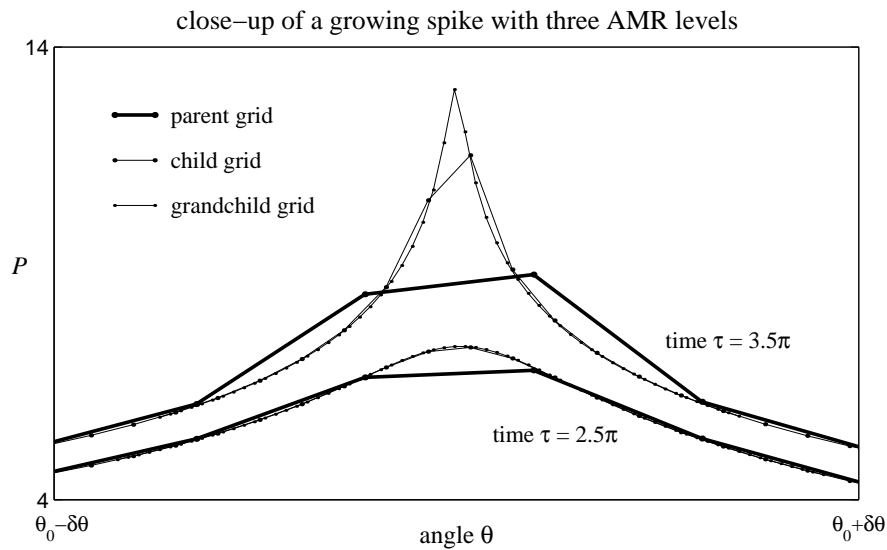


**Figure 6.4:** Data from three generations of grids at an emerging spike in  $P$ . Each sub-grid has a resolution four times greater than that of its parent grid. The spike is located at coordinate  $\theta_0 = 1.8631$ , and the plot shows a region of size  $\delta\theta = 7.5 \times 10^{-3}$  to either side. Two time levels are shown, with the spike well resolved by the two finer grids at the earlier time, but only adequately resolved by the finest grid at the later time.

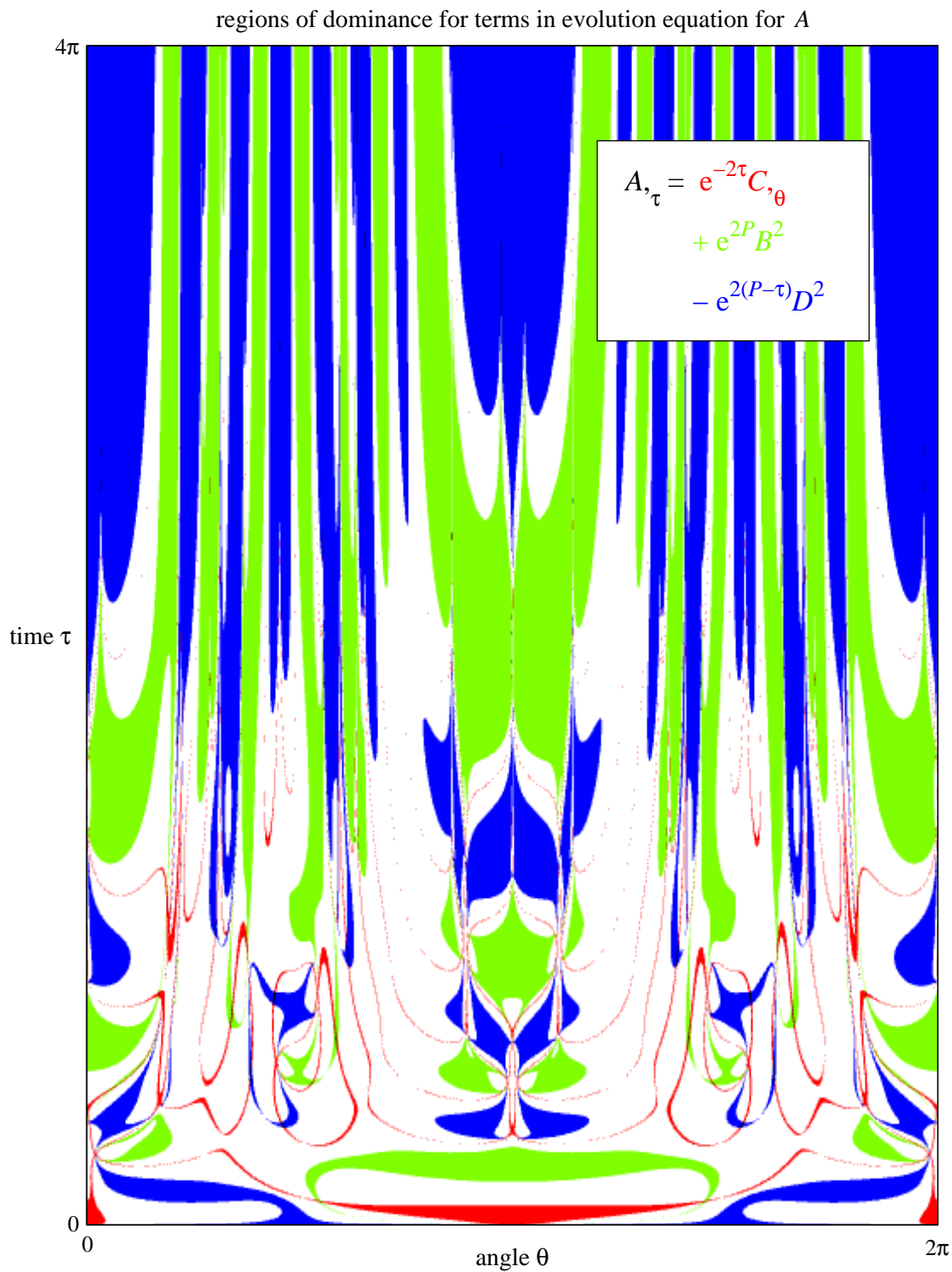


**Figure 6.5:** Dominant terms in the evolution equation (6.16a) for  $A$ . Regions where one of the three terms in the equation dominates the other terms (in the sense described in the text) are coloured red, green or blue as shown in the key. Uncoloured (white) regions are where no terms dominate.

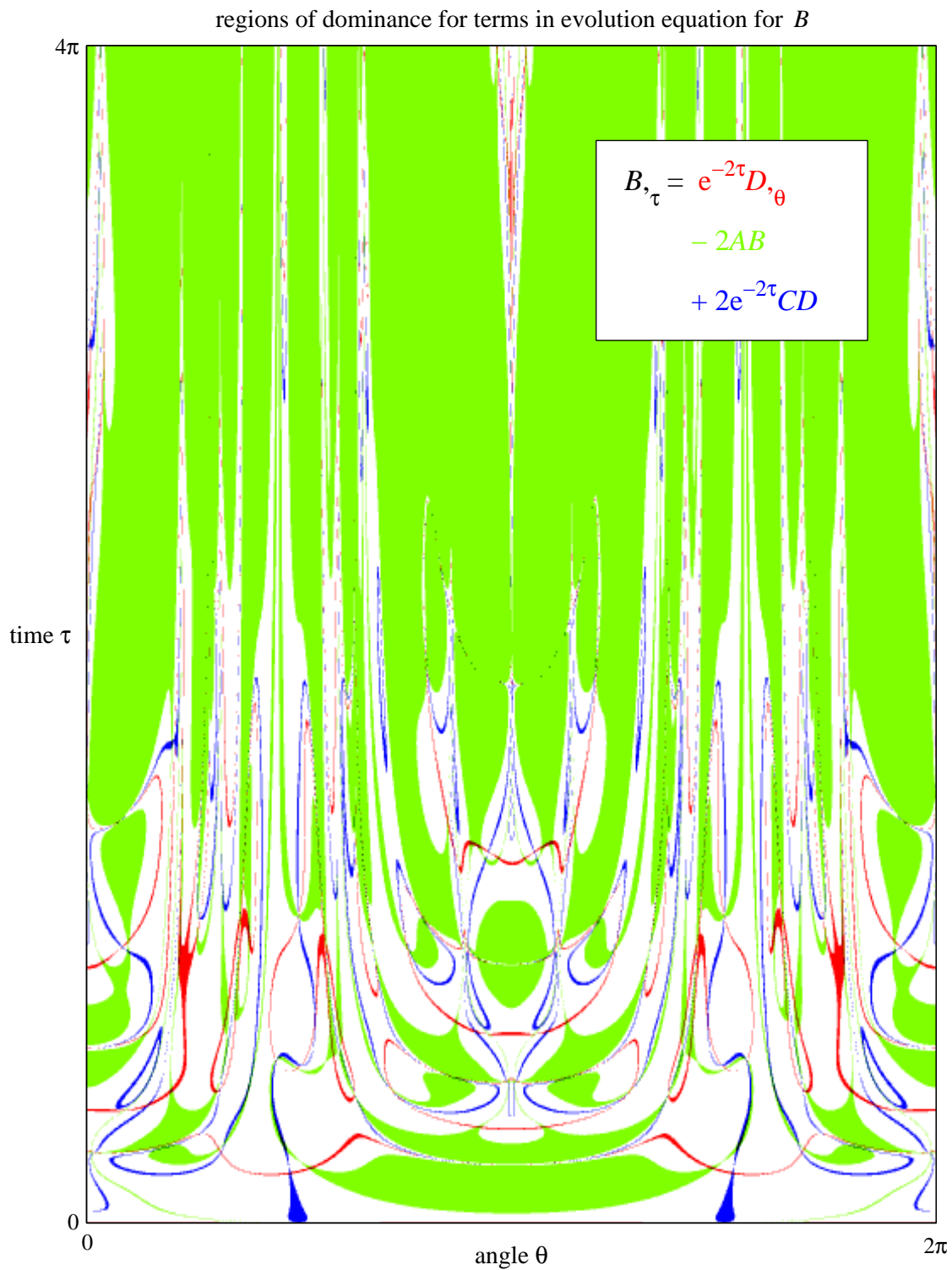


**Figure 6.6:** Dominant terms in the evolution equation (6.16b) for  $B$ . Regions where one of the three terms in the equation dominates the other terms (in the sense described in the text) are coloured red, green or blue as shown in the key. Uncoloured (white) regions are where no terms dominate.

other terms on the right-hand side of the equation. A dominant term effectively determines the behaviour of the equation it is in. Figures 6.5 and 6.6 illustrate this for the wave equations (6.16a) for  $A_{,\tau} \equiv P_{,\tau\tau}$  and (6.16b) for  $B_{,\tau} \equiv Q_{,\tau\tau}$ . The red-coloured regions in  $(\tau, \theta)$ -space are where terms involving  $C_{,\theta}$  or  $D_{,\theta}$  dominate the right-hand sides. The green regions are where terms involving  $A$  or  $B$  dominate, and the blue regions are where terms involving  $C$  or  $D$  dominate. In the white regions no terms dominate. (A slight peculiarity of this definition of dominance is that, since terms can cancel, it is possible for more than one term to dominate an equation at the same time. In figures 6.5 and 6.6 colours merge to black in regions where this happens; it is obvious from the figures that regions of multiple dominance do not play a significant part in the present work.)

It is clear from figures 6.5 and 6.6 that there is very complicated interplay between terms during the early stages of the evolution, and it seems unlikely that the overall behaviour can be traced to simple causes. Berger (1997) notes that spikes form at points where  $D \equiv Q_{,\theta} = 0$  (though not all such zeros produce spikes) and discusses their formation in terms of bounces off of potentials in the evolution equations. In terms of dominance behaviour, spike formation occurs in regions which are blue in figure 6.5 and green in figure 6.6. Berger and Garfinkle (1998) show that approximate versions of the evolution equations (which in effect ignore all but the dominant terms just mentioned) can produce spiky behaviour very much like that observed in the full Gowdy equations.

### *Behaviour of the Second Gowdy Wave Variable*

Sharp features also form in the variable  $Q$  as it evolves. Figure 6.2 shows that between times  $\tau = 2\pi$  and  $\tau = 4\pi$  there develops in  $Q$  a pair of features both comprising a negative spike and a positive spike very close together with a steep gradient between their two peaks. A second, similar pair of double-spike features is also present, but not visible in figure 6.2 because of the scale. The positions of the four double spikes in  $Q$  coincide with the positions of the four negative spikes in the variable  $P$  at time  $\tau = 4\pi$  (see figure 6.1). A close examination of the data reveals that both the positive and negative peaks of each double spike in  $Q$  grow at exponential rates, while the overall width of the feature becomes smaller, and that the negative spikes in  $P$  grow linearly in much the same way that their positive counterparts do. The discussion in the previous subsection regarding the numerical problems caused by the narrowing of spikes applies equally here.

An explanation of how double-spike features form follows from a close examination of the dominance behaviour of the evolution equations for  $A$  and  $B$ . From figures 6.5 and 6.6, together with dominance data produced using finer sub-grids, it can be seen that the region around a double spike is green for both evolution equations, and consequently in such a region the terms proportional to  $\exp(-2\tau)$  are irrelevant and equations (6.16a) and (6.16b) may be approximated as

$$A_{,\tau} \simeq e^{2P} B^2, \quad B_{,\tau} \simeq -2AB.$$

A double spike then forms under the conditions of  $B$  crossing zero at the same time that  $A$  is negative and  $P$  is negative or small and positive. It follows that  $A_{,\tau} \geq 0$  and is small, so that  $A$  remains

negative and  $P$  forms a negative spike. On both sides of the zero  $B$  then grows exponentially, but in opposite directions, and the result is a double spike in  $Q$ . Since  $A_{,\tau} \geq 0$  the region in which  $A < 0$  becomes smaller, and the double spike narrows.

Away from the double spikes,  $Q_{,\tau} \equiv B$  quickly approaches zero and the variable  $Q$  freezes not long after the start of the evolution: except at the double spikes,  $Q$  at late times does not differ from the final plot of figure 6.2. Because of the narrowing effect the second pair of double spikes never becomes a dominant feature in the numerically evolved profile of  $Q$ , although, extrapolating the spikes' initial growth, they quickly become larger than the vertical scale of the figure 6.2.

Considering the steepness of the gradients that develop in the variables  $P$  and  $Q$  it might be expected that the high-resolution wave-propagation scheme for evolving the system (6.16) would perform better than the standard two-step Lax-Wendroff method (see chapter 2 and the discussion at the start of this section). However it turns out that the two integration methods produce nearly identical results. In fact, if wave limiters are used with the high-resolution scheme (see section 2.3) its performance suffers; the loss of second-order accuracy in isolated regions is not compensated for by any improvement in shock resolution. The Gowdy spikes are a different kind of feature to the fluid shock waves that the high-resolution method is designed to track—they are produced by the source rather than the transport part of the evolution equations, as can be deduced from figures 6.5 and 6.6. It is the adaptive mesh refinement code that proves to be the more useful computational tool for this work. The use of mesh refinement here also helps to counteract a shortcoming of the Lax-Wendroff time-stepping scheme: whereas it might be expected that the fine-scale structure in the evolved Gowdy data would be smeared out by the artificial viscosity of the Lax-Wendroff method, the magnitude of the viscosity decreases as the spatial resolution is increased, and regions of fine-scale structure are exactly where the code positions the highest resolution meshes.

### *Behaviour of the Gowdy Background Variable and Conservation of the Constraint*

The evolution of the variable  $\lambda$ , figure 6.3, shows similar features to the evolution of  $P$ , figure 6.1. Negative spikes develop in  $\lambda$  at the same points at which positive spikes develop in  $P$  and, apart from pointing in a different direction, they show the same behaviour: they grow at a constant rate and they narrow until they no longer can be resolved by the simulation. In contrast, no unusual behaviour seems to develop in  $\lambda$  at the points where double spikes form in  $Q$  (although the errors in the data at the double spikes are sufficient to produce erratic behaviour in  $\lambda$  there at late times, as can be seen in figure 6.3).

Equation (6.16g) shows that  $\lambda$  is a decreasing function of time, and it is clear from figure 6.3 that  $\lambda$  becomes large and negative as it evolves. At late times,  $\lambda_{,\tau} \simeq -A^2$  (cf. equation (6.16g)) and  $A$  is approximately constant, so  $\lambda$  grows linearly with a fixed spatial profile.

The constraint equation (6.17) relates the spatial derivative of  $\lambda$  to the values of  $P$  and  $Q$  and their first derivatives. For an exact solution of the evolution equations (6.16) the constraint equation is satisfied at all times if it is satisfied initially, but for a numerical solution this is not necessarily the case. The degree to which the constraint equation fails to hold can be judged by

calculating the total percentage error, defined as

$$\text{error}(\%) = 100 \frac{\|\lambda_{,\theta} + 2(AC + e^{2P}BD)\|}{\|\lambda_{,\theta}\|}, \quad \text{for } \|f\| = \int_0^{2\pi} |f(\theta)| d\theta,$$

where the integrals are evaluated using the trapezium rule and  $\lambda_{,\theta}$  is estimated from  $\lambda$  using second-order finite differencing. Since the errors are known to be disproportionately large at the spikes these points are not included when measuring the constraint. (A region of width 0.02 is excised at each spike, with about ten percent of the total domain being removed.) At time  $\tau = 6\pi$  the error in the constraint is 0.27%, rising to 0.84% by time  $\tau = 50\pi$ .

Instead of evolving  $\lambda$  with equation (6.16g) it could be evaluated at every time step by integrating equation (6.17). This would obviously ensure that the constraint equation is satisfied, and such ‘fully constrained’ approaches are often applied to problems in numerical relativity. However, for this particular problem enforcing the constraint equation in this way would be a very bad idea: the large errors at the spikes would affect the whole of  $\lambda$  rather than being confined to isolated regions.

### *Coordinate Independence of Fine-Scale Structure*

As demonstrated in chapter 5, fine-scale spatial structure can be found even in numerical simulations of homogeneous spacetimes if inappropriate gauge choices are made. The question then arises: is the fine-scale structure found in the unpolarized Gowdy models a coordinate effect? This subsection examines gauge-independent properties of the spacetime and presents evidence for the physical nature of the fine-scale structure (though this evidence is found to be stronger for the positive spikes in  $P$  than it is for the double spikes in  $Q$ ).

The first point to note is that the spiky behaviour in the variables  $P$  and  $Q$  is reflected in the proper lengths of the orbits of the Killing vectors  $\partial/\partial\sigma$  and  $\partial/\partial\delta$  which generate the spacetime’s  $T^2$  isometry group, and so the spikes are not simply a consequence of the choice of variables used to describe the metric. From equation (6.1),

$$\text{proper length of } \sigma\text{-orbits} = 2\pi e^{(P-\tau)/2}, \quad (6.19a)$$

$$\text{proper length of } \delta\text{-orbits} = 2\pi e^{-\tau/2} \sqrt{e^P Q^2 + e^{-P}}. \quad (6.19b)$$

At positive spikes in  $P$  there are spikes in the lengths of both the  $\sigma$ - and the  $\delta$ -orbits (6.19a,b). At negative spikes in  $P$ , corresponding to double-spike features in  $Q$ , there are spikes in the lengths of the  $\delta$ -orbits (6.19b). That the spikes are not a consequence of some kind of local divergence of the spatial coordinates can be seen by examining the proper distance along the  $\theta$ -axis: from the metric (6.1),

$$\text{proper distance element in } \theta\text{-direction} = e^{(\lambda+\tau)/4} d\theta,$$

and since  $\lambda$  either becomes more negative (at positive spikes in  $P$ ) or shows no unusual behaviour (at double spikes in  $Q$ ) in the regions of fine-scale structure, the structure exists on small scales in

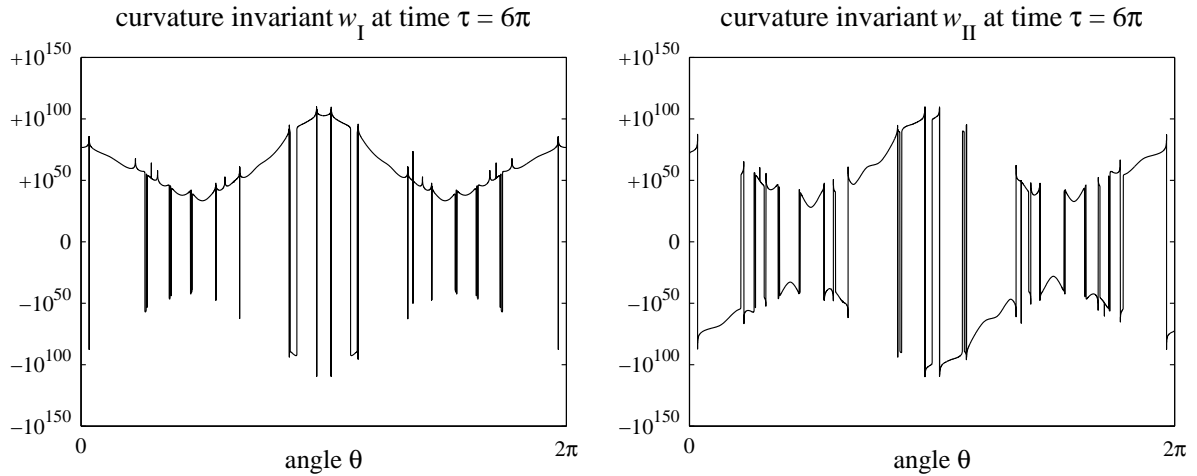


**Figure 6.7:** Curvature invariants  $w_I$  and  $w_{II}$  at time  $\tau = 6\pi$  for initial data set (6.18) evolved using equations (6.16). The curvature invariants are defined by equations (5.1). (A logarithmic vertical scale has been produced by use of the transformation  $w \rightarrow (1/\ln 10) \sinh^{-1}(w/2)$ .)

terms of proper  $\theta$ -distance as well as coordinate  $\theta$ -distance. (This is in contrast to the fine-scale behaviour discovered in section 5.2.)

As discussed in chapter 5 (equations (5.1) in particular), the curvature invariants  $w_I$ ,  $w_{II}$ ,  $w_{III}$  and  $w_{IV}$  provide coordinate-independent information about a spacetime. For the Gowdy metric (6.1) the values of the invariants are calculated using expressions generated by the GRTensorII package (Musgrave, Pollney and Lake 1996) for MapleV. Figure 6.7 shows two of the curvature invariants,  $w_I$  and  $w_{II}$ , evaluated at time  $\tau = 6\pi$ . The following discussion concentrates on these two quantities since  $w_{III}$  and  $w_{IV}$  behave qualitatively the same as, respectively,  $w_I$  and  $w_{II}$ .

The most striking feature of the curvature invariants is their magnitude:  $w_I$  and  $w_{II}$  at  $\tau = 6\pi$  reach both positive and negative values of size greater than ten to the hundredth power. At the start of the evolution  $w_I$  takes values from  $-50$  to  $+30\,000$ , and  $w_{II}$  from  $-2500$  to  $+2500$ . Their subsequent growth is rapid, and shows no signs of reversing. The main influence on the size of the curvature invariants is the factor  $\exp(-\lambda)$  in the expressions for  $w_I$  and  $w_{II}$ . The influence of  $\lambda$  can be seen by comparing the profiles of  $w_I$  in figure 6.7 and  $\lambda$  at  $\tau = 6\pi$  in figure 6.3. The linear growth (towards minus infinity) of  $\lambda$  at late times corresponds to an exponential growth of the curvature invariants.

As figure 6.7 shows, the curvature invariants change sign suddenly at various values of the spatial coordinate  $\theta$ . These sign changes tend to form into clusters which contract in width as the evolution progresses. Figure 6.8 shows a sample of the behaviour of  $w_I$  close up. In  $w_I$  the clusters consist of even numbers of sign changes and the function is predominantly positive, while in  $w_{II}$  they are odd numbered and the function changes sign between clusters. The sign change clusters become narrow in just the same way that the positive spikes in  $P$  do, and indeed the two types of feature coincide spatially. The narrowing, together with the inaccuracies in the data at the

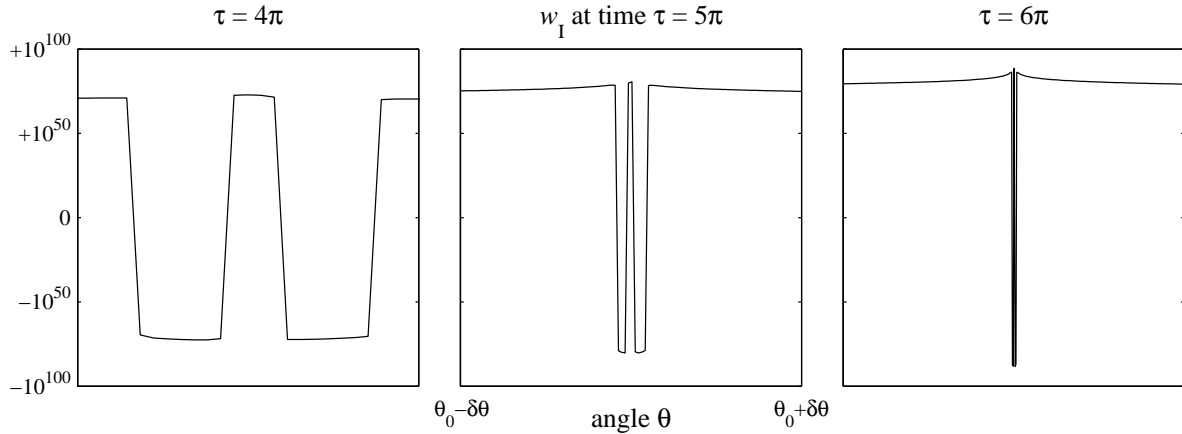


**Figure 6.8:** Close-ups of the curvature invariant  $w_I$  at a positive spike in  $P$  at three different times. The spike is located at coordinate  $\theta_0 = 0.1049$ , and the plots show regions of width  $\delta\theta = 1.0 \times 10^{-2}$  to either side of that point. The axes are the same for all three plots.

spikes, makes determining the precise behaviour of sign changes within a cluster difficult. However, careful examination (figure 6.8) suggests that while the width of a cluster tends to zero, there is no cancellation between the sign changes.

Given the large numbers of terms in the expressions for the curvature invariants, relating their behaviour to features of  $P$ ,  $Q$  and  $\lambda$  is not a simple matter. However, by comparing the magnitudes of individual terms, it is found that at late times the curvature invariants can be approximated by the simplified expressions

$$w_I \simeq (1/32)e^{3\tau-\lambda}(A^2 + 3)(A^2 - 1)^2, \quad (6.20a)$$

$$w_{II} \simeq -(1/16)e^{2\tau+P-\lambda}DA(A + 3)(A - 1)(A + 1)^2. \quad (6.20b)$$

These approximations fail when the values they predict are small: other terms in the curvature invariants clearly cannot be neglected then. The sign changes in  $w_I$  are all clustered around the positive spikes in  $P$ , and this makes sense in terms of the approximation since  $-1 < A < +1$  is found everywhere except at these spikes. (The terms neglected in equation (6.20a) turn out to be negative at the spikes.) The behaviour of  $w_{II}$  is similar, except for the influence of  $D$  in equation (6.20b). At each positive spike in  $P$  there is a zero of  $D$  together with an odd number of sign changes in  $w_{II}$ . Zeros of  $D$  at points where no spikes develop produce isolated sign changes in  $w_{II}$ . However, although a pair of zeros appears in  $D$  where a double spike forms in  $Q$ , no unusual behaviour occurs in  $w_{II}$  there. It seems that zeros in  $A$  counteract the effect of the zeros in  $D$  sufficiently so that terms neglected in equation (6.20b) become significant and prevent  $w_{II}$  from changing sign.

(It should be noted that the sign change clusters in  $w_I$  and  $w_{II}$  evolve at different rates, and this leads to some discrepancies between figure 6.7 and the behaviour described in the paragraph



above. By time  $\tau = 6\pi$  some of the clusters are already too narrow to be resolved and inaccuracies at the double spikes are large enough to cause the invariants to behave erratically there.)

The observed behaviour of the curvature invariants makes it clear that the positive spikes that develop in the variable  $P$  represent physical features of the spacetime and are not simply artifacts of the coordinate system used. However the curvature invariants provide no evidence suggesting any physical significance to the double-spike features that appear in the variable  $Q$ . (Chapter 7 presents results from numerical simulations of cosmological models which have less symmetry than the Gowdy spacetimes, and evidence there suggests that the positive spikes found in the Gowdy variable  $P$  are a generic feature of gravitational collapse.)

Extrapolating the observed behaviour of the curvature invariants forward in time to the singularity at  $\tau = +\infty$  it is clear that they become infinite—except possibly at isolated values of the spatial coordinate  $\theta$  corresponding to the positive spikes in  $P$ . This is in agreement with the curvature behaviour at the singularity conjectured by Moncrief (1981). (The same reference shows that no curvature singularities can develop before  $\tau = +\infty$ , and the results presented here do not suggest otherwise.)

### 6.3 Nature of the Cosmological Singularity

In this section standard pictures of spacetime behaviour close to cosmological singularities are compared to numerically evolved solutions of the Gowdy  $T^3$  model. Evidence suggests that the Gowdy  $T^3$  singularity is asymptotically velocity-term dominated in the sense of Isenberg and Moncrief (1990), but that the evolution of the metric does not spatially decouple as the singularity is approached.

The singularity theorems of Penrose, Hawking and others (see chapter 10 of Hawking and Ellis 1973) show that in general cosmological spacetimes must possess singularities, but they say nothing about the nature of those singularities. Belinskii, Khalatnikov, Lifschitz and co-workers conducted a long-term investigation into spacetime behaviour close to cosmological singularities (work that in fact began some time before the singularities were recognized as being more than a coordinate effect) and their results are collected in the papers Belinskii, Khalatnikov and Lifschitz 1970 and 1982. Aspects of their treatment of singularities in spatially inhomogeneous cosmologies have been extensively criticized (Barrow and Tipler 1979) and much of their reasoning is difficult to follow, but nevertheless the main properties of the Belinskii-Khalatnikov-Lifschitz model of a generic inhomogeneous cosmological singularity have been widely quoted: the presence of matter does not affect the nature of the singularity, and close to it spatial points evolve as independent homogeneous cosmologies of Bianchi type VIII or IX (the ‘mixmaster’ models).

Other early work on the nature of inhomogeneous cosmological singularities was performed by Eardley, Liang and Sachs (1972). They studied families of exact solutions for irrotational dust cosmologies which were found to have ‘velocity-dominated’ behaviour at the singularity: as they approach the singularity the metrics can be approximated by solutions to modified Einstein equations

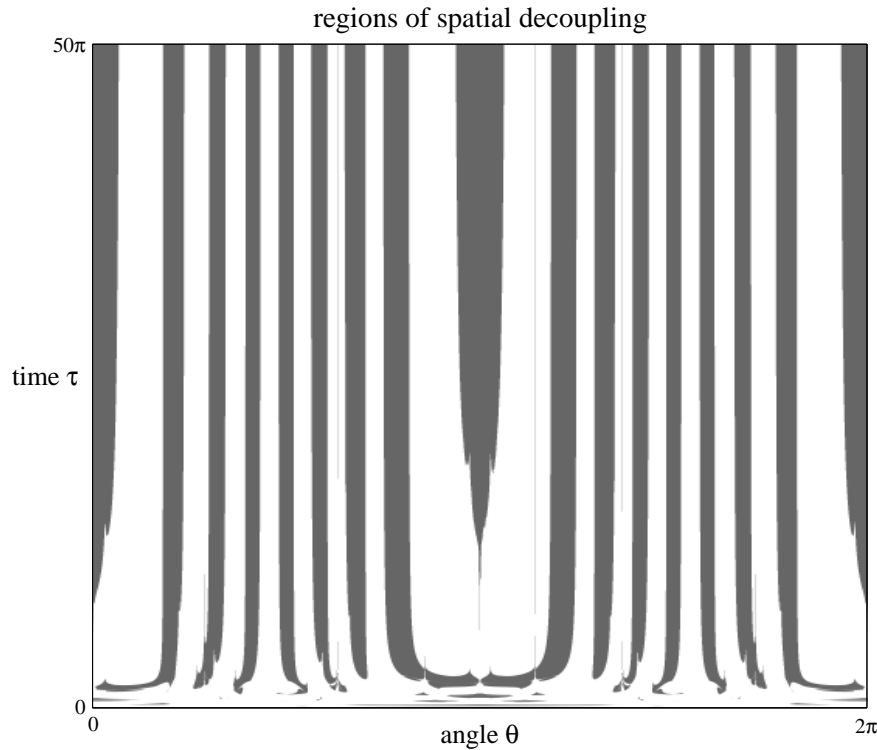


**Figure 6.9:** Shaded regions show where spatial derivative terms in the evolution equations (6.16*a,b*) for the Gowdy  $T^3$  metric are negligible. These regions correspond to the intersection of the green-coloured regions of the two figures 6.5 and 6.6. The evolution does not become completely spatially decoupled within the time range of the simulation.

with spatial curvature terms removed. More recently Isenberg and Moncrief (1990) have reformulated this idea in their definition of asymptotically velocity-term dominated (AVTD) behaviour near a spacelike singularity. A cosmology has AVTD behaviour in the vicinity of the singularity if it admits a foliation by spacelike hypersurfaces on which the metric asymptotically approaches a VTD (velocity-term dominated) solution, the latter being defined as a solution to a modified set of Einstein equations in which spatial derivative terms have been neglected. Although this type of behaviour cannot occur at all cosmological singularities (the mixmaster spacetimes mentioned above are a counter example) the class of spacetimes with AVTD singularities is conjectured to be non-trivial.

Isenberg and Moncrief (1990) have rigorously shown that their definition of AVTD behaviour applies to the polarized Gowdy models with spatial slices defined by the time coordinate  $\tau$  introduced in section 6.1. Perturbative studies of the unpolarized Gowdy  $T^3$  cosmologies led Grubišić and Moncrief (1993) to conjecture that these models also have AVTD behaviour at the singularity, and the numerical simulations of Berger and Moncrief (1993) provide supporting evidence for this conjecture. (See Berger 1998 and Berger et al. 1998 for summaries of numerical investigations of

singularity behaviour in other spacetimes. In particular the Gowdy  $S^1 \times S^2$  model is studied in Garfinkle 1999, and its behaviour is found to be basically the same as that of the Gowdy  $T^3$  model.)

The general VTD solution for the Gowdy  $T^3$  metric (6.1) is given by the equations (6.9) with  $\alpha$ ,  $\beta$ ,  $\eta$ ,  $\chi$  and  $\xi$  now being functions of the spatial coordinate  $\theta$  instead of constants. The behaviour of the VTD solution as the singularity is approached ( $\tau \rightarrow \infty$ ) is then described by

$$P_{\text{AVTD}} = p_0(\theta) + a_0(\theta)\tau, \quad Q_{\text{AVTD}} = q_0(\theta), \quad \lambda_{\text{AVTD}} = l_0(\theta) - a_0(\theta)^2\tau,$$

and this is exactly the form of the numerically evolved solution described in section 6.2 at late times. The present work thus confirms the conclusion of Berger and Moncrief (1993) that the behaviour of numerically evolved Gowdy  $T^3$  solutions is consistent with the presence of an AVTD singularity. Recently Kichenassamy and Rendall (1998) have constructed asymptotic expansions at the singularity for a range of unpolarized Gowdy  $T^3$  solutions and found them all to show AVTD behaviour, further strengthening the case for this being the generic behaviour of the model.

The definitions of velocity-dominated singularities given by Eardley, Liang and Sachs (1972) and Isenberg and Moncrief (1990) are unambiguous. However a commonly used physical picture (possibly deriving from the Belinskii-Khalatnikov-Lifschitz singularity studies) of the spacetime behaviour at inhomogeneous cosmological singularities exchanges mathematical precision for descriptive simplicity: in the approach to a velocity-dominated singularity spatial points are pictured as decoupling, with the spatial derivative terms in the Einstein equations having a negligible effect on the evolution. Although this ‘spatial decoupling’ interpretation of velocity-dominated behaviour is not equivalent to Isenberg and Moncrief’s definition (1990) of AVTD behaviour, it might be hoped that in general the two concepts would apply to the same singularities. Indeed, this idea seems plausible from consideration of the evolution equations (6.2) for the Gowdy  $T^3$  metric (6.1): all spatial derivative terms involve factors of  $\exp(-2\tau)$  and it is not unreasonable to expect that they become negligible as the singularity is approached ( $\tau \rightarrow \infty$ ). However this behaviour is not what is seen in numerical simulations. Figures 6.5 and 6.6 show which terms in the Gowdy evolution equations have most significance at which times, and it is apparent that the terms which are independent of spatial derivatives (the ‘velocity’ terms) do not come to completely dominate the evolution within the time range shown. (Regions where spatial derivatives are negligible are taken here to be those which are coloured green in both figures.) A larger range of time is covered by figure 6.9, but the conclusion is the same: the evidence suggests that it is not the case that spatial derivatives become negligible as the singularity is approached. Thus, although the AVTD hypothesis of Isenberg and Moncrief (1990) holds for the Gowdy  $T^3$  models with the standard choice of time slicing, the spacetime does not spatially decouple as the singularity is approached, in contrast to the picture often presented.

## 6.4 Expanding Planar Cosmologies

In this section the unpolarized Gowdy  $T^3$  models of section 6.1 form the basis of a study of expanding vacuum planar cosmologies. Numerical simulations of the models have been performed to investigate three different types of cosmological behaviour.

In section 6.2, smooth initial fields describing Gowdy cosmologies were evolved backwards in cosmic time towards the ‘big bang’ singularity and were found to develop complicated spatial structure. Reversing the direction of time in these calculations would appear to show that spatial structure is smoothed out by the process of cosmological expansion, a result at odds with the theory of large-scale structure formation. However numerical simulations show that this behaviour is not generic: smooth initial data sets for expanding Gowdy cosmologies can develop complicated spatial structure as they evolve.

The formation of spatial structure in expanding Gowdy cosmologies occurs at times not long after the initial singularity. Numerical simulations have been performed to investigate the behaviour of the Gowdy models at much later times, and it is found that initially strong gravitational waves decrease in amplitude over time and behave qualitatively like standing waves. At sufficiently late times the numerically evolved Gowdy solutions are found to have behaviour similar to that which would be expected for perturbed Kasner spacetimes.

Anninos, Centrella and Matzner (1991b), Shinkai and Maeda (1994), and Ove (1990a) have investigated the properties of nonlinear gravitational waves propagating in expanding cosmological models. Their findings (in particular those concerning the appearance of wave residue and the soliton-like behaviour of gravitational waves) are considered here and compared to results from numerical evolutions of wave packet initial data for the Gowdy metric. The problem of distinguishing nonlinear wave behaviour from gauge effects is discussed.

### *Numerical Simulations of Expanding Gowdy $T^3$ Spacetimes*

The Einstein equations for the metric (6.5) are given as equations (6.6). Recall that the expanding time coordinate  $t$  ranges from 0 to  $+\infty$ , with  $t = 0$  labelling the cosmological singularity. A first-order evolution system is produced by the definition of new variables

$$A \equiv P_{,t}, \quad B \equiv Q_{,t}, \quad C \equiv P_{,\theta}, \quad D \equiv Q_{,\theta},$$

where the variables  $A$  and  $B$  used here differ from the analogous variables of equation (6.15). The first-order evolution equations are then

$$A_{,t} - C_{,\theta} = e^{2P}(B^2 - D^2) - A/t, \tag{6.21a}$$

$$B_{,t} - D_{,\theta} = -2(AB - CD) - B/t, \tag{6.21b}$$

$$C_{,t} - A_{,\theta} = 0, \tag{6.21c}$$

$$D_{,t} - B_{,\theta} = 0, \tag{6.21d}$$

$$P_{,t} = A, \tag{6.21e}$$

$$Q_{,t} = B, \quad (6.21f)$$

$$\lambda_{,t} = t(A^2 + C^2) + te^{2P}(B^2 + D^2), \quad (6.21g)$$

together with the constraint equation

$$\lambda_{,\theta} = 2t(AC + e^{2P}BD). \quad (6.22)$$

The principal part (left-hand side) of the evolution system (6.21) has a particularly simple form: it consists of two flat-space wave equations for the variable pairs  $A$  and  $C$ , and  $B$  and  $D$ .

The code for evolving equations (6.21) has been put through the same set of tests as the code described in section 6.2. In addition, the two codes have been compared to check that evolving data forwards with one produces the same results as evolving data backwards with the other. Approximate solutions to the linearized equations discussed later in this section provide another test of the code.

The general set-up of the numerical simulations discussed here is the same as for those in section 6.2, with the exception that variable-size time steps are not needed since the largest characteristic speed of the system (6.21) is a constant (see equation (6.8)). Three different kinds of simulation are discussed in this section, and further details of the numerical set-ups used are given as appropriate in the following subsections.

### *Spatial Structure Formation in Expanding Gowdy Cosmologies*

In section 6.2 smooth initial data sets (6.18) for the collapsing Gowdy  $T^3$  metric (6.1) were numerically evolved and found to develop complicated spatial structure on very fine scales. Experimentation with a range of initial data sets showed this behaviour to be typical of the collapsing Gowdy models, with the magnitude of the initial data determining the amount of spatial structure that developed. The time-reversals of these simulations provide examples of expanding cosmologies, and present an unexpected picture of cosmological behaviour: spacetimes which have very complicated spatial structures a short time after the big bang lose all of that structure as they expand. It is known (Moncrief 1981) that the Gowdy  $T^3$  metrics contain no singularities apart from the cosmological singularity which is always present. This rules out the possibility of gravitational waves interacting sufficiently strongly to produce black hole-like objects in the models; however it would be surprising if strong gravitational waves were not able to produce some kind of spatial structure in the expanding Gowdy spacetimes.

In this subsection results are presented from numerical simulations of Gowdy cosmologies analogous to the simulations of section 6.2 but with the spacetimes expanding rather than collapsing. For initial data containing ‘strong’ gravitational waves close to the initial singularity, complicated spatial structure develops just as in the collapsing case, and the time-reversed results of section 6.2 are seen not to describe the generic behaviour of expanding cosmologies.

The system of equations (6.21) is evolved numerically using the initial data set

$$\begin{aligned} P &= 0, & Q &= \cos \theta, & \lambda &= 0, \\ P_{,t} &= -v_0 \cos \theta / t_0, & Q_{,t} &= 0, & & \text{at time } t = t_0, \end{aligned} \quad (6.23)$$

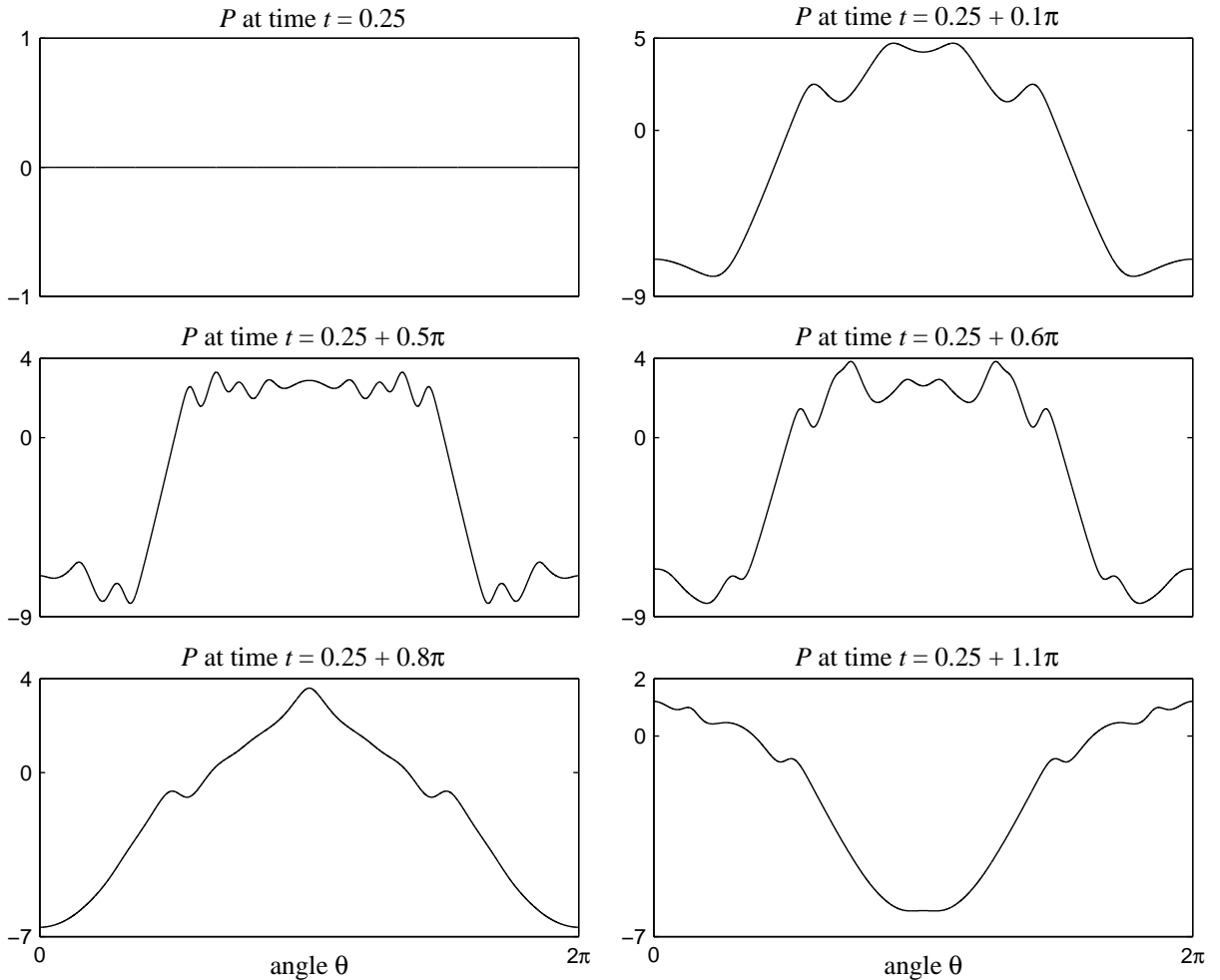


**Figure 6.10:** Wave variable  $P(t, \theta)$  of expanding Gowdy metric (6.5) at six different times. Initial data set (6.23) with  $t_0 = 0.25$  and  $v_0 = 15$  is evolved using equations (6.21). Spatial structure forms at times close to the initial singularity.

which, if the initial time  $t_0$  is taken equal to 1, is the same as the initial data set used in section 6.2 (cf. equation (6.18) with the time coordinate transformed according to equation (6.4)). As in the collapsing case, the parameter  $v_0$  determines the strength (in some sense) of the gravitational waves in the initial data. An initial time of  $t_0 = 0.25$  (corresponding to  $\tau$  equal to 1.386) is used so that the influence of proximity to the cosmological singularity is manifest in the results. The numerical simulations are performed using a base grid of resolution  $\Delta\theta = 2\pi/4000$  with adaptive mesh refinement allowing the resolution to increase up to  $\Delta\theta = 2\pi/64000$ .

Spatial structure forms (in the sense that high frequency modes are excited) for large amplitude waves at times close to the time of the initial singularity. Figure 6.10 shows the wave variable  $P(t, \theta)$  at various stages during the numerical evolution of initial data (6.23) with the choice of amplitude parameter  $v_0 = 15$ , and it is clear that nonlinear effects produce complicated behaviour in the variable. Spatial structure is produced early on in the simulation; at later times the behaviour of

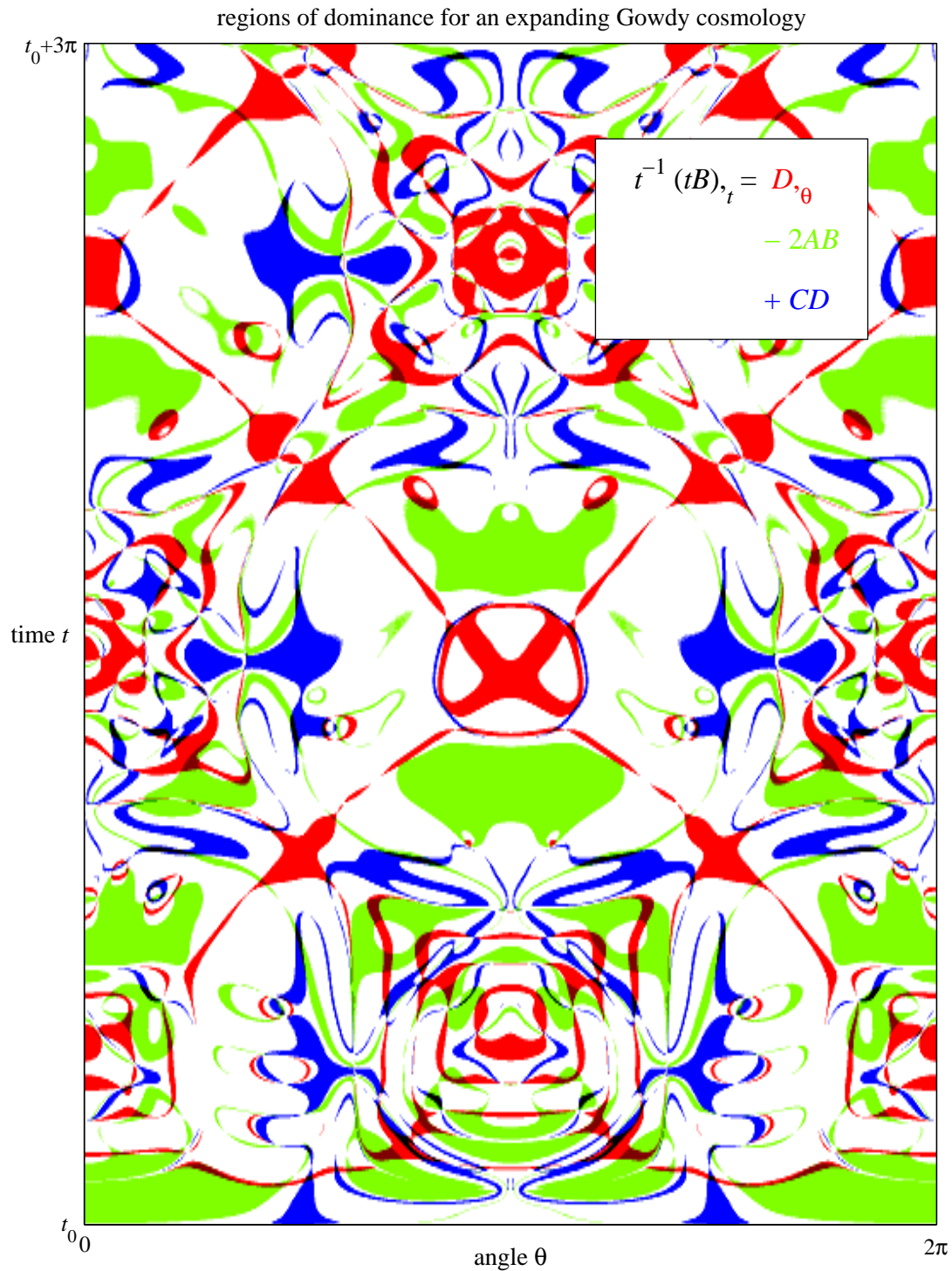


**Figure 6.11:** Dominant terms in the evolution equation (6.21b) for  $B$ . Initial data set (6.23) with  $v_0 = 10$  and  $t_0 = 0.25$  is evolved for the expanding Gowdy model. Regions are coloured red, green or blue according to which term dominates the evolution equation (as shown in the key), or are white if no term dominates. This figure shows for the expanding Gowdy model what figure 6.5 shows for the collapsing model. (The definition of dominance is discussed in section 6.2.)

the variable  $P$  is qualitatively that of a standing wave. Similar behaviour is seen for the second wave variable  $Q$ , while the background variable  $\lambda$  remains relatively smooth throughout. The curvature invariants decrease in magnitude very rapidly during the course of the simulation.

Figure 6.11 provides an illustration of the overall behaviour of an expanding Gowdy  $T^3$  cosmology. The dominant terms in the evolution equation (6.21b) for  $B \equiv Q_{,t}$  are shown for initial data (6.23) with  $v_0 = 10$ ; it is the expanding cosmology version of figure 6.5 from section 6.2. The two main qualitative features of the simulation are apparent in the figure: complex behaviour occurs on small spatial scales, and the overall pattern of the evolution has the form of a standing wave, repeating with time period  $\Delta t = 2\pi$ .

Away from the initial singularity nonlinear effects are much less apparent in the evolution and the amplitudes of the standing waves in the variables  $P$  and  $Q$  are seen to gradually decrease. This motivates the study of late-time behaviour of Gowdy  $T^3$  spacetimes.

### *Late-Time Gowdy Behaviour I: A First-Order Model*

Misner (1968) proposed a programme of cosmological research in which spacetimes with a high degree of anisotropy close to a ‘big bang’ singularity would be examined to see to what extent the properties of the presently observable universe are a typical outcome of evolution by Einstein’s equations (see the comments on ‘chaotic cosmology’ in Carmeli, Charach and Malin 1981). Although the Gowdy spacetimes do not provide realistic models of the observable universe, they can still be used to find a partial answer to the question (in the spirit of Misner’s proposal) of what range of initial data for Einstein’s equations leads to spacetimes which are approximately homogeneous at late times. The next subsection examines numerically evolved cosmologies and shows them to provide evidence that the late-time behaviour of a general Gowdy  $T^3$  spacetime tends towards that of a perturbed homogeneous cosmology. Prior to that, in the present subsection the Gowdy evolution equations are linearized and used to construct a model of the late-time behaviour of an approximately homogeneous Gowdy spacetime.

Consider first the wave variables  $P$  and  $Q$  of the expanding Gowdy  $T^3$  metric (6.5). It is assumed that the late-time (large  $t$ ) behaviour of these variables is close to the form they have in the homogeneous case given in equations (6.9). As the time  $t$  becomes large the homogeneous solution (6.9) approaches

$$P_{\text{homog}} = \ln(\alpha t^\beta), \quad Q_{\text{homog}} = \eta, \quad (6.24)$$

where  $\alpha$ ,  $\beta$  and  $\eta$  are constants with  $\beta$ , the Kasner expansion parameter, being non-negative. (Note that the late-time homogeneous solution (6.24) is an exact solution of the Gowdy equations, as can be seen by comparing it to the general homogeneous solution (6.9).) A Gowdy solution which is approximately homogeneous at late times is then assumed to have the form

$$P = P_{\text{homog}} + \delta P, \quad Q = Q_{\text{homog}} + \delta Q, \quad (6.25)$$

where  $\delta P$  and  $\delta Q$  are small perturbations which are negligible at second order. Substituting the variables  $P$  and  $Q$  of equations (6.25) into the evolution equations (6.6a,b) produces evolution



equations for the perturbations  $\delta P$  and  $\delta Q$ ,

$$\delta P_{,tt} = \delta P_{,\theta\theta} - (1/t)\delta P_{,t}, \quad (6.26a)$$

$$\delta Q_{,tt} = \delta Q_{,\theta\theta} - ((1 + 2\beta)/t)\delta Q_{,t}, \quad (6.26b)$$

where terms of second and higher order in  $\delta P$  and  $\delta Q$  have been omitted. These equations have exact solutions

$$\delta P = a_0 \ln t + b_0 + \sum_{n=1}^{\infty} \left( Z_{+n}(t) \cos(n\theta) + Z_{-n}(t) \sin(n\theta) \right), \quad (6.27a)$$

$$\text{with } Z_{\pm n}(t) = a_{\pm n} J_0(|n|t) + b_{\pm n} Y_0(|n|t) \quad \text{for } n \neq 0,$$

$$\delta Q = \left\{ \begin{array}{l} c_0 \ln t \text{ for } \beta = 0 \\ c_0 t^{-2\beta} \text{ for } \beta > 0 \end{array} \right\} + d_0 + t^{-\beta} \sum_{n=1}^{\infty} \left( W_{+n}(t) \cos(n\theta) + W_{-n}(t) \sin(n\theta) \right), \quad (6.27b)$$

$$\text{with } W_{\pm n}(t) = c_{\pm n} J_{\beta}(|n|t) + d_{\pm n} Y_{\beta}(|n|t) \quad \text{for } n \neq 0,$$

where the  $a_{\pm n}$ ,  $b_{\pm n}$ ,  $c_{\pm n}$  and  $d_{\pm n}$  are constants, and  $J_i(x)$  and  $Y_i(x)$  are Bessel functions. (Note that equation (6.27a) is the same as equation (6.12), the general solution for the polarized Gowdy model with  $Q \equiv 0$ .) The equations (6.27) for  $\delta P$  and  $\delta Q$  include some zeroth-order mode terms which do not tend to zero as the time  $t$  becomes large. The terms  $a_0 \ln t$ ,  $b_0$  and  $d_0$  can be absorbed into the background homogeneous solution (6.24), whereas the term  $c_0 \ln t$  (which can only be present if the constant  $\beta$  is zero) must be neglected on the grounds that it contradicts the assumption that  $\delta Q$  is small at late times. If in addition the Bessel functions in the expressions for  $\delta P$  and  $\delta Q$  are replaced by their approximate forms for late times (see equations (5.20)) then the expressions (6.25) for  $P$  and  $Q$  can be written as

$$P \simeq \ln(\alpha t^{\beta}) + t^{-1/2} \sum \text{oscillations}, \quad (6.28a)$$

$$Q \simeq \eta + \underbrace{c_0 t^{-2\beta}}_{\text{if } \beta > 0} + t^{-\beta-1/2} \sum \text{oscillations}, \quad (6.28b)$$

where each oscillation term has the form  $\mu \cos(n\theta) \cos(nt - \nu)$  for  $\mu$  and  $\nu$  constants, where either or both of the cosines may be replaced by sines.

Equations (6.28) provide a first-order description of the behaviour of the Gowdy wave variables  $P$  and  $Q$  at late times under the assumption that the spacetime is approximately homogeneous then. It is straightforward to check that the expressions (6.28) for  $P$  and  $Q$  are consistent with the evolution equations (6.6a,b) in the sense that the second- and higher-order terms that were omitted from equations (6.26) tend to zero as  $t$  tends to infinity under substitution of these forms for  $P$  and  $Q$ .

The late-time behaviour of the Gowdy background variable  $\lambda$  can now be investigated. As before, the variable is assumed to have the form of a perturbed homogeneous solution, analogous to equations (6.24) and (6.25), and so, from equation (6.9),

$$\lambda = \lambda_{\text{homog}} + \delta\lambda \quad \text{with } \lambda_{\text{homog}} = \chi + \beta^2 \ln t, \quad (6.29)$$

where  $\chi$  is a constant and  $\beta$  has the same value as in equation (6.24). If the evolution and constraint equations (6.6*c,d*) for  $\lambda$  are expanded to first order in the perturbations  $\delta\lambda$ ,  $\delta P$  and  $\delta Q$  using equations (6.29), (6.24) and (6.25), then it is found that  $\delta\lambda = 2\beta\delta P$  to within addition of a constant term which can be absorbed into the value of  $\chi$  in equation (6.29). Using the expression for  $\delta P$  from equation (6.28*a*), the perturbation  $\delta\lambda$  is seen to approach zero as time  $t$  becomes large. However, the long-term behaviour of  $\delta\lambda$  is found to be qualitatively different from this if terms at higher than first order are considered: if the expressions (6.28) for  $P$  and  $Q$  are substituted into the evolution equation (6.6*c*) for  $\lambda$ , then it is found that

$$\delta\lambda_{,t} = \left( \sum \text{oscillations} \right)^2 + (\text{terms that become negligible as } t \rightarrow \infty), \quad (6.30)$$

and so at sufficiently late times  $\delta\lambda$  grows approximately linearly. As a consequence, so does the variable  $\lambda$ . The approximately homogeneous Gowdy model constructed here thus turns out to resemble a homogeneous Gowdy solution at late times only in terms of the wave variables  $P$  and  $Q$ ; not only does the background variable  $\lambda$  have a late-time form which is different from the form it has in a homogeneous solution (equation (6.29)), but also the amplitudes of the oscillations in the variable do not decay to zero as the time  $t$  tends to infinity. (Similar behaviour has been reported for different cosmological models by Adams et al. 1982.)

The linear growth of  $\lambda$  at late times means that perturbations can significantly change the overall behaviour of a homogeneous spacetime. Consider a homogeneous Gowdy solution (6.9) with  $\beta < 1$ . As can be seen from the metric (6.5) this spacetime undergoes collapse in the direction of the  $\theta$ -axis as time  $t$  tends to infinity. (Equation (6.11) shows how this behaviour relates to the standard Kasner cosmologies in which one spatial direction always contracts as the other two expand.) However, if the wave variables  $P$  and  $Q$  of the homogeneous spacetime are perturbed slightly, then at sufficiently late times the variable  $\lambda$  will grow linearly rather than logarithmically, and the spacetime will expand rather than contract along the  $\theta$ -axis. In effect, an infinitesimal amount of gravitational radiation propagating in the direction of contraction of a Kasner spacetime is sufficient to reverse the contraction at late times and cause the spacetime to expand in all spatial directions. This type of behaviour is consistent with Isaacson's work (1968*a,b*) on gravitational waves, and has been previously observed in numerically evolved planar cosmologies by Centrella (1986); the perturbed spacetime can be thought of as a homogeneous solution of Einstein's equations with an effective energy-momentum tensor describing short wave gravitational radiation (Isaacson 1968*a,b*; section 35.13 of Misner, Thorne and Wheeler 1973). (The effective energy-momentum tensor for gravitational waves in a polarized Gowdy  $T^3$  spacetime is constructed in Berger 1974.)

In summary, if a Gowdy spacetime is approximately homogeneous at some time long after the 'big bang' took place, then its subsequent behaviour will be described by equations (6.28) with the background variable  $\lambda$  growing approximately linearly. In the next subsection this model of late-time Gowdy behaviour is compared to results from numerical simulations.

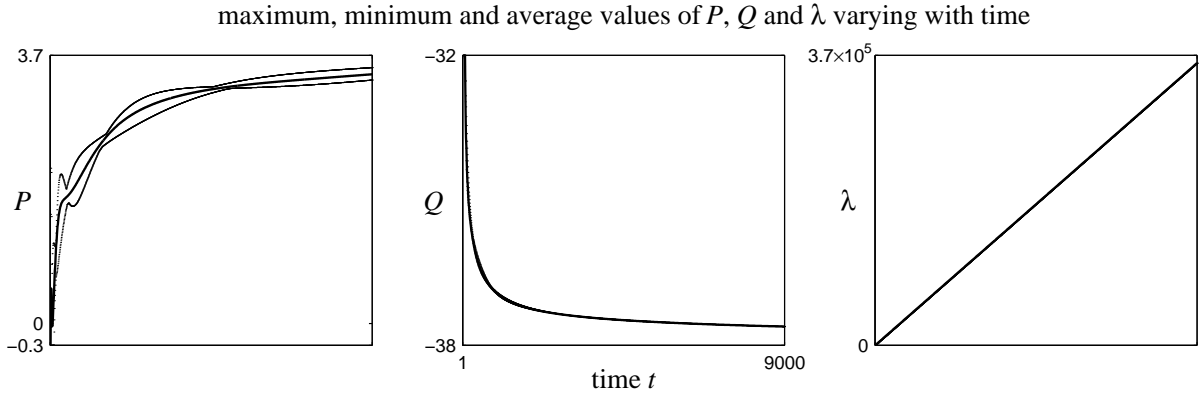


**Figure 6.12:** Behaviour of the variables  $P$ ,  $Q$  and  $\lambda$  at late times. Initial data set (6.31) for the metric (6.5) with  $v_P = v_Q = 7.5$  and  $\beta_0 = 0.75$  is evolved numerically. The average value of each variable is plotted as a solid line together with its maximum and minimum values plotted as individual points. The averages, maxima and minima are taken over all space and over time intervals of size  $\Delta t = 2\pi$ . (The time axis is the same for all three plots and is linear.)

### *Late-Time Gowdy Behaviour II: Numerical Simulations*

Earlier in this section expanding Gowdy  $T^3$  spacetimes containing strong gravitational waves close to the initial singularity were investigated. Numerical simulations showed their behaviour to be complicated with spatial structure forming on fine scales. However, away from the initial singularity it was found that the amplitudes of oscillations in the metric variables tend to decay and their behaviour becomes qualitatively like that of standing waves in flat space (much as would be expected for weak gravitational waves propagating in an expanding spacetime). In this subsection the behaviours of Gowdy cosmologies at times long after the ‘big bang’ are investigated numerically and the results are compared to the model of a perturbed homogeneous cosmology constructed in the previous subsection. (Similar numerical investigations of the approach to homogeneity for initially inhomogeneous expanding planar spacetimes are reported in Shinkai and Maeda 1993 and 1994; there a positive cosmological constant is assumed, and only one polarization of gravitational radiation is considered.)

Numerical simulations are performed using the initial data set (cf. equation (6.23))

$$\begin{aligned} P &= 0, & Q &= v_Q \cos \theta, & \lambda &= 0, \\ P_{,t} &= \beta_0 - v_P \cos \theta, & Q_{,t} &= 0, & & \text{at time } t = 1, \end{aligned} \quad (6.31)$$

where  $v_P$  and  $v_Q$  are viewed as measuring the amplitudes of the initial gravitational waves and  $\beta_0$  as describing the background spacetime in which the waves propagate (it is analogous to the constant  $\beta$  in the homogeneous solution (6.9)). The constraint on the initial data, equation (6.22), is trivially satisfied. When  $v_P$  and  $v_Q$  are small (much less than one) the numerically evolved solution can be compared to the exact linearized solution (6.27) derived in the previous subsection for a perturbed homogeneous spacetime. The good agreement between the two provides evidence

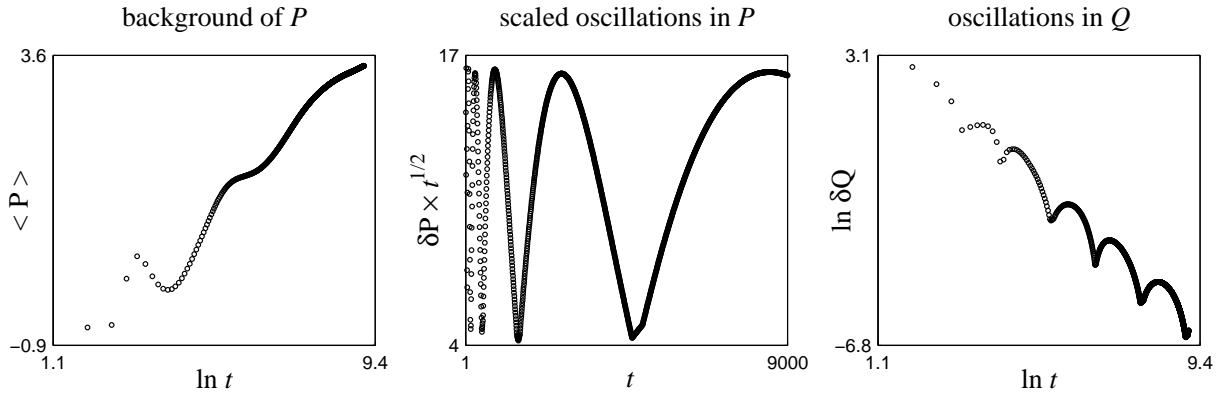


**Figure 6.13:** The numerical results shown in figure 6.12 are re-plotted to allow comparison with the predicted behaviour given in equations (6.28) for  $P$  and  $Q$  in a spacetime which is approximately homogeneous. The quantity  $\langle P \rangle$  is the spatial average of the numerically evolved  $P$  (as plotted in figure 6.12) while the quantity  $\delta P$  is the size of the oscillations in  $P$ , the difference between the maximum and minimum values of the variable. Analogous quantities are defined for the numerically evolved  $Q$ . (As in figure 6.12 each data point plotted here represents a time interval of size  $\Delta t = 2\pi$ .)

for the validity both of the numerical code and of the first-order solution. For larger  $v_P$  or  $v_Q$  the evolution of the numerical solution is initially nonlinear and the late-time behaviour of the spacetime is not easily predicted; in particular the question of whether or not cosmological expansion makes the spacetime homogeneous at late times (in the sense that it behaves then like a perturbed homogeneous spacetime) is investigated here.

Figure 6.12 shows results for the numerical evolution of initial data (6.31) with  $v_P = v_Q = 7.5$  and  $\beta_0 = 0.75$  using the system of equations (6.21). (The value of  $\beta_0$  used here produces a Kasner cosmology which is collapsing in the direction of the  $\theta$ -axis if both  $v_P$  and  $v_Q$  are zero.) The simulation used a spatial resolution of  $\Delta\theta = 2\pi/3200$  and was run for approximately four million time steps. Adaptive mesh refinement (described in chapter 3) was found to be an impractical method for use on this problem; although the local truncation error of the numerical evolution could be estimated in the usual way, the variation in magnitude of the variables (over large time scales in addition to rapid oscillations) made it difficult to define a refinement criterion which was effective throughout the entire time range of the simulation.

It is clear from figure 6.12 that the late-time behaviour of the evolved solution is broadly similar to the behaviour of the perturbed homogeneous model considered in the previous subsection: the variables  $P$  and  $Q$  approach the form of the homogeneous background solution given in equation (6.24) ( $P$  grows logarithmically,  $Q$  tends to a constant, and the amplitudes of the oscillations decrease in size) while the variable  $\lambda$  grows linearly. In figure 6.13 the numerical solution is re-plotted so as to allow a more detailed comparison with the perturbed homogeneous solution (6.28). In the first plot of the figure the spatial average of  $P$  is shown against a logarithmic time axis; for an

approximately homogeneous solution this plot is linear with gradient equal to the background Kasner parameter  $\beta$ . The second plot shows the size of the oscillations in  $P$  scaled by the square root of the time  $t$ ; for an approximately homogeneous solution the peaks in this plot reach a constant height. The third plot shows the size of the oscillations in  $Q$  against time on logarithmic axes; for an approximately homogeneous solution this plot is linear overall with gradient equal to  $-(\beta+1/2)$ . It is apparent from figure 6.13 that as time passes the behaviour of the evolved solution becomes increasingly like that of a perturbed homogeneous cosmology. Numerical evidence thus supports the conjecture that strong initial inhomogeneities in a Gowdy  $T^3$  spacetime do not prevent the spacetime from being close to homogeneous at late times.

The first and third plots of figure 6.13 allow values to be estimated for  $\beta$ , the Kasner parameter for the homogeneous background solution given in equation (6.24). From the first plot it is estimated that  $0.55 < \beta < 0.65$  while from the third plot it is estimated that  $0.65 < \beta < 0.75$ , and the two results suggest a value for  $\beta$  of around 0.65. This estimate is to be compared with the value of 0.75 used for the parameter  $\beta_0$  in the initial data set (6.31). If  $\beta_0$  is thought of as describing an initial homogeneous background in the same way that  $\beta$  describes the late-time homogeneous background then it can be seen from equations (6.10) and (6.11) that the  $\sigma$ - $\delta$  symmetry plane of the Gowdy model is slightly more isotropic at late times than it is initially, but that the isotropy of the spacetime does not increase indefinitely, in contrast to its homogeneity.

Figure 6.13 also reveals a feature of the late-time behaviour of an initially strongly inhomogeneous Gowdy cosmology which is not present in the first-order solution (6.28) (or in numerical simulations based on initial data containing only weak gravitational waves). From the second and third plots it can be seen that the wave variables  $P$  and  $Q$  have oscillatory behaviour on time scales which increase in size exponentially during the course of the simulation. By contrast, from equation (6.28), the longest time period that would be expected for oscillations in an approximately homogeneous spacetime is  $\Delta t = 2\pi$ , and such oscillations would not even be visible in figure 6.13. It would seem that these low frequency oscillations are some kind of nonlinear effect of the Gowdy spacetime's approach to late-time homogeneity. (It is interesting to speculate as to whether there might be an underlying connection between this behaviour and the oscillations on logarithmic time scales that occur during the spherically symmetric collapse of massless scalar fields: there the oscillations have time periods which decrease exponentially prior to the formation of a central singularity, and with the direction of time reversed the third plot of figure 6.13 can be seen to be similar to, for example, figure 5 of Hamadé and Stewart 1996.)

### *Linear and Nonlinear Gravitational Waves*

The general behaviour of gravitational waves in planar cosmologies is well understood only for waves which have amplitudes that are small enough to allow the application of linearized theory. Various researchers have compared perturbative models to numerical solutions at the point at which the first-order approximation becomes inaccurate in order to identify new features that emerge as the behaviour becomes nonlinear. (In addition, linearized gravitational wave models are often used

as code tests; see Centrella 1986, Anninos, Centrella and Matzner 1991a, Anninos et al. 1997, and Anninos 1998a, among others.) In the previous subsection the late-time behaviour of a numerically evolved Gowdy  $T^3$  cosmology was compared to a simple model containing linear gravitational waves; in the present subsection linear and nonlinear gravitational waves are compared and their differences in behaviour are highlighted.

As a first step in the investigation, a family of initial data sets is chosen for which continuous parameters determine the strength (in some sense) of the gravitational waves which are present. When the parameters are zero the initial data set describes an exact homogeneous solution, and for parameter values close to zero the evolution can be approximated by a system of first-order equations produced by linearization about the homogeneous solution. As the parameters become larger the inaccuracies in the linear approximation grow and the wave behaviour in the evolved solution becomes nonlinear. In the present work the axisymmetric Kasner spacetime has been chosen as the homogeneous background solution: it is described by the metric (6.5) with variables  $P$ ,  $Q$  and  $\lambda$  identically zero. (As discussed in section 6.1 wave motion in the Gowdy spacetimes is determined by the variables  $P$  and  $Q$ , and the background variable  $\lambda$  plays no part in the following discussion.) The linear range of initial data sets then comprises values of the variables  $P$  and  $Q$  (and their derivatives) which are close to zero, and for such values the evolution equations (6.6) linearized about the homogeneous solution have exact solutions

$$P_{\text{linear}} = a_0 \ln t + b_0 + \sum_{n=1}^{\infty} \left( Z_{+n}(t) \cos(n\theta) + Z_{-n}(t) \sin(n\theta) \right), \quad (6.32a)$$

$$\text{with } Z_{\pm n}(t) = a_{\pm n} J_0(|n|t) + b_{\pm n} Y_0(|n|t) \quad \text{for } n \neq 0,$$

$$Q_{\text{linear}} = c_0 \ln t + d_0 + \sum_{n=1}^{\infty} \left( W_{+n}(t) \cos(n\theta) + W_{-n}(t) \sin(n\theta) \right), \quad (6.32b)$$

$$\text{with } W_{\pm n}(t) = c_{\pm n} J_0(|n|t) + d_{\pm n} Y_0(|n|t) \quad \text{for } n \neq 0,$$

for  $a_{\pm n}$ ,  $b_{\pm n}$ ,  $c_{\pm n}$  and  $d_{\pm n}$  constants, which were derived earlier as equations (6.27) (with the parameter  $\beta$  here set to zero).

For the polarized Gowdy spacetimes in which the variable  $Q$  is identically zero, the equation (6.32a) for  $P$  is the exact solution even when the variable is large (compare equation (6.12)), and so gravitational waves in a polarized Gowdy spacetime are always linear. (It is interesting to note that many numerical studies of planar cosmological spacetimes have, as noted in the introduction to this chapter, only considered polarized metrics, and this may go some way to explaining why the behaviour observed there has been essentially linear.) Although the linear solution (6.32b) for the variable  $Q$  has the same form as the solution (6.32a) for  $P$ , the behaviour of  $Q$  is genuinely nonlinear for large amplitude waves. In addition, wave motion in  $Q$  excites wave motion in  $P$ : the variable  $P$  cannot be identically zero unless the variable  $Q$  is trivial.

The numerical simulations described in this subsection use initial data sets of the following form, for which the constraint equation (6.22) is satisfied exactly:

$$\begin{aligned} P &= \dots, & Q &= \dots, & \lambda &= 0, \\ P_{,t} &= 0, & Q_{,t} &= 0, & \text{at time } t &= t_0, \end{aligned} \quad (6.33)$$

where  $P$  and  $Q$  have initial values (specified below) based on the Gaussian-like function

$$\varphi(\theta; \mu) = e^{\mu(\sin \theta - 1)}, \quad (6.34)$$

in which  $\mu$  is a measure of the pulse width. This function has a profile similar to a Gaussian distribution, but is preferred for the present work since it is spatially periodic. If a single wave packet having the initial form  $P = \varphi(\theta)$ ,  $P_{,t} = 0$  is evolved with the flat space wave equation  $P_{,tt} = P_{,\theta\theta}$  then the behaviour observed is as follows: the initial wave packet splits into two similar wave packets each of half the original amplitude which travel in opposite directions with unit speed; after one half cycle the two smaller wave packets collide and recombine into their original form. For the linearized Gowdy evolution equations the behaviour is similar to this at late times (as can be seen from equations (6.32) if the large parameter approximations (5.20) to the Bessel functions are used) with the difference that the amplitudes of the wave packets decrease in time. The qualitative behaviour of wave packets in the linear regime can be used as a reference against which the evolution of nonlinear wave packets can be compared.

Ove (1990a,b) examined the nonlinear evolution of planar Gaussian wave packets (of both polarizations) using a numerical code for evolving  $U(1)$ -symmetric cosmologies (discussed further in chapter 7). For a particular choice of background spacetime he found that in the linear limit of his field equations gravitational waves evolved according to the flat space wave equation, and he subsequently identified a qualitative difference between the evolutions of large and small amplitude wave packets which he concluded to be a nonlinear effect: when a large amplitude wave packet splits in two it leaves in its wake an approximately constant value which differs from the value zero which would be expected for linear behaviour. This effect he termed ‘gravitational wave residue’. Anninos, Centrella and Matzner (1991b) also evolved nonlinear wave packet initial data in a cosmological setting, though for a very different choice of metric variables and gauge, and they too reported behaviour consistent with Ove’s wave residue effect. (While similar behaviour is also described in Anninos et al. 1997 for studies of gravitational waves in Minkowski spacetime, in that case it is identified as being an artifact of lack of convergence in the numerical code.)

In the present work, variable and coordinate choices differ from those of the studies mentioned above, and while a gravitational wave residue effect is observed in numerical simulations of wave packet initial data, here it is seen to be more of a linear than a nonlinear effect. Figure 6.14 illustrates this point. Two sets of initial data, both comprising large amplitude wave packets, were evolved:

$$\begin{aligned} \text{case I:} & \quad P = 5\varphi(\theta; 10), & \quad Q = 0, & & \text{for } t_0 = 1, \\ \text{case II:} & \quad P = 0, & \quad Q = 5\varphi(\theta; 10), & & \end{aligned} \quad (6.35)$$

in conjunction with equations (6.33) and (6.34). A base grid of resolution  $\Delta\theta = 2\pi/400$  was used, with adaptive mesh refinement allowing the local resolution to increase to  $\Delta\theta = 2\pi/1600$ . As the figure shows, in both cases a residue is left behind when the wave packet splits, and the residue is larger for the wave variable  $P$  (case I) than for the wave variable  $Q$  (case II). However, since the variable  $Q$  is identically zero in case I, the solution is a polarized Gowdy spacetime. Consequently the evolution of the variable  $P$ , and the appearance of wave residue within it, is

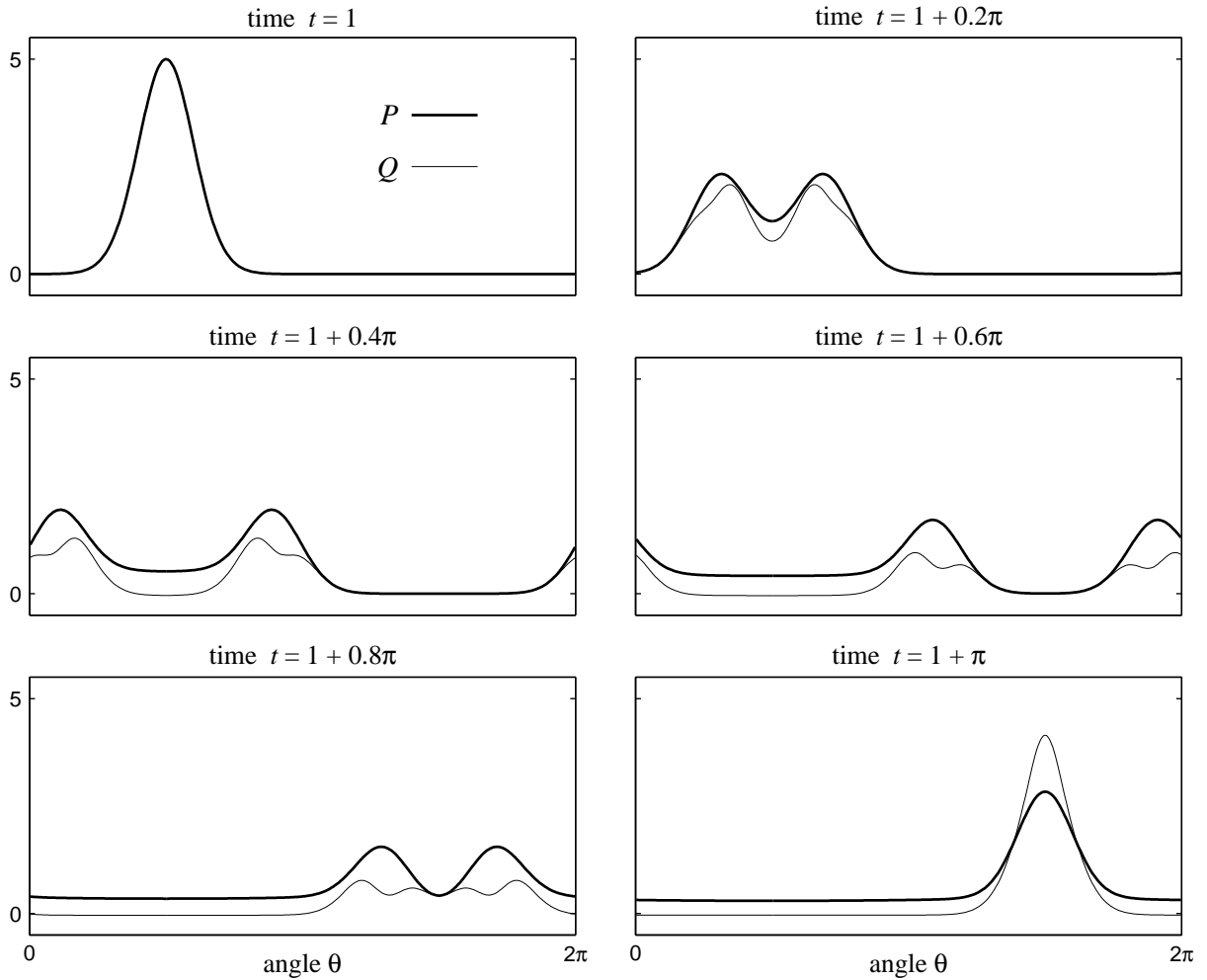


**Figure 6.14:** Two simulations of wave packet break-up and reconciliation. The two initial data sets of equations (6.35) (with equations (6.33) and (6.34)) are evolved numerically in an expanding Gowdy  $T^3$  spacetime. The plots show the variable  $P$  from the ‘case I’ simulation (wave packet in  $P$  only) and the variable  $Q$  from the ‘case II’ simulation (wave packet in  $Q$  only) on the same axes. If the waves were linear the two variables would behave identically. (A ‘residue’ is left when the wave packet in  $Q$  splits apart, but its size is small compared to the vertical scale of the plots.)

completely determined by a linear equation with exact solution (6.32a). While the formation of gravitational wave residue in the cosmological model considered here appears to be principally a linear effect, the residue itself can show nonlinear behaviour: in figure 6.14 the size of the residue is seen to differ for the two cases considered, but in the linear regime (when the amplitudes of the wave packets in equations (6.35) are small) the behaviour, and the size of the residue, is the same for both of the wave variables.



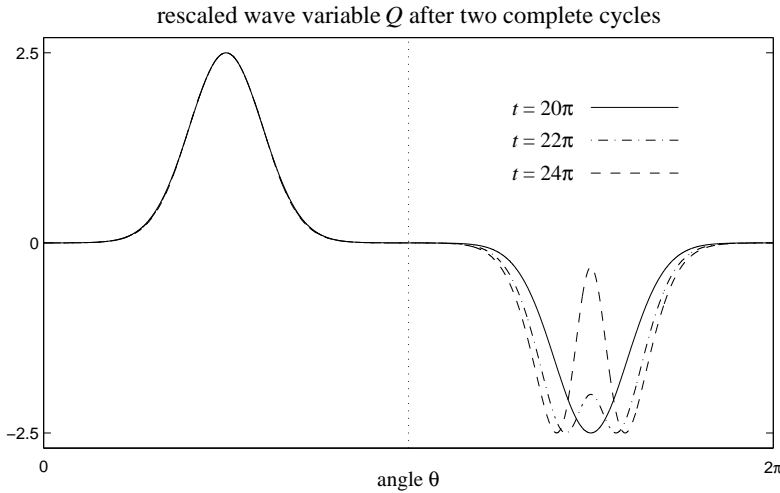


**Figure 6.15:** Deformation of wave packet shape during nonlinear evolution. The initial data set (6.36) (together with equations (6.33) and (6.34)) is evolved numerically for two cycles, each of duration  $\Delta t = 2\pi$ . The variable  $Q$  is plotted at the initial time and at the end of each cycle, and to facilitate comparison it is linearly rescaled: the value of  $Q$  at  $\theta = \pi$  is made to be zero and the amplitude of each wave packet (the two halves of the spatial domain are treated independently) is made to equal the amplitude of the wave packets in the initial data. For linear wave behaviour no deformation of the wave packet shape would be expected.

Another aspect of gravitational wave behaviour that can be investigated numerically is the effect that nonlinearity has on the shape of a propagating wave packet. In their independent studies, Anninos, Centrella and Matzner (1991b) and Shinkai and Maeda (1994) found wave packet behaviour to be predominantly linear, and comparisons can be made with the behaviour of soliton waves (see Boyd, Centrella and Klasky 1991; informally, a *soliton* is a nonlinearly propagating pulse wave which maintains its shape under collision with other solitons). Figure 6.14 shows that for the cosmological model studied here, nonlinear wave packets do not necessarily maintain their pulse shape when they propagate; however when two sub-packets recombine they do seem to take on a form very similar to that of the wave packet that produced them. The following numerical simulation tests how well the shape of a wave packet is maintained between cycles.

It can be seen from equations (6.32) together with the large parameter approximations for the Bessel functions (5.20) that at late times the profiles of the wave variables  $P$  and  $Q$  repeat themselves (to within linear rescaling) with time period  $\Delta t = 2\pi$ , provided that their behaviour is linear (or that the spacetime is polarized). To see to what extent the same statement can be made for nonlinear gravitational waves, the initial data set

$$P = Q = 2.5(\varphi(+\theta; 10) - \varphi(-\theta; 10)) \quad \text{for } t_0 = 20\pi, \quad (6.36)$$

(together with equations (6.33) and (6.34)) is numerically evolved and the results compared at the end of each cycle. (The ‘double pulse’ form of equation (6.36) is used to try to keep the average values of the wave variables around zero; this avoids ambiguity if the waves are to be considered

as propagating in a particular homogeneous background spacetime.) A basic spatial resolution of  $\Delta\theta = 2\pi/8000$  is used for the simulation with adaptive mesh refinement allowing a maximum resolution of  $\Delta\theta = 2\pi/128\,000$ . Figure 6.15 shows the wave variable  $Q$  at time intervals of  $\Delta t = 2\pi$ ; so that changes in shape of the wave packets can be seen clearly, the two halves of the plot have been linearly rescaled. The positive wave packet on the left-hand side of the figure has maintained its shape in just the same way as would be expected for linear wave behaviour, and this is also true of the two wave packets in the variable  $P$  (which is not shown here). In contrast, the influence of nonlinearity on the negative wave packet on the right-hand side of the figure is clear: the wave packet has been deformed from its original shape.

While some of the results of the investigations of gravitational wave behaviour near to the linear regime presented here are in agreement with those of earlier studies, others are not. It is apparent that different conclusions will be drawn for studies based on different cosmological models: in addition to the familiar problems caused by different time slicing conditions (as discussed in chapter 5), the choice of variables used to describe the metric also plays a role (in particular the identification of certain variables as descriptors of wave behaviour), as does the path through parameter space that is taken to relate nonlinear initial data sets to linear ones. In some ways the Gowdy models are a more natural basis for studies of gravitational wave behaviour than other models that have been used (for example they naturally decompose the metric into wave and background variables); however without nonlinear gravitational waves being described in a covariant manner, results produced using one particular model cannot be claimed to be representative of the general case.

# Chapter 7.

## $U(1)$ -Symmetric Cosmologies

This chapter is a continuation of the work described in chapter 6 on numerical simulations of inhomogeneous vacuum cosmological models. The spacetimes considered in the previous chapter had two spacelike Killing vectors and three-torus spatial topology, and were interpreted as closed planar cosmologies. In the present chapter the symmetry restrictions on the spacetimes are relaxed slightly so that only one spacelike Killing vector is present: the cosmologies are spatially compact with spacelike  $U(1)$  isometry groups. In an analogous way to the use in chapter 6 of Gowdy's (1974) reduction of the Einstein equations to describe planar cosmologies, the numerical simulations performed here use the equations of Moncrief's (1986) reduction for  $U(1)$ -symmetric cosmologies, and the relevant features of the reduction are discussed in section 7.1.

In section 7.2 results are presented from numerical simulations performed to investigate the behaviour of collapsing unpolarized  $U(1)$ -symmetric cosmologies. As reported by Berger and Moncrief (1998b), these spacetimes develop spatial structure on very fine scales in an analogous way to the collapsing unpolarized Gowdy cosmologies of section 6.2, and here the adaptive mesh refinement code described in chapter 3 is used to investigate the formation of this fine-scale structure at high grid resolutions.

A series of numerical tests of the Frittelli-Reula formulation of Einstein's equations (introduced in chapter 4) are described in section 7.3, with planar and  $U(1)$ -symmetric spacetimes providing reference solutions against which different evolution systems are compared. The reasons underlying the differences in numerical accuracy of a range of formulations are investigated, and in the process an alternative form of the Frittelli-Reula system is derived in which the variables used are adapted to cosmological spacetimes with  $U(1)$  symmetry.

### 7.1 Cosmologies with Spacelike $U(1)$ Isometry Groups

In chapter 6, Gowdy's (1974) reduction of the Einstein equations for spacetimes with two spacelike Killing vectors and compact spatial hypersurfaces was used as the basis for an investigation of planar cosmological spacetimes. The evolution equations for the Gowdy spacetimes have a particularly simple form, attained through the removal of unnecessary metric variables using coordinate conditions and constraint equations. In the present chapter cosmological models with one spacelike Killing vector are studied, and as before a special form for the metric is assumed so that the Einstein equations can be reduced to a reasonably simple form. The reduction is due to Moncrief (1986), with further specialization by Berger and Moncrief (1998a). The cosmological models that result are vacuum with spacelike  $U(1)$  isometry groups and spatial slices having three-torus ( $T^3$ ) topology, and this section summarizes their derivation, governing equations and basic properties.

*Moncrief's Reduction of the Einstein Equations*

In Moncrief 1986, Gowdy's (1974) approach to the reduction of the Einstein equations for cosmological spacetimes with two spacelike Killing vectors is generalized to cosmologies with a single Killing vector. Two variables representing the dynamical degrees of freedom of the spacetime are identified, and the remaining variables are eliminated by solving constraints and applying coordinate conditions. In this subsection the main features of the reduction are summarized, and in the next subsection the reduced Einstein equations for a particular  $U(1)$ -symmetric cosmological model are presented.

Moncrief's reduction applies to vacuum spacetimes with spacelike  $U(1)$  isometry groups on  $S^1$ -bundles over  $\mathbb{R} \times M$  where  $M$  is an arbitrary compact two-manifold. In Moncrief 1986 the particular case of  $M$  being the two-sphere is considered, since the analysis is then slightly simpler. For the present work the manifold  $M$  is taken to be the two-torus, and the  $S^1$ -bundle is constructed as a simple product so that spatially the cosmologies have three-torus topology. (For simplicity, only product  $S^1$ -bundles are considered in the brief discussion below.) A time coordinate  $\tau$  is introduced together with coordinates  $\{x^1, x^2, x^3\}$  on the spatial slices, with  $\partial/\partial x^3$  being the Killing vector for the isometry group. The metric is then written in the form

$$ds^2 = e^{-2\phi} d\sigma^2 + e^{2\phi} (dx^3 + \boldsymbol{\beta})^2, \quad (7.1a)$$

where

$$d\sigma^2 = -\tilde{N}^2 d\tau^2 + \tilde{g}_{ab} (dx^a + \tilde{N}^a d\tau)(dx^b + \tilde{N}^b d\tau), \quad (7.1b)$$

$$\boldsymbol{\beta} = \beta_0 d\tau + \beta_a dx^a, \quad (7.1c)$$

and summation for the indices  $a, b, \dots$  is over the range  $\{1, 2\}$ . Equation (7.1b) shows  $d\sigma^2$  to have the ADM form for a Lorentzian metric on the three-manifold  $\mathbb{R} \times M$ , with the two-dimensional lapse  $\tilde{N}$ , shift  $\tilde{N}^a$ , and induced metric  $\tilde{g}_{ab}$  all independent of the coordinate  $x^3$ . The scalar field  $\phi$  and the one-form  $\boldsymbol{\beta}$  from equations (7.1a,c) are defined on the same manifold.

The above decomposition of the metric bears a close resemblance to Kaluza-Klein-Jordan theory, but involves one less 'spacetime' dimension. The three-metric  $d\sigma^2$  satisfies the three-dimensional analogue of Einstein's equations with source terms provided by the fields  $\phi$  and  $\boldsymbol{\beta}$ , and as a consequence of its dimensionality  $d\sigma^2$  carries no dynamical degrees of freedom. In Moncrief's reduction the dynamical variables are the fields  $\phi$  and  $\boldsymbol{\beta}$ , and each represents one degree of freedom per spacetime point. The single dynamical degree of freedom present in the one-form  $\boldsymbol{\beta}$  can be made explicit by introducing a new field  $\omega$  which represents the general solution to a constraint imposed on  $\boldsymbol{\beta}$  by the Einstein equations; with  $\beta_0$  in equation (7.1c) set to zero without loss of generality, the one-form  $\boldsymbol{\beta}$  can always be reconstructed from a knowledge of the field  $\omega$ .

If the three-metric  $d\sigma^2$  is given, then the dynamical variables  $\phi$  and  $\omega$  are found to satisfy simple wave equations. Conversely, Moncrief has shown that coordinate conditions can be imposed on the two-dimensional lapse  $\tilde{N}$  and shift  $\tilde{N}^a$  in equation (7.1b) such that the three-metric  $d\sigma^2$  can be uniquely determined from  $\phi$  and  $\omega$  (and their conjugate momenta) on each spatial slice

by solving elliptic equations which derive from the Einstein constraints. (This is subject to the condition that certain constraint equations hold on the initial spatial slice.) Thus, in effect the dynamical variables  $\phi$  and  $\omega$  propagate in a background three-dimensional spacetime described by the metric  $d\sigma^2$  which in turn is determined at every instant by an elliptic system involving  $\phi$  and  $\omega$ .

Moncrief's reduction of the Einstein equations was motivated in part by its possible use as a tool in numerical relativity, and this idea was followed up by Ove (1986, 1989). Ove constructed a code implementing Moncrief's formalism for  $U(1)$ -symmetric cosmologies with three-torus ( $T^3$ ) spatial topology (the numerical boundary conditions in this case being trivial). The code evolved the dynamical variables  $\phi$  and  $\omega$  using a standard time-stepping method, and reconstructed the background metric on each new time slice by solving a system of elliptic equations. Ove used his code to address the question of whether singularities can form in expanding  $U(1)$ -symmetric  $T^3$  cosmologies, and his results support the tentative conclusion that they cannot (Ove 1989, 1990c). (As mentioned in chapter 6, Moncrief 1981 proves the corresponding result for expanding Gowdy  $T^3$  models.) Other work performed with the code (Ove 1990a, 1990b) which investigates the nonlinear behaviour of gravitational waves has been discussed in section 6.4.

The formulation of Moncrief's reduction which is used for the numerical simulations of  $U(1)$ -symmetric  $T^3$  cosmologies described in the present chapter differs from the one used by Ove; it is described in detail in the next subsection. The most significant difference between the formulations is in the choice of time slicing: in the present work harmonic slicing is used so that results can be readily compared with simulations performed using the Frittelli-Reula system, while in Ove's code (as in the original work by Moncrief) a two-dimensional form of constant mean curvature slicing was employed.

Some analytic results have been derived using Moncrief's reduction for  $U(1)$ -symmetric spacetimes on  $S^1$ -bundles over the two-sphere. Choquet-Bruhat and Moncrief (1994) have proved a local (in time) existence and uniqueness theorem. Moncrief (1987) has generated in power series form a family of  $U(1)$ -symmetric spacetimes which have curvature singularities. Grubišić and Moncrief (1994) have used perturbative techniques to find  $U(1)$ -symmetric spacetimes which are related to the mixmaster solutions and which presumably have oscillatory behaviour at the initial singularity (in contrast to the velocity-dominated behaviour typically found in the Gowdy models; see section 6.3).

The approach of Moncrief 1986 has been applied to other  $U(1)$ -symmetric spacetimes. Moncrief 1990 considers the Einstein-Maxwell equations on arbitrary  $S^1$ -bundles over the two-sphere and also the Einstein-Maxwell-Higgs equations on the three-torus (the latter case allowing interactions between parallel cosmic strings to be studied). Varadarajan 1995 reduces the vacuum Einstein equations for spacetimes with one spacelike Killing vector which are asymptotically flat in an appropriate sense. The connection between Moncrief's reduction and the Einstein equations for three-dimensional spacetimes has been mentioned above, and in Moncrief 1989 (2+1)-dimensional pure gravity is considered explicitly.

### A $U(1)$ -Symmetric Cosmological Model on the Three-Torus

Berger and Moncrief (1998a, 1998b) have performed numerical simulations of vacuum  $U(1)$ -symmetric  $T^3$  cosmologies using a formulation based on Moncrief's (1986) reduction of the Einstein equations. Their approach differs from that of Moncrief's original work (and the numerical work of Ove discussed in the previous subsection) in that their evolution system does not involve any elliptic equations: the Einstein constraint equations are not enforced during the evolution and a local time slicing condition is used. The formulation of Berger and Moncrief, described in their 1998a paper, is adopted for the work in the present chapter and is summarized in this subsection.

The metric used is the same as in equations (7.1) but with the following conditions imposed:

$$\tilde{N} = e^{\Lambda-2\tau}, \quad \tilde{N}^a = 0, \quad \tilde{g}_{ab} = e^{\Lambda-2\tau} e_{ab}, \quad \beta_0 = 0. \quad (7.2)$$

The coordinate  $\tau$  denotes time while the spatial slices (of  $T^3$  topology) are described by the coordinates  $\{x^1, x^2, x^3\} = \{u, v, w\}$  which are periodic on the domain  $[0, 2\pi)$ . For the summation convention used in the present work, the indices  $\mu, \nu, \dots$  range over  $\{0, 1, 2, 3\}$ , the indices  $i, j, \dots$  range over  $\{1, 2, 3\}$ , and the indices  $a, b, \dots$  range over  $\{1, 2\}$ . The conformal metric  $e_{ab}$  of the  $u$ - $v$  plane has unit determinant and components

$$\begin{aligned} e_{uu} &= \frac{1}{2}(e^{2z} + e^{-2z}[x+1]^2), & e_{vv} &= \frac{1}{2}(e^{2z} + e^{-2z}[x-1]^2), \\ e_{uv} &= e_{vu} = \frac{1}{2}(e^{2z} + e^{-2z}[x^2-1]). \end{aligned} \quad (7.3)$$

Its inverse has components  $e^{uu} = e_{vv}$ ,  $e^{vv} = e_{uu}$ , and  $e^{uv} = e^{vu} = -e_{uv}$ .

The spacetime is thus described by six variables:  $\Lambda$ ,  $z$ , and  $x$  make up the (2+1)-dimensional 'background' metric while  $\phi$ ,  $\beta_1$  and  $\beta_2$  carry the dynamical degrees of freedom. All of the variables are periodic in  $x^1 = u$  and  $x^2 = v$ , and independent of the symmetry coordinate  $x^3 = w$ . Combining equations (7.1) and (7.2), the metric of the  $U(1)$ -symmetric  $T^3$  model has the form

$$g_{\mu\nu} = \begin{array}{c} \tau \\ u \\ v \\ w \end{array} \begin{array}{cccc} \tau & u & v & w \\ \left( \begin{array}{cccc} -e^{2\Lambda-4\tau-2\phi} & 0 & 0 & 0 \\ 0 & \kappa_{11} & \kappa_{12} & e^{2\phi}\beta_1 \\ 0 & \kappa_{21} & \kappa_{22} & e^{2\phi}\beta_2 \\ 0 & e^{2\phi}\beta_1 & e^{2\phi}\beta_2 & e^{2\phi} \end{array} \right), \end{array} \quad (7.4)$$

where

$$\kappa_{ab} = e^{\Lambda-2\tau-2\phi} e_{ab} + e^{2\phi} \beta_a \beta_b.$$

The ADM lapse and shift of the foliation can be read off equation (7.4) for the metric:

$$\text{lapse } N = e^{\Lambda-2\tau-\phi}, \quad \text{shift } N^i = 0. \quad (7.5)$$

(These quantities are not to be confused with their (2+1)-dimensional analogues  $\tilde{N}$  and  $\tilde{N}^a$  from equation (7.1b).) The determinant of the induced metric is equal to the square of the lapse, and consequently the constant time hypersurfaces slice the spacetime harmonically (with slicing density

identically equal to one; see equation (4.8)). Results produced using this formulation of Moncrief's reduction can thus be readily compared with results from a two-dimensional implementation of the Frittelli-Reula system, as section 7.3 demonstrates.

The number of metric variables used in equation (7.4) is the same as the number used in the standard ADM description of a spacetime (given that the lapse and the shift are known); however Moncrief's reduction allows the two variables  $\beta_1$  and  $\beta_2$  to be replaced by a single variable  $\omega$  defined via

$$\omega_{,\tau} = e^{4\phi} \varepsilon^{ab} \beta_{a,b}, \quad \omega_{,a} = -e^{4\phi+2\tau-\Lambda} e_{ab} \varepsilon^{bc} \beta_{c,\tau}, \quad (7.6)$$

where the alternating symbol  $\varepsilon^{ab}$  has non-zero components  $\varepsilon^{12} = +1$  and  $\varepsilon^{21} = -1$ . (As a simplification of the formulation, two constants that should appear in equation (7.6) have been set to zero; in Moncrief's original work these constants vanish identically because of the two-sphere topology used.) The variables  $\beta_1$  and  $\beta_2$  can be reconstructed from  $\omega$  by integrating in time

$$\beta_{a,\tau} = e^{\Lambda-2\tau-4\phi} e_{ab} \varepsilon^{bc} \omega_{,c}, \quad (7.7)$$

with  $\beta_1$  and  $\beta_2$  being defined on an initial slice  $\tau = \tau_0$  according to

$$\beta_1(u, v, \tau_0) = c_1 + \lambda_{,u} + \int_0^v \Omega(u, \bar{v}, \tau_0) d\bar{v} - \frac{v}{2\pi} \int_0^{2\pi} \Omega(u, \bar{v}, \tau_0) d\bar{v}, \quad (7.8a)$$

$$\beta_2(u, v, \tau_0) = c_2 + \lambda_{,v} - \frac{1}{2\pi} \int_0^u \int_0^{2\pi} \Omega(\bar{u}, \bar{v}, \tau_0) d\bar{v} d\bar{u}, \quad (7.8b)$$

where the function  $\lambda(u, v)$  and the constants  $c_a$  are arbitrary (and here are typically set to zero) and  $\Omega$  is the conjugate momentum of  $\omega$  defined by  $\Omega = \exp(-4\phi) \omega_{,\tau}$ . The requirement that  $\beta_1$  and  $\beta_2$  be periodic translates to a constraint on the initial value of  $\Omega$ :

$$\int_0^{2\pi} \int_0^{2\pi} \Omega(u, v, \tau_0) du dv = 0. \quad (7.9)$$

Evolution equations for the five variables of the Moncrief reduction can be derived by varying the Hamiltonian given in Berger and Moncrief 1998a:

$$\Lambda_{,\tau\tau} = e^{\Lambda-2\tau} (e^{-\Lambda} [e^{\Lambda} e^{ab}]_{,ab} - 2e^{-2z} \varepsilon^{ab} z_{,a} x_{,b} + e^{ab} \Pi_{ab}), \quad (7.10a)$$

$$z_{,\tau\tau} = -\frac{1}{2} e^{-4z} x_{,\tau}^2 - \frac{1}{2} e^{\Lambda-2\tau-2z} \varepsilon^{ab} \Lambda_{,a} x_{,b} - \frac{1}{4} e^{\Lambda-2\tau} e^{ab}_{,z} \Pi_{ab}, \quad (7.10b)$$

$$x_{,\tau\tau} = 4z_{,\tau} x_{,\tau} + e^{\Lambda-2\tau+4z} (2e^{-2z} \varepsilon^{ab} \Lambda_{,a} z_{,b} - e^{ab}_{,x} \Pi_{ab}), \quad (7.10c)$$

$$\phi_{,\tau\tau} = (e^{\Lambda-2\tau} e^{ab} \phi_{,a})_{,b} + \frac{1}{2} e^{-4\phi} (e^{\Lambda-2\tau} e^{ab} \omega_{,a} \omega_{,b} - \omega_{,\tau}^2), \quad (7.10d)$$

$$\omega_{,\tau\tau} = e^{4\phi-2\tau} (e^{\Lambda-4\phi} e^{ab} \omega_{,a})_{,b} + 4\phi_{,\tau} \omega_{,\tau}, \quad (7.10e)$$

where

$$\Pi_{ab} = \Lambda_{,ab} + 2\phi_{,a} \phi_{,b} + \frac{1}{2} e^{-4\phi} \omega_{,a} \omega_{,b}.$$

It is a straightforward matter to put these equations into a conservative first-order form by defining the first derivatives of  $\Lambda$ ,  $z$ ,  $x$ ,  $\phi$  and  $\omega$  to be new variables. (In section 7.3 this is done explicitly.) Considering only the principal part of the evolution system, the wave variables  $\phi$  and  $\omega$  can be

seen to decouple from each other. The wave equations (7.10d) and (7.10e) are strongly hyperbolic and have non-trivial characteristic speeds equal to the coordinate light speeds of the metric (7.4), these being

$$\begin{aligned} \text{coordinate light speed in } u\text{-direction} &= \pm e^{\Lambda/2-\tau} \sqrt{e^{uu}}, \\ \text{in } v\text{-direction} &= \pm e^{\Lambda/2-\tau} \sqrt{e^{vv}}. \end{aligned} \quad (7.11)$$

The sub-system for the evolution of the background variables  $\Lambda$ ,  $z$  and  $x$  has the same characteristic speeds but is only weakly hyperbolic since the eigenvectors of the principal part do not form a complete set. (This lack of strong hyperbolicity is not altogether surprising considering that in Moncrief's original reduction the background variables were determined by a system of elliptic equations.) One method by which the Moncrief equations can be made strongly hyperbolic is explored in section 7.3.

The evolution system (7.10) is constrained by the Hamiltonian constraint equation,  $\mathcal{H}_0 = 0$ , and by two momentum constraint equations,  $\mathcal{H}_u = \mathcal{H}_v = 0$ , where

$$\begin{aligned} \mathcal{H}_0 &= 2z_{,\tau}{}^2 + \frac{1}{2}e^{-4z}x_{,\tau}{}^2 + 2\phi_{,\tau}{}^2 + \frac{1}{2}e^{-4\phi}\omega_{,\tau}{}^2 - \frac{1}{2}(2 - \Lambda_{,\tau})^2 \\ &\quad + e^{\Lambda-2\tau}(\Lambda_{,a}e^{ab}{}_{,b} + e^{ab}{}_{,ab} - 2e^{-2z}\varepsilon^{ab}z_{,a}x_{,b} + e^{ab}\Pi_{ab}), \end{aligned} \quad (7.12a)$$

$$\begin{aligned} \mathcal{H}_a &= 4z_{,\tau}z_{,a} + e^{-4z}x_{,\tau}x_{,a} + (2 - \Lambda_{,\tau})\Lambda_{,a} + \Lambda_{,\tau a} + 4\phi_{,\tau}\phi_{,a} \\ &\quad + e^{-4\phi}\omega_{,\tau}\omega_{,a} + \varepsilon^{bc}(\frac{1}{2}e^{-2z}e_{ab,z}x_{,\tau} - 2e^{2z}e_{ab,x}z_{,\tau})_{,c}. \end{aligned} \quad (7.12b)$$

Moncrief's  $U(1)$ -symmetric cosmologies can be polarized in the same way as the Gowdy spacetimes: as equation (7.10e) shows, if the wave variable  $\omega$  and its time derivative are zero on an initial spatial slice then they are zero throughout the spacetime. The corresponding statement does not hold for the other wave variable  $\phi$  except when both  $\phi$  and  $\omega$  are identically zero. Equations (7.7) and (7.8) show that in a polarized spacetime the vanishing of  $\omega$  implies that the variables  $\beta_1$  and  $\beta_2$  are constants with respect to time and satisfy  $\beta_{1,v} = \beta_{2,u}$ .

If in a numerical simulation the five variables  $\Lambda$ ,  $z$ ,  $x$ ,  $\phi$  and  $\omega$  are evolved using the equations (7.10) then equations (7.7) can be evolved at the same time to find the values of  $\beta_1$  and  $\beta_2$ . Alternatively,  $\beta_1$  and  $\beta_2$  could be used as variables instead of  $\omega$  with the evolution equation (7.10e) being replaced by the two equations

$$\beta_{a,\tau\tau} = (\Lambda_{,\tau} - 2 - 4\phi_{,\tau})\beta_{a,\tau} + e_{ab,\tau}e^{bc}\beta_{c,\tau} + e^{\Lambda-2\tau}e_{ab}\varepsilon^{bc}\varepsilon^{de}(4\phi_{,c}\beta_{d,e} + \beta_{d,ec}), \quad (7.13)$$

and the derivatives of  $\omega$  in equations (7.10a-d) being replaced by derivatives of  $\beta_1$  and  $\beta_2$  using equations (7.6). (Clearly the reintroduction of  $\beta_1$  and  $\beta_2$  as variables in the system is a step backwards in terms of simplifying the Einstein equations; however it is useful when making comparisons between numerical simulations, as section 7.3 demonstrates.) If  $\beta_1$  and  $\beta_2$  are used as variables then the system acquires an additional constraint equation,  $\mathcal{H}_\beta = 0$ , where

$$\mathcal{H}_\beta = e^{ab}(4\phi - \Lambda)_{,a}\beta_{b,\tau} + (e^{ab}\beta_{a,\tau})_{,b}. \quad (7.14)$$

This constraint is equivalent to the requirement that the spatial derivatives of  $\omega$  commute.



A useful coordinate-independent quantity defined at each point of the spacetime is the norm of the Killing vector  $\partial/\partial w$  associated with the  $U(1)$  isometry group, and from equation (7.4) it can be seen that

$$\text{proper length of } \partial/\partial w \text{ symmetry orbits} = 2\pi e^\phi. \quad (7.15)$$

The  $U(1)$  symmetry of the spacetime thus provides the variable  $\phi$  with a simple physical interpretation, and the numerical results presented in section 7.2 focus attention on this variable.

### *Initial Data for Numerical Simulations*

A set of initial data for the system of evolution equations (7.10) comprises values for the variables  $\Lambda$ ,  $z$ ,  $x$ ,  $\phi$  and  $\omega$  and their first time derivatives for which the constraint values  $\mathcal{H}_0$ ,  $\mathcal{H}_u$  and  $\mathcal{H}_v$  from equations (7.12) vanish, and which in addition satisfy equation (7.9). Clearly in the general case constructing sets of initial data requires the numerical solution of elliptic equations; however Berger and Moncrief (1998a) have found a non-trivial family of initial data sets for which the constraint equations can be solved algebraically. This family of initial data sets is used for the numerical simulations performed in the present work, and its construction is summarized in this subsection.

First of all the momentum constraints  $\mathcal{H}_u = \mathcal{H}_v = 0$  (see equation (7.12b)) can be satisfied on an initial hypersurface by requiring that

$$\Lambda_{,\tau} = 2 - ce^\Lambda, \quad z_{,\tau} = x_{,\tau} = 0, \quad \phi = \omega = 0 \quad \text{at time } \tau = \tau_0, \quad (7.16)$$

for some constant value  $c$ . (In fact the requirement is that  $\phi$  and  $\omega$  be spatially constant, not necessarily zero. Here  $\phi$  is set to zero as a slight simplification; there is no loss of generality in taking  $\omega$  to be zero since only its derivatives appear in the evolution equations.) A value for  $\omega_{,\tau}$  is then chosen such that

$$\int_0^{2\pi} \int_0^{2\pi} \omega_{,\tau} du dv = 0 \quad \text{at time } \tau = \tau_0, \quad (7.17)$$

which derives from equation (7.9). The Hamiltonian constraint  $\mathcal{H}_0 = 0$  (see equation (7.12a)) can then be satisfied by allowing it to determine the value of  $\phi_{,\tau}$  at time  $\tau = \tau_0$  given values for  $\Lambda$ ,  $z$ ,  $x$  and  $\omega_{,\tau}$  then:

$$\phi_{,\tau}^2 = \frac{1}{4}c^2 e^{2\Lambda} - \frac{1}{4}\omega_{,\tau}^2 - \frac{1}{2}e^{\Lambda-2\tau_0}(\Lambda_{,ab}e^{ab} + \Lambda_{,a}e^{ab}_{,b} + e^{ab}_{,ab} - 2e^{-2z}\varepsilon^{ab}z_{,a}x_{,b}). \quad (7.18)$$

The right-hand side of this can always be made non-negative by choosing a sufficiently large value for the constant  $c$ . It is convenient to choose the sign of  $\phi_{,\tau}$  to be the same as the sign of  $c$ .

A set of initial data can thus be constructed based on arbitrary (spatially periodic) values of  $\Lambda$ ,  $z$  and  $x$ , and a value of  $\omega_{,\tau}$  satisfying equation (7.17). The sign of the constant  $c$  determines whether the spacetime initially expands ( $c$  is negative) or collapses ( $c$  is positive) as the time  $\tau$  increases. This can be seen from the mean curvature of the spatial slices,

$$\text{mean curvature } K = K^i_i = (\phi_{,\tau} + 2 - \Lambda_{,\tau})e^{\phi+2\tau-\Lambda}, \quad (7.19)$$

where  $K_{ij}$  is the extrinsic curvature tensor of the foliation. The mean curvature  $K$  is a measure of the convergence of the world lines that run normal to the spatial slices: when  $K$  is positive the world lines are converging and when it is negative they are diverging. It is straightforward to show that on the initial slice the sign of  $K$  is the same as the sign of  $c$  (provided that the sign of  $\phi_{,\tau}$  is chosen as described above).

## 7.2 Collapsing $U(1)$ -Symmetric Cosmologies

In this section results are presented from numerical simulations of vacuum  $U(1)$ -symmetric  $T^3$  cosmologies. As mentioned in section 7.1 these spacetimes have also been studied numerically by Ove (1986, 1989, 1990b) and by Berger and Moncrief (1998a, 1998b). Ove investigated nonlinear gravitational wave effects and singularity formation in expanding spacetimes, and while his work is based on the same formulation of Einstein's equations as is used here (Moncrief 1986) the time slicing condition employed is quite different. This difference in gauge, together with differences in the approaches used to generate initial data sets, makes it impractical to use Ove's results to test the code used for the work described in this chapter.

Berger and Moncrief have investigated the behaviour of  $U(1)$ -symmetric cosmologies as they collapse towards 'big bang' singularities. Their findings extend previous results for the Gowdy cosmological models (Berger and Moncrief 1993; see section 6.3): for polarized  $U(1)$ -symmetric spacetimes the approach to the singularity has the quality of a velocity-term dominated solution of the Einstein equations (Berger and Moncrief 1998a), while in the unpolarized case the behaviour close to the singularity is oscillatory, consistent with the Belinskii-Khalatnikov-Lifschitz model of a generic inhomogeneous singularity (Berger and Moncrief 1998b). In the present work the same formulation of Einstein's equations is used as in Berger and Moncrief 1998a, but a different numerical method is used to evolve solutions. (As in their earlier work, Berger and Moncrief use a symplectic integration algorithm.) The behaviour of polarized  $U(1)$ -symmetric spacetimes evolved using the code described in the present work is found to be consistent with the (mostly qualitative) results presented in Berger and Moncrief 1998a.

In their studies of unpolarized  $U(1)$ -symmetric spacetimes, Berger and Moncrief (1998b) found that structure develops in the evolved solutions on very small spatial scales in much the same way as it does in collapsing unpolarized Gowdy  $T^3$  cosmologies (see section 6.2). However, the inability of their code to adequately resolve this spatial structure led to it becoming unstable, and this they countered by spatially averaging the solution data between time steps. The advantage of this smoothing process is that it allows numerical solutions to be evolved up to much later times than would otherwise be possible; the disadvantage is that it prevents the numerical solution from accurately modelling the exact solution. Berger and Moncrief's justification for using spatial averaging is that they are interested in the qualitative behaviour of the spacetime as it approaches the singularity, not in the details of the local features that develop in it.

In this section the adaptive mesh refinement code described in chapter 3 is used to study the formation of fine-scale features in collapsing unpolarized  $U(1)$ -symmetric spacetimes. In contrast

to the work of Berger and Moncrief (1998b), the spacetimes are evolved only for short time periods and the emphasis is on the accurate resolution of the fine-scale features.

### *Numerical Simulations of Collapsing $U(1)$ -Symmetric $T^3$ Cosmologies*

Compared to the numerical simulations of Gowdy spacetimes presented in chapter 6, simulations of  $U(1)$ -symmetric spacetimes are considerably more difficult to perform: more computer resources are needed because of the larger number of variables and spatial dimensions, and there is a greater tendency for the evolution to become unstable because of the complexity of the governing equations. For these reasons the numerical simulations presented in this section explore a narrower range of behaviour than the simulations of chapter 6. This subsection describes the numerical apparatus used to study collapsing unpolarized  $U(1)$ -symmetric  $T^3$  cosmologies; numerical results are presented in the following subsection. Simulations of polarized and expanding spacetimes have also been performed, but the results are less interesting and are not discussed here.

The simulations are based on Moncrief's (1986) reduction of the Einstein equations, detailed in section 7.1. The spacetime is described by five principal variables,  $\Lambda$ ,  $z$ ,  $x$ ,  $\phi$  and  $\omega$ , and by defining the first derivatives of these with respect to the coordinates  $u$ ,  $v$  and  $\tau$  to be additional variables, a first-order flux-conservative form for the evolution equations (7.10) is obtained (recall equation (2.1)). Additional values  $\beta_1$  and  $\beta_2$  are required in order for the metric (7.4) to be reconstructed, and these are evaluated during the course of the simulation by including equations (7.7) as part of the evolution system. Since the variable  $\omega$  does not explicitly appear in the evolution equations (only its derivatives appear) it can be omitted from the system, and so twenty-one variables in total are evolved. The evolution system is unconstrained in the sense that the Hamiltonian and momentum constraints from equations (7.12) are only imposed at the initial time  $\tau = \tau_0$ .

As pointed out in section 7.1 the evolution equations (7.10) are only weakly hyperbolic, and so the high-resolution integration methods of chapter 2 are inapplicable here. The numerical results in this section were generated using the standard two-step Lax-Wendroff method, with a splitting approach being used to separate transport and source terms (the latter are treated using a second-order Runge-Kutta method); details are given in section 2.1. As in the collapsing Gowdy case (section 6.2) the size of the time step  $\Delta\tau$  is allowed to increase during the course of the simulation, up to a maximum size of about twice the spatial mesh width, provided that the Courant-Friedrichs-Lewy condition is not violated (recall the discussion of variable time steps in section 3.2). Periodic boundary conditions are used as appropriate for the toroidal spatial topology of the models under investigation.

Initial data sets for the simulations are constructed using the approach (from Berger and Moncrief 1998a) described in section 7.1. The particular initial data set used to produce the results presented in this section has

$$\begin{aligned} \Lambda &= \alpha \sin u \sin v, & z &= x = \alpha \cos u \cos v, & \omega_{,\tau} &= \alpha \cos u \cos v, \\ \beta_1 &= \alpha \cos u \sin v, & \beta_2 &= 0, & & \text{with } \alpha = 0.1 \text{ and } c = +1.2 \text{ at time } \tau_0 = 0, \end{aligned} \quad (7.20)$$

together with equation (7.16) and  $\phi_{,\tau}$  determined from equation (7.18). The initial value for  $\omega_{,\tau}$  is consistent with the condition (7.17), and the initial values for  $\beta_1$  and  $\beta_2$  come from equations (7.8) with  $c_1$ ,  $c_2$  and  $\lambda$  taken to be zero. The parameter  $\alpha$  measures, in a loose sense, the strength of the gravitational waves present in the initial data: when it is zero the spacetime is a homogeneous Kasner model, and for large values the behaviour of the spacetime becomes complicated very quickly. The initial data sets used in Berger and Moncrief 1998b have larger amplitudes than those used here.

The values of  $\Lambda$ ,  $z$  and  $x$  in the initial data (7.20) can be varied without qualitatively changing the behaviour of the evolved solution. The appearance of interesting features in the spacetimes seems to be largely determined by the value of  $\omega_{,\tau}$ . (The extreme case of  $\omega_{,\tau}$  being everywhere zero results in a spacetime that is polarized.) From figure 7.1 it can be seen that the regions where fine-scale spatial structure develops are close to points at which  $\omega_{,\tau}$  is zero in the initial data (7.20), and this remains true when alternative initial values for  $\omega_{,\tau}$  are used: figure 3.14 shows a plot of the variable  $\phi$  for a simulation in which the initial value of  $\omega_{,\tau}$  is zero at points forming a circle in the spatial domain with centre  $u = v = \pi$ .

The numerical simulations discussed in this section make use of the adaptive mesh refinement algorithm described in chapter 3. The simulations use a coarse base grid of resolution  $\Delta u = \Delta v = 2\pi/200$  which can be locally refined (using two additional levels in the grid hierarchy) up to a maximum resolution of  $\Delta u = \Delta v = 2\pi/3200$ . The main reason for using adaptive mesh refinement in this case is that it allows emerging fine-scale spatial features to be resolved without requiring a very fine mesh to be used over the entire spatial domain (or for the whole duration of the simulation). However, for the collapsing cosmological model studied here the usual approach of selecting regions to be refined based on an estimate of the local truncation error has been found to be inefficient: it leads to the refinement of a much larger portion of the spatial domain than is necessary. To compensate for this the automatic refinement procedure has been set to a relatively low level of sensitivity and the code has been explicitly programmed to refine in regions where fine-scale features are known to appear. By using mesh refinement in this way simulations can be performed (up to a final time of  $\tau \simeq 13$ ) in about five percent of the time that would be required for a simulation based on a single uniform grid as fine as the finest grid used here. Interpolation is used as part of the adaptive mesh refinement algorithm; in section 3.2 the advantages and disadvantages of several different interpolation methods are considered. The simulations described here used piecewise quadratic interpolation to minimize problems caused by interpolating near to poorly resolved fine-scale features, although in practice these problems only occur at late times since the code ensures that the fine-scale features are always refined to the highest level.

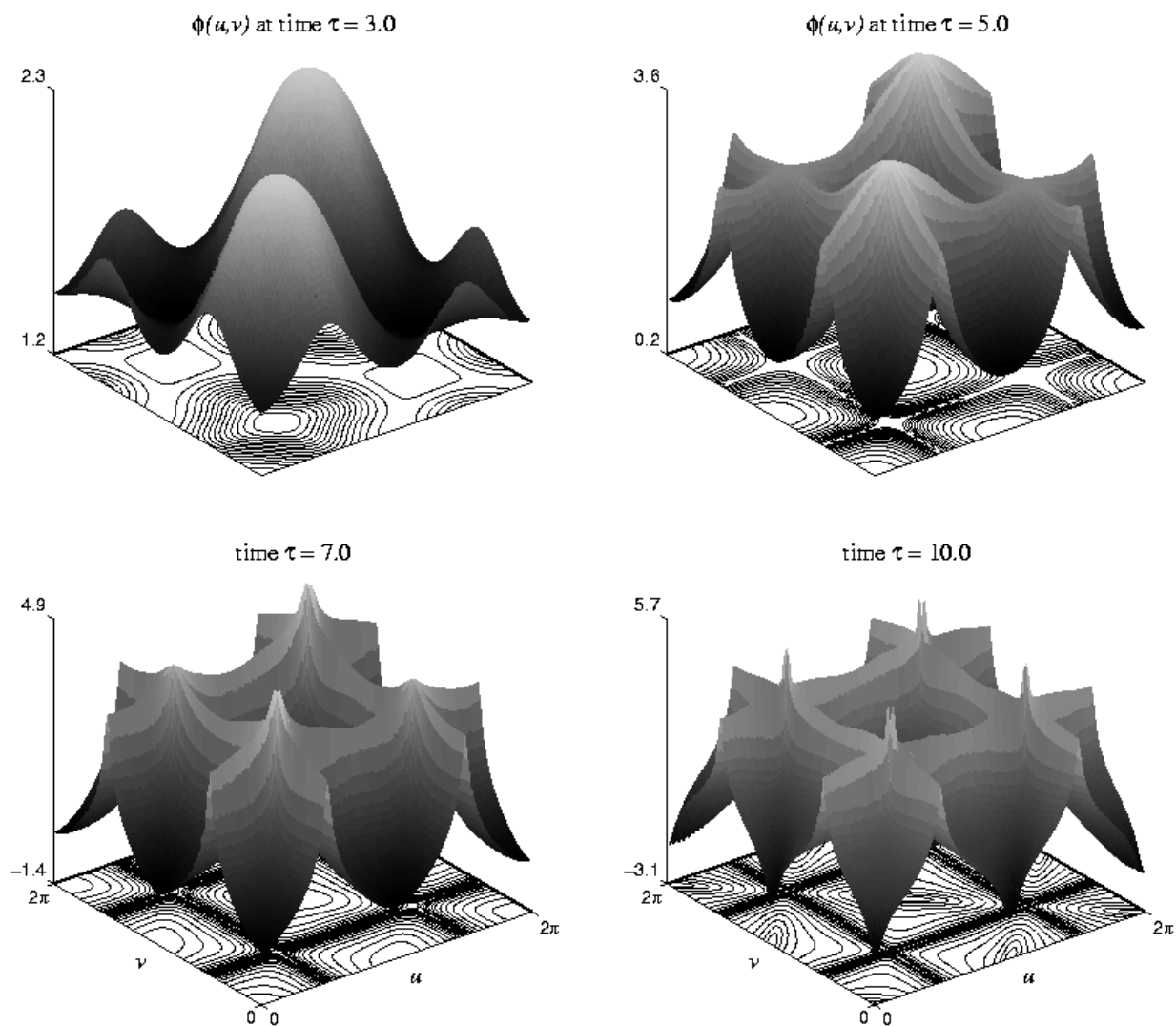
The Gowdy  $T^3$  cosmological models studied in chapter 6 are special cases of  $U(1)$ -symmetric  $T^3$  spacetimes, and they provide a useful test case for the  $U(1)$ -symmetric code. Since the same slicing condition is used for both of the metrics (6.1) and (7.4), it is straightforward to convert between the Gowdy variables  $P$ ,  $Q$  and  $\lambda$  and the Moncrief variables  $\Lambda$ ,  $x$ ,  $z$ ,  $\phi$  and  $\omega$ . The  $U(1)$ -symmetric code has been tested to check that it reproduces the results of the Gowdy code and the exact polarized

solutions known for the Gowdy models. Two further tests provide evidence that the  $U(1)$ -symmetric code performs correctly when evolving more general spacetimes. Firstly, the quantities evolved by the code always converge at second order as the mesh width is reduced (in particular the constraint values of equations (7.12) converge to zero). Secondly, the results produced by the code converge to the same solutions as the results of the independent Frittelli-Reula code (discussed in chapter 4 and also section 7.3) which has itself been tested on a different range of problems. Because of the data smoothing used in their production (recall the comments at the start of this section), the results presented in Berger and Moncrief 1998b do not constitute a ‘known’ solution against which the code used in the present work can be tested; however some qualitative similarities can be seen between figure 8 (at early times) of Berger and Moncrief’s paper and figure 7.1 of the present work despite different initial data sets having been used.

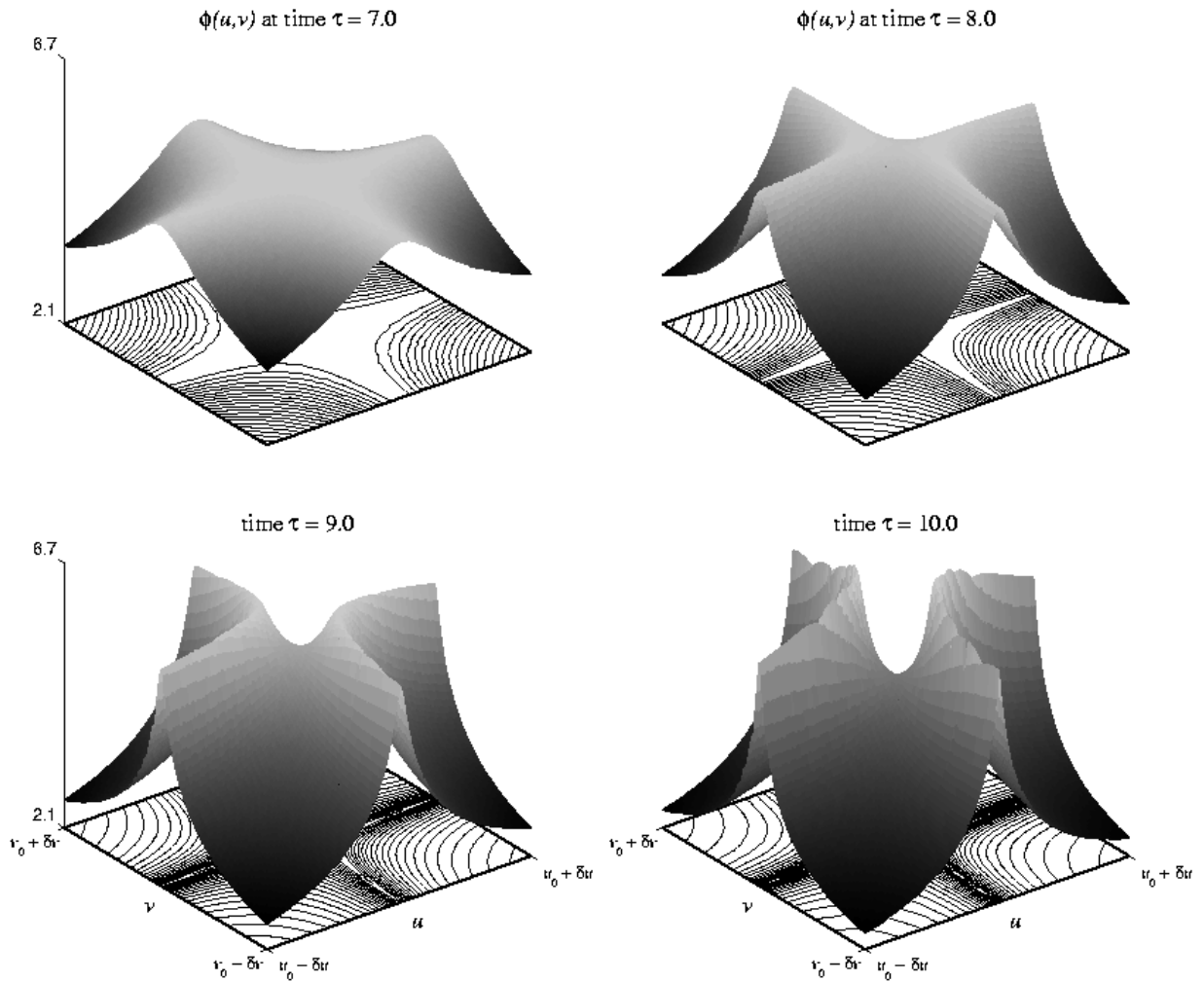
### *Fine-Scale Features in Collapsing $U(1)$ -Symmetric Spacetimes*

Figure 7.1 shows the metric variable  $\phi$  at several stages during the evolution of the initial data (7.20) using the numerical methods outlined in the previous subsection. The variable  $\phi$  is the most easily interpreted of the variables describing the evolved spacetime: as given in equation (7.15), the proper distance around the spacetime in the spacelike direction of symmetry is proportional to  $\exp(\phi)$ . It is clear from the figure that during the collapse of the unpolarized  $U(1)$ -symmetric spacetime, features develop in  $\phi$  on small spatial scales: by time  $\tau \simeq 6$  sharp ridges have formed which run parallel to the  $u$ - and  $v$ -axes with large peaks appearing where two ridges cross, and at later times (less obvious in the figure) deep pits form in between the ridges, oriented at forty-five degrees to the  $u$ - and  $v$ -axes. The nature of these fine-scale features and the difficulties they cause for numerical simulations are the topics of the present subsection.

The sharp ridges that develop in the variable  $\phi$  bear a close resemblance to the spikes that appear in simulations of collapsing unpolarized Gowdy cosmologies, as described in section 6.2. The ridges grow (towards positive infinity) at approximately linear rates while their widths gradually decrease, and as the simulation progresses they become increasingly difficult to resolve. The numerical problems caused by the narrowing of the ridges are similar to the problems caused by the spikes in the Gowdy simulations, but they are more acute because of the additional spatial dimension. In the Gowdy case the narrowing of the spikes causes their heights to be inaccurately represented by the numerical solution; in the  $U(1)$ -symmetric case the heights of the ridges become inaccurate in an analogous manner, but with the error in the height varying along the length of each ridge producing a ‘ripple’ effect in the numerical solution. (Ripples along the ridges are just visible in the last plot of figure 7.1.) The use of mesh refinement techniques (as described in the previous subsection) prolongs the time for which the simulation can keep the ridges well resolved, but since the ridges seem never to stop narrowing, eventually their representation in the numerical solution must become inaccurate. By time  $\tau \simeq 10$  the resolution of the simulation used to produce figure 7.1 is insufficient to adequately resolve the ridge features in the variable  $\phi$ .



**Figure 7.1:** Variable  $\phi(u, v, \tau)$  of collapsing  $U(1)$ -symmetric spacetime (7.4) at four different times. Surface and contour plots of the data are shown. The initial data set (7.20) with equations (7.16) and (7.18) is evolved using equations (7.10). The resolution of the plots ( $100 \times 100$  points in the  $u$ - $v$  domain) is insufficient to resolve the fine-scale features that develop at late times.



**Figure 7.2:** Close-ups of a peak in the variable  $\phi(u, v, \tau)$  for the simulation shown in figure 7.1. The plots are all centred on  $u_0 = v_0 = \pi/2$  and cover a region given by  $\delta u = \delta v = 0.12$ . The resolution of the plots ( $100 \times 100$  points) is slightly less than the resolution of the finest grids used in the simulation. The same vertical axis is used for all the plots.

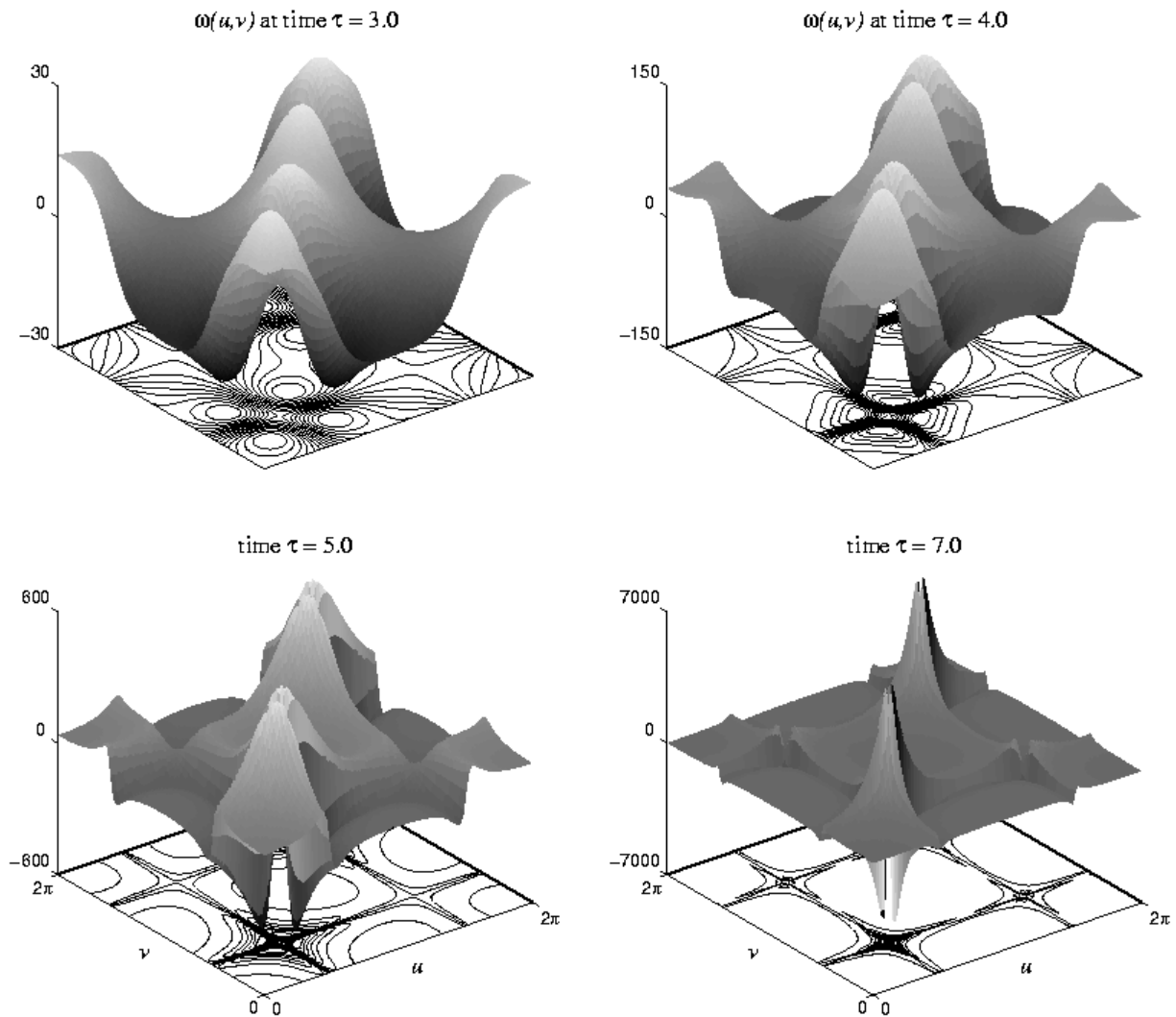


**Figure 7.3:** Variable  $\omega(u, v, \tau)$  of the Moncrief reduction (7.6) for a collapsing  $U(1)$ -symmetric spacetime (7.4) at four different times. Surface and contour plots of the data are shown. The same initial data set is used as in figure 7.1 but the results are plotted at different times. The resolution of the plots ( $100 \times 100$  points in the  $u$ - $v$  domain) is insufficient to resolve the fine-scale features that develop at late times.



As figure 7.1 shows, peaks appear in the variable  $\phi$  at points where ridges cross, and like the ridges the peaks sharpen as the simulation progresses. However in contrast to the other fine-scale features that develop in collapsing unpolarized  $U(1)$ -symmetric and Gowdy cosmologies, the nature of the peaks changes at late times. Figure 7.2 plots the variable  $\phi$  in close-up at the position of one of the peaks ( $u = v = \pi/2$ ), and it can be seen that by time  $\tau \simeq 9$  the peak has split apart, separating the intersecting ridges. The value of  $\phi$  at the point where the peak used to be subsequently decreases while the nearby ridges grow and narrow in the usual way. This behaviour is common to all of the peaks seen in figure 7.1, although it takes place at different times for different peaks. Figure 7.2 is plotted using data from the finest grids used in the simulation; at time  $\tau = 10$  it is clear that the ridges are imperfectly resolved.

A third kind of fine-scale feature appears in the variable  $\phi$  at late times ( $\tau \simeq 8$ ). In between the ridges, at coordinate positions where both  $u$  and  $v$  are multiples of  $\pi$ , linear growth of  $\phi$  towards negative infinity produces steep-sided pits in the variable. The pits are most obvious in the contour plots of figure 7.1. Like the ridge and peak features, the pits become narrow and are difficult for the simulation to resolve. However, unlike the ridges and peaks, the pits do not seem to represent physical features of the spacetime: if  $\exp(\phi)$  (the proper length of an orbit of the  $U(1)$  isometry group; see equation (7.15)) is plotted instead of  $\phi$ , no special features are seen at the positions where pits form. (The pits in  $\phi$  are in some respects similar to the double-spike features that appear in the collapsing Gowdy simulations of section 6.2.)

Figure 7.3 shows the second wave-like variable  $\omega$  of the Moncrief reduction for the same simulation. Like  $\phi$  the variable  $\omega$  is related to the Killing vector field associated with the  $U(1)$  symmetry of the spacetime, but unlike  $\phi$  it does not have a direct physical interpretation. Fine-scale features develop in the variable  $\omega$  in much the same way as they do in the variable  $\phi$ , and at the same locations. At late times the profile of  $\omega$  is dominated by large spikes; only earlier times are shown in the figure.

In the numerical simulations of collapsing Gowdy spacetimes (section 6.2) it was found that although the spiky features of the solution were badly resolved and greatly in error at late times, the simulations could continue to run almost indefinitely. This is not the case for the  $U(1)$ -symmetric simulations: poor resolution of the fine-scale features at times beyond  $\tau \simeq 10$  leads to the evolution becoming unstable in those regions, and the code is forced to terminate at a time around  $\tau \simeq 13$ . (The reason for this seems to be that in the  $U(1)$ -symmetric case lack of resolution tends to occur over extended regions rather than at isolated points.) In section 6.2 it is argued that large errors at the Gowdy spikes do not necessarily contaminate the entire solution because the exponential decay of the characteristic speeds of the model, equation (6.8), implies that the errors can propagate only a finite, and typically very small, distance before the cosmological singularity is reached. In the  $U(1)$ -symmetric case exact values for the characteristic speeds, equation (7.11), are not known and it is harder to make statements about a spacetime's causal structure. However numerical results, plotted in figure 7.4, show that in regions where fine-scale features form the characteristic speeds for information propagating away from the regions decrease at approximately exponential rates, and

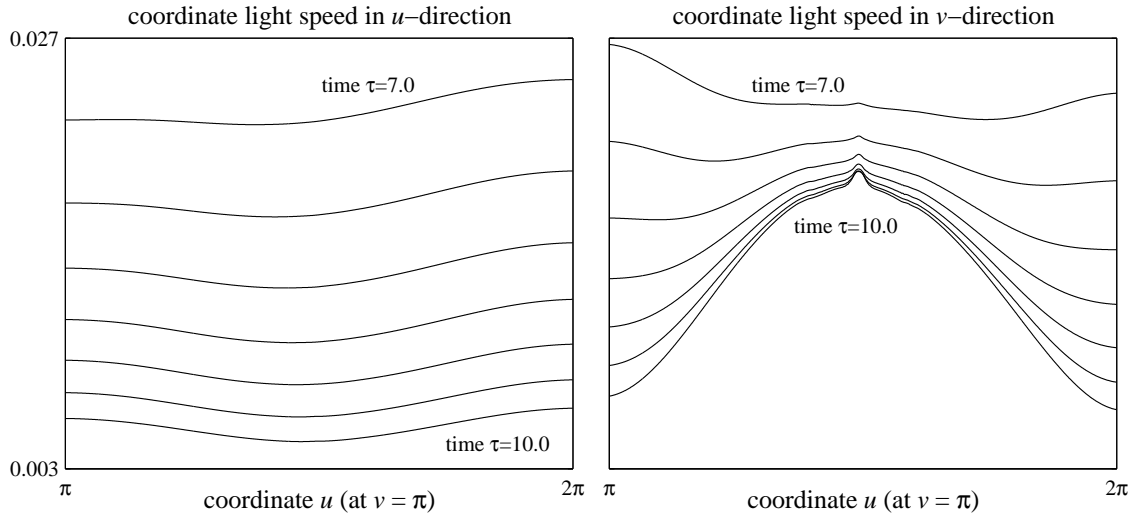


**Figure 7.4:** Characteristic speeds at a ridge feature in  $\phi$ . The speed parallel to the  $u$ -axis and the speed parallel to the  $v$ -axis are plotted along a one-dimensional slice through the spatial domain given by  $\pi \leq u \leq 2\pi$  and  $v = \pi$ . The speeds are given by equation (7.11). The ridge feature runs perpendicular to the slice and crosses it at the centre of the plotted region. The speeds are shown at equal time intervals for  $7 \leq \tau \leq 10$ . While the characteristic speeds in the directions away from the ridge decrease exponentially (left-hand plot), the speeds along the ridge tend to a limiting value greater than zero (right-hand plot). (Inaccuracies at the ridge are responsible for the lump in the middle of the data shown in the right-hand plot.)

so inaccuracies there can only influence a very small part of the complete spacetime. (In contrast the speeds for propagation within the regions do not appear to tend to zero.) This suggests that an approach like Berger and Moncrief's (1998b) in which fine-scale structure is removed from the solution by a smoothing algorithm may be valid if applied selectively: it would help stabilize the evolution beyond the time at which fine-scale structure becomes inadequately resolved without significantly affecting the majority of the solution.

Evidence supports the view that the ridge and peak features found in the numerical solutions are not simply gauge effects. As mentioned above, the proper lengths of the orbits of the  $U(1)$  isometry group (equation (7.15)) are a physical property of the spacetime which is affected by the presence of the features. Furthermore the fine-scale nature of the features is not simply a consequence of a poor choice of spatial coordinates: the proper distances in the  $u$ - and  $v$ -directions (from equation (7.4) for the metric) are found to decrease near to the peaks and ridges, and so the features are small in terms of proper distance as well as coordinate distance. The curvature invariants  $w_I$ ,  $w_{II}$ ,  $w_{III}$  and  $w_{IV}$  were presented in section 5.1 (specifically equation (5.1)) as useful indicators of coordinate-independent behaviour in a spacetime, and they have been evaluated for the  $U(1)$ -symmetric solutions following the approach described in York 1989. (The invariants are constructed

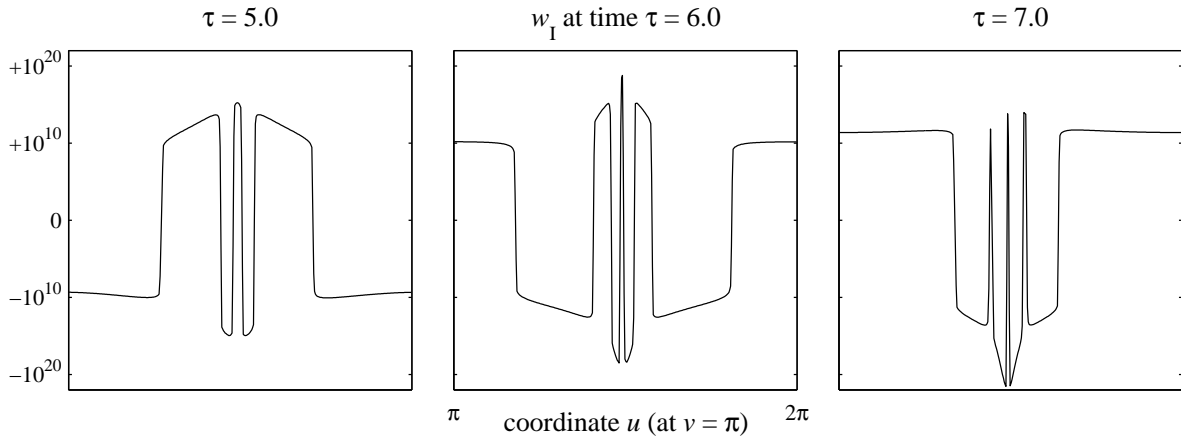


**Figure 7.5:** Curvature invariant  $w_I$  at a ridge feature in  $\phi$  at three different times. The invariant is plotted along a one-dimensional slice through the spatial domain given by  $\pi \leq u \leq 2\pi$  and  $v = \pi$ . The ridge feature runs perpendicular to the slice and crosses it at the centre of the plotted region. The axes are the same for all three plots and a logarithmic scale for the vertical axis has been produced by use of the transformation  $w \rightarrow (1/\ln 10) \sinh^{-1}(w/2)$ .

from the four-dimensional Riemann tensor which in turn is constructed from intermediate quantities  $P_{ijkl}$ ,  $Q_{ijk}$  and  $D_{ij}$  which in turn are constructed from the induced metric, extrinsic curvature and three-dimensional Riemann tensor of the spatial slices.) Figure 7.5 shows the behaviour of the curvature invariant  $w_I$  on a slice through the  $u$ - $v$  domain which crosses an emerging ridge feature; the behaviour of the other invariants is broadly similar. Two features of the behaviour of  $w_I$  are familiar from the study of curvature invariants in the Gowdy models (section 6.2). Firstly, the curvature invariants grow at approximately exponential rates and their magnitudes become very large (compare figure 6.7). Secondly, the zeros of the curvature invariants are found to converge on regions where fine-scale structure forms; figure 6.8 shows the same behaviour occurring at a spike in a Gowdy spacetime.

The ridge features in the unpolarized  $U(1)$ -symmetric cosmologies appear to be the generalization of the spike features in the unpolarized Gowdy cosmologies. Since the Gowdy and Moncrief metrics, equations (6.1) and (7.4), use time coordinates defined by the same harmonic slicing condition, it is a straightforward matter to identify the  $\theta$  coordinate of the former with the  $u$  coordinate of the latter and transform a Gowdy solution (described by variables  $P$ ,  $Q$  and  $\lambda$ ) into expressions for the Moncrief variables. (The reverse transformation is not generally possible: even if a  $U(1)$ -symmetric spacetime possesses Gowdy symmetry it has more coordinate freedom than allowed for by the Gowdy metric.) Positive spikes in the Gowdy variable  $P$  are then seen to transform into ridges in the Moncrief variable  $\phi$  according to

$$\phi(u, v, \tau) \simeq (P(u, \tau) - \tau)/2 + Q_0(u),$$

for some function  $Q_0$ , where the assumptions have been made that  $P$  grows linearly and  $Q$  becomes constant at late times. In the Gowdy spacetimes positive spikes in  $P$  are accompanied by zeros

in  $Q_{,\theta}$ , and the generalization of this for  $U(1)$ -symmetric spacetimes is that ridge features in  $\phi$  are accompanied by zeros in  $\omega_{,\tau}$ . Given this connection between  $\phi$  and  $\omega_{,\tau}$  it is possible to give a very rough sketch of how the process of ridge formation may operate. If  $\phi_{,\tau} = \phi_{,\tau}$  and  $\omega_{,\tau} = \omega_{,\tau}$  are defined as variables and the evolution equations (7.10d) and (7.10e) are simplified so that only terms involving these variables are present then they read as

$$\partial_{\tau}\phi_{\tau} \simeq -\frac{1}{2}e^{-4\phi}\omega_{\tau}^2, \quad \partial_{\tau}\omega_{\tau} \simeq 4\phi_{\tau}\omega_{\tau}.$$

Making the assumptions that  $\omega_{\tau}$  crosses zero at the location of a ridge and that  $\phi_{\tau}$  is positive there, the expected behaviour would be for  $\phi_{\tau}$  to decrease except where  $\omega_{\tau}$  is zero (and consequently for the ridge in  $\phi$  to sharpen) and for  $\omega_{\tau}$  to grow exponentially either side of the zero; evidence of this latter behaviour can be seen in the plots of  $\omega$  in figure 7.3. (In section 6.2 it was noted that in regions where spikes form in the Gowdy variable  $P$  the evolution equations are dominated by spatial derivative terms, and this seems to contradict the simplified model given above in which fine-scale structure is produced by equations containing no spatial derivatives; however equation (7.6) shows that despite appearances the variable  $\omega_{\tau}$  is a spatial rather than a temporal derivative term.)

From the results of this section and of section 6.2 it would seem that the formation of fine-scale spatial structure is a generic feature of collapsing vacuum cosmologies, and presumably of gravitational collapse in general since it can be inferred from the small particle horizon sizes of the models considered here that the effect is a local one. The appearance of fine-scale structure is problematic for attempts to numerically evolve collapsing spacetimes, although in the present work mesh refinement techniques (described in chapter 3) have been used to alleviate the problems to some extent. For the numerical simulations of  $U(1)$ -symmetric cosmologies performed here it has proven to be very difficult to reliably evolve solutions for more than a modest interval of time; the question of what happens to the fine-scale structure in the long-term (particularly as regards the oscillatory behaviour of  $U(1)$ -symmetric spacetimes reported in Berger and Moncrief 1998b) remains unanswered.

### 7.3 $U(1)$ -Symmetric Cosmologies and the Frittelli-Reula System

This section reports on a series of tests carried out to assess the value of the Frittelli-Reula formulation (described in detail in chapter 4) as a tool for the numerical evolution of Einstein's equations. In particular the question is addressed as to whether there are gains to be made in basing numerical simulations on evolution systems which are strongly (or symmetric) hyperbolic or which have only physically relevant characteristic speeds. The parameter range of the generalized Frittelli-Reula formulation (presented in section 4.2) is explored here, and an alternative hyperbolic evolution system is derived based on the variables used in the Moncrief reduction of section 7.1. The tests are based on planar and  $U(1)$ -symmetric vacuum cosmologies.

### *Testing the Frittelli-Reula System I: Planar Cosmologies*

Chapter 4 describes the construction of a computer code for the evolution of numerical solutions to the Frittelli-Reula (henceforth FR) formulation of the Einstein equations. The code has been extensively tested to check that it produces correct results: evolved solutions converge at the expected order to solutions of the Einstein equations. However this says little about the overall accuracy of the code or its stability over long time periods. As a practical test of the suitability of the FR formulation for numerical work the code has been used to evolve initial data for planar and  $U(1)$ -symmetric cosmologies. The results have been compared to numerical solutions produced by codes based on the Gowdy (section 6.1) and Moncrief (section 7.1) reductions of the Einstein equations. The analysis of the results for the  $U(1)$ -symmetric cosmologies is the main topic of the present section; as a prelude to that, the findings from the tests based on Gowdy  $T^3$  spacetimes are summarized below.

The FR system, figure 4.1, is a fully three-dimensional formulation of the Einstein equations—it assumes no symmetries in the spacetimes it describes (although as a simplification for the numerical work performed here, simulated spacetimes are assumed to have at least one spacelike Killing vector, as section 4.3 explains). For spacetimes which have a high degree of symmetry the Einstein equations can often be reduced to very simple forms; the Gowdy  $T^3$  evolution equations (6.2) are a good example of this, with coordinate conditions and constraint equations having been applied to eliminate all but the essential variables. It is to be expected that numerical simulations of planar cosmologies performed using the Gowdy equations will be considerably more accurate than equivalent simulations performed using the FR equations (in addition to the former requiring significantly less computational resources). It is interesting to ask however exactly what the sources of the discrepancies in accuracy are; the answers to this will guide the comparison between the FR system and the Moncrief reduction for  $U(1)$ -symmetric cosmologies later in this section.

It is straightforward to compare results for the FR metric (4.1) with results for the Gowdy metric (6.1). Since in both cases a harmonic time slicing condition is used, the two coordinate systems can be made to coincide by taking the slicing density in the FR formulation to be  $Q(t, x^j) = 1$  (see equation (4.11)) and the shift vector to be  $N^i(t, x^j) = 0$ . It is then a simple matter to convert between the Gowdy variables  $P$ ,  $Q$  and  $\lambda$ , and the FR variables  $h^{ij}$ ,  $M^{ij}_k$  and  $P^{ij}$ . The FR system is then tested as follows: the exact polarized Gowdy solution (6.13) is numerically evolved using both the FR equations of figure 4.1 and the Gowdy equations (6.2), with the same spatial resolution and the same time step being used in both cases. The sizes of the errors in the numerical solutions (always measured with respect to the FR three-metric  $h^{ij}$ ) are monitored.

The test is applied first to the *modified* form of the FR system (figure 4.1 with parameter settings  $\Theta = 0$  and  $\eta = \gamma = 1$ ), and as expected the errors in the evolved solution grow at a substantially faster rate than for the Gowdy evolution system. Part of the reason for this can be traced to the off-diagonal components of the metric: while in the exact polarized solution (and in the simulations based on the Gowdy equations) the metric always maintains a diagonal form, truncation errors in the FR simulations can cause the off-diagonal metric components to take on

non-zero values. (This effect is related to the inclusion of constraint quantities in the FR evolution equations; it does not occur if the parameter  $\eta$  is zero.) The performance of the FR system can thus be improved by reducing it in the following way: assume the spacetime metric to be always diagonal, identify the variables in the system which are identically zero given this assumption, and eliminate them from the evolution equations. This reduction vastly simplifies the evolution system: only nine rather than thirty variables are needed, and as a side effect non-physical characteristic speeds are no longer a feature of the equations.

The diagonal reduction of the FR system still performs significantly less well than the Gowdy system, and the next stage in improving its accuracy is to change the variables used to a set that are better adapted to the behaviour of the evolved spacetime. Since the (non-zero) components of the metric ( $h^{11}$ ,  $h^{22}$  and  $h^{33}$ ) grow or decay exponentially, the metric is better described by the variables  $H_A$ ,  $H_B$  and  $H_C$  where  $h^{11} = e^{H_A}$ ,  $h^{22} = e^{H_B}$  and  $h^{33} = e^{H_C}$ . The other FR variables  $M^{ij}_k$  and  $P^{ij}$  can be changed accordingly, and the result is a set of variables which are very similar to the variables of the Gowdy reduction. In addition to improving its overall performance, this change of variables cures an explicit problem with the FR system: since all real values for the variables  $H_A$ ,  $H_B$  and  $H_C$  describe valid spacetime metrics, the possibility of errors in the variables causing the determinant of the three-metric to become non-positive (with the code crashing as a consequence) is excluded.

A final reduction of the FR system enables it to perform with an accuracy comparable to that of the Gowdy system. For the form of the FR system derived above in which a diagonal metric is represented by the variables  $H_A$ ,  $H_B$  and  $H_C$ , the evolution equations are made conspicuously more complex than they need to be by the presence of constraint terms which vanish for exact solutions of the Einstein equations; these terms can be cancelled from the system without affecting its hyperbolicity or characteristic speeds. The reduced form of the FR system reached in this way is still more general than the (polarized) Gowdy system (in particular it uses more variables to describe the metric), but its accuracy in numerical simulations while worse is only slightly so.

In conclusion, two differences between the FR system and the Gowdy system can be thought of as being responsible for the larger rate of numerical error growth in the former. Firstly, the FR evolution equations are made more complicated than they could be by their inclusion of constraint terms. Secondly, the variables of the FR formulation are not as well adapted as the Gowdy variables to the behaviour of the spacetimes being evolved. When assessing the performance of the FR system in simulating  $U(1)$ -symmetric spacetimes later in this section, these ideas play a central role. The effect that including constraint terms in the FR evolution equations has is investigated by varying the values of the parameters in the generalized FR formulation. Also, in the next subsection, an alternative form of the FR system is produced in which the standard FR variables are replaced by the variables of the Moncrief reduction.

*Adaption of the Frittelli-Reula Formulation to  $U(1)$ -Symmetric Spacetimes*

In this subsection a transformation is applied to the generalized Frittelli-Reula (FR) formulation of Einstein's equations such that the FR variables  $h^{ij}$ ,  $M^{ij}_k$  and  $P^{ij}$  are replaced by the variables  $\Lambda$ ,  $z$ ,  $x$ ,  $\phi$ ,  $\beta_1$  and  $\beta_2$  (together with their first derivatives) that describe the Moncrief form of a  $U(1)$ -symmetric metric, equation (7.4). The reasons for doing this are twofold. Firstly, as suggested by the results of the previous subsection, an evolution system having variables which are adapted to the spacetime under investigation may lead to improved performance in numerical simulations, and this idea is tested for  $U(1)$ -symmetric cosmologies in the next subsection. Secondly, as mentioned in section 7.1, the evolution equations (7.10) of the Moncrief reduction for  $U(1)$ -symmetric spacetimes are only weakly hyperbolic, and the transformation of the FR formulation described here provides a method by which a strongly (or symmetric) hyperbolic version of the Moncrief system can be produced. The new form of the FR system is given schematically by equations (7.23) with explicit expressions for the terms in the system being given in figures 7.6 to 7.11. Only an outline of the derivation is presented here; the algebra involved in changing the variables of the FR system is exceedingly lengthy and was only made practical to perform in this work by the use of the REDUCE computer algebra package (Hearn 1995, MacCallum and Wright 1991).

The generalized (vacuum) FR evolution system, figure 4.1, is used here in a (2+1)-dimensional form:

$$\partial_t \mathbf{h} + \partial_a \mathbf{F}_{(h)\text{evol}}^a(\mathbf{h}, N^i) + \mathbf{S}_{(h)\text{evol}}(\mathbf{h}, \mathbf{P}, Q, N^i) = 0, \quad (7.21a)$$

$$\begin{aligned} \partial_t \mathbf{M}_1 + \partial_a \left[ \mathbf{F}_{(M1)\text{evol}}^a(\mathbf{h}, \mathbf{M}_1, \mathbf{P}, Q, N^i) + \eta \times \mathbf{F}_{(M1)\text{con}}^a(\mathbf{h}, \mathbf{P}, Q) \right] \\ + \mathbf{S}_{(M1)\text{evol}}(\mathbf{h}, \mathbf{M}_b, \mathbf{P}, Q, N^i) + \eta \times \mathbf{S}_{(M1)\text{con}}(\mathbf{h}, \mathbf{M}_b, \mathbf{P}, Q) = 0, \end{aligned} \quad (7.21b)$$

$$\begin{aligned} \partial_t \mathbf{M}_2 + \partial_a \left[ \mathbf{F}_{(M2)\text{evol}}^a(\mathbf{h}, \mathbf{M}_2, \mathbf{P}, Q, N^i) + \eta \times \mathbf{F}_{(M2)\text{con}}^a(\mathbf{h}, \mathbf{P}, Q) \right] \\ + \mathbf{S}_{(M2)\text{evol}}(\mathbf{h}, \mathbf{M}_b, \mathbf{P}, Q, N^i) + \eta \times \mathbf{S}_{(M2)\text{con}}(\mathbf{h}, \mathbf{M}_b, \mathbf{P}, Q) = 0, \end{aligned} \quad (7.21c)$$

$$\partial_t \mathbf{M}_3 + \eta \times \partial_a \mathbf{F}_{(M3)\text{con}}^a(\mathbf{h}, \mathbf{P}, Q) + \eta \times \mathbf{S}_{(M3)\text{con}}(\mathbf{h}, \mathbf{M}_b, \mathbf{P}, Q) = 0, \quad (7.21d)$$

$$\begin{aligned} \partial_t \mathbf{P} + \partial_a \left[ \mathbf{F}_{(P)\text{evol}}^a(\mathbf{h}, \mathbf{M}_b, \mathbf{M}_3, \mathbf{P}, Q, N^i, \Theta) + \gamma \times \mathbf{F}_{(P)\text{con}}^a(\mathbf{h}, \mathbf{M}_b, \mathbf{M}_3, Q) \right] \\ + \mathbf{S}_{(P)\text{evol}}(\mathbf{h}, \mathbf{M}_b, \mathbf{P}, Q, N^i, \Theta) + \gamma \times \mathbf{S}_{(P)\text{con}}(\mathbf{h}, \mathbf{M}_b, \mathbf{P}, Q) = 0, \end{aligned} \quad (7.21e)$$

where it has been assumed that the spacetime being evolved has a symmetry such that none of the quantities in the system depend on the third spatial coordinate  $x^3$ , and the convention used is that the indices  $a, b, \dots$  range over the values  $\{1, 2\}$ . The partial derivatives  $\partial_t$ ,  $\partial_1$  and  $\partial_2$  operate with respect to the coordinates  $t$ ,  $x^1$  and  $x^2$ . The vectors  $\mathbf{h}$ ,  $\mathbf{M}_1$ ,  $\mathbf{M}_2$ ,  $\mathbf{M}_3$  and  $\mathbf{P}$  each represent six variables, the independent components of  $h^{ij}$ ,  $M^{ij}_1$ ,  $M^{ij}_2$ ,  $M^{ij}_3$  and  $P^{ij}$ , recalling that all of these tensor-like quantities are symmetric in their  $i$ - $j$  indices. The slicing density  $Q$  and the shift vector  $N^i$  are fixed functions of the coordinates  $t$ ,  $x^1$  and  $x^2$ . The generalized FR system depends on three parameters: the parameters  $\eta$  and  $\gamma$  determine the amounts of constraint quantities that are added to the evolution equations (7.21b-e), while the parameter  $\Theta$  determines how commuting derivative terms are distributed in the transport part of equation (7.21e).

The variables  $M^{ij}_3$  are related to the derivatives of the three-metric  $h^{ij}$  with respect to the symmetry coordinate  $x^3$ , and for exact solutions of the equations (7.21) they will be identically zero. However, as explained in section 4.3, the variables  $M^{ij}_3$  cannot be omitted from the system (7.21) without affecting its hyperbolicity, although there is no harm in simplifying the system by setting them to zero in the source terms (the undifferentiated expressions  $\mathbf{S}_{(h)\text{evol}}$ , etc.). In numerical simulations truncation errors can lead to the variables  $M^{ij}_3$  becoming non-zero; however simply resetting their values to zero at the end of each time step is not found to cause adverse effects. (Section 4.3 discusses these points in greater depth.)

The FR system (7.21) can be assigned the same coordinate conditions as those used in the Moncrief reduction for  $U(1)$ -symmetric  $T^3$  spacetimes (section 7.1) by choosing the slicing density to be  $Q = 1$  and the shift vector to be  $N^i = 0$ . The FR coordinate system  $\{t, x^1, x^2, x^3\}$  then coincides with the Moncrief coordinate system  $\{\tau, u, v, w\}$ .

The new variables for the FR system are taken to be the variables used in the first-order form of the Moncrief reduction, that is  $\mathbf{\Lambda}$ ,  $\mathbf{\Lambda}_u$ ,  $\mathbf{\Lambda}_v$  and  $\mathbf{\Lambda}_\tau$  where

$$\mathbf{\Lambda} = [\Lambda, z, x, \phi, \beta_1, \beta_2]^T,$$

and  $\mathbf{\Lambda}_u$ ,  $\mathbf{\Lambda}_v$  and  $\mathbf{\Lambda}_\tau$  are the variables defined by the first derivatives of  $\mathbf{\Lambda}$  with respect to the coordinates  $u$ ,  $v$  and  $\tau$ . Here the variables  $\beta_1$  and  $\beta_2$  are used instead of the single variable  $\omega$  so that there is a one-to-one correspondence between the three-metrics described by the variables  $\mathbf{\Lambda}$  and those described by the FR variables  $\mathbf{h}$ . While the variables  $\mathbf{\Lambda}$  replace the variables  $\mathbf{h}$ , and the variables  $\mathbf{\Lambda}_u$ ,  $\mathbf{\Lambda}_v$  and  $\mathbf{\Lambda}_\tau$  replace (respectively) the variables  $\mathbf{M}_1$ ,  $\mathbf{M}_2$  and  $\mathbf{P}$ , the Moncrief formulation presents no new variables to replace the variables  $\mathbf{M}_3$ . As mentioned above, these variables need to be kept in the evolution system for technical reasons, and so in adapting the FR equations they are simply relabelled:  $\mathbf{M}_3 \rightarrow \mathbf{m}$ .

The change in variables from  $\{\mathbf{h}, \mathbf{M}_1, \mathbf{M}_2, \mathbf{M}_3, \mathbf{P}\}$  to  $\{\mathbf{\Lambda}, \mathbf{\Lambda}_u, \mathbf{\Lambda}_v, \mathbf{m}, \mathbf{\Lambda}_\tau\}$  for equations (7.21) could be performed directly using a computer algebra package, but the results would not be in a particularly manageable form. However some thought about the structure of the system (7.21) reveals that it must be equal to

$$H_{(h)} \left[ \partial_\tau \mathbf{\Lambda} - \mathbf{\Lambda}_\tau \right] = 0, \quad (7.22a)$$

$$H_{(M1)} \left[ \partial_\tau \mathbf{\Lambda}_u - \partial_u \mathbf{\Lambda}_\tau \right] + \eta \times \partial_a \mathbf{F}_{(M1)\text{con}}^a + \eta \times \mathbf{S}_{(M1)\text{con}} = 0, \quad (7.22b)$$

$$H_{(M2)} \left[ \partial_\tau \mathbf{\Lambda}_v - \partial_v \mathbf{\Lambda}_\tau \right] + \eta \times \partial_a \mathbf{F}_{(M2)\text{con}}^a + \eta \times \mathbf{S}_{(M2)\text{con}} = 0, \quad (7.22c)$$

$$\partial_\tau \mathbf{m} + \eta \times \partial_a \mathbf{F}_{(M3)\text{con}}^a + \eta \times \mathbf{S}_{(M3)\text{con}} = 0, \quad (7.22d)$$

$$H_{(P)} \left[ \partial_\tau \mathbf{\Lambda}_\tau + \partial_a \mathbf{f}_{(\tau)\text{evol}}^a(\mathbf{\Lambda}, \mathbf{\Lambda}_u, \mathbf{\Lambda}_v, \Theta) + \mathbf{s}_{(\tau)\text{evol}}(\mathbf{\Lambda}, \mathbf{\Lambda}_u, \mathbf{\Lambda}_v, \mathbf{\Lambda}_\tau, \Theta) \right] \\ + \partial_a \mathbf{F}_{(P)m}^a(\mathbf{h}, \mathbf{M}_3, \Theta) + \gamma \times \partial_a \mathbf{F}_{(P)\text{con}}^a + \gamma \times \mathbf{S}_{(P)\text{con}} = 0, \quad (7.22e)$$

where  $H_{(h)}$ ,  $H_{(M1)}$ ,  $H_{(M2)}$  and  $H_{(P)}$  are  $6 \times 6$  matrices depending on the variables  $\mathbf{\Lambda}$ . The terms in the square brackets in these equations are simply the first-order evolution equations for the Moncrief variables; in particular, equation (7.22e) incorporates the Moncrief evolution equations (7.10a–d)



and (7.13). (Ignoring the constraint terms in the equation (7.21e), the FR evolution system would be expected to be the same as the Moncrief evolution system since they both derive from the ADM form of the Einstein equations; checking the final results of the change of variables performed here using computer algebra software reveals that this is indeed the case, and no additional constraint terms need to be included in equation (7.22e).)

There is some flexibility in the first-order form of the Moncrief evolution equations that appears as part of the transformed FR system in that terms of the form  $X_{,uv}$  can be represented as  $\partial_u X_v$  or as  $\partial_v X_u$  or as a combination of the two. A comparison between the principal parts of the FR system and the Moncrief system fixes the form of the latter in equation (7.22e), and in the process introduces a dependence of the flux  $\mathbf{f}_{(\tau)\text{evol}}^a$  and the source  $\mathbf{s}_{(\tau)\text{evol}}$  on the parameter  $\Theta$ . A number of terms involving the variables  $\mathbf{M}_3$  appear in the FR fluxes  $\mathbf{F}_{(P)\text{evol}}^a$  in equation (7.21e) which are not accounted for in the Moncrief evolution system. This leads to the appearance of additional flux terms  $\mathbf{F}_{(P)m}^a$  in the equation (7.22e).

Completing the change of variables for the FR system leads to the set of evolution equations

$$\partial_\tau \mathbf{\Lambda} - \mathbf{\Lambda}_\tau = 0, \quad (7.23a)$$

$$\partial_\tau \mathbf{\Lambda}_u + \partial_u(\eta \times \mathbf{f}_{(u)\text{con}}^u - \mathbf{\Lambda}_\tau) + \eta \times \partial_v \mathbf{f}_{(u)\text{con}}^v + \eta \times \mathbf{s}_{(u)\text{con}} = 0, \quad (7.23b)$$

$$\partial_\tau \mathbf{\Lambda}_v + \eta \times \partial_u \mathbf{f}_{(v)\text{con}}^u + \partial_v(\eta \times \mathbf{f}_{(v)\text{con}}^v - \mathbf{\Lambda}_\tau) + \eta \times \mathbf{s}_{(v)\text{con}} = 0, \quad (7.23c)$$

$$\partial_\tau \mathbf{m} + \eta \times \partial_a \mathbf{f}_{(m)\text{con}}^a + \eta \times \mathbf{s}_{(m)\text{con}} = 0, \quad (7.23d)$$

$$\partial_\tau \mathbf{\Lambda}_\tau + \partial_a \left[ \mathbf{f}_{(\tau)\text{evol}}^a(\Theta) + \gamma \times \mathbf{f}_{(\tau)\text{con}}^a + \mathbf{f}_{(\tau)m}^a(\mathbf{m}, \Theta, \gamma) \right] + \mathbf{s}_{(\tau)\text{evol}}(\Theta) + \gamma \times \mathbf{s}_{(\tau)\text{con}} = 0, \quad (7.23e)$$

where dependence of the flux and source terms on the variables  $\mathbf{\Lambda}$ ,  $\mathbf{\Lambda}_u$ ,  $\mathbf{\Lambda}_v$  and  $\mathbf{\Lambda}_\tau$  is implicit. These equations follow from inversion of the matrices in the equations (7.22), which are seen to be the Jacobian matrices of the change of variables:  $H_{(h)} = \partial \mathbf{h} / \partial \mathbf{\Lambda}$ ,  $H_{(M1)} = \partial \mathbf{M}_1 / \partial \mathbf{\Lambda}_u$ ,  $H_{(M2)} = \partial \mathbf{M}_2 / \partial \mathbf{\Lambda}_v$  and  $H_{(P)} = \partial \mathbf{P} / \partial \mathbf{\Lambda}_\tau$ . (Since the variables  $\mathbf{M}_1$ ,  $\mathbf{M}_2$  and  $\mathbf{P}$  depend on  $\mathbf{\Lambda}$  as well as on  $\mathbf{\Lambda}_u$ ,  $\mathbf{\Lambda}_v$  and  $\mathbf{\Lambda}_\tau$ , it might seem that there should be additional Jacobian matrices in the system reflecting this; however the terms affected are all of the form of equation (7.23a), and when not in the principal parts of evolution systems these terms are trivially zero.) The FR constraint terms in the equations (7.22) are converted into the new variables according to

$$\begin{aligned} \mathcal{C}^0 &= -\frac{1}{2}e^{2\phi+4\tau-2\Lambda}\mathcal{H}_0 - (\partial_u m_A + \partial_v m_B), \\ \mathcal{C}^a &= \frac{1}{2}e^{3\phi+4\tau-2\Lambda}e^{ab}\mathcal{H}_b, \\ \mathcal{C}^3 &= -\frac{1}{2}e^{3\phi+4\tau-2\Lambda}e^{ab}\beta_a\mathcal{H}_b - \frac{1}{2}e^{-\phi+2\tau-\Lambda}\mathcal{H}_\beta, \end{aligned} \quad (7.24)$$

where  $\{\mathcal{C}^\mu\}$  are the FR constraint quantities of equations (4.12) and  $\{\mathcal{H}_0, \mathcal{H}_a, \mathcal{H}_\beta\}$  are the Moncrief constraint quantities of equations (7.12) and (7.14). Undifferentiated  $\mathbf{m}$  terms have been omitted from equations (7.24) since they make no contribution to the system (7.23); however derivatives of the  $\mathbf{m}$  variables (specifically the variables  $m_A$  and  $m_B$  in  $\mathcal{C}^0$ , identified below) must be incorporated into the principal part of the system, and in equation (7.23e) the flux vectors  $\mathbf{f}_{(\tau)m}^a$  represent such terms which come from the constraint quantities  $\mathbf{F}_{(P)\text{con}}^a$  together with the  $\mathbf{M}_3$  terms in the fluxes  $\mathbf{F}_{(P)m}^a$ .

$$\begin{aligned}
\mathbf{f}_{(u)\text{con}}^u &= \begin{bmatrix} \Lambda_\tau + 2xz_\tau + \frac{1}{2}e^{-2z}e_{,z}^{uv}x_\tau \\ \frac{1}{2}x\Lambda_\tau + z_\tau - \frac{1}{2}e^{-2z}e^{uv}x_\tau \\ e^{2z}(\frac{1}{2}e_{,z}^{uv}\Lambda_\tau + 2e^{uv}z_\tau) + x_\tau \\ \frac{1}{2}\Lambda_\tau + xz_\tau + \frac{1}{4}e^{-2z}e_{,z}^{uv}x_\tau + \frac{1}{2}\beta_1\omega_{,v} \\ -\beta_1(\Lambda_\tau + 2xz_\tau + \frac{1}{2}e^{-2z}e_{,z}^{uv}x_\tau) + e^{vv}e^{uc}\beta_{c\tau} \\ -\beta_1(2(x-1)z_\tau - \frac{1}{2}e^{-2z}e_{,z}^{uu}x_\tau) - e^{uv}e^{uc}\beta_{c\tau} \end{bmatrix} \\
\mathbf{f}_{(u)\text{con}}^v &= \begin{bmatrix} -2(x+1)z_\tau + \frac{1}{2}e^{-2z}e_{,z}^{vv}x_\tau \\ -\frac{1}{2}(x+1)\Lambda_\tau - \frac{1}{2}e^{-2z}e^{vv}x_\tau \\ e^{2z}(\frac{1}{2}e_{,z}^{vv}\Lambda_\tau + 2e^{vv}z_\tau) \\ -(x+1)z_\tau + \frac{1}{4}e^{-2z}e_{,z}^{vv}x_\tau - \frac{1}{2}\beta_1\omega_{,u} \\ \beta_1(2(x+1)z_\tau - \frac{1}{2}e^{-2z}e_{,z}^{vv}x_\tau) + e^{vv}e^{vc}\beta_{c\tau} \\ \beta_1(2xz_\tau - \Lambda_\tau + \frac{1}{2}e^{-2z}e_{,z}^{uv}x_\tau) - e^{uv}e^{vc}\beta_{c\tau} \end{bmatrix} \\
\mathbf{S}_{(u)\text{con}} &= \begin{bmatrix} Y_u \\ -\frac{1}{2}e^{2z}e_{,x}^{cv}\Lambda_c(2-\Lambda_\tau) + \frac{1}{2}(x_v-x_u)\Lambda_\tau - (2e^{2z}e_{,x}^{vc}z_c + x_u-x_v)z_\tau + \frac{1}{2}e^{-4z}x_u x_\tau \\ \quad - 2e^{2z}e_{,x}^{vc}\phi_c\phi_\tau + \frac{1}{4}e^{2\tau-\Lambda}\omega_{,\tau}e_{,z}^{vc}\beta_{c\tau} \\ \frac{1}{2}e^{2z}e_{,z}^{cv}\Lambda_c(2-\Lambda_\tau) - [2e^{4z}(z_v-z_u) + xx_u - (x+1)x_v]\Lambda_\tau - (4e^{2z}e^{vc}z_c + 2x_u)z_\tau \\ \quad - [2(1-x)z_u + 2(1+x)z_v + x_u-x_v]x_\tau + 2e^{2z}e_{,z}^{vc}\phi_c\phi_\tau + e^{4z+2\tau-\Lambda}\omega_{,\tau}e_{,x}^{vc}\beta_{c\tau} \\ \frac{1}{2}Y_u - \frac{1}{2}e^{4\phi+2\tau-\Lambda}e^{bc}\beta_{1b}\beta_{c\tau} \\ -\beta_1Y_u + e^{bc}\beta_{b\tau}[e^{vv}(4\phi_c-\Lambda_c) - e^{,c}{}^{vv}] + \beta_{1c}(\frac{1}{2}e^{-2z}e_{,z}^{vc}x_\tau - 2e^{2z}e_{,x}^{vc}z_\tau) + \beta_{1u}\Lambda_\tau \\ -\beta_1Y_v - e^{bc}\beta_{b\tau}[e^{uv}(4\phi_c-\Lambda_c) - e^{,c}{}^{uv}] - \beta_{1c}(\frac{1}{2}e^{-2z}e_{,z}^{uc}x_\tau - 2e^{2z}e_{,x}^{uc}z_\tau) + \beta_{1v}\Lambda_\tau \end{bmatrix}
\end{aligned}$$

where  $Y_a = \Lambda_a(2 - \Lambda_\tau) + 4z_a z_\tau + e^{-4z}x_a x_\tau + 4\phi_a \phi_\tau + e^{-4\phi}\omega_{,\tau}\omega_{,a}$

**Figure 7.6:** Flux and source terms for the evolution equation (7.23b) for  $\Lambda_u$  in the transformed Frittelli-Reula system. These terms derive from the constraint quantities added to the system to ensure hyperbolicity. The definitions of  $\omega_{,u}$ ,  $\omega_{,v}$  and  $\omega_{,\tau}$  are given in equation (7.6).

It turns out that only three of the variables  $\mathbf{m}$ , labelled  $m_A$ ,  $m_B$  and  $m_C$ , have non-trivial evolution equations as represented by equation (7.23d). The three other  $\mathbf{m}$  variables are not affected by the transport part of the evolution system, and consequently can be omitted altogether for the equations without affecting their hyperbolicity. The system (7.23) can thus be simplified by truncating the vector of variables  $\mathbf{m}$  to

$$\mathbf{m} = [m_A, m_B, m_C]^T = [M^{13}_3, M^{23}_3, M^{33}_3]^T.$$

Complete expressions for the flux and source terms in the transformed FR system (7.23) are given in figures 7.6 to 7.11. It is apparent from equations (7.23) that in adapting the FR formulation to  $U(1)$ -symmetric spacetimes, an extended first-order Moncrief evolution system has in effect been constructed, and this has the same hyperbolic properties and characteristic speeds as the

$$\begin{aligned}
\mathbf{f}_{(v)\text{con}}^u &= \begin{bmatrix} 2(x-1)z_\tau - \frac{1}{2}e^{-2z}e_{,z}^{uu}x_\tau \\ \frac{1}{2}(x-1)\Lambda_\tau + \frac{1}{2}e^{-2z}e^{uu}x_\tau \\ -e^{2z}(\frac{1}{2}e_{,z}^{uu}\Lambda_\tau + 2e^{uu}z_\tau) \\ (x-1)z_\tau - \frac{1}{4}e^{-2z}e_{,z}^{uu}x_\tau + \frac{1}{2}\beta_2\omega_{,v} \\ -\beta_2(\Lambda_\tau + 2xz_\tau + \frac{1}{2}e^{-2z}e_{,z}^{uv}x_\tau) - e^{uv}e^{uc}\beta_{c\tau} \\ -\beta_2(2(x-1)z_\tau - \frac{1}{2}e^{-2z}e_{,z}^{uu}x_\tau) + e^{uu}e^{uc}\beta_{c\tau} \end{bmatrix} \\
\mathbf{f}_{(v)\text{con}}^v &= \begin{bmatrix} \Lambda_\tau - 2xz_\tau - \frac{1}{2}e^{-2z}e_{,z}^{uv}x_\tau \\ -\frac{1}{2}x\Lambda_\tau + z_\tau + \frac{1}{2}e^{-2z}e^{uv}x_\tau \\ -e^{2z}(\frac{1}{2}e_{,z}^{uv}\Lambda_\tau + 2e^{uv}z_\tau) + x_\tau \\ \frac{1}{2}\Lambda_\tau - xz_\tau - \frac{1}{4}e^{-2z}e_{,z}^{uv}x_\tau - \frac{1}{2}\beta_2\omega_{,u} \\ \beta_2(2(x+1)z_\tau - \frac{1}{2}e^{-2z}e_{,z}^{vv}x_\tau) - e^{uv}e^{vc}\beta_{c\tau} \\ \beta_2(2xz_\tau - \Lambda_\tau + \frac{1}{2}e^{-2z}e_{,z}^{uv}x_\tau) + e^{uu}e^{vc}\beta_{c\tau} \end{bmatrix} \\
\mathbf{s}_{(v)\text{con}} &= \begin{bmatrix} Y_v \\ \frac{1}{2}e^{2z}e_{,x}^{uc}\Lambda_c(2-\Lambda_\tau) + \frac{1}{2}(x_v-x_u)\Lambda_\tau + (2e^{2z}e_{,x}^{uc}z_c - x_u+x_v)z_\tau + \frac{1}{2}e^{-4z}x_vx_\tau \\ \quad + 2e^{2z}e_{,x}^{uc}\phi_c\phi_\tau - \frac{1}{4}e^{2\tau-\Lambda}\omega_{,\tau}e_{,z}^{uc}\beta_{c\tau} \\ -\frac{1}{2}e^{2z}e_{,z}^{uc}\Lambda_c(2-\Lambda_\tau) - [2e^{4z}(z_v-z_u) + (x-1)x_u - xx_v]\Lambda_\tau + (4e^{2z}e^{uc}z_c - 2x_v)z_\tau \\ \quad + [2(x-1)z_u - 2(x+1)z_v + x_v - x_u]x_\tau - 2e^{2z}e_{,z}^{uc}\phi_c\phi_\tau - e^{4z+2\tau-\Lambda}\omega_{,\tau}e_{,x}^{uc}\beta_{c\tau} \\ \frac{1}{2}Y_v - \frac{1}{2}e^{4\phi+2\tau-\Lambda}e^{bc}\beta_{2b}\beta_{c\tau} \\ -\beta_2Y_u - e^{bc}\beta_{b\tau}[e^{uv}(4\phi_c-\Lambda_c) - e_{,c}^{uv}] + \beta_{2c}(\frac{1}{2}e^{-2z}e_{,z}^{vc}x_\tau - 2e^{2z}e_{,x}^{vc}z_\tau) + \beta_{2u}\Lambda_\tau \\ -\beta_2Y_v + e^{bc}\beta_{b\tau}[e^{uu}(4\phi_c-\Lambda_c) - e_{,c}^{uu}] - \beta_{2c}(\frac{1}{2}e^{-2z}e_{,z}^{uc}x_\tau - 2e^{2z}e_{,x}^{uc}z_\tau) + \beta_{2v}\Lambda_\tau \end{bmatrix}
\end{aligned}$$

**Figure 7.7:** Flux and source terms for the evolution equation (7.23c) for  $\Lambda_v$  in the transformed Frittelli-Reula system. These terms derive from the constraint quantities added to the system to ensure hyperbolicity. The definitions of  $\omega_{,u}$ ,  $\omega_{,v}$  and  $\omega_{,\tau}$  are given in equation (7.6). See figure 7.6 for the definitions of  $Y_u$  and  $Y_v$ .

FR system. The original Moncrief evolution system appears as a special case in equations (7.23): if the parameter choices  $\eta = \gamma = 0$  and  $\Theta = 1/2$  are made, then the evolution equations (7.10a-d) and (7.13) are recovered. (In the case that  $\eta = 0$  the variables  $\mathbf{m}$  can be omitted altogether from the system.) In the next subsection the two FR systems of figure 4.1 and equations (7.23) are compared to see which performs better in numerical simulations of  $U(1)$ -symmetric  $T^3$  spacetimes.

### *Testing the Frittelli-Reula System II: $U(1)$ -Symmetric Cosmologies*

Earlier in this section results were summarized from a set of tests performed on a numerical implementation of the Frittelli-Reula (FR) formulation of Einstein's equations (as described in chapter 4). Those tests were based on vacuum planar spacetimes, and such spacetimes can be described by very simple sets of equations (in particular the Gowdy system of section 6.1). On

$$\begin{aligned}\mathbf{f}_{(m)\text{con}}^a &= \frac{1}{2}e^{2\phi+2\tau-\Lambda}[k^{1a}, k^{2a}, 2k^{3a}]^T \\ \mathbf{s}_{(m)\text{con}} &= \frac{1}{2}e^{2\phi+2\tau-\Lambda}\left([k^1, k^2, 2k^3]^T - (2\phi_c - \Lambda_c)[k^{1c}, k^{2c}, 2k^{3c}]^T\right)\end{aligned}$$

where  $k^{ab} = e^{ab}\Lambda_\tau + e_{,\tau}^{ab}$

$$k^{3a} = -\beta_c k^{ac} - e^{ac}\beta_{c\tau}$$

$$k^a = (2 - \Lambda_\tau)e^{ac}\Lambda_c - \Lambda_\tau e_{,c}^{ac} + 4e^{ac}\phi_c\phi_\tau - e^{2\tau-\Lambda}\omega_{,\tau}\varepsilon^{ac}\beta_{c\tau} + 2e^{-2z}\varepsilon^{ac}(z_c x_\tau - x_c z_\tau)$$

$$k^3 = -\beta_c k^c + k^{bc}\beta_{bc} - (4\phi_b - \Lambda_b)e^{bc}\beta_{c\tau}$$

**Figure 7.8:** Flux and source terms for the evolution equation (7.23d) for  $\mathbf{m}$  in the transformed Frittelli-Reula system. These terms derive from the constraint quantities added to the system to ensure hyperbolicity. The definition of  $\omega_{,\tau}$  is given in equation (7.6). Terms of the form  $e_{,c}^{ab}$  should be expanded as  $e_{,z}^{ab}z_c + e_{,x}^{ab}x_c$ .

$$\begin{aligned}\mathbf{f}_{(\tau)m}^u &= e^{2\Lambda-4\tau-2\phi} \begin{bmatrix} 2(2\gamma - \Theta - 1)m_A \\ (1 - \Theta)(xm_A + (x - 1)m_B) \\ (1 - \Theta)e^{2z}(e_{,z}^{uv}m_A - e_{,z}^{uu}m_B) \\ (\gamma - 2\Theta)m_A - \frac{1}{2}e^{4\phi+2\tau-\Lambda}e^{uc}\beta_c(2\beta_1m_A + 2\beta_2m_B + m_C) \\ - 2e^{uc}\beta_c(e^{vv}m_A - e^{uv}m_B) - 2(1 - 2\Theta)\beta_1m_A - 2(1 - \Theta)(\beta_2m_B + m_C) \\ 2e^{uc}\beta_c(e^{vv}m_A - e^{uu}m_B) + 2\Theta\beta_2m_A \end{bmatrix} \\ \mathbf{f}_{(\tau)m}^v &= e^{2\Lambda-4\tau-2\phi} \begin{bmatrix} 2(2\gamma - \Theta - 1)m_B \\ - (1 - \Theta)((x + 1)m_A + xm_B) \\ (1 - \Theta)e^{2z}(e_{,z}^{vv}m_A - e_{,z}^{uv}m_B) \\ (\gamma - 2\Theta)m_B - \frac{1}{2}e^{4\phi+2\tau-\Lambda}e^{vc}\beta_c(2\beta_1m_A + 2\beta_2m_B + m_C) \\ - 2e^{vc}\beta_c(e^{vv}m_A - e^{uv}m_B) + 2\Theta\beta_1m_B \\ 2e^{vc}\beta_c(e^{uv}m_A - e^{uu}m_B) - 2(1 - 2\Theta)\beta_2m_B - 2(1 - \Theta)(\beta_1m_A + m_C) \end{bmatrix}\end{aligned}$$

**Figure 7.9:** Fluxes for the evolution equation (7.23e) for  $\Lambda_\tau$  in the transformed Frittelli-Reula system. These terms incorporate the  $\mathbf{m}$  variables which are required for hyperbolicity in the Frittelli-Reula formulation but which are not originally present in the Moncrief reduction.

the one hand this is advantageous because it means that the FR formulation can be gradually

$$\begin{aligned}\mathbf{f}_{(\tau)\text{con}}^a &= e^{\Lambda-2\tau}(e^{ac}\Lambda_c + e_{,c}^{ac})[2, 0, 0, \frac{1}{2}, 0, 0]^T \\ \mathbf{s}_{(\tau)\text{con}} &= \left( e^{\Lambda-2\tau}[e^{ab}(2\phi_a\phi_b - \Lambda_a\Lambda_b + \frac{1}{2}e^{-4\phi}\omega_{,a}\omega_{,b}) - e_{,c}^{ac}\Lambda_a - 2e^{-2z}(z_u x_v - z_v x_u)] \right. \\ &\quad \left. + 2z_\tau^2 + \frac{1}{2}e^{-4z}x_\tau^2 + 2\phi_\tau^2 + \frac{1}{2}e^{-4\phi}\omega_{,\tau}^2 - \frac{1}{2}(2 - \Lambda_\tau)^2 \right)[2, 0, 0, \frac{1}{2}, 0, 0]^T\end{aligned}$$

**Figure 7.10:** Flux and source terms for the evolution equation (7.23e) for  $\Lambda_\tau$  in the transformed Frittelli-Reula system. These terms derive from the constraint quantities added to the system to ensure hyperbolicity. The definitions of  $\omega_{,u}$ ,  $\omega_{,v}$  and  $\omega_{,\tau}$  are given in equation (7.6).

$$\begin{aligned}\mathbf{f}_{(\tau)\text{evol}}^a &= e^{\Lambda-2\tau} \begin{bmatrix} -2e^{ac}\Lambda_c - e_{,c}^{ac} \\ \frac{1}{4}e_{,z}^{ac}\Lambda_c - \frac{1}{2}(1-2\Theta)e^{-2z}\varepsilon^{ac}x_c \\ e^{4z}e_{,x}^{ac}\Lambda_c + 2(1-2\Theta)e^{2z}\varepsilon^{ac}z_c \\ -e^{ac}\phi_c \\ \varepsilon^{ab}\varepsilon^{cd}e_{uc}(\beta_{bd} - \Theta\beta_{db}) \\ \varepsilon^{ab}\varepsilon^{cd}e_{vc}(\beta_{bd} - \Theta\beta_{db}) \end{bmatrix} \\ \mathbf{s}_{(\tau)\text{evol}} &= \begin{bmatrix} -e^{\Lambda-2\tau}[e^{ab}(2\phi_a\phi_b + \frac{1}{2}e^{-4\phi}\omega_{,a}\omega_{,b} - \Lambda_a\Lambda_b) - e_{,c}^{ac}\Lambda_a - 2e^{-2z}(z_u x_v - z_v x_u)] \\ \frac{1}{2}e^{-4z}x_\tau^2 - \frac{1}{4}e^{\Lambda-2\tau}[4e^{ab}\Lambda_a z_b - 2e_{,x}^{ab}\Lambda_a x_b + e_{,z}^{ab}(\Lambda_a\Lambda_b - 2\phi_a\phi_b - \frac{1}{2}e^{-4\phi}\omega_{,a}\omega_{,b}) \\ - 4e^{-2z}(1-\Theta)(\Lambda_u x_v - \Lambda_v x_u) + 4e^{-2z}(1-2\Theta)(z_u x_v - z_v x_u)] \\ - 4z_\tau x_\tau - e^{\Lambda-2\tau+4z}[e_{,x}^{ab}(\Lambda_a\Lambda_b + 4z_a\Lambda_b - 2\phi_a\phi_b - \frac{1}{2}e^{-4\phi}\omega_{,a}\omega_{,b}) + e^{-2z}(\Lambda_u - \Lambda_v)(x_u - x_v) \\ - 2e_{,x}^{ab}\Lambda_a z_b + 4(1-\Theta)e^{-2z}(\Lambda_u z_v - \Lambda_v z_u)] \\ - \frac{1}{2}e^{-4\phi}(e^{\Lambda-2\tau}e^{ab}\omega_{,a}\omega_{,b} - \omega_{,\tau}^2) \\ - e_{ub,\tau}e^{bc}\beta_{c\tau} - (\Lambda_\tau - 2 - 4\phi_\tau)\beta_{1\tau} - 4e^{\Lambda-2\tau-4\phi}\omega_{,\tau}e^{vc}\phi_c \\ + e^{\Lambda-2\tau}[(1-\Theta)(E_v^{uv}\beta_{1u} - E_u^{vv}\beta_{2v}) + E_v^{vv}(\beta_{1v} - \Theta\beta_{2u}) + E_u^{uv}(\Theta\beta_{1v} - \beta_{2u})] \\ - e_{vb,\tau}e^{bc}\beta_{c\tau} - (\Lambda_\tau - 2 - 4\phi_\tau)\beta_{2\tau} + 4e^{\Lambda-2\tau-4\phi}\omega_{,\tau}e^{uc}\phi_c \\ + e^{\Lambda-2\tau}[(1-\Theta)(E_u^{uv}\beta_{2v} - E_v^{uu}\beta_{1u}) + E_u^{uu}(\beta_{2u} - \Theta\beta_{1v}) + E_v^{uv}(\Theta\beta_{2u} - \beta_{1v})] \end{bmatrix}\end{aligned}$$

where  $E_a^{bc} = \Lambda_a e^{bc} + e_{,a}^{bc}$

**Figure 7.11:** Flux and source terms for the evolution equation (7.23e) for  $\Lambda_\tau$  in the transformed Frittelli-Reula system. These terms make up a first-order form of the evolution equations (7.10a–d) and (7.13) for the Moncrief reduction. The definitions of  $\omega_{,u}$ ,  $\omega_{,v}$  and  $\omega_{,\tau}$  are given in equation (7.6).

‘dissected’ in order to identify aspects of it which cause poor numerical performance, as was done

with respect to the Gowdy system earlier in this section. On the other hand numerical simulations of simple spacetimes are clearly not a fair test of an evolution system which is designed to deal with the Einstein equations in their full generality. In the present subsection results are presented from numerical tests of the FR system using vacuum  $U(1)$ -symmetric  $T^3$  spacetimes. Although the symmetry of these spacetimes allows them to be described by equations which are simpler than the full Einstein equations (see the system (7.10)), it may be hoped that they none the less provide a comprehensive test of the FR formulation.

In the previous subsection an alternative form of the FR evolution system was derived in which the standard FR variables  $h^{ij}$ ,  $M^{ij}_k$  and  $P^{ij}$  are replaced by the variables used to describe the Moncrief form of a  $U(1)$ -symmetric metric, equation (7.4). This new formulation consists of the equations (7.23) with flux and source terms given explicitly in figures 7.6 to 7.11, and it is tested here alongside the standard FR system given by figure 4.1. In both versions of the FR formulation, three parameters  $\Theta$ ,  $\eta$  and  $\gamma$  control the hyperbolic character of the evolution equations and, as discussed in section 4.2, four ranges of these parameters are of particular interest. The *original* FR system is given by  $\Theta = \eta = \gamma = 1$ ; it is the evolution system described by Frittelli and Reula in their 1996 paper, and though it has physically relevant characteristic speeds it is only weakly hyperbolic. The *modified* FR system is given by  $\Theta = 0$  and  $\eta = \gamma = 1$ ; it corrects the original system to make it consistent with Frittelli and Reula's proof of symmetric hyperbolicity, but in the process it introduces acausal (faster than light) characteristic speeds. The *causal* FR systems are given by  $\Theta = (3\eta - 1)/3\eta$  and  $\gamma = (9\eta - 2)/(12\eta - 3)$  where  $\eta$  can take any value except 0 or  $1/4$ ; these systems are strongly hyperbolic and have only physically relevant characteristic speeds. The ADM systems are given by  $\eta = \gamma = 0$  where  $\Theta$  can take any value; these systems do not incorporate the additional constraint terms that characterize the general FR formulation, and while their characteristic speeds are physically relevant they are only weakly hyperbolic.

The eight variations of the FR formulation listed above (four parameter ranges for each of two variable sets) are tested against the Moncrief evolution system (7.10) for numerical simulations of collapsing  $U(1)$ -symmetric  $T^3$  cosmologies. The initial data set used is the same as equation (7.20) but with  $\alpha = 0.05$  and  $c = +1.0$ . (It is straightforward to convert the initial data from Moncrief variables to FR variables.) A single uniform low-resolution grid is used in all cases with a mesh size of  $\Delta u = \Delta v = 2\pi/40$ , and the time steps used have a fixed size of  $\Delta\tau = 2\pi/100$ . The simulations are run from a start time of  $\tau = 0$  up to time  $\tau = 5$ ; this is not long enough for the fine-scale structure formation reported in section 7.2 to be a factor in the results. All of the simulations use the standard two-step Lax-Wendroff integration method described in chapter 2. (For the modified FR system with standard variables, results using the Lax-Wendroff method have been compared to results using the high-resolution method of chapter 2, and the conclusions are essentially the same as for the Gowdy simulations of chapter 6: despite the appearance of steep gradients at late times in the solutions, the high-resolution method is not found to perform significantly better than the Lax-Wendroff method when used to evolve these vacuum spacetimes.)

The FR Hamiltonian constraint quantity  $\mathcal{C}^0$  from equation (4.12a) is used as a measure of the error in the simulations:

$$\text{error} = \Delta u \Delta v \sum |\mathcal{C}^0|,$$

where for the Moncrief variables the value of  $\mathcal{C}^0$  is calculated from equations (7.24) and (7.12), and second-order estimates of derivatives are used when needed. Each simulation is then rated according to its ‘crash’ time, defined as being the value of the time coordinate  $\tau$  at which the error exceeds the value  $10^4$ . (Since the metric components tend to grow exponentially it is not unreasonable for the error to reach values of this magnitude.) There are of course many different ways in which errors in the simulations could be measured, and it could be argued that constraint quantities are not appropriate measures of error size: the ability of an evolution system to preserve the constraint equations is not necessarily the same as its ability to produce accurate solutions. However it has been found that the performance results for the different FR formulations are qualitatively similar regardless of the error measure used, and the Hamiltonian constraint is in many ways the most practical choice. Typically the ‘crash’ time of a simulation is reached only a short while before the errors in the evolved solution build up to the point that the numerical code is forced to terminate.

The results of the numerical tests are presented in figure 7.12. The crash times for simulations based on the standard FR formulation, figure 4.1, are shown in red while the crash times for simulations based on the transformed FR formulation, equations (7.23), are shown in blue. The crash time of a simulation using the evolution equations (7.10) of the Moncrief reduction for  $U(1)$ -symmetric spacetimes is marked in the figure as a horizontal black line, and the results suggest that this system of equations is in general preferable to any of the FR systems considered. (While the results in figure 7.12 show that for some parameter settings, later crash times are observed for FR systems than for the Moncrief system, the parameter range for which this is true is found to vary depending on the error measure used.)

It is clear from figure 7.12 that of the two classes of FR simulations, those which are based on Moncrief’s choice of variables perform significantly better than those which use the standard FR variables. This adds support to the principle suggested by the numerical studies of planar cosmologies described earlier in this section that the use of a set of variables which are in some sense adapted to the spacetimes being investigated can lead to significant improvements in the accuracy of numerical simulations. While the FR formulation applies to any spacetime, this generality is not without its disadvantages.

Considering now variations in numerical performance related to changes in the FR parameter settings, it can be seen from figure 7.12 that while the variations may be large, it is not easy to identify an underlying pattern to them. Evidence from the ADM and the modified and original FR systems suggests that changes in the parameter  $\Theta$  (with  $\eta$  and  $\gamma$  remaining constant) have relatively small effects on the accuracies of simulations, while changes in the parameters  $\eta$  and  $\gamma$  (which are responsible for the addition of constraint quantities to the evolution equations) seem to have more significant effects. Within the family of causal FR systems sizeable variations in numerical performance are seen as the parameter  $\eta$  is varied. As  $\eta$  approaches the value 0, the

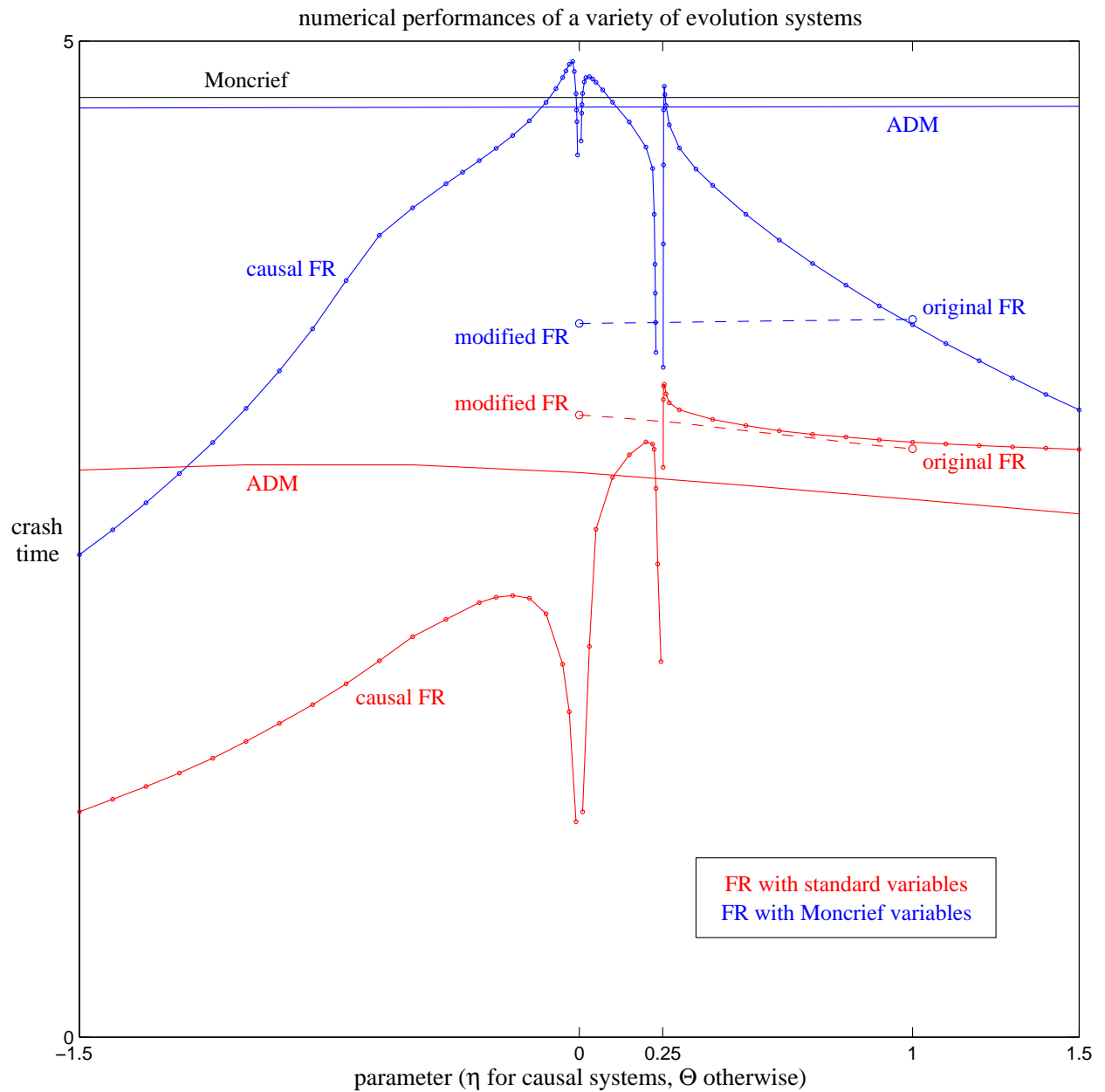


**Figure 7.12:** Evolution systems compared for numerical simulations of a  $U(1)$ -symmetric spacetime. For each system tested, the time at which the simulation ‘crashes’ (as determined by the error in the Hamiltonian constraint becoming larger than a specified limit) is recorded. The crash time for a simulation based on the reduced Moncrief evolution system (7.10) is shown as a black line. Results for the standard Frittelli-Reula formulation (figure 4.1) are plotted in red while results for the transformed formulation (7.23) are plotted in blue. For the ADM family of evolution systems and the original and modified Frittelli-Reula systems the horizontal axis shows the parameter  $\Theta$ . For the causal Frittelli-Reula family of evolution systems the horizontal axis shows the parameter  $\eta$ .



associated value for the parameter  $\Theta$  diverges, and the same behaviour occurs in the parameter  $\gamma$  as  $\eta$  approaches  $1/4$ ; in both cases the performance of the simulations deteriorates. In general it would seem to be the case that when any of the parameters (but particularly  $\eta$  or  $\gamma$ ) are large, the numerical performance of the FR system suffers. However it is not generally true that small parameter values are responsible for good simulation accuracies, as can be seen from the results for the ADM systems in which  $\eta = \gamma = 0$ .

Figure 7.12 shows that the optimal choice of values for the parameters  $\Theta$ ,  $\eta$  and  $\gamma$  in the FR formulation is dependent on the problem being solved and the variables being used, and experimentation may be the only method of distinguishing a ‘good’ evolution system from a ‘bad’ one. One way of picturing the growth of inaccuracies in evolved solutions is to consider an exact solution  $\mathcal{G}$  of Einstein’s equations which, because of numerical errors, is perturbed by an initially small amount to give a solution  $\mathcal{G} + \varepsilon$ ; while the exact solution  $\mathcal{G}$  is the same for all of the evolution systems, the perturbed solution  $\mathcal{G} + \varepsilon$  will be different in each case. Analysis of the linearized evolution equations for  $\varepsilon$  about  $\mathcal{G}$  may then give an indication of how fast errors in the numerical solutions can be expected to grow, and such an approach has been used by Scheel et al. (1998) to remedy a ‘continuum instability’ in a numerical code used to evolve the Schwarzschild solution. However this kind of analysis may prove to be difficult to apply to the present work: since the metric components of the cosmological spacetimes studied here typically vary in magnitude over very large ranges, the exponential growth of errors may be unavoidable even for very accurate numerical simulations.

The results shown in figure 7.12 can be used to answer two specific questions about the numerical performances of evolution systems: whether there is a connection between performance and the presence of non-physical characteristic speeds, and whether strongly hyperbolic evolution systems perform better than weakly hyperbolic ones. The dashed lines in the figure show crash times for the FR parameter range  $0 \leq \Theta \leq 1$  with  $\eta = \gamma = 1$ , where the modified FR and the original FR systems are at the end points of the interval. Although there are no significant variations in numerical performance across this parameter range, the properties of the evolution systems vary substantially: only the original FR system ( $\Theta = 1$ ) has characteristic speeds which all respect causality, and the sizes of the characteristic speeds increase up to  $\sqrt{5}$  times the speed of light as  $\Theta$  decreases to zero; only for  $\Theta < 1$  are the evolution systems strongly hyperbolic, and the modified FR system ( $\Theta = 0$ ) has been shown (Frittelli and Reula 1996) to be symmetric hyperbolic. Furthermore, figure 7.12 compares results for the ADM systems, which are weakly hyperbolic, and the causal FR systems, which are strongly hyperbolic, with both families of evolution systems having only physically relevant characteristic speeds, and it is clearly not the case that the latter systems perform consistently better than the former in numerical simulations. In conclusion, there is no reason to believe that weakly hyperbolic evolution systems produce less accurate numerical results than strongly (or symmetric) hyperbolic ones in general, or that non-physical characteristic speeds adversely affect the numerical performance of a system.

The results of this section show that the FR evolution system is in general out-performed by systems which are adapted to the symmetries of the spacetimes under investigation. However when compared with evolution systems which use the same set of variables, the FR system may (for appropriate parameter settings) produce more accurate results, although the gain in these cases is typically small. It is worth recalling here some of the potential advantages of hyperbolic formulations such as the FR system which motivate their development for use in numerical work: for a hyperbolic evolution system, well-posed boundary conditions can in principle be constructed; hyperbolicity allows analytic results concerning existence and uniqueness of solutions to be proved; sophisticated numerical methods can be applied to first-order systems for which the eigenfields of the principal part are known; and for relativistic hydrodynamics a hyperbolic formulation allows matter fields and metric fields to be treated in a unified manner. These advantages may be expected to become significant for numerical simulations of spacetimes which have no simplifying symmetries or in which realistic matter fields are present.

(As a final remark in this section it is noted that, for the numerical implementations of the evolution systems used here, the simulations based on the Moncrief equations (7.10) run about twice as fast as those based on the transformed FR formulation (7.23), which in turn run about fifteen percent faster than those based on the standard FR formulation, figure 4.1.)

# Chapter 8.

## Summary of Results

In this work, a computer code has been developed for the generation of numerical solutions to the vacuum Einstein equations; different formulations of the equations have been constructed, implemented, and tested; and one- and two-dimensional cosmological models have been numerically simulated and studied.

What follows is a chapter-by-chapter summary of the main results together with suggestions for future work.

### *Chapter 2*

The numerical simulations reported on in this work have been performed using standard finite difference integration methods together with a multi-dimensional high-resolution wave-propagation algorithm developed by LeVeque (1997). Through the implementation of appropriate Riemann solvers, the wave-propagation algorithm has been used to evolve one-dimensional spacetimes described by the Gowdy equations and two-dimensional spacetimes described by the Frittelli-Reula hyperbolic formulation of Einstein's equations. Second-order accuracy of the wave-propagation algorithm has been confirmed in both cases.

While numerical methods based on Riemann solvers have previously been used to evolve matter fields in relativistic spacetimes, this has been the first application of such methods to the evolution of gravitational fields. The natural extension of this work is to the situation in which gravitational fields are coupled to hydrodynamical sources; the full potential of the high-resolution method would then be demonstrated, with shock waves in the fluid producing non-smooth behaviour in the spacetime metric.

### *Chapter 3*

An adaptive mesh refinement algorithm has been implemented for problems in one and two spatial dimensions. The basic design of the algorithm follows the work of Berger and Oliger (1984) but with enhancements in grid management and interpolation techniques, among other things. The implementation of the algorithm has made use of object-oriented features of the C++ programming language and has been parallelized for use on multi-processor systems.

The adaptive mesh refinement algorithm has been used to significantly decrease the running times of simulations of Gowdy cosmologies and to reduce the demands made on computational resources by simulations of  $U(1)$ -symmetric cosmologies. To date, this has been one of only a small number of applications of adaptive mesh refinement to relativistic simulations in more than one spatial dimension. However, the importance of adaptive mesh refinement in numerical relativity should not be underestimated: such methods are almost certain to be required for the accurate simulation of three-dimensional spacetimes describing situations of astrophysical significance.

## Chapter 4

Frittelli and Reula's (1996) hyperbolic formulation of the Einstein equations has been generalized to include a one-parameter family of evolution systems which have only physically relevant characteristic speeds. The generalized formulation has been implemented in a numerical code for the evolution of vacuum spacetimes which have one spacelike Killing vector. This is the first time the Frittelli-Reula formulation has been used in numerical simulations. Exact and approximate Riemann solvers for the principal part of the evolution system have been developed and used to enable the code to generate numerical solutions using the wave-propagation algorithm.

While in this work difficulties with boundary conditions have been avoided by considering only periodic spatial domains, the use of hyperbolic formulations in the specification of stable boundary conditions for numerical simulations is potentially a fruitful line of research. Analysis of the initial boundary value problem for general relativity is simplified if the evolution system is hyperbolic; however this idea has to date received only limited attention (for example, Stewart 1998 and Friedrich and Nagy 1999).

## Chapter 5

Methods for comparing results from numerical simulations of the same spacetime produced using different gauge conditions have been investigated, and, as part of this, a numerical algorithm for tracking observer world lines has been developed. An analytic approach has been used to study foliations of Kasner and Gowdy spacetimes generated using the harmonic time slicing condition. Coordinate singularities of the type originally reported by Alcubierre (1997) have been shown to develop in these foliations under reasonably general conditions. They have been demonstrated to cause fine-scale features to appear in numerical solutions; these features are similar to but distinct from ones found in simulations of collapsing inhomogeneous cosmologies. The formation of coordinate singularities is potentially a serious drawback to the use of the harmonic time slicing condition in numerical simulations, and more research needs to be done to find out under what circumstances it occurs and how in practice it can be avoided.

## Chapter 6

Numerical simulations have been performed of Gowdy  $T^3$  cosmological models. Berger and Moncrief's (1993) numerical studies of collapsing cosmologies have been repeated and extended: the fine-scale spatial features that develop in the solutions have been tracked using adaptive mesh refinement and shown to have a physical origin. The evolved solutions have been found to be consistent with the conjecture that the Gowdy models are asymptotically velocity-term dominated at the singularity (although it is not true that the spatial derivative terms become negligible there).

For expanding Gowdy cosmologies, numerical evidence has been used to show that, while complex behaviour can occur at times soon after the initial 'big bang', at late times the spacetimes behave like perturbed homogeneous cosmologies. Results in the literature on the properties of

nonlinear gravitational waves have been examined and found to be inconsistent with some of the behaviour observed in the Gowdy models; the differences have been attributed to gauge effects.

While the frontiers of research in numerical relativity lie in the simulation of spacetimes which have no simplifying symmetries, there is a lot still to be learnt from one-dimensional models. Gowdy spacetimes with alternative spatial topologies and generalized models containing matter fields have not to date been studied in as much detail as the vacuum three-torus models. Furthermore, it is possible that methods could be developed for improving the resolution of spikes in collapsing metrics without the use of adaptive mesh refinement; for example it may be possible to introduce a non-trivial shift vector into the evolution system which would cause grid points to migrate towards the emerging spikes.

### *Chapter 7*

Numerical simulations have been performed of collapsing vacuum  $U(1)$ -symmetric  $T^3$  cosmologies using Moncrief's (1986) reduction of the Einstein equations. Mesh refinement techniques have been used to study the emergence in the spacetimes of fine-scale features which are related to the ones found in collapsing Gowdy cosmologies. However, the difficulty in evolving these spacetimes has meant that many aspects of their behaviour are as yet unexplored; in particular, nothing is known about the long-term behaviour of the fine-scale features.

A comparison has been made between numerical solutions produced for  $U(1)$ -symmetric spacetimes using three different evolution systems: Moncrief's reduction, the Frittelli-Reula formulation, and a hybrid of these. The use of a set of metric variables which are adapted to the nature of the spacetime under investigation has been shown to be a major factor contributing to the accuracy of numerical results; variations in the hyperbolicity and characteristic speeds of the evolution equations (as controlled by parameters in the generalized Frittelli-Reula system) have been shown to be a less significant factor, although still an important one.

While many hyperbolic formulations of Einstein's equations have been proposed in recent years, only a small number of these have to date been used in numerical simulations, and there has been little in the way of comparison between results produced using different formulations. The development of formulations of Einstein's equations which are well-suited to numerical work is an important line of research in numerical relativity; it is likely that the current generation of hyperbolic formulations represent only a first step in this direction.

## References

- Abrahams, A., Anderson, A., Choquet-Bruhat, Y., and York, J. W. 1995, “Einstein and Yang-Mills Theories in Hyperbolic Form without Gauge Fixing,” *Phys. Rev. Lett.*, **75**, 3377–3381.
- Abrahams, A., Anderson, A., Choquet-Bruhat, Y., and York, J. W. 1996, “A Non-Strictly Hyperbolic System for the Einstein Equations with Arbitrary Lapse and Shift,” *C. R. Acad. Sci. Paris, Série II*, **323**, 835–841.
- Abrahams, A., Anderson, A., Choquet-Bruhat, Y., and York, J. W. 1997, “Geometrical Hyperbolic Systems for General Relativity and Gauge Theories,” *Class. Quantum Grav.*, **14**, A9–A22.
- Abramowitz, M., and Stegun, I. A. 1964, *Handbook of Mathematical Functions* (Dover Publications, Inc).
- Adams, P. J., Hellings, R. W., Zimmerman, R. L., Farhoosh, H., Levine, D. I., and Zeldich, S. 1982, “Inhomogeneous Cosmology: Gravitational Radiation in Bianchi Backgrounds,” *Astrophys. J.*, **253**, 1–18.
- Alcubierre, M. 1997, “Appearance of Coordinate Shocks in Hyperbolic Formulations of General Relativity,” *Phys. Rev. D*, **55**, 5981–5991.
- Alcubierre, M., Brügmann, B., Miller, M., and Suen, W.-M. 1999, “A Conformal Hyperbolic Formulation of the Einstein Equations,” e-print [gr-qc/9903030](http://arxiv.org/abs/gr-qc/9903030).
- Alcubierre, M., and Massó, J. 1998, “Pathologies of Hyperbolic Gauges in General Relativity and Other Field Theories,” *Phys. Rev. D*, **57**, 4511–4515.
- Anderson, A., Abrahams, A. M., and Lea, C. 1998, “Curvature-Based Gauge-Invariant Perturbation Theory for Gravity: A New Paradigm,” *Phys. Rev. D*, **58**, 064015 (15 pages).
- Anderson, A., Choquet-Bruhat, Y., and York, J. W. 1997, “Einstein-Bianchi Hyperbolic System for General Relativity,” *Topol. Meth. Nonlinear Anal.*, **10**, 353–373.
- Anderson, A., and York, J. W. 1999, “Fixing Einstein’s Equations,” *Phys. Rev. Lett.*, **82**, 4384–4387.
- Andréasson, H. 1998, “Global Foliations of Matter Spacetimes with Gowdy Symmetry,” e-print [gr-qc/9812035](http://arxiv.org/abs/gr-qc/9812035).
- Anninos, P. 1998a, “Plane-Symmetric Cosmology with Relativistic Hydrodynamics,” *Phys. Rev. D*, **58**, 064010 (12 pages).
- Anninos, P. 1998b, “Computational Cosmology: from the Early Universe to the Large Scale Structure,” Living Review, <http://www.livingreviews.org/Articles/Volume1/1998-9anninos>.
- Anninos, P., Centrella, J., and Matzner, R. A. 1991a, “Numerical Methods for Solving the Planar Vacuum Einstein Equations,” *Phys. Rev. D*, **43**, 1808–1824.
- Anninos, P., Centrella, J., and Matzner, R. A. 1991b, “Nonlinear Wave Solutions to the Planar Vacuum Einstein Equations,” *Phys. Rev. D*, **43**, 1825–1838.

- Anninos, P., Massó, J., Seidel, E., Suen, W.-M., and Tobias, M. 1997, “Dynamics of Gravitational Waves in 3D: Formulations, Methods and Tests,” *Phys. Rev. D*, **56**, 842–858.
- Arbona, A., and Bona, C. 1999, “Dealing with the Center and Boundary Problems in 1D Numerical Relativity,” *Comp. Phys. Commun.*, **118**, 229–235.
- Ashtekar, A., and Husain, V. 1998, “Symmetry Reduced Einstein Gravity and Generalized  $\sigma$  and Chiral Models,” *Int. J. Mod. Phys. D*, **7**, 549–566.
- Barrow, J. D., and Tipler, F. J. 1979, “Analysis of the Generic Singularity Studies by Belinskii, Khalatnikov, and Lifschitz,” *Phys. Rep.*, **56**, 371–402.
- Belinskii, V. A., Khalatnikov, I. M., and Lifschitz, E. M. 1970, “Oscillatory Approach to a Singular Point in the Relativistic Cosmology,” *Adv. Phys.*, **19**, 525–573.
- Belinskii, V. A., Khalatnikov, I. M., and Lifschitz, E. M. 1982, “A General Solution of the Einstein Equations with a Time Singularity,” *Adv. Phys.*, **31**, 639–667.
- Bell, J., Berger, M., Saltzman, J., and Welcome, M. 1994, “Three-Dimensional Adaptive Mesh Refinement for Hyperbolic Conservation Laws,” *SIAM J. Sci. Comput.*, **15**, 127–138.
- Berger, B. K. 1974, “Quantum Graviton Creation in a Model Universe,” *Ann. Phys. (N.Y.)*, **83**, 458–490.
- Berger, M. J. 1982, “Adaptive Mesh Refinement for Hyperbolic Partial Differential Equations,” Ph.D. dissertation, Department of Computer Science, Stanford University.
- Berger, B. K. 1984, “Quantum Effects in the Gowdy  $T^3$  Cosmology,” *Ann. Phys. (N.Y.)*, **156**, 155–193.
- Berger, M. J. 1985, “Stability of Interfaces with Mesh Refinement,” *Math. of Comput.*, **45**, 301–318.
- Berger, M. J. 1986, “Data-Structures for Adaptive Grid Generation,” *SIAM J. Sci. Stat. Comput.*, **7**, 904–916.
- Berger, M. J. 1987, “On Conservation at Grid Interfaces,” *SIAM J. Num. Anal.*, **24**, 967–984.
- Berger, B. K. 1997, “Numerical Investigation of Singularities,” e-print [gr-qc/9512003](http://arxiv.org/abs/gr-qc/9512003), in *Proceedings of the 14th International Conference on General Relativity and Gravitation*, edited by M. Francaviglia, G. Longhi, L. Lusanna and E. Sorace (World Scientific).
- Berger, B. K. 1998, “Numerical Approaches to Spacetime Singularities,” Living Review, <http://www.livingreviews.org/Articles/Volume1/1998-7berger/>.
- Berger, B. K., Chruściel, P. T., Isenberg, J., and Moncrief, V. 1997, “Global Foliations of Vacuum Spacetimes with  $T^2$  Isometry,” *Ann. Phys. (N.Y.)*, **260**, 117–148.
- Berger, M. J., and Colella, P. 1989, “Local Adaptive Mesh Refinement for Shock Hydrodynamics,” *J. Comput. Phys.*, **82**, 64–84.
- Berger, B. K., and Garfinkle, D. 1998, “Phenomenology of the Gowdy Universe on  $T^3 \times R$ ,” *Phys. Rev. D*, **57**, 4767–4777.

- Berger, B. K., Garfinkle, D., Isenberg, J., Moncrief, V., and Weaver, M. 1998, “The Singularity in Generic Gravitational Collapse is Spacelike, Local, and Oscillatory,” *Mod. Phys. Lett. A*, **13**, 1565–1574.
- Berger, B. K., Garfinkle, D., and Swamy, V. 1995, “Detection of Computer Generated Gravitational Waves in Numerical Cosmologies,” *Gen. Rel. Grav.*, **27**, 511–527.
- Berger, M. J., and LeVeque, R. J. 1997, AMRCLAW source code, beta version 0.3, available at <http://www.amath.washington.edu/~rjl/amrclaw/index.html>.
- Berger, M. J., and LeVeque, R. J. 1998, “Adaptive Mesh Refinement using Wave-Propagation Algorithms for Hyperbolic Systems,” *SIAM J. Numer. Anal.*, **35**, 2298–2316.
- Berger, B. K., and Moncrief, V. 1993, “Numerical Investigation of Cosmological Singularities,” *Phys. Rev. D*, **48**, 4676–4687.
- Berger, B. K., and Moncrief, V. 1998a, “Numerical Evidence that the Singularity in Polarized  $U(1)$  Symmetric Cosmologies on  $T^3 \times R$  is Velocity Dominated,” *Phys. Rev. D*, **57**, 7235–7240.
- Berger, B. K., and Moncrief, V. 1998b, “Evidence for an Oscillatory Singularity in Generic  $U(1)$  Symmetric Cosmologies on  $T^3 \times R$ ,” *Phys. Rev. D*, **58**, 064023 (8 pages).
- Berger, M. J., and Olinger, J. 1984, “Adaptive Mesh Refinement for Hyperbolic Partial Differential Equations,” *J. Comput. Phys.*, **53**, 484–512.
- Bona, C., and Massó, J. 1988, “Harmonic Synchronizations of Spacetime,” *Phys. Rev. D*, **38**, 2419–2422.
- Bona, C., and Massó, J. 1989, “Einstein’s Evolution Equations as a System of Balance Laws,” *Phys. Rev. D*, **40**, 1022–1026.
- Bona, C., and Massó, J. 1992, “Hyperbolic Evolution System for Numerical Relativity,” *Phys. Rev. Lett.*, **68**, 1097–1099.
- Bona, C., and Massó, J. 1993, “Numerical Relativity: Evolving Spacetime,” *Int. J. Mod. Phys. C*, **4**, 883–907.
- Bona, C., Massó, J., Seidel, E., and Stela, J. 1995, “New Formalism for Numerical Relativity,” *Phys. Rev. Lett.*, **75**, 600–603.
- Bona, C., Massó, J., Seidel, E., and Stela, J. 1997, “First Order Hyperbolic Formalism for Numerical Relativity,” *Phys. Rev. D*, **56**, 3405–3415.
- Bona, C., Massó, J., Seidel, E., and Walker, P. 1998, “Three Dimensional Numerical Relativity with a Hyperbolic Formulation,” e-print [gr-qc/9804052](http://arxiv.org/abs/gr-qc/9804052).
- Bona, C., Massó, J., and Stela, J. 1995, “Numerical Black Holes: A Moving Grid Approach,” *Phys. Rev. D*, **51**, 1639–1645.
- Boyd, P. T., Centrella, J. M., and Klasky, S. A. 1991, “Properties of Gravitational ‘Solitons’,” *Phys. Rev. D*, **43**, 379–390.
- Brodbeck, O., Frittelli, S., Hübner, P., and Reula, O. A. 1999, “Einstein’s Equations with Asymptotically Stable Constraint Propagation,” *J. Math. Phys.*, **40**, 909–923.



- Brügmann, B. 1996, “Adaptive Mesh and Geodesically Sliced Schwarzschild Spacetime in  $3 + 1$  Dimensions,” *Phys. Rev. D*, **54**, 7361–7372.
- Brügmann, B. 1999, “Binary Black Hole Mergers in 3D Numerical Relativity,” *Int. J. Mod. Phys.*, **8**, 85–100.
- Carmeli, M., Charach, Ch., and Malin, S. 1981, “Survey of Cosmological Models with Gravitational, Scalar and Electromagnetic Waves,” *Phys. Rep.*, **76**, 79–156.
- Centrella, J. 1979, “Plane-Symmetric Cosmologies: a Study of Inhomogeneities in the Universe using Numerical Relativity,” Ph.D. dissertation, University of Cambridge.
- Centrella, J. 1980a, “Gravitational Wave Perturbations and Gauge Conditions,” *Phys. Rev. D*, **21**, 2776–2784.
- Centrella, J. 1980b, “Interacting Gravitational Shocks in Vacuum Plane-Symmetric Cosmologies,” *Astrophys. J.*, **241**, 875–885.
- Centrella, J. M. 1986, “Nonlinear Gravitational Waves and Inhomogeneous Cosmologies,” in *Dynamical Spacetimes and Numerical Relativity*, edited by J. M. Centrella (Cambridge University Press).
- Centrella, J., and Matzner, R. A. 1979, “Plane-Symmetric Cosmologies,” *Astrophys. J.*, **230**, 311–324.
- Centrella, J., and Matzner, R. A. 1982, “Colliding Gravitational Waves in Expanding Cosmologies,” *Phys. Rev. D*, **25**, 930–941.
- Centrella, J., Matzner, R. A., Rothman, T., and Wilson, J. R. 1986, “Cosmic Nucleosynthesis and Nonlinear Inhomogeneities,” *Nuc. Phys. B*, **266**, 171–227.
- Centrella, J., and Wilson, J. R. 1983, “Planar Numerical Cosmology. I. The Differential Equations,” *Astrophys. J.*, **273**, 428–435.
- Centrella, J., and Wilson, J. R. 1984, “Planar Numerical Cosmology. II. The Difference Equations and Numerical Tests,” *Astrophys. J. Suppl.*, **54**, 229–249.
- Choptuik, M. W. 1989, “Experiences with an Adaptive Mesh Refinement Algorithm in Numerical Relativity,” in *Frontiers in Numerical Relativity*, edited by C. Evans, S. Finn and D. Hobill (Cambridge University Press).
- Choptuik, M. W. 1992, “‘Critical’ Behaviour in Massless Scalar Field Collapse,” in *Approaches to Numerical Relativity*, edited by R. D’Inverno (Cambridge University Press).
- Choptuik, M. W. 1993, “Universality and Scaling in Gravitational Collapse of a Massless Scalar Field,” *Phys. Rev. Lett.*, **70**, 9–12.
- Choptuik, M. W., Chmaj, T., and Bizoń, P. 1996, “Critical Behaviour in Gravitational Collapse of a Yang-Mills Field,” *Phys. Rev. Lett.*, **77**, 424–427.
- Choquet-Bruhat, Y., and Moncrief, V. 1994, “An Existence Theorem for the Reduced Einstein Equations,” *C. R. Acad. Sci. Paris, Série I*, **319**, 153–159.

- Choquet-Bruhat, Y., and York, J. W. 1995, “Geometrical Well Posed Systems for the Einstein Equations,” *C. R. Acad. Sci. Paris, Série I*, **321**, 1089–1095.
- Choquet-Bruhat, Y., York, J. W., and Anderson, A. 1998, “Curvature-Based Hyperbolic Systems for General Relativity,” e-print [gr-qc/9802027](https://arxiv.org/abs/gr-qc/9802027), in *Proceedings of the Eighth Marcel Grossmann Meeting on General Relativity*, edited by T. Piran.
- Chrusciel, P. T., Isenberg, J., and Moncrief, V. 1990, “Strong Cosmic Censorship in Polarised Gowdy Spacetimes,” *Class. Quantum Grav.*, **7**, 1671–1680.
- Cook, G. B., and Scheel, M. A. 1997, “Well-Behaved Harmonic Time Slices of a Charged, Rotating, Boosted Black Hole,” *Phys. Rev. D*, **56**, 4775–4781.
- Cook, G. B., and Teukolsky, S. A. 1999, “Numerical Relativity: Challenges for Computational Science,” *Acta Numerica*, **8**, 1–45.
- Cortesi, D. 1998, “Origin2000 and Onyx2 Performance Tuning and Optimization Guide,” Silicon Graphics, Inc., Document Number 007-3430-002, see <http://techpubs.sgi.com:/library/>.
- Cosnard, M., and Trystram, D. 1995, *Parallel Algorithms and Architectures* (International Thompson Computer Press).
- Courant, R., and Hilbert, D. 1962, *Methods of Mathematical Physics, Volume II* (Interscience Publishers).
- Diener, P., Jansen, N., Khokhlov, A., Novikov, I. 1999, “Adaptive Mesh Refinement Approach to Construction of Initial Data for Black Hole Collisions,” e-print [gr-qc/9905079](https://arxiv.org/abs/gr-qc/9905079).
- Eardley, D., Liang, E., and Sachs, R. 1972, “Velocity-Dominated Singularities in Irrotational Dust Cosmologies,” *J. Math. Phys.*, **13**, 99–107.
- Eardley, D. M., and Smarr, L. 1979, “Time Functions in Numerical Relativity: Marginally Bound Dust Collapse,” *Phys. Rev. D*, **19**, 2239–2259.
- Estabrook, F. B., Robinson, R. S., and Wahlquist, H. D. 1997, “Hyperbolic Equations for Vacuum Gravity Using Special Orthonormal Frames,” *Class. Quantum Grav.*, **14**, 1237–1247.
- Fier, J. 1996, “Origin2000 Performance Tuning and Optimization,” Silicon Graphics, Inc., Document Number 007-3430-001, see <http://techpubs.sgi.com:/library/>.
- Font, J. A., Miller, M., Suen, W.-M., and Tobias, M. 1998, “Three Dimensional General Relativistic Hydrodynamics. I. Formulations, Methods and Code Tests,” e-print [gr-qc/9811015](https://arxiv.org/abs/gr-qc/9811015).
- Frauenhdiener, J. 1998, “Numerical Treatment of the Hyperboloidal Initial Value Problem for the Vacuum Einstein Equations. I. The Conformal Field Equations,” *Phys. Rev. D*, **58**, 064002 (10 pages).
- Friedrich, H. 1996, “Hyperbolic Reductions for Einstein’s Equations,” *Class. Quantum Grav.*, **13**, 1451–1469.
- Friedrich, H. 1998, “Evolution Equations for Gravitating Ideal Fluid Bodies in General Relativity,” *Phys. Rev. D*, **57**, 2317–2322.

- Friedrich, H., and Nagy, G. 1999, “The Initial Boundary Value Problem for Einstein’s Vacuum Field Equations,” *Commun. Math. Phys.*, **201**, 619–655.
- Frittelli, S. 1997, “Note on the Propagation of the Constraints in Standard 3+1 General Relativity,” *Phys. Rev. D*, **55**, 5992–5996.
- Frittelli, S., and Reula, O. 1994, “On the Newtonian Limit of General Relativity,” *Commun. Math. Phys.*, **166**, 221–235.
- Frittelli, S., and Reula, O. A. 1996, “First-Order Symmetric Hyperbolic Einstein Equations with Arbitrary Fixed Gauge,” *Phys. Rev. Lett.*, **76**, 4667–4670.
- Frittelli, S., and Reula, O. A. 1999, “Well-Posed Forms of the 3+1 Conformally-Decomposed Einstein Equations,” e-print gr-qc/9904048.
- Garfinkle, D. 1999, “Numerical Simulations of Gowdy Spacetimes on  $S^2 \times S^1 \times R$ ,” e-print gr-qc/9906019.
- Geyer, A., and Herold, H. 1995, “Slicing the Schwarzschild Spacetime: Harmonic versus Maximal Slicing,” *Phys. Rev. D*, **52**, 6182–6185.
- Geyer, A., and Herold, H. 1997, “Slicing the Oppenheimer-Snyder Collapse: Harmonic versus Maximal Slicing,” *Gen. Rel. Grav.*, **29**, 1257–1268.
- Godlewski, E., and Raviart, P.-A. 1996, *Numerical Approximation of Hyperbolic Systems of Conservation Laws* (Springer-Verlag).
- Gowdy, R. H. 1971, “Gravitational Waves in Closed Universes,” *Phys. Rev. Lett.*, **27**, 826–829 and erratum p1102.
- Gowdy, R. H. 1974, “Vacuum Spacetimes with Two-Parameter Spacelike Isometry Groups and Compact Invariant Hypersurfaces: Topologies and Boundary Conditions,” *Ann. Phys. (N.Y.)*, **83**, 203–241.
- Griffiths, J. B., and Alekseev, G. A. 1998, “Some Unpolarized Gowdy Cosmologies and Noncolinear Colliding Plane Wave Spacetimes,” *Int. J. Mod. Phys. D*, **7**, 237–247.
- Grubišić, B., and Moncrief, V. 1993, “Asymptotic Behaviour of the  $T^3 \times R$  Gowdy Space-Times,” *Phys. Rev. D*, **47**, 2371–2382.
- Grubišić, B., and Moncrief, V. 1994, “Mixmaster Spacetime, Geroch’s Transformation, and Constants of the Motion,” *Phys. Rev. D*, **49**, 2792–2800.
- Gustafsson, B., Kreiss, H.-O., and Olinger, J. 1995, *Time Dependent Problems and Difference Methods* (Wiley).
- Hamadé, R. S. 1997, “Critical Phenomena in Gravitational Collapse,” Ph.D. dissertation, University of Cambridge.
- Hamadé, R. S., Horne, J. H., and Stewart, J. M. 1996, “Continuous Self-Similarity and  $S$ -Duality,” *Class. Quantum Grav.*, **13**, 2241–2253.
- Hamadé, R. S., and Stewart, J. M. 1996, “The Spherically Symmetric Collapse of a Massless Scalar Field,” *Class. Quantum Grav.*, **13**, 497–512.

- Hawking, S. W., and Ellis, G. F. R. 1973, *The Large Scale Structure of Space-Time* (Cambridge University Press).
- Hearn, A. C. 1995, “REDUCE User’s Manual, Version 3.6,” available at <http://www.uni-koeln.de/REDUCE/3.6/doc/reduce/>.
- Hern, S. D., and Stewart, J. M. 1998, “The Gowdy  $T^3$  Cosmologies Revisited,” *Class. Quantum Grav.*, **15**, 1581–1593.
- Hirsch, C. 1988, *Numerical Computation of Internal and External Flows. Volume 1: Fundamentals of Numerical Discretization* (Wiley).
- Hirsch, C. 1990, *Numerical Computation of Internal and External Flows. Volume 2: Computational Methods for Inviscid and Viscous Flows* (Wiley).
- Hobill, D. W., and Smarr, L. L. 1989, “Supercomputing and Numerical Relativity: A Look at the Past, Present and Future” in *Frontiers in Numerical Relativity*, edited by C. Evans, S. Finn and D. Hobill (Cambridge University Press).
- Horowitz, E., Sahni, S., and Rajasekaran, S. 1998, *Computer Algorithms* (Computer Science Press).
- Hübner, P. 1998, “How to Avoid Artificial Boundaries in the Numerical Calculation of Black Hole Spacetimes,” e-print [gr-qc/9804065](http://arxiv.org/abs/gr-qc/9804065).
- Iriondo, M. S., Leguizamón, E. O., and Reula, O. A. 1997, “Einstein’s Equation in Ashtekar’s Variables Constitutes a Symmetric Hyperbolic System,” *Phys. Rev. Lett.*, **79**, 4732–4735.
- Iriondo, M. S., Leguizamón, E. O., and Reula, O. A. 1998, “On the Dynamics of Einstein’s Equations in the Ashtekar Formulation,” *Adv. Theor. Math. Phys.*, **2**, 1075–1103.
- Isaacson, R. A. 1968a, “Gravitational Radiation in the Limit of High Frequency. I. The Linear Approximation and Geometrical Optics,” *Phys. Rev.*, **166**, 1263–1271.
- Isaacson, R. A. 1968b, “Gravitational Radiation in the Limit of High Frequency. II. Nonlinear Terms and the Effective Stress Tensor,” *Phys. Rev.*, **166**, 1272–1280.
- Isenberg, J., and Moncrief, V. 1982, “The Existence of Constant Mean Curvature Foliations of Gowdy 3-Torus Spacetimes,” *Commun. Math. Phys.*, **86**, 485–493.
- Isenberg, J., and Moncrief, V. 1990, “Asymptotic Behaviour of the Gravitational Field and the Nature of Singularities in Gowdy Spacetimes,” *Ann. Phys. (N.Y.)*, **199**, 84–122.
- John, F. 1982, *Partial Differential Equations, Fourth Edition* (Springer-Verlag).
- Kichenassamy, S., and Rendall, A. D. 1998, “Analytic Description of Singularities in Gowdy Spacetimes,” *Class. Quantum Grav.*, **15**, 1339–1355.
- Krasiński, A. 1997, *Inhomogeneous Cosmological Models* (Cambridge University Press).
- Kreiss, H.-O., and Lorenz, J. 1989, *Initial-Boundary Value Problems and the Navier-Stokes Equations* (Academic Press).
- Kurki-Suonio, H., Centrella, J., Matzner, R. A., and Wilson, J. R. 1987, “Inflation from Inhomogeneous Initial Data in a One-Dimensional Back-Reacting Cosmology,” *Phys. Rev. D*, **35**, 435–448.

- Langseth, J. O., and LeVeque, R. J. 1999, “A Wave Propagation Method for Three-Dimensional Hyperbolic Conservation Laws,” pre-print available at <http://www.amath.washington.edu/~rjl/publications.html>.
- LeVeque, R. J. 1992, *Numerical Methods for Conservation Laws* (Birkhäuser-Verlag).
- LeVeque, R. J. 1996, “High-Resolution Conservative Algorithms for Advection in Incompressible Flow,” *SIAM J. Numer. Anal.*, **33**, 627–665.
- LeVeque, R. J. 1997, “Wave Propagation Algorithms for Multi-Dimensional Hyperbolic Systems,” *J. Comput. Phys.*, **131**, 327–353.
- LeVeque, R. J. 1998, “CLAWPACK User Notes,” available together with source code (version 3.0) at <http://www.amath.washington.edu/~rjl/clawpack.html>.
- Lippman, S. B., and Lajoie, J. 1998, *C++ Primer* (Addison-Wesley Publishing Company).
- MacCallum, M. A. H., and Wright, F. J. 1991, *Algebraic Computing with REDUCE* (Oxford University Press).
- Massó, J., Seidel, E., and Walker, P. 1995, “Adaptive Mesh Refinement in Numerical Relativity,” e-print [gr-qc/9412057](http://arxiv.org/abs/gr-qc/9412057), in *General Relativity (MG7 Proceedings)*, edited by R. Ruffini and M. Keiser (World Scientific).
- Massó, J., and Walker, P. 1999, “Cactus: Thorny Problems in Numerical Relativity,” web page at <http://cactus.aei-potsdam.mpg.de/>.
- McGuigan, M. 1991, “Gowdy Cosmology and Two-Dimensional Gravity,” *Phys. Rev. D*, **43**, 1199–1211.
- Misner, C. W. 1968, “The Isotropy of the Universe,” *Astrophys. J.*, **151**, 431–457.
- Misner, C. W. 1973, “A Minisuperspace Example: The Gowdy  $T^3$  Cosmology,” *Phys. Rev. D*, **8**, 3271–3285.
- Misner, C. W., Thorne, K. S., and Wheeler, J. A. 1973, *Gravitation* (W. H. Freeman and Company).
- Mitra, S., Parashar, M., and Browne, J. 1998, “DAGH: User’s Guide,” at <http://www.cs.utexas.edu/users/dagh>.
- Moncrief, V. 1981, “Global Properties of Gowdy Spacetimes with  $T^3 \times R$  Topology,” *Ann. Phys. (N.Y.)*, **132**, 87–107.
- Moncrief, V. 1986, “Reduction of Einstein’s Equations of Vacuum Space-Times with Spacelike  $U(1)$  Isometry Groups,” *Ann. Phys. (N.Y.)*, **167**, 118–142.
- Moncrief, V. 1987, “An Infinite-Dimensional Family of Curvature Singular Vacuum Spacetimes with  $U(1)$  Isometry Groups,” *Class. Quantum Grav.*, **4**, 1555–1563.
- Moncrief, V. 1989, “Reduction of the Einstein Equations in  $2 + 1$  Dimensions to a Hamiltonian System over Teichmüller Space,” *J. Math. Phys.*, **30**, 2907–2914.
- Moncrief, V. 1990, “Reduction of the Einstein-Maxwell and Einstein-Maxwell-Higgs Equations for Cosmological Spacetimes with Spacelike  $U(1)$  Isometry Groups,” *Class. Quantum Grav.*, **7**, 329–352.

- Musgrave, P., Pollney, D., and Lake, K. 1996, "GRTensorII," documentation available at <http://www.astro.queensu.ca/~grtensor/>.
- New, K. C. B., Watt, K., Misner, C. W., and Centrella, J. M. 1998, "Stable 3-Level Leapfrog Integration in Numerical Relativity," *Phys. Rev. D*, **58**, 064022 (14 pages).
- Ove, R. 1986, "Numerical Investigations of Cosmic Censorship on  $T^3 \times R$ ," in *Dynamical Spacetimes and Numerical Relativity*, edited by J. M. Centrella (Cambridge University Press).
- Ove, R. 1989, "Symmetry and Singularity Formation in Expanding Spacetimes," *Phys. Rev. D*, **39**, 3587–3595.
- Ove, R. 1990a, "Nonlinear Gravitational Effect," *Phys. Rev. Lett.*, **64**, 1200–1203.
- Ove, R. 1990b, "Analysis of Cosmological Gravitational Wave Residue," *Class. Quantum Grav.*, **7**, 2225–2236.
- Ove, R. 1990c, "Anomalous Foliations of Einstein Space-Times," *J. Math. Phys.*, **31**, 2688–2693.
- Papadopoulos, P., Seidel, E., and Wild, L. 1998, "Adaptive Computation of Gravitational Waves from Black Hole Interactions," *Phys. Rev. D*, **58**, 084002 (15 pages).
- Petrich, L. I., Shapiro, S. L., and Teukolsky, S. A. 1985, "Oppenheimer-Snyder Collapse with Maximal Time Slicing and Isotropic Coordinates," *Phys. Rev. D*, **31**, 2459–2469.
- Petrich, L. I., Shapiro, S. L., and Teukolsky, S. A. 1986, "Oppenheimer-Snyder Collapse in Polar Time Slicing," *Phys. Rev. D*, **33**, 2100–2110.
- Piran, T. 1981, "Problems and Solutions in Numerical Relativity," *Ann. N. Y. Acad. Sci.*, **375**, 1–14.
- Plewa, T. 1999, "Adaptive Mesh Refinement for Structured Grids," web page at <http://www.camk.edu.pl/~tomek/AMRA/amr.html>.
- Potter, D. 1973, *Computational Physics* (Wiley).
- Press, W. H., Teukolsky, S. A., Vetterling, W. T., and Flannery, B. P. 1992, *Numerical Recipes, Second Edition* (Cambridge University Press).
- Quirk, J. J., and Hanebutte, U. R. 1993, "A Parallel Adaptive Mesh Refinement Algorithm," NASA Contractor Report 191530, ICASE Report No. 93-63.
- Reula, O. A. 1998, "Hyperbolic Methods for Einstein's Equations," Living Review, <http://www.livingreviews.org/Articles/Volume1/1998-3reula/>.
- Roe, P. L. 1981, "Approximate Riemann Solvers, Parameter Vectors, and Difference Schemes," *J. Comp. Phys.*, **43**, 357–372.
- Rupright, M. E., Abrahams, A. M., and Rezzolla, L. 1998, "Cauchy-Perturbative Matching and Outer Boundary Conditions. I. Methods and Tests," *Phys. Rev. D*, **58**, 044005 (9 pages).
- Ryan, M. P., and Shepley, L. C. 1975, *Homogeneous Relativistic Cosmologies* (Princeton University Press).

- Scheel, M. A., Baumgarte, T. W., Cook, G. B., Shapiro, S. L., and Teukolsky, S. A. 1997, “Numerical Evolution of Black Holes with a Hyperbolic Formulation of General Relativity,” *Phys. Rev. D*, **56**, 6320–6335.
- Scheel, M. A., Baumgarte, T. W., Cook, G. B., Shapiro, S. L., and Teukolsky, S. A. 1998, “Treating Instabilities in a Hyperbolic Formulation of Einstein’s Equations,” *Phys. Rev. D*, **58**, 044020 (12 pages).
- Seidel, E. 1996, “New Developments in Numerical Relativity,” *Helv. Phys. Acta*, **69**, 454–471.
- Seidel, E. 1998, “Numerical Relativity: Towards Simulations of 3D Black Hole Coalescence,” e-print [gr-qc/9806088](https://arxiv.org/abs/gr-qc/9806088), to appear in GR15 proceedings.
- Shinkai, H., and Maeda, K. 1993, “Can Gravitational Waves Prevent Inflation?” *Phys. Rev. D*, **48**, 3910–3913.
- Shinkai, H., and Maeda, K. 1994, “Generality of Inflation in a Planar Universe,” *Phys. Rev. D*, **49**, 6367–6378.
- Shinkai, H., and Yoneda, G. 1999, “Asymptotically Constrained and Real-Values System Based On Ashtekar’s Variables,” e-print [gr-qc/9906062](https://arxiv.org/abs/gr-qc/9906062).
- Smarr, L., and York, J. W. 1978, “Kinematical Conditions in the Construction of Spacetime,” *Phys. Rev. D*, **17**, 2529–2551.
- Sod, G. A. 1985, *Numerical Methods in Fluid Dynamics: Initial and Initial Boundary-Value Problems* (Cambridge University Press).
- Stewart, J. M. 1984, “Numerical Relativity,” in *Classical General Relativity*, edited by W. B. Bonnor, J. N. Islam and M. A. H. MacCallum (Cambridge University Press).
- Stewart, J. M. 1998, “The Cauchy Problem and the Initial Boundary Value Problem in Numerical Relativity,” *Class. Quantum Grav.*, **15**, 2865–2889.
- Strang, G. 1968, “On the Construction and Comparison of Difference Schemes,” *SIAM J. Numer. Anal.*, **5**, 506–517.
- Stroustrup, B. 1997, *The C++ Programming Language, Third Edition* (Addison-Wesley Publishing Company).
- Tanimoto, M. 1998, “New Varieties of Gowdy Spacetimes,” *J. Math. Phys.*, **39**, 4891–4898.
- Toro, E. F. 1997, *Riemann Problems and Numerical Methods for Fluid Dynamics: A Practical Introduction* (Springer-Verlag).
- van Elst, H., and Ellis, G. F. R. 1999, “Causal Propagation of Geometrical Fields in Relativistic Cosmology,” *Phys. Rev. D*, **59**, 024013 (22 pages).
- van Putten, M. H. P. M. 1997, “Numerical Integration of Nonlinear Wave Equations for General Relativity,” *Phys. Rev. D*, **55**, 4705–4711.
- van Putten, M. H. P. M., and Eardley, D. M. 1996, “Nonlinear Wave Equations for Relativity,” *Phys. Rev. D*, **53**, 3056–3063.

- Varadarajan, M. 1995, “Gauge Fixing of One Killing Field Reductions of Canonical Gravity: The Case of Asymptotically Flat Induced Two-Geometry,” *Phys. Rev. D*, **52**, 2020–2029.
- Wald, R. M. 1984, *General Relativity* (University of Chicago Press).
- Wild, L. A. 1996, “Adaptive Mesh Refinement in Numerical Relativity,” Ph.D. dissertation, University of Wales.
- Witten, L. 1959, “Invariants of General Relativity and the Classification of Spaces,” *Phys. Rev.*, **113**, 357–362.
- Yoneda, G., and Shinkai, H. 1999a, “Symmetric Hyperbolic System in the Ashtekar Formulation,” *Phys. Rev. Lett.*, **82**, 263–266.
- Yoneda, G., and Shinkai, H. 1999b, “Constructing Hyperbolic Systems in the Ashtekar Formulation of General Relativity,” e-print [gr-qc/9901053](#).
- York, J. W. 1979, “Kinematics and Dynamics of General Relativity,” in *Sources of Gravitational Radiation*, edited by L. Smarr (Cambridge University Press).
- York, J. W. 1989, “Initial Data for Collisions of Black Holes and Other Gravitational Miscellany,” in *Frontiers in Numerical Relativity*, edited by C. Evans, S. Finn and D. Hobill (Cambridge University Press).



This figure "figure-314.jpg" is available in "jpg" format from:

<http://arxiv.org/ps/gr-qc/0004036v1>